# NUMERICAL BEAM STABILITY STUDIES IN EXTERNAL INJECTION PLASMA-WAKEFIELD ACCELERATION REGIMES

Dissertation
zur Erlangung des Doktorgrades
an der Fakultät für
Mathematik, Informatik und Naturwissenschaften
Fachbereich Physik
der Universität Hamburg

vorgelegt von
Alexander Aschikhin

Hamburg
2019

Gutachter der Dissertation:
PD Dr. Bernhard Schmidt
Prof. Dr. Brian Foster

Zusammensetzung der Prüfungskommission:
PD Dr. Bernhard Schmidt
Prof. Dr. Brian Foster
Prof. Dr. Caren Hagner
Prof. Dr. Gudrid Moortgat-Pick
Prof. Dr. Christian Schwanenberger

Datum der Disputation: 18.03.2019

| | |
|---|---|
| Vors. der Prüfungskommission: | Prof. Dr. Caren Hagner |
| Vors. Fach-Promotionsausschusses Physik: | Prof. Dr. Wolfgang Hansen |
| Leiterin des Fachbereichs Physik: | Prof. Dr. Michael Potthoff |
| Dekan der MIN Fakultät: | Prof. Dr. Heinrich Graener |

ALEXANDER ASCHIKHIN

# NUMERICAL BEAM STABILITY STUDIES IN EXTERNAL INJECTION PLASMA-WAKEFIELD ACCELERATION REGIMES

Hamburg, January 2019

# ABSTRACT

This work considers the phase-space evolution of an externally injected electron beam under various plasma-based acceleration scenarios using numerical methods.

Plasma wakefield acceleration, an exceptional technology with the potential to drive the next generation of particle accelerators, uses a particle driver to excite a wakefield carrying gradients in the range of $10\,\mathrm{GV\,m^{-1}}$ to $100\,\mathrm{GV\,m^{-1}}$, orders of magnitude higher than the conventional cavities currently available. However, the plasma environment has stringent requirements with respect to acceptable beam parameters which need to be carefully analyzed to enable stable beam transport and acceleration. Since the analytic description of electron-plasma interactions is all but impossible given the nature of the problem, the approach taken in this work relies on the dominant numerical method in the field of plasma-based acceleration, the Particle-in-Cell approach, supported by analytic and semi-analytic descriptions of special cases. It focuses on the behavior of a preaccelerated beam and the mechanisms involved in its phase-space evolution, aiming to preserve beam-quality parameters and potentially minimize the energy spread using the dechirping approach.

After introducing a simplified analytic method for the calculation of uncorrelated emittance evolution and finding it in agreement with simulated results, the studies focused on the selection, vacuum-to-plasma transport and acceleration of an idealized beam, identifying a suitable working point for efficient energy gain and witness-beam parameter preservation. The wakefield encountered by the witness in such an acceleration scenario can increase its energy spread, a detrimental effect which can potentially be reversed using so-called dechirping. This work studied its applicability, finding that the reduction in projected energy spread is followed by an increase in the slice energy spread, before identifying a promising parameter range for a planned experiment and presenting data obtained from a successful demonstration at FLASHForward, concluding with a discussion of the dechirping potential of the beam obtained from earlier simulations. Finally, the studies focused on beam distributions obtained from a particle-tracking method, which showed clear deviations, both from the symmetric picture and the longitudinal current profiles. The asymmetries of the beams obtained after the separation of the initial bunch interfered with the acceleration process and necessitated the introduction of mitigation strategies, which were successfully implemented, resulting in tangible improvements in beam stability.

# ZUSAMMENFASSUNG

Diese Arbeit benutzt numerische Methoden zur Betrachtung der Phasenraumentwicklung eines extern injizierten Elektronenstrahls in verschiedenen plasmabasierten Beschleunigungsszenarien. Plasmakielwellenbeschleunigung („plasma wakefield accleration“) ist eine außergewöhnliche Technologie mit den Potential, die nächste Generation von Teilchenbeschleunigern anzutreiben. Sie benutzt dazu einen Teilchenstrahltreiber um Kielwellen anzuregen, die Feldgradienten im Bereich von $10\,\mathrm{GV\,m^{-1}}$ bis $100\,\mathrm{GV\,m^{-1}}$ tragen können, mehrere Größenordnungen über den aktuell verfügbaren konventionellen Kavitäten. Die Plasmaumgebung stellt jedoch strikte Voraussetzungen an die Strahlparameter, die präzise analysiert werden müssen, um stabilen Strahltransport und -beschleunigung zu ermöglichen. Da die analytische Beschreibung von Elektronen-Plasma-Interaktionen aufgrund der betrachteten Problemparameter praktisch unmöglich ist, nutzt die vorliegende Arbeit die auf dem Feld der Plasmabasierten Beschleunigung vorherrschende numerische Methode, den sogenannten „Particle-in-Cell“-Ansatz, unterstützt von analytischen und semianalytischen Beschreibungen ausgewählter Spezialfälle.

Die Arbeit fokussiert sich auf das Verhalten vorbeschleunigter Strahlen sowie die für ihre Phasenraumentwicklung relevanten Mechanismen, mit dem Ziel, die Strahlqualität zu erhalten und potentiell die Energiebandbreite durch den Einsatz des „Dechirping“-Ansatzes zu minimieren. Nach der Vorstellung einer vereinfachten analytischen Berechnungsmethode für die Entwicklung der unkorrelierten Emittanz, fokussierten sich die Studien auf die Auswahl, den Vakuum-Plasma-Transport sowie die Beschleunigung eines idealisierten Elektronenstrahls und identifizierten dabei passende Einstellungen für die effiziente Beschleunigung eines „Witness“-Strahls unter Erhaltung seiner Qualitätsparameter.

Der Feldgradient in einem solchen Beschleunigungsszenario kann die Energiebandbreite des „Witness“-Strahls erheblich vergrößern. Dieser Effekt kann potentiell durch den Einsatz der sogenannten „Dechirping“-Technik rückgängig gemacht werden. Die vorliegende Arbeit befasste sich mit der Anwendbarkeit dieser Methode und fand dabei, dass eine Verringerung der projizierten Energiebandbreite mit einer Erhöhung der unkorrelierten Energiebandbreite einhergeht. Anschließend wurde ein vielversprechender Parameterbereich für ein geplantes Experiment idenzifiziert sowie Daten einer erfolgreichen Demonstration dieser Technik, aufgenommen bei FLASHForward, präsentiert. Das Kapitel endet mit einer Diskussion des „Dechirping“-Potentials des im vorherigen Kapitel beschleunigten Strahls.

Schließlich befassten sich die Studien mit Strahlverteilungen, die aus einem „Particle tracking“-Programm stammen und deutliche Abweichungen zeigten, sowohl in ihrer Symmetrie als auch bei den longitudinalen Stromprofilen. Die Asymmetrie der Elektronenpakete, die nach der Auftrennung des ursprünglichen Strahls erhalten wurden, hatte negative Auswirkungen auf den Beschleunigungsprozess. Dies erforderte die Einführung von Bewältigungsstrategien, deren erfolgreiche Umsetzung eine deutliche Verbesserung der Strahlstabilität ermöglichte.

# CONTENTS

# INTRODUCTION

When an international collaboration, comprised of thousands of scientists, announced the discovery of the Higgs boson in 2013, it not only marked a momentous achievement in the study of the Standard Model, it also helped put a machine that enabled the observation of this elusive particle into the spot light. The Large Hadron Collider is part of a long tradition of instruments which enabled the scientific study of nature on scales far beyond the limits of human perception. Particle accelerators are commonly found on the forefront of studies involving atomic to subatomic scales—either by providing the relativistic particles needed for collision experiments probing the constituents of matter and the forces they are subjected to, or driving synchrotron radiation sources analyzing molecular and atomic interactions critical for applications such as medical research, material science and chemistry. In their wake, a multitude of accelerator designs with a diverse set of application profiles — from historical record dating [Grolimund et al., 2004] to medical therapy [Levin et al., 2005; Suortti et al., 2003] — have been introduced and implemented, further enlarging the footprint of this technology on the current scientific and industrial landscape.

Mirroring their impact and the increasing demand, new facilities are either already online (e.g. the European X-Ray Free Electron Laser, XFEL) or being planned (such as the International Linear Collider ILC). However, the promised increases in temporal and spatial resolutions come at a significant cost, often requiring large international collaborations and complex funding structures. Current acceleration technologies are ultimately limited to gradients of $100\,\mathrm{MV\,m^{-1}}$, while currently used structures are rated significantly lower (as an example, the European XFEL has cavities designed for $23.6\,\mathrm{MV\,m^{-1}}$, necessitating an acceleration section of 1.7 km to reach its final energy of 17.5 GeV [Altarelli, 2011]). To reach higher energies for collision experiments thus requires increasingly large accelerating structures, raising the question whether potential new technologies can help reach higher gradients and thus reduce the necessary footprint and corresponding investment.

Plasma-based acceleration [Esarey et al., 2009], a proposal which uses the high field gradients available due to charge separation of the electron-ion mixture in the wake of a high-intensity laser or particle driver, is currently seen as one of the most promising candidates for a new generation of cost-effective accelerator designs. Offering accelerating gradients in the range of 10 GeV to 100 GeV [Modena et al., 1995], machines implementing this technology either by using short laser pulses for so-called laser wakefield acceleration (LWFA) or charged particle beams as drivers for plasma wakefield acceleration (PWFA) promise an orders-of-magnitude reduction in the size of corresponding accelerating structures. Since its inception in 1979 [Tajima et al., 1979], the exceptional potential of plasma-based accelerators has prompted an increasing number of experiments to probe its many aspects and deliver promising results. From the production of ultra-relativistic narrow-band electron beams [Geddes et al., 2004] in LWFA, to the energy doubling of a bunch on a meter scale [I. Blumenfeld et al., 2007] and the successful acceleration of an electron bunch up to 2 GeV in the wake of a proton driver [Adli et al., 2018] in PWFA, towards the demonstration of X-ray radiation generation either in the plasma channel [Kneip et al., 2010] or the undulator structures downstream [Fuchs et al., 2009], this field has seen significant advances driving the implementation of dedicated facilities such as FLASHForward [Aschikhin et al., 2016] and FACET-II [Joshi et al., 2018].

Concurrent developments in the numerical description of the processes under consideration have provided the sound theoretical footing required for all scientific advancement. Originating in the methods which quickly followed the original proposals [John M Dawson, 1983] and recognized the need to side-step the impossible task of a complete analytic description of the constituent processes, they instead rely on highly performant simulations fine-tuned to the targeted parameter space. It is not surprising, therefore, that major strides in the understanding of plasma behavior have happened in lock-step with significant developments in the fields of corresponding numerical methods, long established as a third pillar between theory and experiment. Among those, the Particle-in-Cell (PIC) approach [Charles et al., 1985; John M Dawson, 1983; Harlow et al., 1955] can be seen as the dominant one, covering a wide range of acceleration and injection scenarios and providing a robust and straightforward description mechanism. It is implemented by subsuming the individual particles into so-called macroparticles, representations of the local phase-space density structure, and placing them into a grid harboring the field components. This allows for the complete evaluation of the kinetic and electromagnetic aspects of plasma-bunch interactions, made possible by highly parallized codes running on supercomputers. However, it too can be further optimized by carefully focusing the considered parameter range. When analyzing PWFA scenarios, the observation of vastly different dominant time and length scales between the plasma and the electron bunches leads to the introduction of the quasistatic approximation scheme [Mora and Antonsen Jr, 1996; Whittum, 1997], which enables significant increases in efficiency for scenarios considered in this dissertation.

Despite the substantial advances presented above, the technology of plasma-based acceleration still faces a multitude of challenges with respect to the stability of the process and the provision of resulting beams of consistently high quality. The shift from vastly different environments, from the conventional beam line to a plasma stage and back into the focusing structures, requires careful tuning of the simulated process to avoid severe degradation of quality parameters such as emittance and energy spread, both figures of merit for beam transport and potential downstream applications such as FELs. Quasi-static PIC codes such as HiPACE [T. Mehrling, C. Benedetti, et al., 2014], by virtue of their focus on the efficient description of the beam phase-space development, allow for wide-ranging parameter scans to establish configurations which allow either the preservation of the beam phase-space. The present work applies this approach to demonstrate the numerical description of a successful acceleration process within a parameter range motivated by the FLASHForward accelerator, helped by a newly introduced analytic description of emittance evolution and leading to a so-called start-to-end treatment of the acceleration involving a simulated preaccelerator beam line. It additionally explores advantageous phase-space modifications permitted by the plasma environment in the case of dechirping. This technique uses the longitudinal field properties in the wake of an electron beam to reduce its negative energy chirp and minimize its energy spread.

# Part I

# THEORY

# 1 PLASMA PHYSICS

As the name suggests, one of the the crucial components of plasma-based acceleration is the plasma environment itself — a *quasineutral* distribution of ionized particles showing *collective* effects. It is these two characteristic attributes [F. F. Chen, 2012] which help distinguish plasma from other forms of ionized matter, forming the basis for a useful classification among the wide range of possible plasma densities and temperatures. Their thorough theoretical definition is a required foundation to allow for the discussion of possible effects and associated length and time scales.

## 1.1 PLASMA DEFINITION

As a form of ionized matter, plasma is composed of positive and negative charges occupying a volume in space. Its *quasineutral* nature becomes apparent when a test particle charge $q$ is introduced in this environment, causing plasma particles of opposite charge to cluster around it an effect known as *Debye shielding* and causing the test particle's potential $\Phi$ to decay as

$$\Phi \sim \frac{q}{r} e^{-r/\lambda_D}, \tag{1.1}$$

as a function of radial distance $r$, instead of the normal Coulomb dependency $\Phi \sim q/r$, with the characteristic decay length $\lambda_D$ defined as the *Debye length* [Spatschek et al., 1990],

$$\frac{1}{\lambda_D^2} = \frac{1}{\lambda_{D,e}^2} + \frac{1}{\lambda_{D,i}^2}, \tag{1.2}$$

composed of the shielding contributions from electrons $\lambda_{D,e}$ and ions $\lambda_{D,i}$, respectively. However, it is common to ignore the ion contribution to the shielding process itself, based on the significant difference in weight and thus response times and frequencies [F. F. Chen, 2012] — an approach adapted in the following discussion and throughout this work. The electron contribution to the Debye length is given by [F. F. Chen, 2012]

$$\lambda_{D,e}^2 = \frac{\varepsilon_0 k_B T_e}{n_e e^2}, \tag{1.3}$$

with the particle density $n_e$, the temperature $T_e$, the Boltzmann constant $k_B$, and the vacuum permittivity $\varepsilon_0$. A higher particle density reduces the Debye length, providing more particles to shield the potential, while a higher temperature increases it, inhibiting the shielding response.

Thus, a plasma appears *quasineutral* on length scales much larger than the Debye length, $L \gg \lambda_D$, shielding charge imbalances through the arrangement of its constituent particles. This definition can be coupled to the second condition for a plasma — the emergence of *collective effects* — since it requires enough particles to be present around the charge to allow for a statistical consideration. In other words, a Debye sphere must contain a distribution with a sufficient number of particles,

$$\frac{4}{3}\pi n_e \lambda_D^3 \gg 1. \tag{1.4}$$

This condition for collective behavior can be expressed using the so-called *plasma parameter*,

$$\Lambda = \frac{4\pi}{3} n \lambda_D^3, \tag{1.5}$$

so that a plasma where $\Lambda \gg 1$ is called an *ideal plasma* (following the definition of an ideal gas, where collective thermal effects dominate individual particle interactions). Thus, both conditions for a plasma environment can be seen as closely connected ($L \gg \lambda_D$, $\Lambda \gg 1$). However, it remains to consider the conditions and typical time scales for both the collective processes as well as individual particle interactions.

The response frequencies for plasma electrons and ions carrying a single charge are given by [F. F. Chen, 2012]

$$\omega_{\mathrm{pe}} = \sqrt{\frac{n_e e^2}{m_e \varepsilon_0}} \tag{1.6a}$$

$$\omega_{\mathrm{pi}} = \sqrt{\frac{n_i e^2}{m_i \varepsilon_0}}, \tag{1.6b}$$

with the respective weights $m_{\mathrm{i,e}}$ and particle densities $n_{\mathrm{i,e}}$. Considering the respective frequencies supports the argument made above in favor of ignoring ion contributions to the shielding and collective effects for cases relevant in the following sections — with a ratio of $m_{\mathrm{e}}/m_{\mathrm{i}} \approx 5.49 \cdot 10^{-4}$ for even a hydrogen plasma, the resulting plasma frequency $\omega_{\mathrm{p}}^2 = \omega_{\mathrm{e}}^2 + \omega_{\mathrm{i}}^2$ is almost fully defined by the quick electron response,

$$\omega_{\mathrm{p}} \simeq \omega_{\mathrm{pe}} = \sqrt{\frac{n_0 e^2}{m_{\mathrm{e}} \varepsilon_0}}. \tag{1.7}$$

This frequency is an important parameter defining the typical time scales of the plasma response to external perturbations and thus of great importance to the discussion of acceleration processes. Additionally, it can be used to formulate a condition for the transition into a state where collective effects are dominant. Considering the frequency of Coulomb collisions between ions and electrons — a typical example of particle interactions in plasma, given by (cf. [F. F. Chen, 2012])

$$\nu_m \approx \frac{n_0 e^4}{\varepsilon_0 v^3 m_e^2} \log(\Lambda), \tag{1.8}$$

with the average particle velocity $v$, the ratio between the frequencies of the two processes can be approximated as

$$\frac{\omega_p}{\nu_m} \approx \frac{\Lambda}{\log(\Lambda)} \approx \Lambda \gg 1, \tag{1.9}$$

recovering the condition for the collective effects within a Debye sphere presented above.

In addition to the plasma frequency, which provides a typical time scale, the following sections will use a so-called *skin depth* to provide a typical length scale based on considerations related to the propagation of electromagnetic waves in its environment. The corresponding dispersion relation is given by [F. F. Chen, 2012]

$$\omega^2 = \omega_p^2 + c^2 k^2, \tag{1.10}$$

with the frequency $\omega$ and the wave number $k$ for a given light pulse. Rearranging this equation for the wave number,

$$k = \sqrt{\frac{\omega^2 - \omega_p^2}{c^2}}, \tag{1.11}$$

shows a decreasing $k$ for higher densities (since $\omega_p \sim n_0^{1/2}$), reaching zero at a critical density,

$$n_c = \frac{\omega^2 m_e \varepsilon_0}{e^2}. \tag{1.12}$$

For values above this boundary, the once transparent (so-called *under-dense*) plasma turns opaque to incident light of the considered frequency (consequently known as *over-dense plasma*), its dispersion relation now having the form

$$k = i \frac{|\omega_p^2 - \omega^2|^{1/2}}{c}, \tag{1.13}$$

with the characteristic decay length of the wave amplitude, termed the *skin depth*, $|k^{-1}| = c/(\omega_p^2 - \omega^2)^{1/2}$. Its asymptotic form, $k_p^{-1} = c/\omega_p$, while limited to the description of attenuation in over-dense plasma in the physical sense, is commonly used as a typical length-scale for plasma-based acceleration processes.

In summary, the crucial plasma parameters that determine its classification and suitability for acceleration, all depend on plasma density and temperature — the Debye length $\lambda_D \sim (T_e/n_0)^{1/2}$, the plasma frequency $\omega_p \sim n_0^{1/2}$ and the plasma parameter $\Lambda \sim n_0\,(T_e/n_0)^{3/2}$.

The plasma available for acceleration processes is commonly obtained through photo-ionization at densities $1 \times 10^{15}\,\mathrm{cm}^{-3} \leq n_0 \leq 1 \times 10^{22}\,\mathrm{cm}^{-3}$ and temperatures $1\,\mathrm{eV} \leq T_e \leq 1000\,\mathrm{eV}$, forming an ideal plasma which allows particle collisions and associated effects to be ignored and to focus on collective processes only — a restriction valid for all subsequent discussions.

## 1.2 MODELS FOR THEORETICAL PLASMA DESCRIPTION

After the initial classification and corresponding introduction of typical parameters and its specific time and length scales, a more thorough description of the plasma is required for a better understanding of the acceleration and focusing processes discussed below. A naive interpretation would aim for the consideration of all plasma particles to allow for the most accurate description possible, evaluating particle motions within the fields generated by the surrounding particles. It should be clear, however, that such an approach is neither practical nor necessary for a system consisting of a large particle population dominated by collective effects (see classification above). The most common solution, therefore, is to employ models with varying degree of granularity supported by specific assumptions about plasma properties and behavior and limited by the required accuracy, usually hierarchically structured as follows:

- **Microscopic Picture**: Describing individual plasma particles and their self-consistent fields, this is the most accurate model with little practical use for typical descriptions in plasma-acceleration cases;

- **Kinetic Picture**: Replacing individual particles with corresponding statistical averages of their distribution, this picture is a widely used approximation in the description of plasma processes;

- **Macroscopic Picture**: Treating the plasma as a fluid allows for a potentially straightforward description, however at the cost of more restrictions on its applicability;

### 1.2.1 *Microscopic Picture and the Klimontovich Equation*

This description can be seen as the most straightforward one—focusing on point-like particles in plasma together with their self-consistent fields generated by their charge and current, given by

$$\rho^m(\mathbf{r}, t) = \sum_s q_s \int d\mathbf{p} f_s^m(\mathbf{r}, \mathbf{p}, t), \tag{1.14a}$$

$$\mathbf{J}(\mathbf{r}, t) = \sum_s q_s \int d\mathbf{p}\mathbf{v} f_s^m(\mathbf{r}, \mathbf{p}, t) \tag{1.14b}$$

in the macroscopic picture denoted by the superscript $m$ for a specific particle $s$, with charge $q_s$ and mass $m_s$, where

$$\mathbf{v} = \frac{\mathbf{p}}{m_s\sqrt{1 + (\mathbf{p}/m_s c)^2}}. \tag{1.15}$$

Here, $f_s^m$ denotes the microscopic time-dependent density distribution in six-dimensional phase space,

$$f_s^m(\mathbf{r}, \mathbf{p}, t) = \sum_{i=1}^{N_s} \delta(\mathbf{r} - \mathbf{R}_i(t))\delta(\mathbf{p} - \mathbf{P}_i(t), \tag{1.16}$$

for a species with $N_s$ constituent particles evaluated at the individual particle position $\mathbf{R}_i$ and momentum $\mathbf{P}_i$ using the Dirac delta function, making them *Lagrangian* quantities of the particle ($\mathbf{r}$ and $\mathbf{p}$ refer to coordinates in 6D phase space). Their description is complemented by the *Eulerian* field, charge and current density quantities, in turn described given the well-known Maxwell equations [Maxwell, 1873]

$$\nabla \cdot \mathbf{E} = \frac{\rho}{\varepsilon_0}, \tag{1.17a}$$
$$\nabla \cdot \mathbf{B} = 0, \tag{1.17b}$$
$$\nabla \times \mathbf{E} = -\frac{\partial \mathbf{B}}{\partial t}, \tag{1.17c}$$
$$c^2\nabla \times \mathbf{B} = \frac{\partial \mathbf{E}}{\partial t} + \frac{\mathbf{j}}{\varepsilon_0}, \tag{1.17d}$$

forming the basis for the equations of motion for the individual particles,

$$\frac{d\mathbf{R}_i}{dt} = \mathbf{V}_i(t), \tag{1.18a}$$
$$\frac{d\mathbf{P}_i}{dt} = q_s\mathbf{E}(\mathbf{R}_i(t), t) + \frac{q_s}{c}\mathbf{V}_i(t) \times \mathbf{B}(\mathbf{R}_i(t), t), \tag{1.18b}$$

the right-hand side of the latter equation describing the Lorentz force acting on the particle moving with individual velocity $\mathbf{V}_i$.

Based on these equations, a description of the exact plasma evolution can be found, first considering the time derivative of its density [Nicholson, 1983]

$$\begin{aligned}\frac{\partial f_s^m(\mathbf{r}, \mathbf{p}, t)}{\partial t} &= -\sum_{i=1}^{N_s} \frac{\partial \mathbf{R}_i}{\partial t}\frac{\partial}{\partial \mathbf{r}}\delta(\mathbf{r} - \mathbf{R}_i(t))\delta(\mathbf{p} - \mathbf{P}_i(t)) \\ &\quad - \sum_{i=1}^{N_s} \frac{\partial \mathbf{P}_i}{\partial t}\frac{\partial}{\partial \mathbf{p}}\delta(\mathbf{r} - \mathbf{R}_i(t))\delta(\mathbf{p} - \mathbf{P}_i(t)).\end{aligned} \tag{1.19}$$

Using equations (1.18) to (1.18a), the equation above can be written as

$$\begin{aligned}\frac{\partial f_s^m(\mathbf{r}, \mathbf{p}, t)}{\partial t} &= -\mathbf{v}\sum_{i=1}^{N_s} \delta(\mathbf{r} - \mathbf{R}_i(t))\delta(\mathbf{p} - \mathbf{P}_i(t)) \\ &\quad - q_s\left[\mathbf{E}^m(\mathbf{r}, t) + \frac{\mathbf{v}}{c} \times \mathbf{B}^m(\mathbf{r}, t)\right]\frac{\partial}{\partial \mathbf{p}}\sum_{i=1}^{N_s} \delta(\mathbf{r} - \mathbf{R}_i(t))\delta(\mathbf{p} - \mathbf{P}_i(t)),\end{aligned} \tag{1.20}$$

with the field quantities provided using the superscript $m$ denoting the microscopic notation. Observing that the Dirac delta functions on the right-hand side of this equation provide the plasma particle density equation (1.15), yields the *Klimontovich* equation [Nicholson, 1983],

$$\frac{\partial f_s^m(\mathbf{r},\mathbf{p},t)}{\partial t} + \mathbf{v}\cdot\frac{\partial f_s^m(\mathbf{r},\mathbf{p},t)}{\partial \mathbf{r}} + q_s\left[\mathbf{E}(\mathbf{r},t) + \frac{\mathbf{v}}{c}\times\mathbf{B}^m(\mathbf{r},t)\right]\cdot\frac{\partial f_s^m(\mathbf{r},\mathbf{p},t)}{\partial \mathbf{p}} = 0. \tag{1.21}$$

This equation, together with the Maxwell field equations, provides a complete classical description for the deterministic evolution of all $N_s$ plasma particles of a given species, while ignoring quantum-mechanical effects. It should be clear, however, that such an approach is highly impractical for typical plasma acceleration cases at the appropriate densities, where it is dominated not by individual trajectories but by collective effects which can be described much more elegantly by appropriate methods such as the *kinetic* description.

### 1.2.2 *Kinetic Picture and the Vlasov Equation*

To avoid the impractical evaluation requirements of the Microscopic description outlined above, a typical approach converts the discrete particle positions into a distribution function. While based on a statistical formulation of the collective effects within the plasma particle ensemble, this description is nevertheless concerned with its motion, thus termed a *kinetic description*. The essential idea (cf. [Nicholson, 1983]) is to introduce statistical averaging over the particle distribution as employed in the Klimontovich equation (1.20), where it serves to indicate whether a provided coordinate is occupied by a particle at a specific point in time. When averaged over a small phase-space volume $\Delta V = \Delta x\Delta y\Delta z\Delta p_x\Delta p_y\Delta p_z$, the notion of individual particle locations is replaced by a smooth distribution, given as [Callen, 2006]

$$\begin{aligned}\langle f_s^m(\mathbf{r},\mathbf{p},t)\rangle &= \lim_{n^{-1/3}\ll\Delta x\ll\lambda_D}\frac{1}{\Delta V}\int_{\Delta V} d\mathbf{r}d\mathbf{p} f_s^m(\mathbf{r},\mathbf{p},t)\\ &= \lim_{n^{-1/3}\ll\Delta x\ll\lambda_D}\frac{\int_{\Delta V} d\mathbf{r}d\mathbf{p} f_s^m(\mathbf{r},\mathbf{p},t)}{\int_{\Delta V} d\mathbf{r}d\mathbf{p}}.\end{aligned} \tag{1.22}$$

The limit in the equation serves to guarantee a smooth distribution, requiring a sufficiently large phase-space volume to contain enough particles—both in configuration space $\Delta x \gg n^{-1/3}$ and momentum space $\Delta p_x \gg m_s v_t n^{-1/3}\lambda_D^{-1}$ [Callen, 2006]. The upper limit for the volume is given by the Debye length itself, since the averaging should capture variations due to collective effects. The averaged particle distribution for a given species $s$ thus describes its parameters with an associated error $\delta f_s^m = f_s^m - \langle f_s^m\rangle$ which in turn has a vanishing average $\langle \delta f_s^m \rangle = 0$. The description based on averaged quantities is not limited to the particle distribution, requiring averaging of the field, current and charge quantities as well,

$$\mathbf{E}^m = \langle \mathbf{E}^m \rangle + \delta \mathbf{E}, \tag{1.23a}$$
$$\mathbf{B}^m = \langle \mathbf{B}^m \rangle + \delta \mathbf{B}, \tag{1.23b}$$
$$\mathbf{J}^m = \langle \mathbf{J}^m \rangle + \delta \mathbf{J}, \tag{1.23c}$$
$$\rho^m = \langle \rho^m \rangle + \delta \rho. \tag{1.23d}$$

Similar to the smooth particle distribution, the error associated with their averaging has a vanishing average itself, $\langle \delta \mathbf{E}^m \rangle = \langle \delta \mathbf{B}^m \rangle = \langle \delta \mathbf{J}^m \rangle = \langle \delta \rho^m \rangle = 0$. Using the averages so defined, the Klimontovich equation (1.20) thus becomes [Callen, 2006]

$$\begin{aligned} &\langle f_s^m(\mathbf{r},\mathbf{p},t) \rangle + \mathbf{v} \cdot \frac{\langle f_s^m \rangle}{\delta \mathbf{r}} \\ &+ q_s \left( \langle \mathbf{E}^m + \frac{\mathbf{v}}{c} \times \langle \mathbf{B}^m \rangle \right) \cdot \frac{\partial \langle f_s^m \rangle}{\partial \mathbf{p}} = -q_s \left\langle \left( \delta \mathbf{E}^m + \frac{\mathbf{v}}{c} \times \delta \mathbf{B}^m \right) \cdot \frac{\partial \delta f_s^m}{\partial \mathbf{p}} \right\rangle . \end{aligned} \tag{1.24}$$

While the error averages of the individual smoothed quantities vanish as per the definition above, the average of their products in general does not. Therefore, the right-hand side of equation (1.23d) is kept and incorporates microscopic effects not captured by averaging, such as elastic Coulomb collisions between the constituent plasma particles.

The transition away from the microscopic regime requires that the averaged quantities be replaced by representations of their smoothed counterparts, $\mathbf{E} = \langle \mathbf{E}^m \rangle$, $\mathbf{B} = \langle \mathbf{B}^m \rangle$, together with the introduction of the fundamental particle distribution function $f_s(\mathbf{r},\mathbf{p},t) = \langle f_s^m(\mathbf{r},\mathbf{p},t) \rangle$. The more concise description results in the plasma kinetic equation,

$$\frac{\partial f_s}{\partial t} + \mathbf{v} \cdot \frac{\partial f_s}{\partial \mathbf{r}} + q_s \left( \mathbf{E} + \frac{\mathbf{v}}{c} \times \mathbf{B} \right) \cdot \frac{\partial f_s}{\partial \mathbf{p}} = C(f_s), \tag{1.25}$$

featuring the Coulomb collision term introduced on the right-hand side of equation (1.23d). As discussed above, the collision processes can be neglected as a major contribution to particle processes compared to collective effects for the plasma regime of interest for acceleration, due to the different associated time scales (and a large plasma parameter $\Lambda \gg 1$). Assuming $C(f_s) \simeq 0$ leads to the collisionless plasma kinetic equation, known as the *Vlasov* equation,

$$\frac{\partial f_s}{\partial t} + \mathbf{v} \cdot \frac{\partial f_s}{\partial \mathbf{r}} + q_s \left( \mathbf{E} + \frac{\mathbf{v}}{c} \times \mathbf{B} \right) \cdot \frac{\partial f_s}{\partial \mathbf{p}} = 0. \tag{1.26}$$

Connected to the Maxwell equations by the charge and current densities,

$$\rho(\mathbf{r},t) = \sum_s q_s \int d\mathbf{p} f_s(\mathbf{r},\mathbf{p},t) \tag{1.27a}$$

$$\mathbf{J}(\mathbf{r},t) = \sum_s q_s \int d\mathbf{p} \mathbf{v} f_s(\mathbf{r},\mathbf{p},t), \tag{1.27b}$$

the Maxwell-Vlasov system of equations — equations (1.17) to (1.17c), equation (1.27), equation (1.27a) and equation (1.26) — is of fundamental importance for the theoretical treatment of plasma acceleration processes described below. Its implications, such as the time-reversible nature and the incompressibility of the phase-space volume occupied by the particle distribution, will be discussed in more detail in the following sections.

### 1.2.3 *Macroscopic Picture and Fluid Equations*

The essential mechanism for the simplification of the plasma description has been the introduction of statistical averages with an associated particle distribution, moving away from a Lagrangian treatment towards a Eulerian fluid picture. Consequently, the complexity of the Vlasov equation can be further reduced provided the plasma particles exhibit only a small deviation from a macroscopic thermal velocity, which allows them to be treated within a two-fluid model (electron and ion fluids) through the introduction of momentum moments. Using the definitions for the spatial particle density as well as the fluid-momentum and fluid-velocity distributions,

$$n_s(\mathbf{r},t) = \int d\mathbf{p} f_s(\mathbf{r},\mathbf{p},t) \tag{1.28a}$$

$$\mathbf{p}_s(\mathbf{r},t) = \frac{1}{n_s}\int d\mathbf{p}\ \mathbf{p}\ f_s(\mathbf{r},\mathbf{p},t) \tag{1.28b}$$

$$\mathbf{v}_s(\mathbf{r},t) = \frac{1}{n_s}\int d\mathbf{p}\ \mathbf{v}\ f_s(\mathbf{r},\mathbf{p},t), \tag{1.28c}$$

the Vlasov equation (1.26) can be converted into a density continuity equation after its integration over all momentum space,

$$\frac{\partial}{\partial t}n_s + \nabla_{\mathbf{r}}\cdot(n_s\mathbf{v}_s) = 0, \tag{1.29}$$

provided the particle distribution decays to zero outside the relevant area. The fluid force equation, the second fundamental element of the fluid model, can be found by multiplying the Vlasov equation with $\mathbf{p}$, again integrating over all momentum space [Nicholson, 1983],

$$\frac{\partial}{\partial t}(n_s\mathbf{p}_s) + \left[\nabla_{\mathbf{r}}\cdot\left(\int d\mathbf{p}(\mathbf{v}\mathbf{p}^{\intercal}f_s)\right)\right]^{\intercal} = n_s q_s\left(\mathbf{E} + \frac{\mathbf{v}_s}{c}\times\mathbf{B}\right), \tag{1.30}$$

with outer vector product $\mathbf{v}\mathbf{p}^{\intercal}$. Assuming a cold plasma (where $f_s(\mathbf{r},\mathbf{p},t) = n_s(\mathbf{r},t)\delta(\mathbf{p}-\mathbf{p}_s)$), the equation can be simplified to

$$\frac{\partial}{\partial t}(n_s\mathbf{p}_s) + \left[\nabla_{\mathbf{r}}\cdot\left(n_s\mathbf{v}_s\mathbf{p}_s^{\intercal}\right)\right]^{\intercal} = n_s q_s\left(\mathbf{E} + \frac{\mathbf{v}_s}{c}\times\mathbf{B}\right), \tag{1.31}$$

which, given the identity $(\nabla\cdot(\mathbf{a}\mathbf{b}^{\intercal})^{\intercal} = \mathbf{b}(\nabla\cdot\mathbf{a}) + (\mathbf{a}\cdot\nabla)\mathbf{b}$ becomes

$$\begin{aligned} n_s\frac{\partial\mathbf{p}_s}{\partial t} + \mathbf{p}_s\frac{\partial n_s}{\partial t} + \mathbf{p}(\nabla_{\mathbf{r}}\cdot(n_s\mathbf{v}_s)) \\ + (n_s\mathbf{v}_s\cdot\nabla_{\mathbf{r}})\mathbf{p}_s = n_s q_s\left(\mathbf{E} + \frac{\mathbf{v}_s}{c}\times\mathbf{B}\right). \end{aligned} \tag{1.32}$$

Using the density continuity equation (1.28c) multiplied by $\mathbf{p}$ allows the fluid momentum equation,

$$\frac{\partial \mathbf{p}_s}{\partial t} + (\mathbf{v}_s \cdot \nabla_{\mathbf{r}})\mathbf{p}_s = q_s \left( \mathbf{E} + \frac{\mathbf{v}_s}{c} \times \mathbf{B} \right) \tag{1.33}$$

to be obtained. Both the density continuity and the fluid momentum equations, equation (1.28c) and equation (1.33), complete the plasma-fluid picture, presenting the basis for an adequate description for its perturbation by a laser or electron driver. The specifics of such a scenario are the subject of the following section.

# 2 BEAM-DRIVEN PLASMA WAVES

This section continues elaborating the theoretical description of the acceleration process, now adding the plasma response to an external perturbation by a driver. The assumptions that permit the fluid description, most importantly the *Vlasov* system, to be introduced, still hold—the plasma is defined by collective effects, its response dominated by electron motion occurring at much shorter time scales than both the ion background motion (assumed static) and ion-electron collisions, while the electron velocity closely follows the mean local thermal velocity. In other words, a driver in this scenario approaches a pre-ionized plasma considered to be a *cold electron fluid*, governed by the smooth distribution functions and momentum moments introduced in chapter 1, above all the density continuity equation (1.28c), the fluid momentum equation (1.33) and the Maxwell equations (1.17) to (1.17c), which are connected to the fluid density and velocity via $\rho = e(n_0 - n_e)$ and $\mathbf{J} = -en_e\mathbf{v}_e$, respectively. With the addition of the *scalar potential* $\Phi$ and the *vector potential* $\mathbf{A}$, related to the fields as

$$\mathbf{E} = -\nabla\Phi - \frac{\partial \mathbf{A}}{\partial ct}, \tag{2.1a}$$

$$\mathbf{B} = \nabla \times \mathbf{A}, \tag{2.1b}$$

both the density continuity and fluid momentum equations can now be expressed as

$$\frac{\partial n}{\partial ct} + \nabla \cdot (n\boldsymbol{\beta}) = 0, \tag{2.2}$$

$$\frac{\partial \mathbf{p}_e}{\partial t} + (\mathbf{v}_e \cdot \nabla)\,\mathbf{p}_e = -e\left(-\nabla\Phi - \frac{\partial \mathbf{A}}{\partial t} + \frac{\mathbf{v}_e}{\partial t} \times (\nabla \times \mathbf{A})\right), \tag{2.3}$$

with the normalized electron fluid velocity $\boldsymbol{\beta} = \mathbf{v}_e/c$ and the local electron density now and in the following denoted as $n = n_e$. Using the normalized versions of the scalar potential $\phi = e\Phi/m_ec^2$, the vector potential $\mathbf{a} = e\mathbf{A}/m_ec^2$ and the electron fluid momentum $\mathbf{u} = \mathbf{p}_e/m_ec$, equation (2.3) can be rewritten as

$$\frac{\partial \mathbf{u}}{\partial ct} + \left(\frac{\mathbf{u}}{\gamma} \cdot \nabla\right)\mathbf{u} = \nabla\phi + \frac{\partial \mathbf{a}}{\partial ct} - \frac{\mathbf{u}}{\gamma} \times (\nabla \times \mathbf{a}). \tag{2.4}$$

Using the identity $(\mathbf{u} \cdot \nabla)\mathbf{u} = \nabla\mathbf{u}^2/2 - \mathbf{u} \times (\nabla \times \mathbf{u})$, the above equation now reads (cf. [Meyer-ter-Vehn et al., 2001])

$$\frac{\partial}{\partial ct}(\mathbf{u} - \mathbf{a}) = \nabla(\phi - \gamma) + \frac{\mathbf{u}}{\gamma} \times (\nabla \times (\mathbf{u} - \mathbf{a})), \tag{2.5}$$

with the Lorentz factor $\gamma = 1/\sqrt{(1 - \mathbf{v}^2/c^2)}$. Taking the curl of the above equation and using $\nabla \times (\nabla\phi) = 0$,

$$\frac{\partial}{\partial ct}(\nabla \times (\mathbf{u} - \mathbf{a})) = \nabla \times \left(\frac{\mathbf{u}}{\gamma} \times (\nabla \times (\mathbf{u} - \mathbf{a}))\right), \tag{2.6}$$

leads to an important observation—if $\nabla \times (\mathbf{u} - \mathbf{a})$ is initially zero, it will remain so for all times. Since the assumed unperturbed and cold plasma without a laser field initially exhibits $\mathbf{u} = \mathbf{a} = 0$, the second term of the right-hand side of equation (2.5) can be ignored, allowing it to be simplified into the *fluid momentum equation* [Esarey et al., 2009]

$$\frac{\partial}{\partial ct}(\mathbf{u} - \mathbf{a}) = \nabla(\phi - \gamma). \tag{2.7}$$

The electrostatic force term $\nabla\phi$ offers a straightforward interpretation for a charged driver beam, while the nonlinear term $\nabla\gamma$ is associated with the *general non-linear ponderomotive force* [Esarey et al., 2009],

$$\mathbf{F}_{p,n} = -m_e c^2 \nabla\gamma, \tag{2.8}$$

which expels electrons out of regions of high field magnitude or intensity. Now that the framework for the description of the plasma fluid response is in place, the focus of the theoretical consideration can shift towards the incident driver itself, to account for its specific parameter range and evolution, as part of the commonly used quasi-static approximation.

## 2.1 QUASI-STATIC APPROXIMATION

The general picture of the process under consideration is that of a laser or highly relativistic charged particle bunch entering the pre-ionized plasma. Since its behavior and the immediate plasma response are normally the features of interest, the theoretical formulation is conducted after a Galilean transformation into the *co-moving frame* of reference, with

$$\zeta = z - vt, \tag{2.9}$$

$$\tau = t, \tag{2.10}$$

centered around the driver propagating with velocity $v$ in the positive z-direction. The corresponding derivatives of a dependent quantity $\mathcal{Q} = \mathcal{Q}(\zeta, t)$,

$$\frac{\partial}{\partial z}\mathcal{Q}(\zeta, t) = \frac{\partial\tau}{\partial z}\frac{\partial\mathcal{Q}}{\partial\tau} + \frac{\partial\zeta}{\partial z}\frac{\partial\mathcal{Q}}{\partial\zeta} = \frac{\partial\mathcal{Q}}{\partial\zeta}, \tag{2.11}$$

$$\frac{\partial}{\partial t}\mathcal{Q}(\zeta, t) = \frac{\partial\tau}{\partial t}\frac{\partial\mathcal{Q}}{\partial\tau} + \frac{\partial\zeta}{\partial t}\frac{\partial\mathcal{Q}}{\partial\zeta} = \frac{\partial\mathcal{Q}}{\partial\tau} - v\frac{\partial\mathcal{Q}}{\partial\zeta}, \tag{2.12}$$

while further considerations are done in the *speed-of-light frame*, so that $v \equiv c$.

The essential idea of the *quasi-static approximation* is based on the observation that there is a significant disparity between the typical time scales dominating plasma and electron behavior. While the plasma response occurs at the inverse of its frequency $\tau_p \sim \omega_p^{-1}$, the time scale of the particle-beam evolution is defined by its betatron frequency, connected to the plasma in this picture by [Esarey et al., 2009]

$$t \sim \omega_\beta^{-1} \simeq \frac{\sqrt{2\gamma}}{\omega_p^{-1}}, \tag{2.13}$$

which can be larger by orders of magnitude for highly relativistic beams with $\gamma \gg 1$. In other words, the charge distribution of a particle driver does not change significantly during the typical time scale of the plasma response. In the speed-of-light frame, Eulerian quantities transform as $\partial_t \mathcal{Q} = \partial_\tau \mathcal{Q} - c\partial_\zeta \mathcal{Q}$, where the time-scale disparity implies [Eric Esarey, Sprangle, Krall, Ting, and Joyce, 1993]

$$|\partial_\tau \mathcal{Q}| \sim \tau_b^{-1} |\mathcal{Q}|, \tag{2.14}$$

$$c \left|\partial_\zeta \mathcal{Q}\right| \sim \tau_p^{-1} |\mathcal{Q}|, \tag{2.15}$$

so that for typical driver beams the evolution of Eulerian quantities such as charge and current densities as well as the corresponding fields in the speed-of-light frame is dictated by their $\zeta$-dependency,

$$\frac{\partial \mathcal{Q}}{\partial t} \simeq -c\frac{\partial \mathcal{Q}}{\partial \zeta}. \tag{2.16}$$

In other words, the beam encounters an environment that reconfigures itself quickly enough to appear quasi-static over its defining time scale.

## 2.2 PLASMA DENSITY PERTURBATIONS

The quasi-static approximation allows for an adequate treatment of plasma-beam interactions, as depicted in the following descriptions, where a cold, initially unperturbed plasma is assumed. The resulting environment is commonly described using the *wakefield potential*

$$\psi = \phi - a_z, \tag{2.17}$$

with the normalized scalar potential and the $z$-component of the normalized vector potential $\mathbf{a}$. Its structure given an incident particle beam with density $n_b$ is governed by the second-order differential equation (cf. [Timon Johannes Mehrling, 2014] and for a detailed discussion)

$$k_p^{-2} \frac{\partial^2 \psi(\zeta)}{\partial \zeta^2} = \frac{1 + \mathbf{a}^2(\zeta)}{2(1+\psi)^2} \pm \frac{n_b(\zeta)}{n_0} - \frac{1}{2}, \tag{2.18}$$

with the plasma skip depth $k_p$, the ambient plasma electron density $n_0$ and the sign of $n_b$ defined as the opposite of the charge of the particles in the beam. The resulting fluid quantities—the relativistic factor of the electron fluid $\gamma$, the $z$-component of the fluid momentum and the local plasma electron density $n$, are given as [Esarey et al., 2009]

$$\gamma(\zeta) = \frac{1 + \mathbf{a}^2 + (1+\psi)^2}{2(1+\psi)}, \tag{2.19}$$

$$\frac{n(\zeta)}{n_0} = \frac{1 + \mathbf{a}^2 + (1+\psi)^2}{2(1+\psi)^2}, \tag{2.20}$$

$$u_z(\zeta) = \frac{1 + \mathbf{a}^2 - (1+\psi)^2}{2(1+\psi)},, \tag{2.21}$$

and form a complete description of longitudinal plasma waves in the one-dimensional cold-fluid picture.

As a general consideration, a particle beam in a radially symmetric quasi-static system will be subjected to wakefields with their longitudinal $E_z$ and transverse $E_r - B_\theta$ field components connected to the wakefield potential by [Timon Johannes Mehrling, 2014]

$$\frac{E_z}{E_0} = -k_p^{-1}\frac{\partial\psi}{\partial\zeta}, \tag{2.22}$$

$$\frac{E_r - B_\theta}{E_0} = -k_p^{-1}\frac{\partial\psi}{\partial r}, \tag{2.23}$$

where $E_0 = \omega m_e c/e$ is the *cold non-relativistic wave-breaking field* [J. M Dawson, 1959]. A perturbation in plasma, caused by a radially symmetric beam, can thus support fields with both accelerating (for $qE_z > 0$) and focusing (for $q\partial_r(E_r - B_\theta < 0)$) properties for a test charge $q$ following in the same direction in its wake, forming the basis for the plasma-wakefield acceleration process at the core of this work. The specifics of the acceleration itself are defined by the peak densities of the beam or peak intensities of the laser driver, separately considered as

- *Linear regime* ($\psi \ll 1$)
- *Nonlinear regime* ($\psi \sim 1$)
- *Blowout regime* ($\psi \gg 1$)

whose specifics will be described in more detail in the following

## 2.3 LINEAR REGIME

The linear regime describes a perturbation scenario caused by a driver of relatively low density ($n_b/n_0 \ll 1$, thus $\psi \ll 1$) with a density distribution $f$. The resulting wakefield structure is found to be [Gorbunov et al., 1987]

$$\psi(\zeta, r) = k_p \int_{\infty}^{\zeta} \sin(k_p(\zeta - \zeta'))f(\zeta', r)d\zeta', \tag{2.24}$$

with the amplitude of a particle driver given as

$$f(\zeta, r) = \pm \frac{n_b(\zeta, r)}{n_0}, \tag{2.25}$$

with a plus sign for negative charges and vice versa. For the commonly assumed Gaussian beam distribution,

$$f(\zeta, r) = f_0 \exp\left(-\frac{(\zeta - \zeta_c)^2}{2\sigma_\zeta^2}\right) \exp\left(-\frac{r^2}{2\sigma_r^2}\right), \tag{2.26}$$

the wakefield structure for positions behind the driver (so that $(\zeta_c - \zeta)/\sigma_\zeta \gg 1$ can be expressed as (compare [Timon Johannes Mehrling, 2014])

$$\psi(\zeta, r) = -f_0 \sqrt{2\pi} k_p \sigma_\zeta \exp\left(-\frac{(k_p \sigma_\zeta)^2}{2}\right) \sin(k_p(\zeta - \zeta_c)) \exp\left(-\frac{r^2}{2\sigma_r^2}\right), \tag{2.27}$$

while the field structures are provided by evaluating equation (2.22) and equation (2.23), obtaining [Gorbunov et al., 1987]

$$\frac{E_z}{E_0} = f_0 \sqrt{2\pi} k_p \sigma_\zeta \exp\left(-\frac{(k_p \sigma_\zeta)^2}{2}\right) \cos(k_p(\zeta - \zeta_c)) \exp\left(-\frac{r^2}{2\sigma_r^2}\right) \tag{2.28a}$$

$$\begin{aligned} \frac{E_r - B_\theta}{E_0} = &-f_0 \sqrt{2\pi} k_p \sigma_\zeta \exp\left(-\frac{(k_p \sigma_\zeta)^2}{2}\right) \\ &\times \sin(k_p(\zeta - \zeta_c)) \frac{k_p r}{(k_p \sigma_r)^2} \exp\left(-\frac{r^2}{2\sigma_r^2}\right). \end{aligned} \tag{2.28b}$$

Figure 2.1 shows the wakefield potential and the longitudinal field component on axis, evaluated based on both the analytic approximations equation (2.27) and equation (2.28) as well as a numerical solution of equation (2.18) (where **a** was neglected due to the absence of a laser beam). Mirroring the assumption of positions situated behind the driver, the analytic deviations align well with their numerical counterparts in the wake of the particle beam.

## 2.4 NON-LINEAR REGIME

The cold-fluid description of the plasma electrons is valid for perturbations by low-density drivers causing plasma electron oscillations with momenta not significantly different from the thermal plasma average. within the picture of a thermal plasma without a significant deviation from a momentum average. Higher density beams with $n_b/n_0 \simeq 1$ and above allow the plasma electrons to reach relativistic velocities and thus relativistic mass, altering the plasma frequency

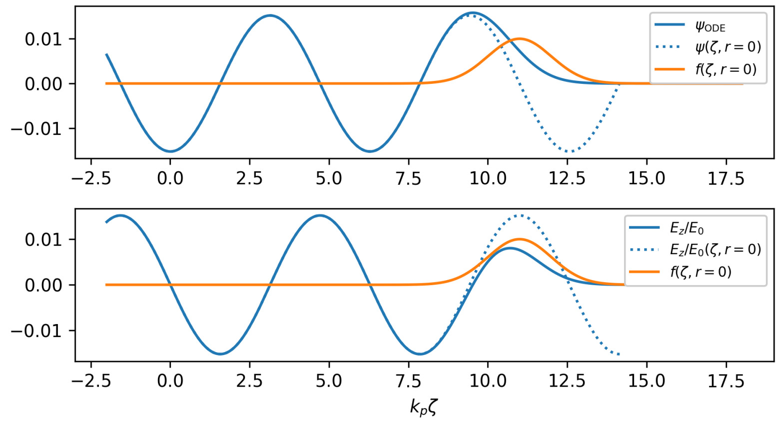


Figure 2.1: Particle beam profile (with $k_p\sigma_\zeta = 1.0$, $f_0 = 0.01$, solid orange lines) and resulting wakefield potential (upper plot) and longitudinal field component on axis (lower plot), obtained from analytic descriptions in equations (2.27) to (2.28) (dashed lines) as well as numerical evaluations based on equation (2.18) (solid lines).

through its inverse mass dependency (see [Esarey et al., 2009] for more details regarding relativistic plasma waves). To study the subsequent deviation from a linear plasma response with sinusoidal wakefield properties, a Gaussian particle drive beam is introduced with different peak densities, followed by a numerical interpretation of the wakefield potential equation (2.18) and derived quantities (the beam is assumed to be of sufficient transverse size to allow for the one-dimensional wave description to hold $k_p\sigma_r \gtrsim 1$). Figure 2.2 depicts the resulting wakefield potential and longitudinal field component at varying peak densities for an incident driver. The deviation from sinusoidal structures is evident for both quantities, together with a non-linear increase in respective peak values. The high-density perturbation causes a significant deviation from the presumed cold-fluid picture of the plasma, with distinct regions not governed by the presumed thermal picture, necessitating a different model to correctly describe their behavior.

## 2.5 BLOWOUT REGIME

The linear regime caused by a sufficiently broad driver of low ambient peak density can be seen as a purely longitudinal effect, causing a sinusoidal wake structure with a potential radial dependency in the case of a Gaussian beam. The last section described a deviation from that regime through the introduction of higher-density beams, which caused non-linear wakefields to form in their wake. However, the assumptions of a fluid description are rendered invalid in the case of a high-density particle beam with a spot size on the order of the plasma skin depth $k_p^{-1} = c/\omega_p$ propagating through the plasma. The beam expels plasma electrons in its path, forming a cavity surrounded by a

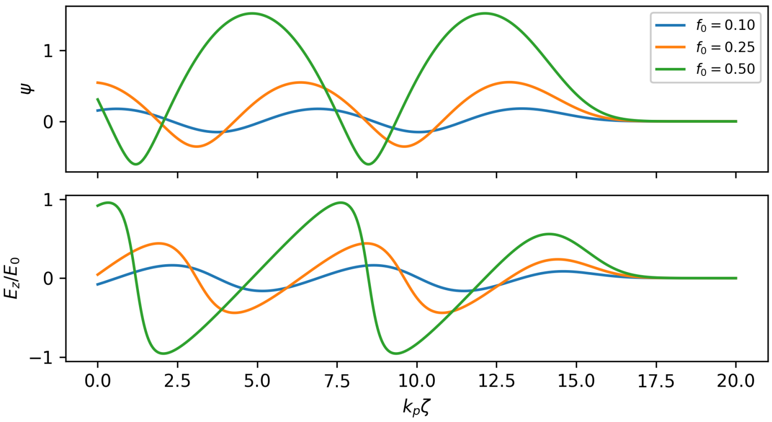


Figure 2.2: Wakefield structure (top) and longitudinal wakefield component (bottom), both for driver beam peak densities $n_b/n_0 = 0.1$, $n_b/n_0 = 0.25$, $n_b/n_0 = 0.5$ (top plot) and evaluated on axis, derived from a numerical evaluation based on equation (2.18).

sheath of electrons which converges to a high-density crest behind the driver. Such an environment does not follow the cold fluid assumption presented above, exhibiting non-thermal transverse momentum spreads in clearly defined regions of the beam wake. The study of such a system is best conducted using a numerical implementation of the Maxwell-Vlasov framework of equations. While it does not allow for an analytical solution, it has been successfully implemented numerically (see [Rosenzweig et al., 1991]), e.g. in the form of so-called Particle-in-Cell simulations (described in chapter 5).

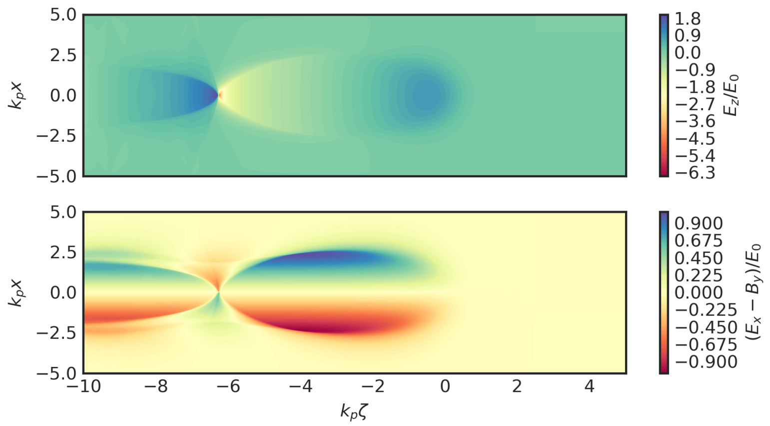


Figure 2.3: Longitudinal (top) and transverse focusing (bottom) wakefield components taken in the $\zeta - x$ plane on the central axis. The wakefield structure is established behind the driver positioned at $k_p\zeta = 0$ with $n_b/n_p = 4.0$ and shows clear indications of a blowout regime, with a linear dependency in the longitudinal component and a radial dependency in the transverse component, respectively.

Figure 2.3 depicts two components of the plasma wakefield environment created by a high-density particle beam with a limited transverse spot size below the skin depth, taken from a PIC simulation. The density distribution of the plasma follows the cavity structure described above, with its electrons expelled from a bubble-like region in the wake of the driver, forming a sheath which closes into a high-density region approximately a plasma wavelength behind the beam. Within this cavity, the longitudinal field shows no significant variation in the radial domain, while the transverse focusing fields remain mostly constant over the longitudinal coordinate for a fixed radial position.

To a first approximation, the blowout can be assumed to follow a spherical structure, with a radius $R$, so that the wakefield potential is given by [Michail Tzoufras et al., 2008]

$$\psi(\zeta, t) = \frac{(k_p R)^2}{4} - \frac{k_p^2(\zeta^2 + r^2)}{4} - 1, \tag{2.29}$$

with the resulting fields given as

$$\frac{E_z}{E_0} = \frac{k_p \zeta}{2}, \tag{2.30}$$

$$\frac{E_r - B_\theta}{E_0} = \frac{k_p r}{2}. \tag{2.31}$$

# 3 PLASMA-WAKEFIELD ACCELERATION

## 3.1 INTRODUCTION AND OVERVIEW

The preceding sections focused on the description of plasma density variations following a perturbation caused by an incident driver beam. The motivation for this specific setup becomes clear once the resulting field distributions, or *wakefields* are considered for their potential accelerating and focusing properties. A relativistic *driver* beam of sufficient density with a spatial distribution tuned to the wavelength of the plasma environment will create a wake following at a phase velocity close to the speed of light. A particle distribution placed at an offset behind the driver (referred to as a *witness*) traveling at relativistic velocities in the same direction will be subjected to the gradients in the driver wake. These wakefields can lead to an energy gain of the witness, provided it is placed in their accelerating region. This acceleration technology is known as *plasma-wakefield acceleration*. Conceptually developed by [Veksler, 1956] and [P. Chen et al., 1985], followed by analytical investigations [Keinigs et al., 1987] and numerical studies [Lotov, 2004; Rosenzweig et al., 1991], its potential as a future acceleration technology saw significant experimental validation at an experiment conducted at the Stanford Linear Accelerator Center (SLAC) [I. Blumenfeld et al., 2007]. Following their propagation through 85 cm of plasma, a small fraction of the electrons from a 42 GeV bunch were demonstrated to have energies over 80 GeV. Modern accelerator facilities are capable of providing high-current beams with sufficiently small dimensions to allow for the establishment of the blowout regime at plasma densities permitting gradients of $\sim 30\,\mathrm{GV\,m^{-1}}$ (for a plasma of $n_p = 1 \times 10^{23}\,\mathrm{m^{-3}}$), with focusing properties advantageous for witness beam transport and quality preservation, a fact several currently proposed experimental facilities (FACET-I, FACET-II and FLASHForward, the latter the focus of this work) are aiming to explore.

It should also be noted that the theoretical description of the plasma perturbation process can also involve the displacement of its electrons through the ponderomotive force of a high-intensity laser beam, forming the foundation of the alternative plasma-based acceleration approach, known as *laser-wakefield acceleration* [Esarey et al., 2009] and offering the potential to realize a true 'tabletop' accelerator structure. Its treatment and appropriate description, however, is beyond the focus of this work. To exploit the promising wakefield properties to full effect, both bunches still need to be *injected* with a well-defined offset with appropriate phase-space properties at a particular place in the plasma bubble.

## 3.2 WITNESS BEAM INJECTION

One of the defining characteristics of a plasma-based acceleration regime is its stability over the relevant beam length scales, provided the driver remains relativistic over the acceleration period to sustain the wake. This ability is compromised, however, since the driver also scans a decelerating region of the longitudinal wakefield component (see figure 2.1), which causes energy loss in the tail portion of its distribution during its propagation, followed by charge depletion and finally a collapse of the wakefield. This natural limit on the length (or duration) of the acceleration process can be associated with a depletion length,

$$L = \frac{m_e c^2 \gamma_b}{e E_z^-}, \tag{3.1}$$

for a driver with an initial energy $m_e c^2 \gamma_b$ and the decelerating longitudinal field value $E_z^-$. Below this limit, however, it is the placement of the witness beam or its transition into the wakefield environment which has the potential to have the most profound effect on its properties and the effectiveness and stability of the acceleration process. Additionally, the incompressibility of the phase-space volume governed by the Vlasov system means that the initial distribution has a profound effect on the parameters obtainable after the acceleration. As a general consideration, an injection process should allow for the selection of a well-defined phase-space region with optimal initial parameters into a controlled spatial location behind the driver. Several of the more prominent methods used in PWFA are presented below.

### 3.2.1 *Density-gradient injection*

The density perturbation following the highly relativistic driver beam is stable within the limit of its own typical time scales, propagating with a phase velocity close to the speed of light. Electrons from the plasma background, lacking the necessary longitudinal momentum, thus cannot propagate into a region behind the driver to gain energy in a sustainable manner. However, if the typical plasma length and time scales change during the driver propagation, a defined phase-space region of plasma electrons can be caught in the driver wake and accelerated. This is the essential idea of density gradient injection [Bulanov et al., 1998], considered either as a step-like shift with the typical transition length $L \lesssim \lambda_p$ or as a gradual transition with $L \gg \lambda_p$.

Considering the linear regime for a step-wise shift with the wakefield potential expressed as $\psi = \psi_0 \cos(k_p \zeta)$, a phase location $N_{\text{per}} \lambda_{p,1}$

for the wave period number $N_{\text{per}}$ will see a shift to $N_{\text{per}}\lambda_{p,2}$ between two plasma density regions with the corresponding wave lengths $\lambda_{p,1}$ and $\lambda_{p,2}$. If this region, $\Delta\zeta = N_{\text{per}}(\lambda_{p,1} - \lambda_{p,2})$ corresponds to positions behind the driver with a sufficiently large gradient, background electrons might gain enough velocity to be carried into the wake and see further acceleration behind the transition [Suk et al., 2000].

For a transition on a length scale much bigger than the plasma wavelength, the phase position can be expressed as

$$\phi(z) = k_p(z)(z - ct), \tag{3.2}$$

for a highly relativistic drive beam, with the corresponding effective plasma frequency and wave number thus given as

$$\omega_{p,\text{eff}} = -\frac{\partial \phi}{\partial t}, \tag{3.3}$$

$$k_{p,\text{eff}} = \frac{\partial \phi}{\partial z}, \tag{3.4}$$

The phase velocity of the plasma wave can thus be given as [Esarey et al., 2009]

$$\beta_{ph} = \frac{\omega_{p,\text{eff}}}{ck_{p,\text{eff}}} = \left[1 + k_p^{-1}\zeta \frac{dk_p(z)}{dz}\right]^{-1}, \tag{3.5}$$

which can be expanded for small variations in density $n$ and positions behind the driver (with $k_p^{-1}\zeta dk_p/dz \ll 1$) and thus approximated as

$$\beta_{ph} \simeq 1 - k_p^{-1}\zeta \frac{dk_p}{dz} = 1 - \frac{\zeta}{2n}\frac{dn}{dz}. \tag{3.6}$$

For electrons with a normalized velocity $\beta = v/c$, the trapping condition can be formulated as $\beta = \beta_{ph}$, which according to the equation above is valid for positions behind the driver where

$$\zeta_{tr} = 2(\beta^{-1} - 1)n \left(\frac{dn}{dz}\right)^{-1}. \tag{3.7}$$

A density transition will thus define an acceptable region behind the driver where plasma background electrons can be injected into the wake and accelerated, making it a crucial parameter influencing a wide range of the resulting witness-bunch properties (see studies done by [Grebenyuk et al., 2014] and [Ossa, Hu, et al., 2017]).

### 3.2.2 *Ionization injection*

Every injection method relying on the plasma electron background to obtain its witness bunch must define a narrow phase-space region for the injected particles to avoid instabilities and limit the range of quality parameters — for example by fine-tuning the plasma density gradient, as mentioned above. Another method involves an introduction of additional electrons (from either an admixture of additional gas species — a dopant gas — or a higher ionization potential of the main plasma) through a precisely timed ionization into an accelerating plasma wake behind the driver. This can be caused by a laser beam, the space-charge fields of the driver itself or the wakefields it creates. The first method in the PWFA regime can be realized by a laser beam focused into the plasma channel following the drive beam. In the case of a transverse Gaussian mode with a spot size at focus $r_0$ and peak intensity $I_0$, its intensity evolution in vacuum can be described as [Esarey et al., 2009]

$$I(r,z) = I_0 \left( \frac{r_0}{r_s(z)} \right)^2 \exp \left( -\frac{2r^2}{r_s(z)^2} \right), \tag{3.8}$$

where the spot size $r_s(z)$ is given as $r_s = 2\sigma_r$ and evolves as

$$r_s(z) = r_0 \sqrt{1 + \left( \frac{z}{z_R} \right)^2}. \tag{3.9}$$

The beam thus diffracts during its propagation in vacuum (with similar behavior in plasma [Eric Esarey, Sprangle, Krall, and Ting, 1996]), with the characteristic length of this process given by the Rayleigh length,

$$z_R = \frac{r_0^2 \pi}{\lambda}, \tag{3.10}$$

and the intensity decaying as $I \propto z^{-2}$ for $z \gg z_R$. A laser pulse can thus be focused to a predefined region behind the driver to reach the necessary ionization threshold of either the higher-order plasma potential or dopant gas and enable the acceleration of emitted electrons in the driver's wake [Hidding et al., 2012].

The necessary ionization threshold can also be reached by the transverse modulation of a non-matched driver beam (see matching explanations below), its space-charge fields undergoing a modulation following its compression and potentially reaching intensities sufficient for ionization [Oz et al., 2007] and subsequent trapping of background electrons.

Finally, the wakefields of a driver of sufficiently high density were found to have regions with both sufficient magnitude for dopant gas ionization and subsequent trapping of the released electrons, allowing for the generation, focusing and acceleration of a witness beam [Ossa, Grebenyuk, et al., 2013].

### 3.2.3 *External injection*

All injection methods discussed above can be seen as instances of *internal injection*, relying on the electrons obtained from the plasma background to construct and accelerate a witness beam distribution.

However, the witness beam can also be introduced from a preaccelerating structure as a second bunch co-propagating with a well-defined spatial offset behind the driver, a method consequently termed *external injection*. Originally introduced in the context of an alternative to the laser-wakefield accelerator concept [P. Chen et al., 1985], it saw increased interest as facilities began exploring this regime, supported by the demonstration of energy doubling of a tail section of a single driver bunch [I. Blumenfeld et al., 2007] which proved the viability of a particle-beam-driven acceleration setup.

While conceptually straightforward in nature, this injection method nevertheless requires careful consideration both of the preaccelerating structures used to obtain the necessary double-bunch setup and the plasma cavity itself. For the combination of a conventional linear accelerator with a plasma stage—the main focus of this work—it is the profound shift from the vacuum beamline to the plasma wakefield environment which needs to be carefully navigated to facilitate the efficient acceleration and transport of the witness. Due to the stringent matching conditions [T. Mehrling, J. Grebenyuk, et al., 2012], the beams need to be focused far below the typical meter-length scales of the betatron function for all relevant density regions. A special interface between the two regimes is required for stable beam transport into the accelerating stage, facilitating an adiabatic or semi-adiabatic phase-space shift in the witness (cf. section 7.3). The energy gain itself is very sensitive to the offset between the two beams, while the high gradient can also imprint an energy chirp on the witness (as seen in section 7.4). In other words, the promising properties afforded by the plasma environment can also have potentially negative side effects which can be mitigated by careful adjustment of the preaccelerator settings. To identify this optimal working point for an existing accelerator design is one of the main topics of this work (see chapter 7).

# 4 PARTICLE BEAM DYNAMICS

The considerations focusing on the theoretical descriptions of acceleration processes above have used individual particles or particle bunches almost interchangeably. As a general rule, the *beam* is a collection of particles with a longitudinal momentum that is much larger than the transverse momentum $\langle p_z \rangle \gg \langle p_{x,y} \rangle$. The specifics of the accelerating structures in accelerators lead to the formation of particle bunches, individual beams or their separated substructures with distinct dimensions in both the longitudinal and transverse directions $\sigma_z$, $\sigma_{x,y}$. The following sections aim to provide a clear picture of the accelerated particle beam and its properties, placing it within the well-established context of accelerator physics.

## 4.1 PARTICLE TRANSPORT IN AN IDEAL SYSTEM

Considering the plasma wakefield regimes introduced above, a single particle placed in a favorable position within can, in the case of a blowout regime, be approximated as being subjected to linear focusing factors defined by the position along the propagation axis only, while the particle beam itself has a negligible energy spread and follows the approximation of paraxial motion [Reiser, 2008]. Such a particle has the equation of motion describing its transverse position (applicable to both directions)

$$x'' + K(z)x = 0, \tag{4.1}$$

where the transverse position $x$, and its derivative $x'' = d^2x/dz^2$ for a focusing function $K = K(z)$ are expressed in *trace-space coordinates*, a system of variables $x - x', y - y', x' = dx/dz = \dot{x}/\dot{z} = p_x/p_z$ (thus $y' = dy/dz = p_y/p_z$) commonly used in accelerator physics. The equation can be solved as [Reiser, 2008]

$$x(z) = Aw(z)\cos[\psi(z) + \phi], \tag{4.2}$$

with a constant amplitude $A$ and phase $\phi$ defined by initial conditions and the phase advance $\psi$ and amplitude functions $w(z)$ depend on the longitudinal position only. Assuming the equation carries an additional degree of freedom allows for the definition $\psi' = w^{-2}$ [Reiser, 2008], so that equation (4.1) can be expressed as an amplitude function for the beam-particle oscillations,

$$w'' + Kw - \frac{1}{x^3} = 0. \tag{4.3}$$

A function describing the closed particle trajectories in trace-space can be found from equation (4.3) and the derivative of equation (4.1) as

$$\frac{x^2}{w^2} + (wx' - w'x) = A^2. \tag{4.4}$$

A particular choice of variables,

$$\hat{\beta} = w^2, \tag{4.5}$$

$$\hat{\alpha} = -ww' = -\frac{\hat{\beta}'}{2}, \tag{4.6}$$

$$\hat{\gamma} = \frac{1}{w^2} + w'^2 = \frac{1 + \hat{\alpha}^2}{\hat{\beta}}, \tag{4.7}$$

transforms equation (4.4) into the equation of an ellipse,

$$\hat{\gamma}(z)x^2 + 2\hat{\alpha}(z)xx' + \hat{\beta}(z)x'^2 = \hat{\epsilon}, \tag{4.8}$$

where the amplitude term was set as $A^2 = \hat{\epsilon}$, showing its conservation in the process.

## 4.2 TRACE-SPACE EMITTANCE AND COURANT-SNYDER PARAMETERS

The above description for the particle trajectory in an ideal system serves as the motivation for the general beam description in trace-space, since the amplitude term can be associated with the *trace-space emittance* [Floettmann, 2003],

$$\hat{\epsilon} = \sqrt{\langle x_c^2 \rangle \langle x'^2_c \rangle - \langle x_c x'_c \rangle^2}, \tag{4.9}$$

with the trace-space variables $x_c = x - \langle x \rangle$, $x'_c = x' - \langle x' \rangle$ (assumed to be centered in the following unless stated otherwise) after transitioning into the moment description (introduced in chapter 1) for a particle distribution function $f$,

$$\langle \Phi(\mathbf{r}, \mathbf{p}) \rangle = \frac{1}{N} \int d\mathbf{r} d\mathbf{p} \Phi(\mathbf{r}, \mathbf{p}) f(\mathbf{r}, \mathbf{p}, t). \tag{4.10}$$

The variables introduced in equations (4.5) to (4.7) can be associated with the *Courant-Snyder parameters* [E. D. Courant et al., 1958] with their general definition given as

$$\hat{\beta} = \frac{\langle x^2 \rangle}{\hat{\epsilon}}, \tag{4.11}$$

$$\hat{\gamma} = \frac{\langle x'^2 \rangle}{\hat{\epsilon}}, \tag{4.12}$$

$$\hat{\alpha} = -\frac{\langle xx' \rangle}{\hat{\epsilon}}. \tag{4.13}$$

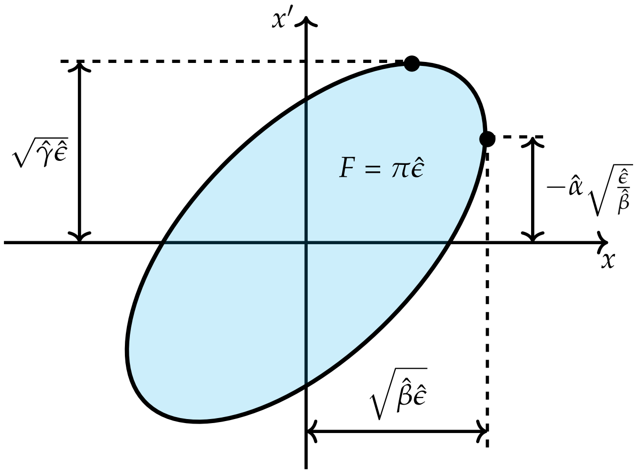


Figure 4.1: Idealized depiction of the trace-space ellipse as defined in equation (4.14), along with the relationships of all Courant-Snyder parameters as well as the trace-space emittance—having a direct geometric interpretation as proportional to the area of the ellipse $F \propto \hat{\epsilon}$ (see [Reiser, 2008]).

For a given trace-space distribution, the Courant-Snyder parameters can be understood as normalized moments, related to the beam size $\sigma_x = \sqrt{\hat{\beta}\hat{\epsilon}}$, the transverse momentum spreads $\sigma_{x'} = \sqrt{\hat{\gamma}\hat{\epsilon}}$ as well as the beam convergence or divergence given by $\hat{\alpha}$. The ellipse equation for an ideal system equation (4.8) can thus be seen as a special interpretation of the general emittance relation,

$$\hat{\gamma}x^2 + 2\hat{\alpha}xx' + \hat{\beta}x'^2 = \hat{\epsilon}, \tag{4.14}$$

connecting the Courant-Snyder parameters through the relation

$$\hat{\beta}\hat{\gamma} = 1 + \hat{\alpha}^2. \tag{4.15}$$

Figure 4.1 provides a depiction of such a trace-space ellipse relating the introduced quantities.

## 4.3 BETATRON OSCILLATIONS IN FOCUSING CHANNELS OF IDEAL SYSTEMS

The $\hat{\beta}$ parameter can also be interpreted as the *betatron function* $\hat{\beta}(z)$ of the beam, related to both the beam size and the local betatron-oscillation length, as introduced for the theoretical depiction of the beam-particle trajectory in the ideal system above. Returning to that configuration, the beta-function can be expressed using 4.3 and 4.5 as

$$\hat{\beta}\hat{\beta}'' - \frac{\hat{\beta}'^2}{2} + 2K\hat{\beta}^2 - 2 = 0, \tag{4.16}$$

or in Courant-Snyder parameters,

$$K\hat{\beta} = \hat{\gamma} + \hat{\alpha}'. \tag{4.17}$$

Assuming a plasma-blowout environment, the main focus of this work, allows the focusing parameter tp be set constant or slowly varying with $K > 0$ (see section 2.5), so that the beta function is given by [Reiser, 2008]

$$\hat{\beta}(z) = \hat{\beta}_0 \cos^2\left(\sqrt{K}z\right) + \frac{1}{\hat{\beta}_0 K}\sin^2\left(\sqrt{K}z\right), \tag{4.18}$$

making the beta function oscillate between two boundaries — $\hat{\beta}_0$ and $1/(\hat{\beta}_0 K)$. Therefore, the condition which must be fulfilled to avoid these oscillations, that is for a beam to be *matched* into a focusing channel, is found from $\hat{\beta}' = 0 = \hat{\alpha}$ and equation (4.18) as

$$\hat{\beta}_0 = \hat{\beta}_m = \frac{1}{\sqrt{K}}, \tag{4.19}$$

together with the other Courant-Snyder parameters,

$$\hat{\alpha}_m = 0, \tag{4.20}$$

$$\hat{\gamma}_m = \sqrt{K}, \tag{4.21}$$

now denoted in their matched variants. This description is of particular interest for beams which deviate from the ideal system description specifically through a non-negligible energy spread, as can be seen in chapter 7.

## 4.4 BEAM-EMITTANCE EVOLUTION

Every accelerator design process must be tuned to potential downstream applications to maximize its usefulness — simply providing a particle bunch with more energy is of no use to applications with stringent beam-quality requirements. It is therefore important to consider figures of merit inherent in processes targeted by the particles provided by plasma-based acceleration. Luminosity and brightness are two such major areas in particle physics research.

### 4.4.1 *Luminosity and Brightness as figures of merit*

The event rate in high-energy colliders is given by $dN_{ev}/dt = \mathcal{L} \cdot \sigma_l$, with the interaction cross section $\sigma_l$ and the *luminosity* $\mathcal{L}$. The former is determined by the physical process under consideration, while the latter represents both the flux and frequency of bunch crossings. The luminosity for two Gaussian bunches is given by [Edwards et al., 2008]

$$\mathcal{L} = \frac{N^2 f_{\text{coll}}}{4\pi\sigma_x\sigma_y}, \tag{4.22}$$

with the particle number $N$, the bunch collision frequency $f_{\text{coll}}$ and the RMS bunch sizes $\sigma_x, \sigma_y$. As mentioned above, the beam size is related to the beta-function, $\sigma_x = \sqrt{\hat{\beta}_x \hat{\epsilon}_x}$ (analogous in the $y$ direction), so that the above equation can be rewritten as

$$\mathcal{L} = \frac{N^2 f_{\text{coll}}}{4\pi\sqrt{\hat{\beta}_x \hat{\epsilon}_x \hat{\beta}_y \hat{\epsilon}_y}}. \tag{4.23}$$

Since the beta function is an inherent property of the beamline design, it is the beam emittance which can be seen as the free parameter determining the intensity of collision processes.

Another prominent application for accelerated particles, specifically electrons, is their use as sources of radiation in a free-electron laser (FEL). The corresponding figure of merit for such a process is the *brightness*, given by [Reiser, 2008]

$$B = \frac{dI}{dSd\Omega}, \tag{4.24}$$

with the current $I$, the transverse area $S$ and the solid angle of the particles in phase-space $\Omega$. The associated transverse phase-space volume $V_4$ can be expressed by integrating over the population hyperellipsoid $K$ [Reiser, 2008]

$$V_4 = \int_K dSd\Omega \simeq \int_K dxdydx'dy' = \frac{\pi^2}{2}\hat{\epsilon}_x \hat{\epsilon}_y. \tag{4.25}$$

For a box-shaped current profile with $I = I_0$, the brightness can be directly obtained as

$$B = \frac{I_0}{V_4} = \frac{2I_0}{\pi^2 \hat{\epsilon}_x \hat{\epsilon}_y}, \tag{4.26}$$

which also allows to approximate beams with non-constant profiles by current-weighted integration over longitudinal beam slices. Again, it is the beam emittance which proves pivotal in determining the output of the physical application downstream.

### 4.4.2 *Emittance degradation processes*

Conservation of emittance is of crucial importance to all acceleration processes — an accelerator providing high gradients at the cost of significant emittance increases is of no use to applications with stringent demands for high luminosity or brightness. To measure emittance and its evolution, two additional definitions are commonly used. To compensate for the compression of the trace-space volume during acceleration through the damping of $x' = p_x/p_z$, a *normalized transverse trace-space emittance* is introduced, defined as

$$\hat{\epsilon}_n = \frac{\langle p_z \rangle}{m_e c}\hat{\epsilon} = \frac{\langle p_z \rangle}{m_e c}\sqrt{\langle x^2 \rangle \langle x'^2 \rangle - \langle xx' \rangle^2}. \tag{4.27}$$

Often, another definition is used, especially in the context of a numerical analysis, the *normalized transverse phase-space emittance* [Floettmann, 2003],

$$\epsilon_n = \frac{1}{m_e c}\sqrt{\langle x^2\rangle\langle p_x^2\rangle - \langle x p_x\rangle^2}. \tag{4.28}$$

While both definitions are equal for beams at the waist $\langle xx'\rangle = 0$, they can deviate significantly in the case of divergent beams with significant energy spreads—while the normalized trace-space emittance remains constant during free drifts, its phase-space counterpart can vary when a correlation between the transverse position and longitudinal momentum emerges [Floettmann, 2003].

Conceptually, the emittance is related both to the beam phase-space volume and its shape [Reiser, 2008]. While the phase-space volume and particle density can be shown to be constant for a trajectory governed by the Vlasov system which ignores particle collisions or radiation effects (a result of the second statement of the Liouville's theorem, see [Nicholson, 1983]), it is the shape of the volume which can change significantly in the acceleration processes described in the main sections of this work. The main influences on emittance development for plasma-based acceleration systems are (compare [Timon Johannes Mehrling, 2014; Reiser, 2008])

1. Off-axis injections into the plasma channel (especially relevant in external injection scenarios, see chapter 9)

2. Parameter mismatch between beam and focusing channel (presented for an ideal system above)—for both beams with non-negligible correlated or uncorrelated energy spreads and non-constant fields over the beam length (see the considerations in chapters 6 to 7.)

3. Nonlinear transverse forces and the resulting beam filamentation

4. Nonlinear coupling of the transverse and longitudinal motion

5. Scattering and collision effects, both within the beam and between the beam particles and the background

In the scope of this work, it is the first two points on this list that can cause significant increases in emittance during the plasma-based acceleration process, while the last item is ignored both because of the assumptions made for the plasma environment and its interaction limitations (see chapter 1) and the longer time-scales for intrabunch scattering processes (see [Reiser, 2008]).

The general aim of the main analysis section will be the treatment of a PWFA acceleration process using well-established numerical methods, complementing the discussion with a new analytic description (see chapter 6). The parameter range for the beams and plasma configurations, while motivated by a current experiment and its requirements, represents a generally promising foundation for PWFA studies. Within this context, the discussion of beam evolution and the mechanisms responsible for emittance growth as well as strategies for its preservation will play a defining role, given its importance for downstream applications briefly motivated above.

Part II

# NUMERICAL METHODS AND TOOLS

# 5 THE PARTICLE-IN-CELL AND SANA METHODS

The aim of this work is the appropriate description of the requirements, limitations and proposed solutions for a plasma-based acceleration process in the PWFA regime, using an externally injected witness beam—helped by a new description of its emittance evolution (see chapter 6) and phase-space modulations (see chapter 8). As seen in the last section, the theoretical treatment of such processes is all but impractical in a microscopic regime treating the Lagrangian particle quantities. By building an argument around the introduction of appropriate requirements, a theoretical framework, centered around the Maxwell-Vlasov system, can be formed to facilitate workable depictions of plasma-bunch interactions. Its concrete implementations, mostly focused on the environment of high-performance computing, have always happened in tune with new proposals and experiments, starting with the introduction of the initial concept for plasma-based accelerators by Tajima and Dawson in 1979 [Tajima et al., 1979] and reflecting the increasing relevance of *computational physics* in the field of plasma physics studies [Pritchett, 2003]. Among those, the *Particle-in-Cell* (PIC) ([Charles et al., 1985; John M Dawson, 1983; Harlow et al., 1955]) method is the most prevalent one in the plasma-based acceleration domain, allowing the relevant processes for both the LWFA and PWFA regimes to be resolved.

## 5.1 THEORETICAL FOUNDATIONS OF PARTICLE-IN-CELL

One of the essential principles of the Particle-in-Cell method, and by extension the root of its name, is the separation of the Maxwell-Vlasov system for a collisionless plasma into two domains, reflecting both Eulerian and Lagrangian quantities and their intertwined development (the depiction follows [Timon Johannes Mehrling, 2014]). As a potential starting point, the particle density so relevant for the theoretical derivations used in chapter 1 (and specifically the Vlasov equation, equation (1.26) is replaced by a collection of discrete particles, representing sections of the phase-space of a species $s$ divided into $M_s$ so-called *macroparticles* (sometimes also called *numerical* or *quasi particles*). The corresponding discretization of the distribution function (see equation (1.15)) is then given by

$$f_s(\boldsymbol{r}, \boldsymbol{p}, t) \approx \sum_{\alpha=1}^{M_s} \tilde{n}_{s,\alpha} \left(\boldsymbol{r} - \boldsymbol{R}_{s,\alpha}(t)\right) \delta \left(\boldsymbol{p} - \boldsymbol{P}_{s,\alpha}(t)\right), \tag{5.1}$$

based on the spatial shape function $\tilde{n}_{s,\alpha}$ of the macroparticles at positions $\boldsymbol{R}_{s,\alpha}$ and moments $\boldsymbol{P}_{s,\alpha}$ commonly set to zero outside of a defined region of interest. This function should provide the smoothness necessary to approach a valid description of the continuous density distribution, while the macroparticle number is required to be sufficiently high to approximate the momentum component of $f_s(\boldsymbol{r}, \boldsymbol{p}, t)$ despite the point-like nature of equation (5.1).

The discrete particle trajectories, reflecting equation (1.20), are given by

$$\frac{d\boldsymbol{R}_{s,\alpha}}{dt} = \boldsymbol{V}_{s,\alpha}, \tag{5.2}$$

$$\frac{d\boldsymbol{P}_{s,\alpha}}{dt} = Q_{s,\alpha}\left(\boldsymbol{E} + \frac{\boldsymbol{V}_{s,\alpha}}{c} \times \boldsymbol{B}\right), \tag{5.3}$$

$\boldsymbol{V}_{s,\alpha}$ being the macroparticle velocity and $Q_{s,\alpha}$ its integrated charge. The corresponding charge and current densities are then given by

$$\rho(\boldsymbol{r}, t) \approx \sum_s q_s \sum_{\alpha=1}^{M_s} \tilde{n}_{s,\alpha}\left(\boldsymbol{r} - \boldsymbol{R}_{s,\alpha}(t)\right), \tag{5.4}$$

$$\boldsymbol{J}(\boldsymbol{r}, t) \approx \sum_s q_s \sum_{\alpha=1}^{M_s} \boldsymbol{V}_{s,\alpha}\tilde{n}_{s,\alpha}\left(\boldsymbol{r} - \boldsymbol{R}_{s,\alpha}(t)\right), \tag{5.5}$$

The discretization represents the Lagrangian aspect of PIC simulations by introducing distinct particles. They are complemented by Eulerian quantities, the charge and current densities above, together with the electric and magnetic fields, which are then evaluated on a spatial mesh structure, forming a system of particles interacting with a grid of cells, hence giving the method its name and pointing the way towards a numerical implementation.

## 5.2 IMPLEMENTATION OF PARTICLE-IN-CELL

The theoretical description above served as a stepping stone between the density-distribution-based methods described in chapter 1 and the concrete implementation of the PIC method. Within this picture of distinct macroparticles located within a grid-based evaluation of Eulerian quantities, the focus can switch to the steps involved in their evolution. For the typical PIC loop, the steps are

1. Current Deposition
2. Field Solver
3. Field Interpolation and Particle pusher

This loop repeats in time steps $\Delta t$, following an important initial configuration—both the charge and current densities need to be zero at the start of the simulation to fulfill the time-independent Maxwell equations (equations (1.17) to (1.17a)), which are then implicitly correct if the time-dependent Maxwell equations (equations (1.17b) to (1.17c)) and the charge continuity equation (see equation (1.28c)) are valid for all time steps.

### 5.2.1 *Current Deposition*

The current of the configuration of macroparticles, given in equation (5.5), is evaluated by a predefined grid mesh using an interpolation of the underlying density shape function, which is usually decomposed into a particular magnitude $\tilde{N}_\alpha$ and a normalized shape function,

$$\tilde{n}_\alpha\left(\boldsymbol{r}-\boldsymbol{R}\right)=\tilde{N}_\alpha S\left(x-X_\alpha,y-Y_\alpha,z-Z_\alpha\right), \tag{5.6}$$

with the normalization

$$\int dxdydzS(x-X_\alpha,y-Y_\alpha,z-Z_\alpha)=1. \tag{5.7}$$

Starting with a one-dimensional grid with constant grid spacing $\Delta x$, a simple linear interpolation scheme for a macroparticle at position $X_\alpha$ and the nearest grid indices $i, i+1$ (and the corresponding grid mesh coordinates $x_i$, $x_{i+1}$) can be formulated as [Pritchett, 2003]

$$S_i^{1\mathrm{D}}(X_\alpha)=1-\frac{x_i-X_\alpha}{\Delta x}, \tag{5.8}$$

$$S_{i+1}^{1\mathrm{D}}(X_\alpha)=\frac{x_i-X_\alpha}{\Delta x}, \tag{5.9}$$

while a more precise deposition using a second-order polynomial and three closest grid points is given by [Esirkepov, 2001]

$$S_i^{1\mathrm{D}}(X_\alpha)=\frac{3}{4}-\left(\frac{x_i-X_\alpha}{\Delta x}\right)^2, \tag{5.10}$$

$$S_{i+1}^{1\mathrm{D}}(X_\alpha)=\frac{1}{2}\left[\frac{1}{2}\mp\left(\frac{x_i-X_\alpha}{\Delta x}\right)\right]^2, \tag{5.11}$$

where $|x_i-X_\alpha|\leq\Delta x/2$. Consequently, for the three-dimensional case, the function is given by

$$S_{i,j,k}^{3\mathrm{D}}(X_\alpha,Y_\alpha,Z_\alpha)=S_i^{1\mathrm{D}}(X_\alpha)S_j^{1\mathrm{D}}(Y_\alpha)S_k^{1\mathrm{D}}(Z_\alpha), \tag{5.12}$$

which allows for the current density to be deposited on the grid as

$$\boldsymbol{J}_{i,j,k}=Q_\alpha\boldsymbol{V}_\alpha S_{i,j,k}^{3\mathrm{D}}\left(X_\alpha,Y_\alpha,Z_\alpha\right), \tag{5.13}$$

with the corresponding charge simply $Q_\alpha=q_\alpha\tilde{N}_\alpha$. This procedure is performed for all particles present in the simulation, summing up their contributions on the grid.

### 5.2.2 *Field Solver*

Once the grid-based current information is available, the corresponding Maxwell equations, equations (1.17b) to (1.17c) can be evaluated using finite differences based on the time steps of the simulation. However, to minimize the error stemming from the spatial and temporal approximations, the commonly used scheme is based on the Yee lattice employing a finite-difference time-domain (FDTD) method [Yee, 1966].

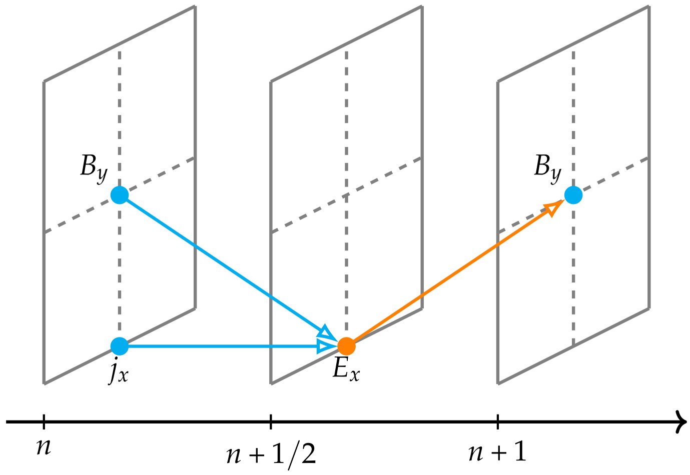


Figure 5.1: Simplified depiction of the Yee mesh in two dimensions, additionally showing its time-centered FDTD method evaluation. The staggering is done through a grid-based offset—the electric fields are defined at the center positions of the cell edges together with the currents, while the magnetic fields are positioned at the center of the cell faces. The time-centering is done by evaluating the two sets of quantities at differing time steps, shown here based on equations (5.14) to (5.15).

Depicted in figure 5.1, the Yee lattice is shifted by half-cell lengths between both field quantities. Additionally, a temporal integration scheme is used which evaluates the field quantities at different time steps, known as a *leap-frog* method. The errors associated with the finite-difference approximations are on the order of $\mathcal{O}(\Delta x^2)$ and $\mathcal{O}(\Delta t^2)$, respectively. A corresponding time-staggered evaluation is then given by [Pritchett, 2003]

$$\boldsymbol{E}^{n+1/2} = \boldsymbol{E}^{n-1/2} + \Delta t \left( c\nabla \times \boldsymbol{B}^n - 4\pi \boldsymbol{J}^n \right), \tag{5.14}$$

$$\boldsymbol{B}^{n+1} = \boldsymbol{B}^n - c\Delta t \nabla \times \boldsymbol{E}^{n+1/2}, \tag{5.15}$$

given here and in the remainder of the chapter in Gaussian units for convenience. This explicit numerical scheme to solve partial differential equations is considered robust and stable, provided it is evaluated on a grid which additionally fulfills the Courant-Friedrichs-Lewy (CFL) condition [R. Courant et al., 1928],

$$\Delta t = C_{\mathrm{CFL}} \frac{\sqrt{\Delta x^2 + \Delta y^2 + \Delta z^2}}{c}, \tag{5.16}$$

where $C_{\mathrm{CFL}}$ is required to be both close to one but bounded below it.

### 5.2.3 *Particle Pusher*

With the grid-based field information available from equations (5.14) to (5.15), an interpolation scheme can be introduced to obtain the field components at the particle position of interest, such as the quadratic spline interpolation introduced above,

$$\boldsymbol{E}_\alpha = \sum_{\lambda,\mu,\nu=\{-1,0,1\}} \boldsymbol{E}_{i+\lambda,j+\mu,k+\nu} S^{1\mathrm{D}}_{i+\lambda}(X_\alpha) S^{1\mathrm{D}}_{j+\mu}(Y_\alpha) S^{1\mathrm{D}}_{k+\nu}(Z_\alpha), \tag{5.17}$$

$$\boldsymbol{B}_\alpha = \sum_{\lambda,\mu,\nu=\{-1,0,1\}} \boldsymbol{B}_{i+\lambda,j+\mu,k+\nu} S^{1\mathrm{D}}_{i+\lambda}(X_\alpha) S^{1\mathrm{D}}_{j+\mu}(Y_\alpha) S^{1\mathrm{D}}_{k+\nu}(Z_\alpha), \tag{5.18}$$

so that the particle position and velocity can be updated using [Vay, 2008]

$$\frac{\gamma^{n+1}_\alpha \boldsymbol{V}^{n+1}_\alpha - \gamma^n_\alpha \boldsymbol{V}^n_\alpha}{\Delta t} = \frac{q}{m}\left(\boldsymbol{E}^{n+1/2}_\alpha + \frac{\bar{\boldsymbol{V}}^{n+1/2}_\alpha}{c} \times \boldsymbol{B}^{n+1/2}_\alpha\right), \tag{5.19}$$

$$\frac{\boldsymbol{R}^{n+3/2}_\alpha - \boldsymbol{R}^{n+1/2}_\alpha}{\Delta t} = \boldsymbol{V}^{n+1}_\alpha. \tag{5.20}$$

The above equation relies on the particle velocity at half-integer time steps, which is not known explicitly. However, a possible solution is based on the separation of the magnetic and electric field contributions to the particle motion, since the unknown quantity can be rewritten as [Vay, 2008]

$$\bar{\boldsymbol{V}}^{n+1/2}_\alpha = \frac{\gamma^n_\alpha \boldsymbol{V}^n_\alpha + \gamma^{n+1}_\alpha \boldsymbol{V}^{n+1}_\alpha}{2\bar{\gamma}^{n+1/2}\alpha}, \tag{5.21}$$

which allows the Lorentz factor to be expressed as

$$\bar{\gamma}^{n+1/2}_\alpha = \sqrt{1 + \left(\gamma^n_\alpha \boldsymbol{V}^n_\alpha + \frac{q\Delta t}{2m}\boldsymbol{E}^{n+1/2}_\alpha\right)}, \tag{5.22}$$

since the magnetic field cannot change the particle's kinetic energy. Equation (5.19) now contains a closed system allowing the calculation of $\gamma^{n+1}_\alpha \boldsymbol{V}^{n+1}_\alpha$ given the fields. The particle positions are then evaluated as

$$\boldsymbol{R}^{n+1}_\alpha = \frac{\left(\boldsymbol{R}^{n+1/2}_\alpha + \boldsymbol{R}^{n+3/2}_\alpha\right)}{2} = \boldsymbol{R}^{n+3/2}_\alpha - \frac{\Delta t \boldsymbol{V}^{n+1}_\alpha}{2} \tag{5.23}$$

closing the evaluation loop.

## 5.3 HIPACE - A QUASISTATIC PARTICLE-IN-CELL METHOD

A fully explicit Particle-in-Cell code is capable of describing all processes prevalent in a plasma-based acceleration scenario for both the LFWA and PWFA regimes, including its constituent elements such as lasers and particle bunches and their typical length and time scales. It is this versatility, however, that also requires significant computing resources, with typical simulations of acceleration processes taking on the order of $10^5$ CPU core hours to run. The explicit FDTD schemes used for PIC calculations place stringent limits on the length and time scales of the simulations (see the CFL condition, equation (5.16)), which aim to resolve the propagation and interaction between high-intensity lasers with sub-micron wavelengths or micron-scale beams in centimeter- or even meter-scale plasma targets. Multiple proposals have been put forward to minimize the effects of this disparity, from implicit schemes [Petrov et al., 2011] to laser envelope models for LWFA regimes [Benedetti et al., 2010] to boosted frame transitions [Vay, 2007].

Considering the arguments summarized in section 2.1, an arguably more fundamental departure from the fully explicit model is centered around the *quasi-static approach* (QSA) [Mora and Antonsen Jr, 1996; Whittum, 1997]. Based on the significant disparities in the typical time-scales of both the plasma-electron background evolution and the developments of both the laser envelope and particle bunches, the QSA argues for a separation of the two domains, allowing for a time step orders of magnitude larger then the one afforded by fully explicit codes. The proposal was quickly followed by its numerical implementations such as WAKE [Mora and Antonsen Jr, 1996] or LCODE [Lotov, 2003], both two-dimensional Cartesian/Cylindrical codes, or the 3D Particle-in-Cell codes QuickPIC [Chengkun Huang et al., 2006] and HiPACE [T. Mehrling, C. Benedetti, et al., 2014]. The latter, a comparatively recent addition to the options available for QSA-based plasma-acceleration studies, was developed at DESY in collaboration with the Lawrence Berkeley National Laboratory (LBNL) and used extensively for the description of the PWFA regime studies discussed in this work.

### 5.3.1 *Physical foundations and numerical implementations in HiPACE*

#### 5.3.1.1 *Plasma-based normalizations*

HiPACE is based on the Maxwell-Vlasov system of equations, normalizing them to the plasma environment, so that the field quantities become $\mathcal{E} = \boldsymbol{E}/E_0$ and $\mathcal{B} = \boldsymbol{B}/E_0$ given the cold nonrelativistic wave-breaking field $E_0 = \omega_p mc/e$. The corresponding Maxwell equations are expressed as (unless stated otherwise, the descriptions in this section follow [T. Mehrling, C. Benedetti, et al., 2014; Timon Johannes

Mehrling, 2014] while employing the Gaussian unit system for convenience)

$$\tilde{\nabla} \cdot \boldsymbol{\mathcal{E}} = \varrho, \tag{5.24}$$

$$\tilde{\nabla} \cdot \boldsymbol{\mathcal{B}} = 0, \tag{5.25}$$

$$\tilde{\nabla} \times \boldsymbol{\mathcal{E}} + \frac{\partial \boldsymbol{\mathcal{B}}}{\partial \tilde{t}} = 0, \tag{5.26}$$

$$\tilde{\nabla} \times \boldsymbol{\mathcal{B}} - \frac{\partial \boldsymbol{\mathcal{E}}}{\partial \tilde{t}} = \boldsymbol{\mathcal{J}}, \tag{5.27}$$

with the normalized charge and current densities, $\varrho = \rho/en_0$ and $\boldsymbol{\mathcal{J}} = \boldsymbol{J}/ecn_0$, respectively. The length and time scales are given by $\tilde{x} = k_p x$ and $\tilde{t} = \omega_p t$, reflected in the differential operator $\tilde{\nabla}$, with the plasma skin depth $k_p = \omega_p/c$ and frequency $\omega_p \sqrt{4\pi n_0 e^2/m_e}$ (compare chapter 1).

Both the plasma and beam particle densities are approximated using discrete macroparticles (see above), their motion and momentum again normalized by $\boldsymbol{X} = k_p \boldsymbol{R}$ and $\boldsymbol{U} = \boldsymbol{P}/Mc$ respectively and governed by the Newtonian and Lorentz-force equations,

$$\frac{d\boldsymbol{X}}{d\tilde{t}} = \boldsymbol{\beta}, \tag{5.28}$$

$$\frac{d\boldsymbol{U}}{d\tilde{t}} = \eta \left( \boldsymbol{\mathcal{E}} + \boldsymbol{\beta} \times \boldsymbol{\mathcal{B}} \right), \tag{5.29}$$

introducing the normalized macro-particle velocity $\boldsymbol{\beta} = \boldsymbol{V}/c = \boldsymbol{U}/\gamma$ and charge-mass ratio $\eta = Qm_e/eM$ (yielding $\eta = -1$ for electrons).

#### 5.3.1.2 *Plasma macroparticle pushing*

Returning to the specifics of the QSA section 2.1, the fundamental assumption of HiPACE states that the Eulerian quantities $\mathcal{Q}$ can be considered in the speed-of-light frame as

$$\frac{\partial \mathcal{Q}}{\partial \tilde{t}} \simeq -\frac{\partial \mathcal{Q}}{\partial \tilde{\zeta}}, \tag{5.30}$$

with the transformation $\tilde{\zeta} = \tilde{z} - \tilde{t} = k_p z - \omega_p t$ and $\tilde{\tau} = \tilde{t}$. The macroparticles describing the plasma electrons are considered Lagrangian in the transverse and Eulerian in the longitudinal domain. For the latter, a given macroparticle quantity $\chi_p$ is described using the normalized particle velocity $\beta_{p,z} = V_{p,z}/c$ in the $z$-direction under the QSA

$$\frac{d\chi_p}{d\tilde{t}} = \left(\beta_{p,z} - 1\right) \frac{\partial \chi_p}{\partial \tilde{\zeta}} + \frac{\partial \chi_p}{\partial \tilde{\tau}} \simeq \left(\beta_{p,z} - 1\right) \frac{\partial \chi_p}{\partial \tilde{\zeta}}. \tag{5.31}$$

Their transverse position can be described using their normalized velocity in the $x$- and $y$-directions $\boldsymbol{U}_{p,\perp}$ by

$$\frac{\partial \boldsymbol{X}_{p,\perp}}{\partial \tilde{\zeta}} = \boldsymbol{F}_{X,\perp} = -\frac{\boldsymbol{U}_{p,\perp}}{1 + \psi_p}, \tag{5.32}$$

where the wakefield potential $\psi = \phi - a_z$ (see section 2.2) is assumed to be a Lagrangian quantity of the plasma macroparticles $\psi = \psi_p$. Its evolution is given by

$$\frac{\partial \psi_p}{\partial \tilde{\zeta}} = F_\psi = \frac{\boldsymbol{U}_{p,\perp}}{1+\psi_p} \cdot \begin{pmatrix} \mathcal{E}_x - \mathcal{B}_y \\ \mathcal{E}_y + \mathcal{B}_x \end{pmatrix} - \mathcal{E}_z. \tag{5.33}$$

The macroparticle transverse momentum evolves according to

$$\frac{\partial \boldsymbol{U}_{p,\perp}}{\partial \tilde{\zeta}} = \boldsymbol{F}_{U,\perp} = \frac{\gamma_p}{1+\psi_p} \cdot \begin{pmatrix} \mathcal{E}_x - \mathcal{B}_y \\ \mathcal{E}_y + \mathcal{B}_x \end{pmatrix} + \begin{pmatrix} \mathcal{B}_y \\ -\mathcal{B}_x \end{pmatrix}, \tag{5.34}$$

with the plasma macroparticle Lorentz factor, $\gamma_p = \sqrt{1 + \boldsymbol{U}_{p,\perp}^2 + U_{p,z}^2}$ defined as

$$\gamma_p = \frac{1 + \boldsymbol{U}_{p,\perp}^2 + (1+\psi_p)^2}{2(1+\psi_p)}. \tag{5.35}$$

In the concrete numerical implementation, the plasma macroparticles and unperturbed fields are initialized on a two-dimensional sublattice at the upper simulation box boundary after the deposition of the beam current density according to the typical PIC methods described above (see section 5.2.1). The routine then moves towards the lower boundary, pushing the particles in each slice using the right-hand side information of equations (5.32) to (5.34) in the transverse directions, while the longitudinal positions are always moved by $-\Delta\tilde{\zeta}$ owing to the QSA.

### 5.3.2 *Plasma current deposition*

When depositing the plasma current based on the plasma macroparticle evolution, the charge and current densities need to be weighted by a particle-specific factor compensating the contribution of the longitudinal velocity which is neglected,

$$w_\alpha = \frac{Q_a}{e} \frac{\gamma_{p,\alpha}}{1+\psi_{p,\alpha}}, \tag{5.36}$$

which results in the corresponding quantities,

$$\varrho = \sum_\alpha w_\alpha S^{2D}\left(\tilde{\boldsymbol{r}}_\perp - \boldsymbol{X}_{\alpha,\perp}(\tilde{\zeta})\right), \tag{5.37}$$

$$\boldsymbol{\mathcal{J}} = \sum_\alpha \boldsymbol{\beta}_\alpha w_\alpha S^{2D}\left(\tilde{\boldsymbol{r}}_\perp - \boldsymbol{X}_{\alpha,\perp}(\tilde{\zeta})\right). \tag{5.38}$$

The transverse shape function has the normalization,

$$\int S^{2D}\left(\tilde{\boldsymbol{r}}_\perp - \boldsymbol{X}_{\alpha,\perp}(\tilde{\zeta})\right) d\tilde{\boldsymbol{r}}_\perp = 1, \tag{5.39}$$

and allows for higher-order depositions in the transverse directions.

### 5.3.3 *Field solver*

Under the QSA, the Maxwell equations in the system given by equations (5.24) to (5.27), together with the source term of the wake potential $\psi = \phi - A_z$,

$$\tilde{\nabla}_\perp \psi = -(\varrho - \mathcal{J}_z), \tag{5.40}$$

allow for the field component equations to be expressed as (see [Weiming An et al., 2013])

$$\tilde{\nabla}_\perp^2 (\boldsymbol{\mathcal{E}}_\perp + \hat{z} \times \boldsymbol{\mathcal{B}}_\perp) = \tilde{\nabla}_\perp (\varrho - \mathcal{J}_z), \tag{5.41}$$

$$\tilde{\nabla}_\perp^2 \boldsymbol{\mathcal{B}}_\perp = \hat{z} \times \left( \frac{\partial}{\partial \tilde{\zeta}} \boldsymbol{\mathcal{J}}_\perp + \tilde{\nabla}_\perp \mathcal{J}_z \right), \tag{5.42}$$

$$\tilde{\nabla}_\perp^2 \mathcal{B}_z = -\tilde{\nabla}_\perp \times \boldsymbol{\mathcal{J}}_\perp, \tag{5.43}$$

$$\tilde{\nabla}_\perp^2 \mathcal{E}_z = \tilde{\nabla}_\perp \cdot \boldsymbol{\mathcal{J}}_\perp. \tag{5.44}$$

with equation (5.41) obtained from,

$$\boldsymbol{\mathcal{E}}_\perp + \hat{z} \times \boldsymbol{\mathcal{B}}_\perp = -\tilde{\nabla}_\perp \psi. \tag{5.45}$$

The particular quantities so depicted can then be directly mapped to the relevant equations in the particle pusher routines.

In the numerical implementation, the first step consists of a charge and current density deposition. This allows for the solution of equation (5.41), corresponding to the focusing force acting on the particles, via the wakefield potential. This is done using a two-dimensional *fast Poisson solver* based on the fast Fourier transform mechanism (FFT) parallelized over the transverse slice domain. Equations (5.43) to (5.44) are solved the same way, after deriving the curl and divergence of the transverse current component. These equations all have source terms limited to the transverse domain, allowing their evaluation at the given longitudinal position within the HiPACE algorithm which performs the calculation on individual grid slices, starting at the front of the simulation and progressing towards the end. Within this context, equation (5.42) demands special consideration, since it features a longitudinal dependency on the current. Since it requires information contained in the next slice and inaccessible in the backpropagation scheme used, a predictor-corrector method [Mora and Antonsen, 1997] is used to solve equation (5.42) in an iterative way for the transverse magnetic field components, terminating this loop once the corresponding error function falls under a certain threshold.

### 5.3.4 *Beam pushing*

Since the beam macroparticles are highly relativistic, they do not adhere to the QSA, instead evolving on the characteristic time scale $\tilde{t}$.

Thus, they are treated separately from the slice-based plasma-particle mechanism described above, governed by the set of equations

$$\frac{d\boldsymbol{X}_{b,\perp}}{d\tilde{t}} = \frac{\boldsymbol{U}_{b,\perp}}{\gamma_b}, \tag{5.46}$$

$$\frac{d\boldsymbol{U}_{b,\perp}}{d\tilde{t}} = \eta \begin{pmatrix} \mathcal{E}_x - \mathcal{B}_y \\ \mathcal{E}_y + \mathcal{B}_x \end{pmatrix}, \tag{5.47}$$

$$\frac{dU_{b,z}}{d\tilde{t}} = \eta \left( E_z + \frac{U_{b,x}B_y - U_{b,y}B_x}{\gamma_b} \right), \tag{5.48}$$

$$\gamma_b = \sqrt{1 + \boldsymbol{U}_{b,\perp}^2 + U_{b,z}^2}. \tag{5.49}$$

Provided with the grid-based field component values obtained in the plasma-based iteration, the macroparticle information can now be updated, first moving them by a half time-step,

$$\boldsymbol{X}_{b,\perp}^{n+1/2} = \boldsymbol{X}_{b,\perp}^{n} + \frac{\Delta\tilde{t}}{2}\frac{\boldsymbol{U}_{b,\perp}^{n}}{\gamma_b^n}, \tag{5.50}$$

followed by the interpolation of the field quantities to the new positions. Subsequently, the particle moments can be updated based on the above equations,

$$\frac{\boldsymbol{U}_{b,\perp}^{n+1} - \boldsymbol{U}_{b,\perp}^{n}}{\Delta\tilde{t}} = \eta \begin{pmatrix} \mathcal{E}_x - \mathcal{B}_y \\ \mathcal{E}_y + \mathcal{B}_x \end{pmatrix}^{n+1/2}, \tag{5.51}$$

$$\boldsymbol{U}_{b,\perp}^{n+1/2} = \frac{\boldsymbol{U}_{b,\perp}^{n+1} + \boldsymbol{U}_{b,\perp}^{n}}{2}, \tag{5.52}$$

$$\frac{U_{b,z}^{n+1} - U_{b,z}^{n}}{\Delta\tilde{t}} = \eta \left( E_z^{n+1/2} + \frac{U_{b,x}^{n+1/2}B_y^{n+1/2} - U_{b,y}^{n+1/2}B_x^{n+1/2}}{\bar{\gamma}_b^{n+1/2}} \right), \tag{5.53}$$

$$\bar{\gamma}_b^{n+1/2} = \sqrt{1 + \left(\boldsymbol{U}_{b,\perp}^{n+1/2}\right)^2 + \left(U_{b,z}^{n} + \frac{\Delta\tilde{t}}{2}\eta\mathcal{E}_z^{n+1/2}\right)^2}. \tag{5.54}$$

After the momentum has been updated, the final half-step can be performed for the position pusher,

$$\boldsymbol{X}_{b,\perp}^{n+1} = \boldsymbol{X}_{b,\perp}^{n+1/2} + \frac{\Delta\tilde{t}}{2}\frac{\boldsymbol{U}_{b,\perp}^{n+1/2}}{\bar{\gamma}_b^{n+1/2}}, \tag{5.55}$$

while the longitudinal position is updated to first order only,

$$\boldsymbol{X}_{b,z}^{n+1} = \boldsymbol{X}_{b,z}^{n} + \Delta\tilde{t}\frac{\boldsymbol{U}_{b,z}^{n+1/2}}{\bar{\gamma}_b^{n+1/2} - 1}, \tag{5.56}$$

a new feature introduced as part of this work and allowing for the consistent description of processes where a significant loss in energy results in beam loss.

Because of the QSA-based decoupling of the plasma and beam macroparticle descriptions, the time stepping follows the typical length scales of the particle bunches present in the system, with $\Delta\tilde{t}$ chosen to best describe their dynamics based on the macroparticle energy and the local plasma density. This can be seen as a crucial advantage over fully explicit PIC codes, which resolve the propagation on the length scales determined by the plasma itself and limited by the CFL condition. For highly relativistic beams, this difference can be expressed using the typical length scales, the plasma skin depth $k_p^{-1}$ and the betatron oscillation length $k_\beta^{-1}$, related by $k_\beta^{-1} = \sqrt{2\gamma} k_p^{-1}$, with an intuitive reduction in the steps necessary to resolve a simulation following a particle beam evolution in the quasistatic regime.

HiPACE thus provides an excellent tool for the description of the processes prevalent in the PWFA regime given an externally injected bunch, one of the main topics of this work. In that regard, it was especially useful for iterations probing parameter ranges often inaccessible to simplified analytic descriptions, as well as the study of preaccelerated beams obtained from particle tracking codes. The capabilities of HiPACE to interface with external codes and provide its data in a well-structured format for further analysis were improved as part of this work, as discussed below.

## 5.4 EXTENDED HIPACE CAPABILITIES

At the start of this work, HiPACE already provided well-tested mechanisms for the efficient simulation of PWFA processes involving highly relativistic beams. The additional capabilities added during the progress of the analyses presented in the following main sections, therefore, were aimed more at enhancing the interfacing options available to potential developers and users. Consequently, the focus was mostly on the input and output — that is, the initial HiPACE configuration, beam setup or import of macroparticles from other codes and the subsequent output of the information generated during the simulations.

The focus of this work was the introduction of a HiPACE setup approach revolving around a configuration file based on the YAML specification [Ben-Kiki et al., 2005]. This hierarchically structured file format offers the most relevant data types for the construction of a simulation domain with incident particles and plasma profiles (floats, integers, strings and arrays) as built-in structures and is implemented by a well-documented library provided in the programming language of HiPACE. Furthermore, the configuration file is a simple human-readable text file, which allows for easy manipulation and parsing by external tools, an important capability with respect to automated iteration runs needed for some analysis sections of this work, where a specific beam- or plasma-profile attribute could be changed to take on many values and thus find an optimal point with respect to a predefined quality parameter.

Two additional aspects can be seen as related to this input and output standardization—the capacity to define arbitrary beam-density functions to mimic known or expected distributions and a widely accepted data storage format for both simulation quantity output and beam distribution input.

### 5.4.1 *Beam-density-function definition*

The capability to initialize beams with arbitrary current profiles is an important requirement in multiple studies such as beam loading [Lotov, 2005], and is used extensively in this work (cf. the distributions presented in chapter 9). The corresponding implementation in HiPACE relies on the specifics of the beam macroparticle initialization. HiPACE allows for the introduction of variable-weight macroparticles on a sub-grid mesh within each cell, approximating a density distribution according to principles of the Particle-in-Cell method outlined above. During the initial setup, the provided profile function is evaluated on each sub-mesh position, introducing macroparticles of corresponding density provided it is above a predefined threshold value. A simplified representation of this method is depicted in figure 5.2. The function itself is provided in the configuration file, which is parsed using the *GNU libmatheval* library and turned into an internal function representation allowing for the evaluation of the respective longitudinal macroparticle position. The specific density value is then obtained after a convolution with the transverse Gaussian profile function.

As an additional feature, this capability was extended to allow the definition of arbitrary plasma profiles. These can be provided for both the longitudinal and transverse domains. While the latter is of interest to descriptions relying on non-constant transverse electron background distributions such as a plasma lens [Forsyth et al., 1965], the former was directly applied in the course of this work to model beneficial vacuum-plasma transitions (cf. chapter 7).

### 5.4.2 *Data input and output using the HDF5 format*

Every high-performance code requires a stable, efficient and potentially fault-tolerant interface between the in-memory data structures and the file system. Simply writing the relevant quantities to disk is a simple method especially useful for debugging, but reaches its limits quickly once the program matures beyond the initial implementation stages towards user-facing applications with corresponding requirements with respect to stability and standardization. This is especially relevant for highly parallelized PIC codes, where the simulation domain is divided among up to hundreds or thousands of nodes. The

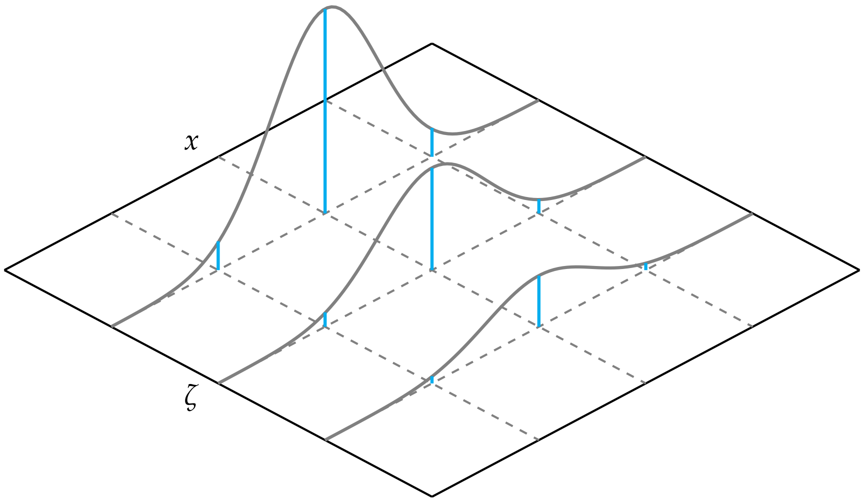


Figure 5.2: HiPACE macroparticle deposition using a variable-weight scheme and a predefined sub-mesh cell division using a 3x3 structure in two dimensions, placing the particles at the corresponding equidistant positions within the cell. The longitudinal profile is evaluated using an arbitrary mathematical function and convoluted with a transverse Gaussian description (in this case, a linear function was used).

corresponding grid-based quantities need to be carefully mapped onto the respective substructures of a data file, while maintaining low-latency communication over the available communicator points. The same is true for the macroparticle information, with the added complication of variable particle structure sizes subject to change during the simulation process (e.g. due to charge depletion).

The *HDF5* data format [Folk et al., 1999] is not only widely used in the context of high-performance computing applications, but also offers a straightforward interface to the MPI standard used by HiPACE for parallelization. The standard uses binary files with a hierarchy similar to a file-system, allowing for efficient data storage and access. The simulation domain quantities are mapped onto array structures, complete with attributes providing additional information potentially useful for further analysis steps. However, while this is straightforward for grid-based information such as the plasma density distribution where the array dimensions and thus the required file structure are known at the initialization and for all following time steps, the particular nature of the HiPACE node communication and evaluation loop requires a more elaborate approach for the beam macroparticle phase-space.

Due to the restrictions of the quasistatic implementation in HiPACE, its internode communication process in the longitudinal direction follows the backstreaming mechanism of the plasma macroparticles introduced in the previous sections (cf. section 5.3.1.2). The solution used for the macroparticle phase-space output was to communicate

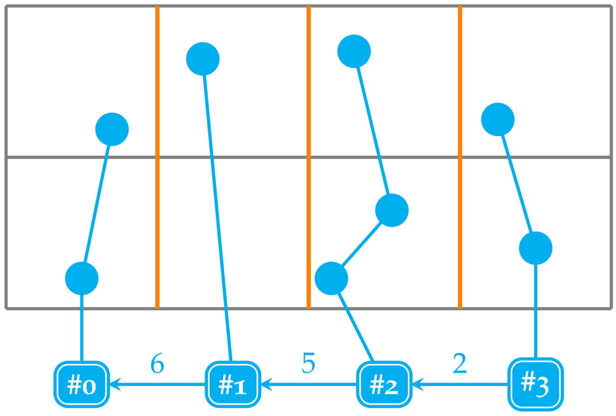


Figure 5.3: Representation of the offset communication mechanism for macroparticle information output. The number of particles is passed on to the next slice, where it is used as an offset in the file structure.

the number of particles along the same direction, thus informing the following nodes of the necessary offset parameter and avoiding data corruption. In the transverse domain, the data output is handled by a single *root* node, which collects the grid-based information and macroparticle quantities within its slice and writes them to the respective offsets, as depicted in figure 5.3.

The adoption of the HDF5 format had an additional benefit with respect to data input into HiPACE. Together with the output, HiPACE gained the capability to read its macroparticle data from a standardized HDF5 file. This allows to interface with other simulation codes using the macroparticle concept for the particle beam description. A prominent example is the fully explicit PIC code OSIRIS [Ricardo A Fonseca et al., 2002], which is able to describe a wide range of plasma-acceleration-related processes currently inaccessible in the quasistatic approximation—specifically the LWFA regime and certain injection methods. In a symbiotic setup, this capacity could be used to obtain a macroparticle distribution which is then read into HiPACE and propagated through the plasma in a much more efficient way. A different interface is used directly in this work, where the distributions from the particle-tracking code ELEGANT [Michael Borland, 2000] are used to approximate the expected beam configurations at the plasma cell (chapter 9). The ability to exchange information in a standardized way between different numerical implementations is an important capability, allowing HiPACE to act as a mediating mechanism between diverse applications, parameter ranges and environments. Consequently, simulation quantities produced by HiPACE can serve as a foundation for a system which otherwise foregoes elaborate PIC simulations to directly evaluate the Vlasov equation based on mono-energetic subsets of the particle beam phase space, as described in the next section.

## 5.5 SANA - A SEMI-ANALYTIC NUMERICAL APPROACH

The *semi-analytic numerical approach* (SANA) (unless otherwise noted, the following derivations follow [T. J. Mehrling et al., 2016]) was introduced with the aim of calculating the emittance evolution of a witness beam propagating in a blowout-regime wakefield environment. The beam, while non- to mildly relativistic in the transverse directions, is assumed to be highly relativistic in the longitudinal domain, so that the Lorentz factor is expressed as $p_z \simeq \gamma \gg 1$. The corresponding phase-space distribution function is therefore defined by $f = f(x, p_x, \zeta, \gamma, t)$ and is evaluated in the system normalized to plasma-based units introduced above—the time to the plasma frequency $\omega_{p,0}^{-1}$, the momentum to $m_e c$ and both the transverse position and the longitudinal coordinate in the co-moving frame $\zeta = z - t$ to the skin depth $k_{p,0}^{-1} = c/\omega_{p,0}$. Both transverse directions are assumed symmetric and centered around zero for both the position and momentum.

As explained above, the temporal evolution of this distribution is governed by the *Vlasov equation* (see section 1.2.2). Introducing the two transverse and longitudinal forces acting on the particles as $F_x$ and $F_z$, both normalized to $\omega_{p,0} m_e c$, allows for this description to be approximated as

$$\left(\partial_t + \frac{p_x}{\gamma}\partial_x + \partial_{p_x} F_x + \partial_\gamma F_z\right) f = 0. \tag{5.57}$$

Since the aim is to calculate the transverse phase-space emittance,

$$\epsilon = \sqrt{\langle x^2\rangle\langle p_x^2\rangle - \langle x p_x\rangle^2}, \tag{5.58}$$

which requires the knowledge of averages only, given by

$$\langle\Phi(x, p_x, \zeta, t)\rangle = \frac{1}{N}\int dx \int dp_x \int d\zeta \int d\gamma \Phi f, \tag{5.59}$$

with the particle number

$$N = \int dx \int dp_x \int d\zeta \int d\gamma, f, \tag{5.60}$$

the above Vlasov approximation can be replaced with the general moment equation [Robson et al., 2015]

$$\partial_t\langle\Phi\rangle = \langle\frac{p_x}{\gamma}\partial_x\Phi\rangle + \langle F_x \partial_{p_x}\Phi\rangle + \langle F_z \partial_\gamma \Phi\rangle, \tag{5.61}$$

after its multiplication with $\Phi$, followed by an integration by parts over the phase-space variables.

The restriction of the considerations to a blowout regime (see section 2.5) additionally allows a depiction of the transverse force to be found

$$F_x(x, t) = -\hat{k}_x(t) x, \tag{5.62}$$

with a focusing parameter $\hat{k}_x$, yielding

$$\partial_t \langle x^2 \rangle = 2\langle x\frac{p_x}{\gamma}\rangle, \tag{5.63}$$

$$\partial_t \langle xp_x \rangle = \langle \frac{p_x^2}{\gamma}\rangle - \hat{k}_x\langle x^2\rangle, \tag{5.64}$$

$$\partial_t \langle p_x^2 \rangle = -2\hat{k}_x\langle xp_x\rangle, \tag{5.65}$$

$$\partial_t \langle \gamma \rangle = \langle F_z\rangle. \tag{5.66}$$

While equations (5.63) to (5.66) can be related to the beam-envelope equations for *mono-energetic beams* [Reiser, 2008], one of the essential ideas of the semi-analytical numerical approach is to replace the distribution function by a discretized variant,

$$f(x, p_x, \zeta, \gamma, t) \simeq \sum_{k=1}^{M} N_k\delta(\gamma - \gamma_k(t))\delta(\zeta - \zeta_k)f_k(x, p_x, t), \tag{5.67}$$

with the total number of mono-energetic subsets $M$, each carrying an invariant number of electrons $N_k$ all exhibiting the same Lorentz factor $\gamma_k(t)$ and governed by the transverse-phase-space distribution subset $f_k(x, p_x)$. The discretization can thus approximate beams with correlated and uncorrelated energy spreads, their total electron number then given by $N = \sum_{k=1}^{M} N_k$. Assuming the phase-space averages are separable, $\Phi(x, p_x, \zeta, \gamma) = \Phi_t(x, p_x) \cdot \Phi_l(\zeta, \gamma)$ allows for the phase-space averages to be expressed as [T. J. Mehrling et al., 2016]

$$\langle\Phi(x, p_x, \zeta, \gamma)\rangle = \frac{1}{N}\int dxdp_xd\zeta d\gamma\Phi(x, p_x, \zeta, \gamma)f(x, p_x, \zeta, \gamma, t) \tag{5.68}$$

$$= \frac{1}{N}\sum_{k=1}^{M} N_k\langle\Phi_l(\zeta, \gamma)\rangle_k \cdot \langle\Phi_t(x, p_x)\rangle_k. \tag{5.69}$$

In other words, the phase-space averages are constructed by forming sums over the products of both the longitudinal and transverse averages,

$$\langle\Phi_l(\zeta, \gamma)\rangle_k = \Phi_l(\zeta_k, \gamma_k) \tag{5.70}$$

$$\langle\Phi_t(x, p_x)\rangle_k = \int dx \int dp_x\Phi_t(x, p_x)f_k(x, p_x, t), \tag{5.71}$$

which finally allows the general phase-space moment equations (equations (5.63) to (5.66)) to be transferred into the energy subset description,

$$\partial_t \langle x^2 \rangle_k = 2\frac{\langle xp_x\rangle_k}{\gamma_k}, \tag{5.72}$$

$$\partial_t \langle xp_x \rangle_k = \frac{\langle p_x^2\rangle_k}{\gamma_k} - \hat{k}_x(t)\langle x^2\rangle_k, \tag{5.73}$$

$$\partial_t \langle p_x^2 \rangle_k = -2\hat{k}_x(t)\langle xp_x\rangle_k, \tag{5.74}$$

$$\partial_t \gamma_k = F_z(\zeta_k, t). \tag{5.75}$$

For highly relativistic beams not exhibiting charge depletion and slippage (a valid assumption in typical PWFA blowout regimes), this allows their emittance evolution and corresponding transverse-phase-space moments to be described using a priori knowledge of the blowout environment and the longitudinal wakefield gradient. For a potential application, see the analysis section of this work (chapter 6), where an idealized beam slice is propagated in a plasma-blowout regime to benchmark an analytic model for the description of uncorrelated emittance evolution given a finite beam-energy spread. However, SANA is not limited to descriptions of single-slice scenarios experiencing a constant accelerating gradient $F_z$. Its formulation allows for the approximation of a longitudinal wakefield distribution, constructing the beam from subsets placed at distinct co-moving positions. The demand for an existing wakefield distribution can be mitigated by a short HiPACE simulation which allows the necessary information to be extracted after a few time steps.

## 5.6 CONCLUDING REMARKS

The adequate description of plasma-based acceleration processes is a challenging requirement for the investigation of its capacities, restrictions and potential applications. From the microscopic picture, to the Klimontovich equation and the Maxwell-Vlasov system, the approaches have been narrowed to focus predominantly on the expected parameter range, gaining efficiency at the cost of a potentially wider view including processes argued to be irrelevant (e.g. interparticle collisions). The Particle-in-Cell framework can be understood as following this trajectory into the numerical domain, enabling a robust and stable description of processes involving large quantities of particles in regimes inaccessible to analytical treatments. The theme of specific parameter ranges and appropriate assumptions and limitations is carried forward by quasistatic approaches, exemplified by HiPACE. Through the focus on the particle beam and its inherent time domain, significant gains in efficiency are possible, again at the cost of a narrowed applicability. However, the final focus is often on the statistical quantities representing parameters which can be extracted in an experimental acceleration setup such as emittance and energy spread. Taking the idea of a moment-based description and assuming a preexisting wakefield environment allows the numerical descriptions of the evolution of corresponding beam attributes for a collection of beam phase-space subsets, which can often serve as a good benchmark leading into PIC simulations or avoid them altogether, as shown in the SANA framework.

The theme of narrowing the parameter range, process space and interactions towards highly specialized tools is mirrored in the following main analysis sections of this work. Starting from a theoretical description of the emittance evolution that is comparatively narrow in scope (chapter 6), the work will use the methods introduced above to construct the descriptions of more complex or elaborate interaction schemes (chapters 7 to 8), finishing with a simulation incorporating and discussing distributions from another simulation code, as mentioned above (chapter 9).

# Part III

# BEAM STUDIES

# 6 ANALYTICAL MODEL FOR THE UNCORRELATED EMITTANCE EVOLUTION

## 6.1 INTRODUCTION

This chapter introduces a novel approach to calculate the evolution of uncorrelated emittance in linear focusing environments (e.g. the plasma blowout regimes discussed above). It can provide important insights on its development without the need for numerical methods such as PIC (cf. chapter 5), avoiding the need for potentially time-consuming calculations in certain cases. The model is thus an important addition to the subsequent discussion of external injection scenarios presented in the following chapters, offering best-case approximations of important parameters such as emittance growth length scales.

As an essential beam-quality parameter, e.g. for FEL applications, the transverse phase-space emittance received extensive attention in several works concerned with plasma-based acceleration processes [T. Mehrling, J. Grebenyuk, et al., 2012; Michel et al., 2006]. Furthermore, it was shown that transitions into and the propagation within multiple stages can lead to significant emittance growth if the beams are not matched and the vacuum-to-plasma and plasma-to-vacuum transitions not tapered properly [Dornmair et al., 2015; Floettmann, 2014; K. A. Marsh et al., 2005; T. Mehrling, J. Grebenyuk, et al., 2012].

In general, an emittance increase is related to a change in the shape of the phase-space volume occupied by the beam. This effect can be caused by multiple factors, from an off-axis injection to nonlinear transverse forces or coupling effects in the transverse-longitudinal beam-particle motion. In the context of the blowout regime considered in this chapter, however, it is the mismatch between the beam and the plasma environment, together with significant correlated or uncorrelated energy spreads or variations of the longitudinal fields over the intra-bunch length, that most strongly contribute to an emittance degradation.

The extensive analysis of such a critical component and the corresponding processes typically involves the use of particle-in-cell (PIC) simulations, which offer valuable insights at the cost of time consuming computations, especially when performing parameter scans. While models such as the semi-analytic numerical approach [T. J. Mehrling et al., 2016] provide a significant increase in efficiency, the analytic model has the advantage that it not only immediately delivers the relevant parameters and their evolution, but also offers direct insights on the impact of the different factors involved in the acceleration process.

This chapter presents a set of analytic descriptions of the evolution of beam moments in a PWFA process for two different scenarios. The first scenario involves a slice of the witness beam with a specific uncorrelated energy spread propagating in a PWFA blowout regime without energy gain. The second scenario considers the same situation, additionally taking into account an energy gain along the propagation axis. Both scenarios are discussed within their respective sections, which follow the same structure — an initial introduction of the physical and mathematical basis for the consideration, a description of the physical environment, as well as a depiction and analysis of the resulting formulas where appropriate, followed by a comparison with PIC simulations and the aforementioned SANA calculation results.

## 6.2 SCENARIO I — BEAM SLICE WITHOUT ENERGY GAIN

In general, the beam emittance is a six-dimensional phase-space volume with a conserved density along any particle trajectory [Floettmann, 2003]. Usually, however, two-dimensional projections into orthogonal planes are considered (e.g. $x$-$p_x$), occupying an area comprised of those particles positions at the core of a given distribution. In the following section, an analytic description of the evolution of such a phase-space area is derived, starting with individual particle trajectories and considering their phase-space distribution to arrive at a description of their beam moments and, consequently, the beam emittance.

### 6.2.1 *Mathematical Model*

The starting point for this analysis is the differential equation for the transverse position $x$ of a single electron with constant energy within a linearly focusing ion channel forming an harmonic oscillator,

$$\frac{d^2x}{dt^2} + \omega_\beta^2 x = 0, \tag{6.1}$$

with the betatron frequency $\omega_\beta = \omega_p/\sqrt{2\gamma}$, the Lorentz factor $\gamma$, and where $\omega_p = \sqrt{4\pi n_0 e^2/m}$ is the plasma frequency, with the ambient plasma density $n_0$, the elementary charge $e$ and the electron rest mass $m$. The solution for equation (6.1) is given by

$$x(t) \simeq x_0 \cos[\varphi(t)] + \frac{p_{x,0}}{m\gamma_0\omega_{\beta,0}} \sin[\varphi(t)], \tag{6.2}$$

with the initial position $x_0$, the initial transverse particle momentum $p_{x,0}$ as well as the initial Lorentz factor $\gamma_0$ and betatron frequency $\omega_{\beta,0}$. The phase advance, defined as the argument in the trigonometric functions, is $\varphi(t) = \int \omega_\beta$, with $\varphi(t) = \omega_{\beta,0} t$ in this consideration.

In the following, the description evolves from a single-particle picture towards a statistical approach involving collective beam-slice averages in order to arrive at an analytic formulation of the normalized transverse phase-space emittance [Floettmann, 2003]

$$\epsilon_n = \frac{1}{m_e c}\sqrt{\langle x^2\rangle \langle p_x^2\rangle - \langle x p_x\rangle^2}, \tag{6.3}$$

with the phase-space beam moments $\langle x^2\rangle$, $\langle p_x^2\rangle$, $\langle x p_x\rangle^2$ (cf. equations (6.4) to (6.6) for a suitable definition). It is necessary to chose an ansatz to evaluate equation (6.2) that relies on a separable beam distribution function (as outlined in [T. J. Mehrling et al., 2016]). The assumption is that the beam particle slice possesses an initial phase-space distribution $f_0(x_0, p_0, \gamma_0)$ (with the normalization $\int f_0 dx_{x,0} dp_{x,0} d\gamma_0 = 1$), where the initial transverse position $x_0$ and the initial transverse momentum $p_{x,0}$ are not correlated with the energy. This means that the beam distribution is separable $f_0 = f_\perp(x_0, p_{x,0}) f_\gamma(\gamma_0)$, thus allowing for the reconstruction of the phase-space moments using

$$\langle x^2\rangle(t) = \int_{-\infty}^{\infty} (x^2(t)) f_0 dx_0 dp_{x,0} d\gamma_0 \tag{6.4}$$

$$\langle p_x^2\rangle(t) = \int_{-\infty}^{\infty} (p_x^2(t)) f_0 dx_0 dp_{x,0} d\gamma_0 \tag{6.5}$$

$$\langle x p_x\rangle(t) = \int_{-\infty}^{\infty} \left(x(t) p_x(t)\right) f_0 dx_0 dp_{x,0} d\gamma_0, \tag{6.6}$$

with an arbitrary $f_\perp(x_0, p_{x,0})$ except that $f_\perp = 0$ outside of the ion-channel and the energy distribution is assumed to follow a Gaussian form with $f_\gamma = (\sqrt{2\pi}\sigma_\gamma)^{-1} \exp(-\delta\gamma^2/2\sigma_\gamma^2)$, where $\delta\gamma = \gamma - \overline{\gamma}$, describes a deviation of individual particles from the mean slice energy, $\overline{\gamma}$. Assuming a small relative energy deviation of the electrons, $|\delta\gamma/\overline{\gamma}| \ll 1$, allows for an approximation of the betatron frequency

$$\omega_\beta \simeq \overline{\omega_\beta}\left(1 - \delta\gamma/2\overline{\gamma}\right), \tag{6.7}$$

with the mean betatron frequency $\overline{\omega_\beta} = \omega_p/\sqrt{2\overline{\gamma}}$. Since the energy variations are ignored in this scenario, the betatron frequency remains constant, $\omega_\beta = \omega_{\beta,0}$, making it possible to determine the phase advance as $\varphi(t) = \overline{\omega_{\beta,0}}\left(1 - \delta\gamma/2\overline{\gamma_0}\right) t$. Using this expression, together with the original solution for the individual particle position, equation (6.2) as well as $p_x(t) = m\gamma dx/dt$, allows the transverse beam moments to be obtained and hence the transverse phase-space emittance, which can be written analytically as

$$\begin{aligned}\epsilon_n^2(t) = \frac{1}{4} & \left( \left(\overline{\gamma_0}\overline{k_\beta}\right)^2 \left\langle x_0^2 \right\rangle^2 + \frac{1}{\left(\overline{\gamma_0}\overline{k_\beta}\right)^2} \left\langle u_{x,0}^2 \right\rangle^2 \right) \\ & \times \left(1 - e^{-bt^2}\right) \\ & + \frac{1}{2} \left\langle x_0^2 \right\rangle \left\langle u_{x,0}^2 \right\rangle \left(1 + e^{-bt^2}\right) \\ & - \left\langle x_0 u_{x,0} \right\rangle^2 e^{-bt^2},\end{aligned} \tag{6.8}$$

with the normalized momentum $u_x = p_x/m_e c$, the mean betatron oscillation wave number $\overline{k_\beta} = \overline{\omega_\beta}/c$, together with an emittance growth factor $b = \overline{\omega_\beta}^2 \Delta\gamma^2$ (using the common depiction of the energy spread $\Delta\gamma = \sigma_\gamma/\gamma$). It is straightforward to recover the initial normalized phase-space emittance $\epsilon_0 = \sqrt{\left\langle x_0^2 \right\rangle \left\langle u_{x,0}^2 \right\rangle - \left\langle x_0 u_{x,0} \right\rangle^2}$ of the slice, by setting $t = 0$. It can also be observed that the subsequent time-dependent change in emittance is driven by the exponential terms and thus, through the growth factor, the initial energy spread of the slice. This betatron-phase mixing effect, owing to the finite energy spread in the slice and the corresponding energy-dependent oscillations of the electrons, is an example of the so-called betatron decoherence. Its influence on the development of emittance growth can be seen from the prominent role of the betatron wave number (or frequency) in the first term. It can be observed from equation (6.8) that the emittance growth reaches a saturation point once the contribution from the exponential term is sufficiently small, providing a time scale for the decoherence as $t_d \gg b^{-1/2} = 1/\left(\Delta\gamma\overline{\omega_\beta}\right)$. Assuming $t \to \infty$, an expression for the final beam emittance—that is, once full decoherence is reached—can be derived,

$$\epsilon_n^2 = \frac{\left(\overline{\gamma_0}\overline{k_\beta}\right)^2}{4} \left\langle x_0^2 \right\rangle^2 + \frac{\left\langle u_{x,0}^2 \right\rangle^2}{4\left(\overline{\gamma_0}\overline{k_\beta}\right)^2} + \frac{1}{2} \left\langle x_0^2 \right\rangle \left\langle u_{x,0}^2 \right\rangle. \tag{6.9}$$

It is relevant to note that the energy spread of the beam slice does not play a role in this expression (reproducing previous results, see [T. Mehrling, J. Grebenyuk, et al., 2012]). While it is the driving factor behind the betatron decoherence and determines the time-scale of its progression, the final emittance is dictated by the initial beam parameters. This means that a beam not properly matched to the intrinsic betatron motion in the plasma will exhibit emittance growth [T. Mehrling, J. Grebenyuk, et al., 2012]. This behavior can be avoided if matching conditions are met. These conditions can be translated into quantities relevant for this formulation as $\left\langle x u_x \right\rangle_m = 0$, $\overline{k_\beta} \left\langle x^2 \right\rangle_m = \epsilon_0/\overline{\gamma_0}$,

$\langle u_x^2 \rangle_m / \overline{k_\beta} = \epsilon_0 \overline{\gamma_0}$. Together with these expressions for matched beam moments and equation (6.8), the emittance growth factor is found as

$$\begin{aligned}\left(\frac{\epsilon_n(t)}{\epsilon_0}\right)^2 =& \frac{1}{4}\left(\left(\frac{\langle x_0^2\rangle}{\langle x^2\rangle_m}\right)^2 + \left(\frac{\langle u_{x,0}^2\rangle}{\langle u_x^2\rangle_m}\right)^2\right) \\ & \times \left(1 - e^{-bt^2}\right) \\ & + \frac{1}{2}\frac{\langle x_0^2\rangle}{\langle x^2\rangle_m}\frac{\langle u_{x,0}^2\rangle}{\langle u_x^2\rangle_m}\left(1 + e^{-bt^2}\right) \\ & - \frac{\langle x_0 u_{x,0}\rangle^2}{\epsilon_0^2} e^{-bt^2}.\end{aligned} \tag{6.10}$$

Following the matching requirements in the above equation results in a growth factor of one for sufficiently long time scales $t \gg b^{-1/2} = 1/\left(\Delta\gamma\overline{\omega_\beta}\right)$, equivalent to a preservation of the initial transverse phase-space emittance.

### 6.2.2 *Physical Studies*

The analytic description presented above is benchmarked using a Particle-in-Cell (PIC) simulation provided by the 3D quasi-static code HiPACE [T. Mehrling, C. Benedetti, et al., 2014]. The blowout regime, which allows an assumption of no radial dependence of the longitudinal wakefield and thus decouples the radial and longitudinal phase-space distributions, was established using a Gaussian drive beam with a peak current $I_b = 3\,\text{kA}$, total charge $Q_b = 240\,\text{pC}$, mean energy $\overline{\gamma_0} = 2000$, energy spread $\sigma_\gamma/\overline{\gamma_0} = 0.1\,\%$ and a transverse phase-space emittance $\epsilon_n = 2.0\,\mu\text{m}$, moving through a homogeneous plasma of constant density (i.e. without a tapered vacuum-to-plasma transition) of $n_p = 1 \times 10^{23}\,\text{m}^{-3}$ (with the local peak density of the beam $n_b/n_p = 28.5 \gg 1.0$). The witness beam was modeled as a slice of macroparticles with a mean energy $\overline{\gamma_0} = 2000$, an energy spread of $\sigma_\gamma/\overline{\gamma_0} = 10\,\%$, a transverse phase-space emittance of $\epsilon_0 = 2.0\,\mu\text{m}$ and initial root-mean-square (rms) beam moments $\sigma_{x,0} = \sqrt{\langle x_0^2\rangle} = 5\,\mu\text{m}$, $\langle x_0 u_{x,0}\rangle = 0$, and the momentum spread thus given by

$$\sigma_{p_x,0} = \sqrt{\left\langle u_{x,0}^2 \right\rangle} = \epsilon_0 / \sqrt{\langle x_0^2\rangle}\,. \tag{6.11}$$

Apart from the energy spread, which was chosen to be relatively high in order to observe the effects leading to beam-quality loss more easily, the particular values reflect a commonly encountered parameter range (e.g. at the FLASHForward experiment [Aschikhin et al., 2016], where $\sigma_\gamma/\overline{\gamma_0} \simeq 0.1\,\%$, see also chapter 7).

Following the requirements of the analytic model, the witness slice was placed behind the driver at the zero-crossing of the electric field, avoiding changes in its energy as much as possible. An additional benchmark was provided by an implementation of the semi-analytic numerical approach (SANA) (cf. section 5.5), using a calculation based on the parameters provided for the PIC simulation.

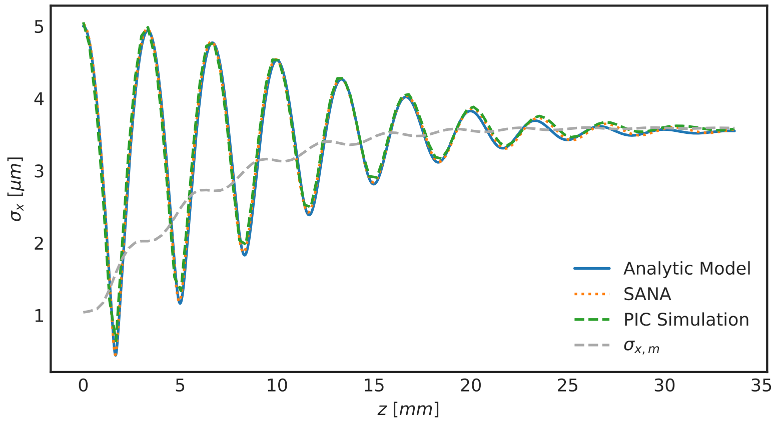


Figure 6.1: Evolution of the beam size $\sigma_x$ and the instantaneously matched parameter $\sigma_{x,m}$.

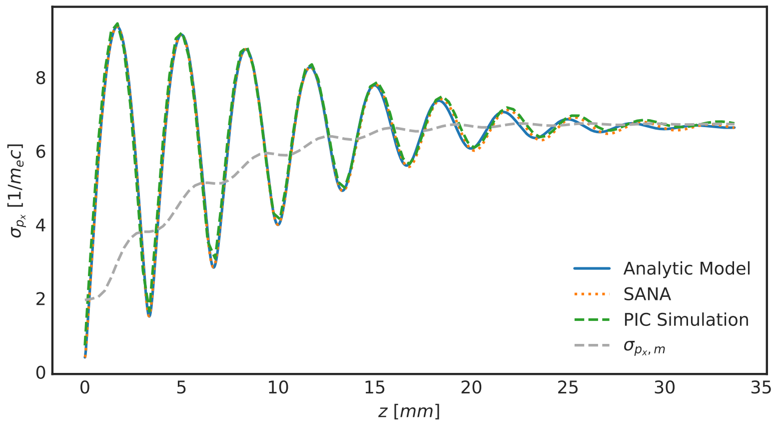


Figure 6.2: Evolution of the rms beam moment $\sigma_{p_x}$ and the instantaneously matched parameter $\sigma_{p_x,m}$.

The results are provided in figures 6.1 to 6.4 depicted in SI units using a notation for the rms beam moments where $\sigma_x = \sqrt{\langle x^2 \rangle}$, $\sigma_{p_x} = \sqrt{\langle p_x^2 \rangle}$. Additionally, the provided beam parameters are dynamically matched to the current emittance and energy, given as $\sigma_{x,m} = \sqrt{\epsilon / k_p \sqrt{2/\overline{\gamma}}}$ and $\sigma_{p_x,m} = \sqrt{\epsilon k_p \sqrt{\overline{\gamma}/2}}$. This definition is also reused for the physical studies of the next section, when both the emittance and the energy vary over the simulation length. Because of the mismatched initial beam parameters, the emittance of the slice grows significantly during the propagation. As mentioned above, this is due to the energy dependence of the betatron frequency, causing its decoherence and thus an increase in the emittance of the slice. The decoherence can be observed as a damping effect on the beam moment

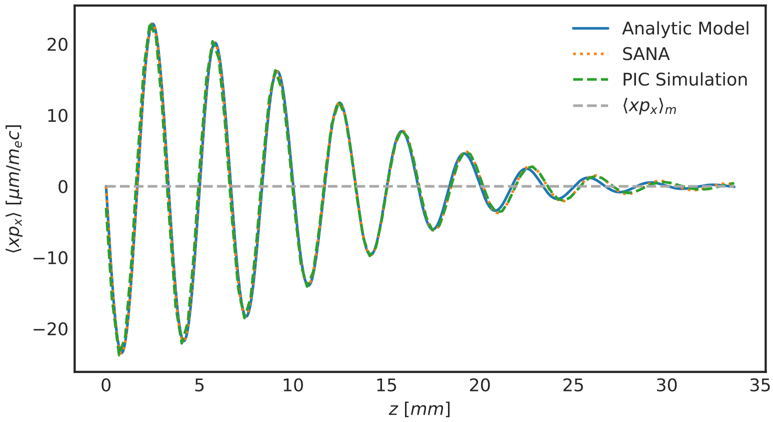


Figure 6.3: Evolution of the correlation beam moment $\langle x \cdot p_x \rangle$ and the matched parameter $\langle x \cdot p_x \rangle_m$.

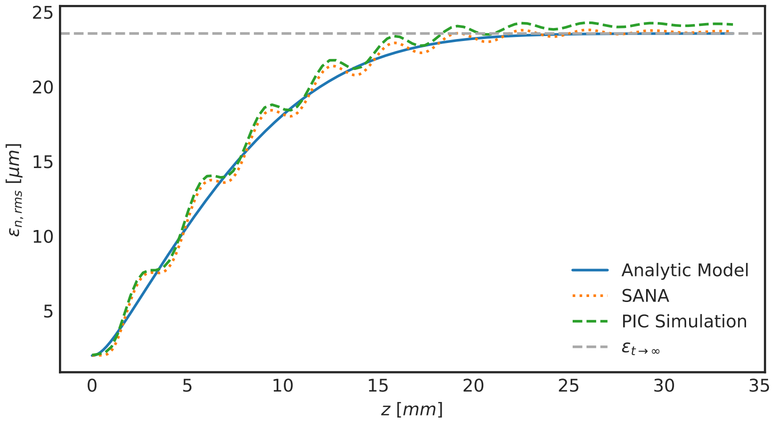


Figure 6.4: Evolution of the transverse phase-space emittance $\epsilon_n$ together with the value for the final emittance obtained from the analytic model according to equation (6.9), and plotted as an upper boundary.

oscillations, which ultimately approach their matched values once complete decoherence is reached. Using the growth factor derived above allows a time scale for full decoherence for the given parameters to be provided as $t_d \gg b^{-1/2} = 1/\left(\Delta\gamma\overline{\omega_\beta}\right)$, or $z_d \gg c/\left(\Delta\gamma\overline{\omega_\beta}\right) \approx 10.6\,\mathrm{mm}$) in units of distance used in the plots. Over these lengths, no significant drive-beam head erosion can be observed in the simulations, resulting in a constant $E_z$ for the simulation time and distance. Since the description considers a single slice of electrons without acceleration, the correlated emittance growth due to an energy chirp for a witness beam of finite length (see [T. J. Mehrling et al., 2016; T. Mehrling, J. Grebenyuk, et al., 2012]) can be ignored, keeping the focus on the uncorrelated emittance growth. However, while the macroparticle slice in the PIC simulations was chosen to be as thin as possible in the longitudinal direction ($\sigma_\zeta \ll k_{p,0}^{-1}$), it nevertheless samples the electric field variation over its length, thus deviating from the assumption of no energy variation for the witness beam, potentially contributing to a slightly higher emittance value than the one calculated using the analytic model. Otherwise, an excellent agreement between the analytic model and the numerical results is found.

## 6.3 SCENARIO II – BEAM SLICE WITH ENERGY GAIN

### 6.3.1 *Mathematical Model*

The second scenario exhibits an increase in complexity, by allowing energy to vary, while keeping the single-slice picture, again allowing to ignore the correlated emittance growth to be ignored. In more physical terms, translated into a PIC simulation setup, it can be thought of as a thin layer of macroparticles with a transverse distribution following a driver in the blowout regime at an offset where a non-negligible longitudinal electric field is providing an accelerating gradient.

The change in energy is reflected in an updated differential equation for the transverse position of a single particle [T. Mehrling, R. A. Fonseca, et al., 2017],

$$\frac{d^2x}{dt^2} + \frac{\dot{\gamma}}{\gamma}\frac{dx}{dt} + \omega_\beta^2(t)x = 0, \tag{6.12}$$

with $\dot{\gamma} = d\gamma/dt$ and where the acceleration of the electron leads to a damping of the particle oscillation through the term $\dot{\gamma}/\gamma$ (conversely, a loss in energy would result in an amplification of the oscillation amplitude). Equation (6.12) has the solution (cf. [T. Mehrling, R. A. Fonseca, et al., 2017] for derivation)

$$x(t) \simeq x_0 A(t)\cos[\varphi(t)] + \frac{p_{x,0}}{m_e\gamma_0\omega_{\beta,0}} A(t)\sin[\varphi(t)], \tag{6.13}$$

with the amplitude term $A(t) = [\gamma_0/\gamma(t)]^{1/4}$. The energy of a single electron is again expressed through the Lorentz factor, given as $\gamma(t) = \overline{\gamma_0} + \mathcal{E}t + \delta\gamma$, again with the initial mean energy $\overline{\gamma_0}$, the uncorrelated energy spread $\delta\gamma$ and a linear term incorporating a change in energy, where $\mathcal{E} = -eE_z/m_ec$ and $E_z = E_z(\zeta)$ is the longitudinal electric field. The variation in energy also means a time-dependent electron betatron oscillation term $\omega_\beta(t)$ and the resulting phase advance

$$\varphi(t) = \int \omega_\beta \mathrm{d}t = \overline{\varphi}\left(1 - \frac{\delta\gamma}{2\overline{\gamma_0}}\frac{\overline{\omega_\beta}}{\overline{\omega_{\beta,0}}}\right), \tag{6.14}$$

with the mean phase advance $\overline{\varphi} = 2\left(\overline{\omega_{\beta,0}}/\overline{\omega_\beta} - 1\right)/\epsilon$, mean betatron frequency $\overline{\omega_\beta}(t) = \overline{\omega_{\beta,0}}/\sqrt{\epsilon\overline{\omega_{\beta,0}}t + 1}$ and the finite relative energy change per betatron cycle $\epsilon = -\sqrt{2/\overline{\gamma_0}}E_z/E_0$, with the cold nonrelativistic wavebreaking field $E_0 = \omega_p mc/e$ [J. M Dawson, 1959]. Using the phase-advance description together with the term for energy development allows the beam moment equations and the emittance to be calculated. The resulting formulas are given in appendix A, while the results from their application are presented in the following section.

### 6.3.2 *Physical Studies*

The setup chosen for bench-marking the model developed following the restrictions imposed by the second scenario is similar to the one used for the first — a beam slice with an uncorrelated energy spread following a driver at an offset, this time with a non-zero longitudinal electric field resulting in an energy gain. With the other values such as the transverse beam moments kept the same, the slice placement was chosen so that the longitudinal field is $E_z(\zeta) \approx 0.3 \cdot E_0$.

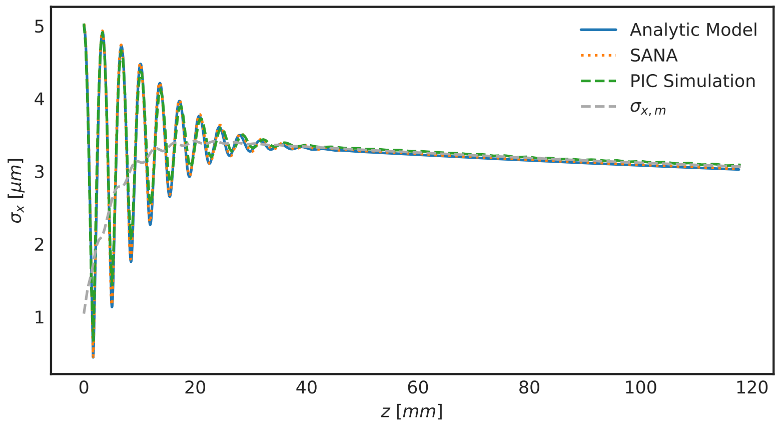


Figure 6.5: Evolution of the beam size $\sigma_x$ and the instantaneously matched parameter $\sigma_{x,m}$.

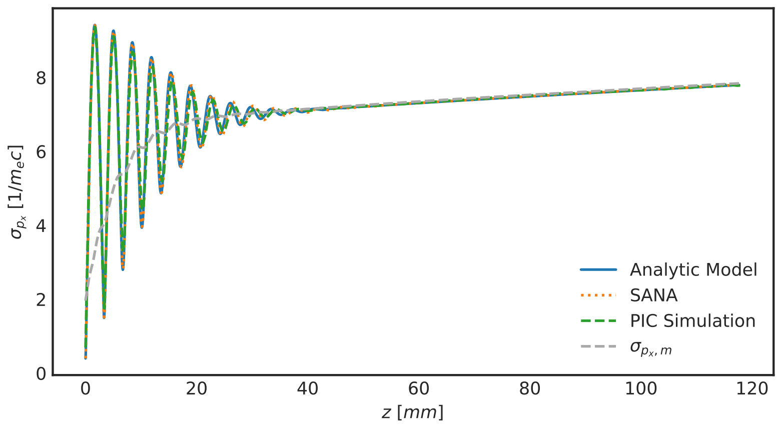


Figure 6.6: Evolution the rms beam moment $\sigma_{p_x}$ and the instantaneously matched parameter $\sigma_{p_x,m}$.

Figures 6.5 to 6.8 show the evolution of the respective beam parameters with energy gain, provided with the respective matched

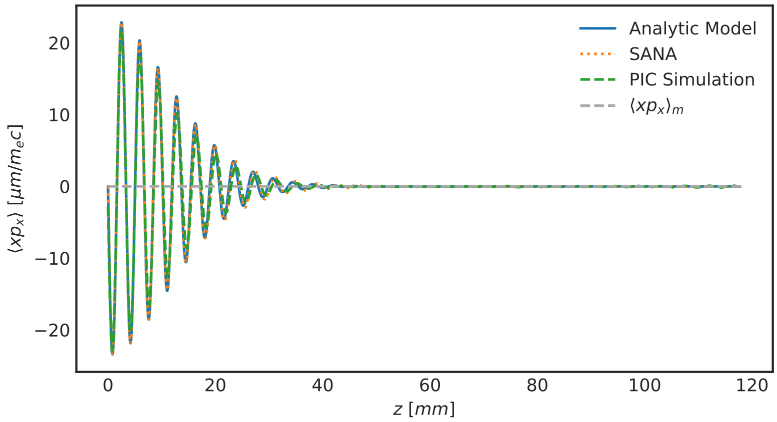


Figure 6.7: Evolution of the correlation beam moment $\langle x \cdot p_x \rangle$ and the matched parameter $\langle x \cdot p_x \rangle_m$.

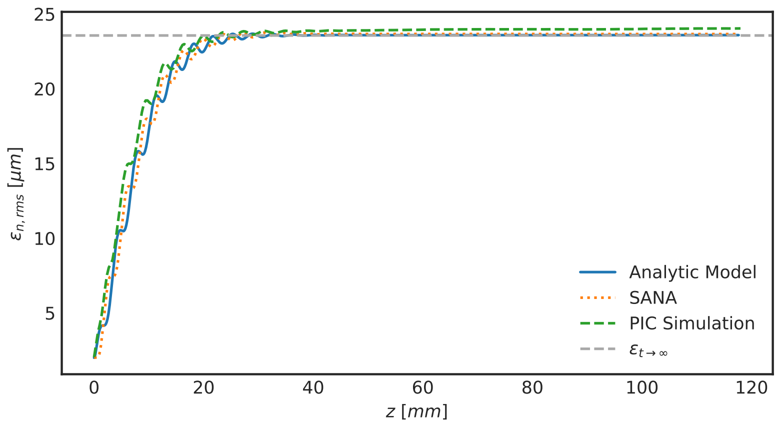


Figure 6.8: Evolution of the transverse phase-space emittance $\epsilon_n$, together with a final emittance value obtained from the analytic model according to equation (6.9).

parameters for the varying emittance and energy. Again, oscillations of the beam moments are observed for the chosen, mismatched initial transverse beam parameters, eventually approaching the matched parameters after full decoherence. The subsequent propagation within the plasma shows a variation in the rms beam moments $\sigma_x$ and $\sigma_{p_x}$ resulting from the energy dependence of the matched parameters $\sigma_{x,m}$ and $\sigma_{p_x,m}$ (or equivalently $\langle x^2 \rangle_m$ and $\langle p_x^2 \rangle_m$) that originates from the amplitude term in equation (6.13).

In addition, the energy spread drives a significant increase in emittance until the matched values are reached. Since the mechanism for the emittance growth is the decoherence effect caused by the energy-dependent oscillations of particles, the subsequent acceleration within the plasma is expected to have no effect on the development of the normalized emittance once the matched parameters are reached (see [T. Mehrling, J. Grebenyuk, et al., 2012; Michel et al., 2006]). Thus, the final value of the emittance obtained from equation (6.9) is plotted, showing that it can indeed be seen as a target value for the evolution of the emittance over the propagation length. All three models follow each other closely in their description of the overall emittance evolution, while the specific deviations observable during its initial degradation can be attributed to the particular properties of the numerical methods (such as the approximations for the longitudinal beam-slice position in the PIC simulation and the blowout-regime model used in SANA). Additionally, it should be noted that the energy spread used for benchmarking the presented results is assumed to be much higher than expected for externally injected witness beams in proposed PWFA experiments [Aschikhin et al., 2016], with typical values of $\Delta\overline{\gamma_0} = 0.1\,\%$. Using such an energy spread while keeping all the other parameters fixed and recalculating the decoherence time scale using the growth-factor $b$ results in a distance on the order of $z_d \gg c/\left(\Delta\gamma\overline{\omega_\beta}\right) \approx 1.06\,\mathrm{m}$. While beyond the plasma-target dimensions proposed, it is nevertheless of the order of the plasma-cell length and can thus play a role during the internal acceleration process.

The emittance plots again show a slightly higher value for the PIC simulation, due to the finite beam length and the resulting contribution from correlated emittance growth, mirroring the observation from the first scenario. Apart from these minor deviations, the analytic model shows a very high accuracy when describing the beam moment and the emittance developments.

## 6.4 SUMMARY AND CONCLUSION

In this chapter, the development of an analytical model for the calculation of the evolution of transverse beam moments and the normalized phase-space emittance has been presented, together with an investigation of the uncorrelated emittance growth of externally injected beams in plasma wakefield accelerators. The models allow for a quick evaluation not only of initial beam parameters with respect to their matching conditions, but also of their development over an acceleration length within a section of homogeneous plasma, providing important information such as typical length scales for emittance growth and final emittance values. The validity of both models is presented by benchmarking it against results obtained from two different approaches — a standard Particle-in-Cell simulation following the scenario restrictions as closely as possible, together with the semi-analytic numerical approach (SANA). The model's limitations are given by the assumption of a constant longitudinal field and a constant focusing environment. As such, the study of a more complex acceleration process for a whole beam — possibly involving plasma-vacuum transition regions or variations of intra-bunch longitudinal fields — is not possible within this model at the moment. Nevertheless, it provides valuable insights into the decoherence process and its drivers, together with potential estimates as to the time and length scales involved. The model can also form the basis of a semi-analytic numerical calculation, using beam slices with varying parameters to approximate a beam within a varying longitudinal field.

# 7 EXTERNAL INJECTION IN THE PWFA BLOWOUT REGIME

## 7.1 INTRODUCTION

Accelerator designs aiming to make use of the promising features of plasma-based acceleration are generally classified based on the driver used for wakefield generation and the origin of the witness. For a project such as FLASHForward [Aschikhin et al., 2016], which aims to use a pregenerated beam of electrons for a driver in a scheme known as beam-driven plasma-wakefield acceleration (PWFA) [Seryi et al., 2009], external injection offers a versatile and valuable option for the demonstration of plasma-based acceleration. In this approach, the driver generating the wakefield is followed by a second beam with a specific temporal and spatial offset. The aim of the project is to use a driver strong enough to cause the establishment of a so-called blowout regime [Lotov, 2004], which not only supports high-gradient acceleration fields, but also a linearly focusing transverse environment offering the potential for the preservation of witness-beam phase-space. However, it is also this environment which poses a challenge to driver and witness design. The accelerating fields can cause the formation of an energy chirp along the length of the witness beam, while the focusing fields will lead to energy-dependent oscillations of the constituent particles inside witness beams with non-negligible energy spread. Both of these effects can contribute to the so-called betatron decoherence, a phase-space rotation driven by the energy spread in the case of a blowout regime, and originating from energy-dependent betatron oscillations [K. A. Marsh et al., 2005]. The decoherence can affect the shape and size of the phase-space area occupied by the beam and thus its emittance [Floettmann, 2003]

In order to facilitate successful acceleration in the external injection regime and demonstrate its usefulness, the effects driving betatron decoherence need to be understood and mitigated. This chapter focuses on the properties of external injection in the blowout regime and the implications for the parameter space of experiments at facilities such as FLASHForward. An initial introduction to the theory and phenomenology is followed by the depiction of limitations and problems that need to be addressed to facilitate an acceleration process that conserves the advantageous beam properties that FLASH accelerator offers. Potential mitigation strategies for beam quality loss such as parameter matching, tailored transition sections from vacuum to plasma as well as beam loading, are introduced successively and discussed, including supporting Particle-in-Cell simulations and numeric studies.

## 7.2 THEORETICAL CONSIDERATIONS

One of the defining characteristics of the blowout regime (see section 2.5) is a wakefield distribution that can be factorized into transverse and longitudinal dimensions. The high-current driver expels all plasma electrons in its wake, thus creating a region of charge depletion behind it. This bubble or blowout exhibits a transversely focusing field without a longitudinal dependence and a longitudinal wakefield without a radial dependence. It is this property that allows the phase-space development of a potential witness beam to be separated into transverse and longitudinal components. However, its highly nonlinear nature limits theoretical descriptions of the blowout mostly to its phenomenology [Lotov, 2003] or special scenarios limited by certain assumptions concerning the acceleration process (see chapter 6). A valid description of acceleration in the blowout regime is possible, however, using PIC codes described earlier and applied here within HiPACE. Where appropriate, this description will be accompanied by an implementation of the SANA [T. J. Mehrling et al., 2016] approach, allowing the results to be more clearly interpreted.

The starting point is the transverse motion of an individual particle in a transversely focusing field, defined by the focusing parameter $K$,

$$x'' + Kx = 0, \tag{7.1}$$

where $K$ for the blowout regime is given as

$$K = \frac{k_p^2}{2\gamma}, \tag{7.2}$$

with the plasma wave number $k_p$ and the individual particle energy proportional to the Lorentz factor $\gamma$. Two characteristics define this depiction. First, since the wave number $k_p$ depends on the surrounding plasma density, so does the focusing force acting on each particle. Additionally, the energy dependence means that a beam with non-negligible energy spread will be subjected to a differential phase-space rotation. Both the focusing environment and the energy dependence lead to a differential rotation of the witness phase-space until saturation is reached. This effect, known as betatron decoherence, can cause severe emittance growth and thus beam-quality degradation.

Figure 7.1 depicts the transverse phase-space of a witness beam with typical parameters (provided in the appendix) before and after propagation through the plasma blowout. The area occupied by the individual beam slices grows, reflected in the corresponding increase of the beam emittance. Additionally, there is a strong longitudinal

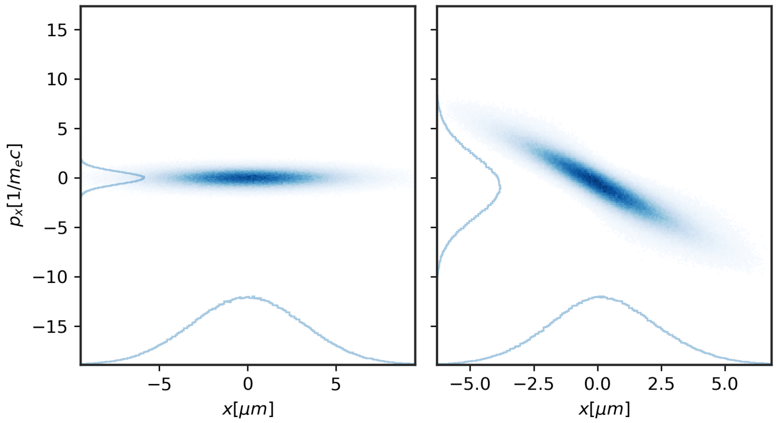


Figure 7.1: Transverse phase-space of a witness beam before (left) and after (right) propagating through about 42 mm of plasma with density $n_p = 1 \times 10^{23}\,\mathrm{m}^{-3}$ (right), undergoing differential phase-space rotation and showing significant changes in the projected phase-space distributions.

dependence of the accelerating field, which would imprint an externally injected bunch with a chirped energy profile, thus increasing the correlated energy spread over the acceleration length.

Mitigation strategies aiming to avoid severe beam-quality degradation for an externally injected beam in the blowout regime can be divided into two main subsets. One focuses on emittance growth induced by the transverse properties of the beam and dealing with mismatching and tailored transition regions. The other is related to quality degradation stemming from the longitudinal field distribution. Both of these areas will be addressed in the following two sections.

## 7.3 UNCORRELATED EMITTANCE GROWTH AND MATCHING CONDITIONS

As outlined in the previous section, the blowout regime of charge depletion after the driver produces a focusing environment for particles placed behind it. Their behavior can be compared to a harmonic oscillator with an energy-dependent frequency dictated by the plasma density. A beam with a non-negligible energy spread will thus experience a differential phase-space rotation until saturation, increasing the projected phase-space area it occupies and thus the corresponding emittance – an effect already introduced as betatron decoherence. A possible approach to mitigate this effect stemming from the specifics of the plasma environment is to match the beam parameters to that allowed by current regulations. The so-called matched parameters can be provided using the corresponding phase-space parameters as (see also chapter 6)

$$\langle x u_x \rangle_m = 0 \tag{7.3a}$$

$$\overline{k_\beta} \left\langle x^2 \right\rangle_m = \epsilon_0 / \overline{\gamma} \tag{7.3b}$$

$$\left\langle u_x^2 \right\rangle_m / \overline{k_\beta} = \epsilon_0 \overline{\gamma}, \tag{7.3c}$$

provided here using a plasma-based normalization of the particle position in units of the plasma wave number $k_p^{-1}$ (also known as the plasma skin depth $c/\omega_p$), the normalized momentum given in $u_x = p_x/m_e c$), the mean betatron-oscillation wave number $\overline{k_\beta} = \overline{\omega_\beta}/c$, and the mean particle energy, $\overline{\gamma}$. Matching the beam to these parameters will avoid a betatron decoherence and will guarantee preservation of the beam emittance. However, the idea of external injection is to use a preaccelerated beam to follow the driver at a predefined offset. Because of its nature, this process is limited by the beam parameters that the accelerator can provide before the plasma stage.

The parameter space of the following study is based on the values encountered in the FLASH accelerator and thus proposed for the FLASHForward facility. They are represented by an electron beam with a Gaussian distribution in all directions, carrying a total charge of 1.0 nC, with a longitudinal beam size of $\sigma_\zeta \approx 40\,\mu\text{m}$ and a symmetric transverse size of $\sigma_{x,y} \approx 3.12\,\mu\text{m}$, entering the plasma with a normalized phase-space emittance of $\epsilon_n = 2.0\,\mu\text{m}$, an energy of $E = 1.0\,\text{GeV}$ and an energy spread of $\sigma_\gamma/\overline{\gamma} = 0.1\,\%$. Where appropriate, this beam is split into two smaller Gaussian beams with identical transverse properties, resulting in a driver-witness pair setup. The specifics of the splitting method are ignored for now, but will be treated subsequently . The beam properties presented above result in a beta function of $\beta \approx 10\,\text{mm}$.

Figure 7.2 shows the phase-space development of a witness beam with the energy, energy spread and transverse phase-space parameters given above propagating through a plasma with a flat-top profile and a constant plasma density of $n_p = 5.0 \times 10^{22}\,\text{m}^{-3}$. An immediate onset of oscillations in the transverse beam size can be observed, which subsequently follows and approaches the corresponding matched value, which is $\sigma_{x,m} \approx 1.23\,\mu\text{m}$ at the onset of the stage and increases due to the growing emittance according to equation (7.3c).

Since the matched parameters for the considered plasma-density range are all but impossible to obtain using classical beam-line optics (e.g. the matched beta function for $n_p = 5.0 \times 10^{22}\,\text{m}^{-3}$ is $\hat{\beta}_m \approx 1.5\,\text{mm}$), the proposed solution to the mismatch problem consists of a tailored vacuum-to-plasma transition region, allowing for an adiabatic change of beam parameters until they match the plasma environment. This transition region is commonly described by either an exponential or power-law profile, the latter introduced in [Floettmann, 2014].

In the following, the transition region is defined to be

$$n_p(z) = n_0 e^{(z-z_0)/L}, \tag{7.4}$$

with the end of the transition section located at $z_0$ and a scaling parameter $L$, which in turn defines the adiabatic nature of the region.

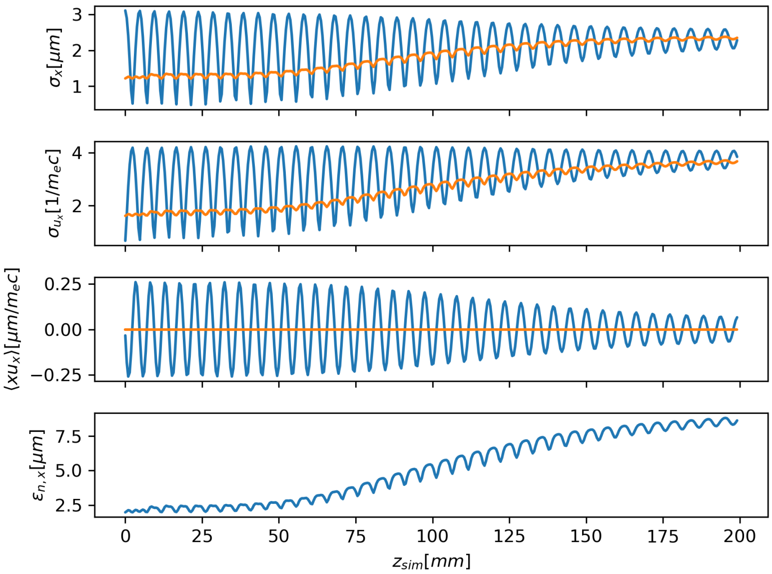


Figure 7.2: Evolution of the beam phase-space parameters and the core phase-space emittance (defined here and in the following using a cutoff function excluding values higher than $3 \cdot \sigma_{x,y,\zeta}$ to avoid errant particles ejected from the cavity from skewing the calculation) (blue line), together with the matched parameters (orange line). The beam enters the plasma through a step-wise transition at $z_{\text{sim}} = 0$.

As presented in [Timon Johannes Mehrling, 2014], the transition fulfills the matching requirement when $\hat{\beta}/L \ll 1.0$, with the total length of the section usually determined as $z_0 = 5.0 \cdot L$. Given the parameters introduced, a proper vacuum-to-plasma transition would thus need to be $z_0 \gg 5 \cdot \hat{\beta} \gg 10\,\text{cm}$, an unrealistic requirement given the total plasma cell length of $z_c \approx 25\,\text{cm}$ considered in this chapter.

However, the time scale of the emittance growth process is defined not by the parameter mismatch, but by the magnitude of the energy spread of the beam. Using the considerations presented in chapter 6 and ignoring changes in energy and energy spread, a decoherence distance scale of $z_d \gg \sqrt{2\overline{\gamma}}/\Delta\gamma \cdot k_p^{-1} \approx 1.5\,\text{m}$ can be calculated for the beam considered in this chapter — a length far beyond the considered total plasma cell length of $z_c \approx 25\,\text{cm}$. However, this value can be significantly shorter once the energy spread increases due to the aforementioned chirp of the accelerating field, an effect which can be observed in figure 7.2 after a propagation distance of about 40 mm. The resulting final emittance reached after decoherence, given a non-negligible energy spread, is the same irrespective of the particular value of the energy spread.

For the particular case of a pre-accelerated beam with a relatively low energy spread, the approach is thus to introduce a transition section to reduce the degree of parameter mismatch and thus the

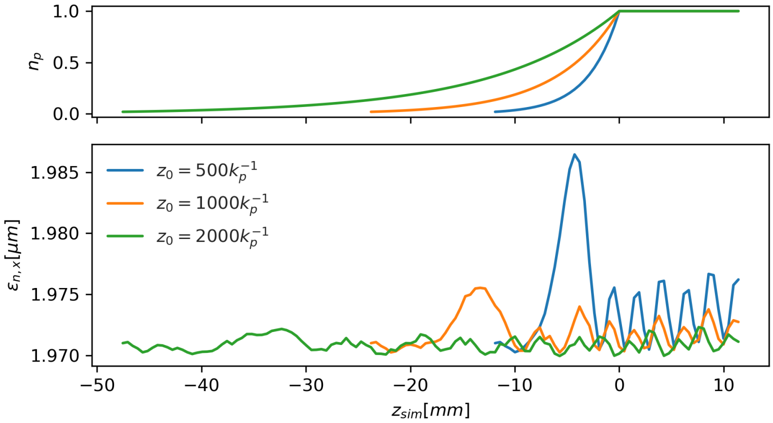


Figure 7.3: Plasma density profiles (top) and normalized phase-space emittance evolution (bottom) during and after propagation through several transition sections for three different transition-region lengths. The corresponding scaling parameter $L$ was set to $L = 1/4 \cdot z_0$.

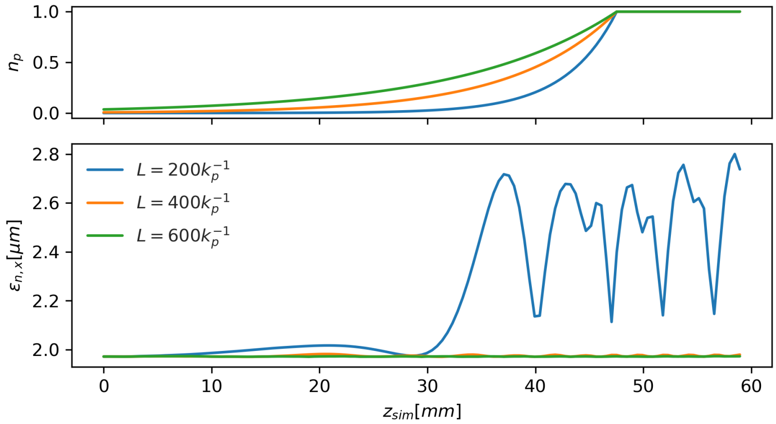


Figure 7.4: Plasma density profiles (top) and normalized phase-space emittance evolution (bottom) during and after propagation through several transition sections for three different scaling parameters $L$.

final emittance value while preserving the energy spread to avoid a decrease in the decoherence length. By fine-tuning the two parameters defining the exponential section, the beam can matched into the plasma environment without significant losses in beam quality, as shown in figure 7.3 and figure 7.4 for a beam with the same parameters as in the step-wise transition study described above. In general, every transition region helps reduce emittance growth significantly, when compared to figure 7.1. Considering the length of the transition region, figure 7.3 shows that a longer and thus more adiabatic region reduces emittance growth. Considering the scaling parameter based on figure 7.4, it is the most gradual and smooth transition which guarantees emittance preservation.

In the ideal adiabatic case, once the beam has reached the parameters corresponding to the intrinsic beam-particle motion in the plasma environment following the transition region, it can be considered matched. After that, all changes to its properties which happen on adiabatic scales — that is, in distances much larger than the betatron length — will have no negative effects on beam quality. The transition region introduced above helps to minimize emittance growth by bringing the crucial beam parameters such as beta function and beam size closer to the matched values semi-adiabatically. However, because of the low energy spread of the beam under consideration, a matched state cannot be reached within the proposed cell size. Figure 7.5 shows the principles of this argument – higher energy spreads allow the beam to decohere more quickly, reaching the final emittance values much earlier than the witness under consideration. Because of the low energy spread and the corresponding low growth rate, this has no significant degrading effect on the beam emittance within the length scales considered for the transition region. However, a growing energy spread during the main acceleration procedure could lead to a reduction of the decoherence length and thus faster emittance growth.

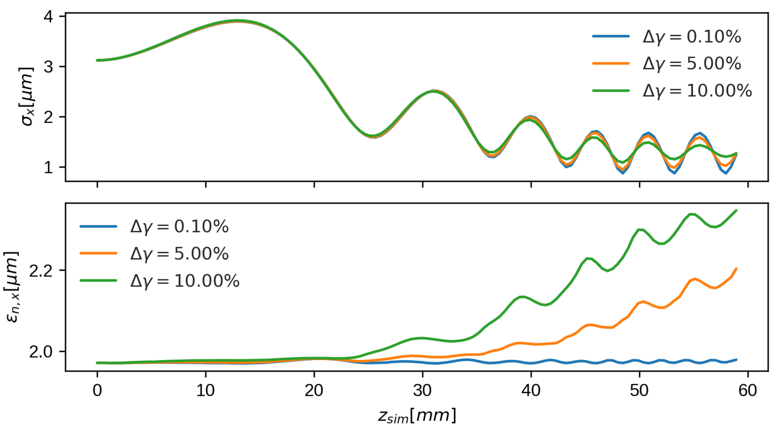


Figure 7.5: Evolution of the beam size (top) and emittance (bottom) for different initial energy spreads $\Delta\gamma$ given a transition region of $z_0 \approx 47.5\,\mathrm{mm}$ with a scaling parameter $L = 400k_p^{-1}$. A damped oscillation for higher energy spread values can be observed, showing earlier decoherence towards the final emittance value, while the beam with a low energy spread, $\Delta\gamma = 0.1\,\%$ oscillates without significant emittance growth.

Based on previous observations, a transition region can be introduced which allows a Gaussian beam with parameters which are comparable to the FLASH characteristics to remain close to its initial beam quality parameters in a plasma environment with a density of $n_p = 5.0 \times 10^{22}\,\mathrm{m}^{-3}$, as shown in figure 7.6.

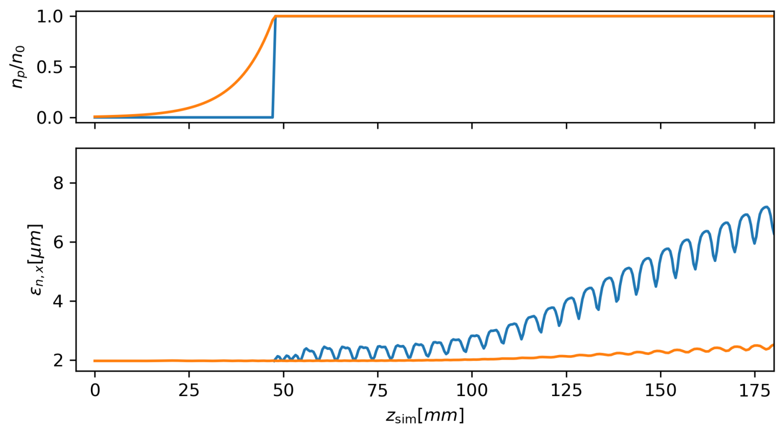


Figure 7.6: Evolution of the core phase-space emittance for two different transition regions — a step-wise (blue) and an exponential (red) (the latter defined using $L = 400k_p^{-1}$ and $z_0 = 2000k_p^{-1}$ based on equation (7.4)). The simulation employing a tailored transition shows a significantly lower emittance growth compared to the step-wise profile.

The tailored transition section is a very useful mitigation strategy helping with transitioning from the vacuum to the plasma focusing environments without significant losses in beam quality. It provides a method to transport the beam into the blowout cavity while avoiding decoherence through a gradual increase of the surrounding plasma density. Moreover, transitions with an exponential profile are closely related to profiles suggested by [Floettmann, 2014], which in turn have been demonstrated using gas capillaries [Schaper et al., 2014] and thus proven viable for an experimental setup. However, the particular problem of uncorrelated emittance growth caused by parameter mismatch is only one potential effect leading to beam quality degradation in external injection. As mentioned in the introductory section of this chapter, the beam can also be subjected to an accelerating field with a strong longitudinal dependency, causing the development of an energy chirp over its length, corresponding to an increase in correlated energy spread for both a mismatched and a matched beam. The next section will thus focus on mitigation strategies for this particular effect.

## 7.4 CORRELATED EMITTANCE GROWTH AND BEAM LOADING

Because of the energy-dependency of the focusing force acting on the witness beam, it will exhibit a differential phase-space rotation given a non-negligible energy spread. When considering a single slice of the beam, it is the energy spread within the slice which determines the length scales involved until total decoherence as well as the final emittance value, dictated by the degree of mismatch between the beam parameters and the plasma environment. However, when considering a witness beam of finite length propagating behind a driver generating an accelerating wakefield, another effect can contribute to the degradation of the beam quality. As shown before, the resulting wakefields can vary significantly in the longitudinal domain within the blowout cavity, giving the witness beam an energy chirp as it is accelerated. This process can lead to a significant increase in projected energy spread, as seen in figure 7.7, in turn a crucial parameter emittance preservation efforts, as previously discussed. Not only does this process contribute to higher correlated energy spread, but for a mismatched beam, the individual slices along the beam exhibit a differential phase-space rotation according to their longitudinal position, which in turn results in a growth of the correlated emittance.

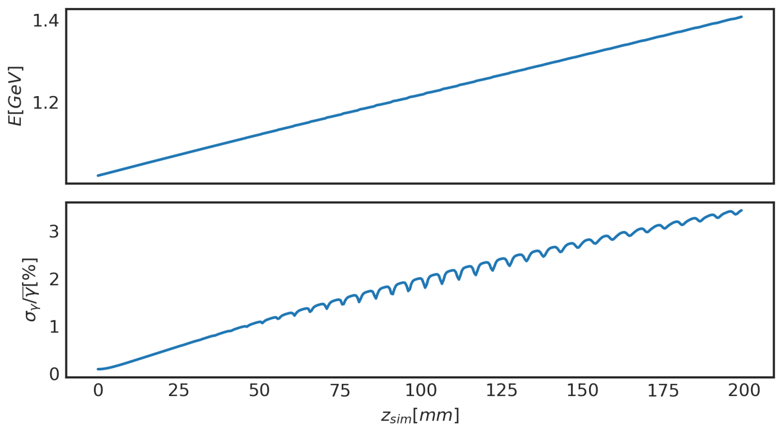


Figure 7.7: Evolution of the energy (top) as well as the projected energy spread (bottom) of a witness beam in the blowout regime subject to a gradient with strong longitudinal dependency.

A potential mitigation strategy for correlated energy-spread growth involves the use of the beam loading effect. A beam placed in the wake of a driver can influence the motion of the plasma electrons around itself, thus distorting the corresponding wakefields. This phenomenon is known as beam loading – shown for two Gaussian beams in figure 7.8 and apparent in the change of the longitudinal accelerating field when compared to a witness-free, or non-loaded wake.

The ability of the loaded beam to feed back on the wake it is subject to offers the potential to overcome the field variation along its length and thus minimize an energy chirp and an increase in projected energy spread and emittance. The core idea is to use a specially tailored longitudinal beam profile to guarantee a constant accelerating field. Taking the longitudinal profile proposed in [M. Tzoufras et al., 2009],

$$\lambda(\zeta) = \sqrt{E_t^4 + \frac{R_b^4}{2^4}} - E_t(\zeta - \zeta_t), \tag{7.5}$$

expressed here as charge per unit length, $\lambda(\zeta) = \int_0^\infty r[n_b(r)/n_p]dr$ with the wakefield at the front of the witness $E_t$, the maximum of the bubble

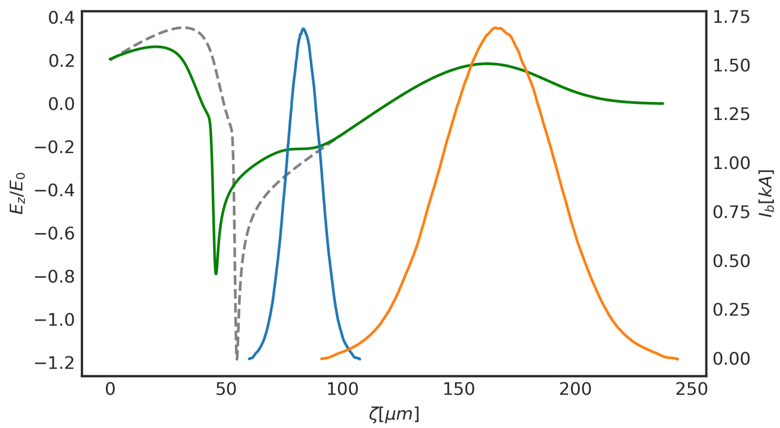


Figure 7.8: Comparison of non-loaded (dashed grey line) and loaded (green line) longitudinal fields. The former was obtained from a PIC simulation that used only a Gaussian driver (orange line), while the latter included a witness beam (blue line) as well. Both beams are shown using their current $I_b$, mapped to the right axis, while the non-loaded and loaded longitudinal fields are mapped to the left axis. A clear modification of the loaded wakefield can be observed, with implications for the energy profile of the accelerated witness.

radius $R_b$ and the rightmost coordinate of witness-beam profile $\zeta_t$, the following longitudinal witness beam density profile can be derived

$$\frac{n_b(\zeta)}{n_p} = \frac{1}{\sigma_r^2}\left(\sqrt{E_t^4 + \frac{R_b^4}{2^4}} - E_t(\zeta - \zeta_t)\right), \tag{7.6}$$

using the transverse rms beam size $\sigma_r$. This was done by assuming a Gaussian distribution in the transverse domain with a local peak beam density $n_{b,0}$,

$$n_b(r) = n_{b,0} \cdot e^{-\frac{r^2}{2\sigma_r^2}}, \tag{7.7}$$

and performing the integration in $\lambda(\zeta)$. According to the discussion presented in [M. Tzoufras et al., 2009], equation (7.6) represents a witness-beam profile that minimizes longitudinal field variation along its length.

Figure 7.9 shows various current profiles based on the beam-density profiles calculated using equation (7.6), together with the resulting longitudinal fields, which clearly deviate from an ideal case of a near-constant gradient over the beam length. This is due to the limitations of the model underlying the formula in equation (7.5), which assumes a highly nonlinear blowout regime where the cavity radius is much larger than the plasma skin depth, $R_b \gg 1.0 \cdot c/\omega_p \gg 1.0 \cdot k_p^{-1}$. The present study is limited, however, by the properties of the beam to be expected from the FLASH accelerator, which delivers a bubble with

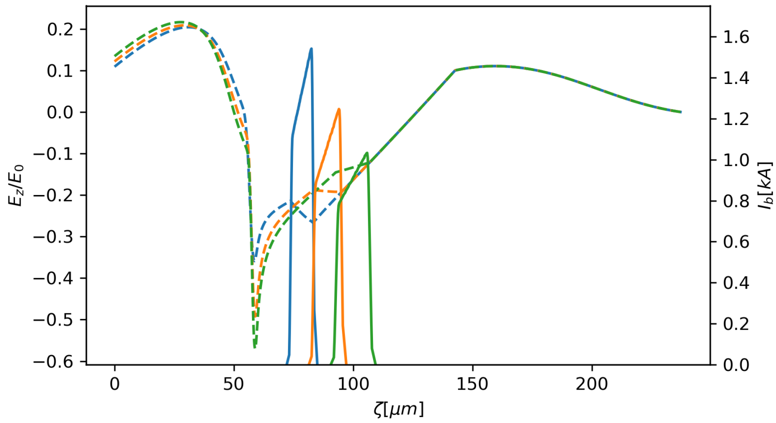


Figure 7.9: Longitudinal fields (dashed lines) with witness beam current profiles (solid lines) taken from three different PIC simulations (grouped by line color) featuring a bubble regime generated by a driver (not shown). The witness beams were placed at different longitudinal positions for each simulation. Their profiles were defined according to the formula shown in equation (7.6). The ideal case of a near-constant longitudinal field over the witness-beam length can be observed for only one position, showing the model's limitations for the considered blowout regime.

$R_b \sim 1.0 \cdot k_p^{-1}$ for a density of $n_p = 5 \times 10^{22}\,\mathrm{m}^{-3}$. Unfortunately, the beam properties expected from the preaccelerator do not allow for significantly higher bubble sizes because of the peak current available — scaling studies for PWFA blowout regimes have shown $R_b \approx 2.0 k_p^{-1}$ for driver peak currents $I_b \approx 10\,\mathrm{kA}$, while the current FLASH beam allows for peak currents $I_b \approx 2.5\,\mathrm{kA}$.

Alternatively, the witness-beam profile can be obtained based on the given wakefield environment in an iterative process. Starting with a Gaussian beam, a scraper can be used to remove a section of its charge distribution along the propagation axis to obtain a driver-witness pair. This process imitates the experimental setup currently proposed for the FLASHForward external injection experiment (cf. chapter 9). Figure 7.10 shows a possible procedure to find the cutoff points and scraper width most suitable to obtain an optimal, or near-constant, longitudinal field over the witness length. This process can be formalized further by calculating the standard deviation of the longitudinal field over the witness length, $\sigma_{E_z}$ and choosing the scraper position and width that is associated with its minimum.

Additionally, the changes to the witness phase space imprinted by the transition region introduced in the previous section need to be taken into consideration. Because of the plasma-density variation, the bubble size together with the wakefield dimensions will vary until the final density is reached, imprinting this variation on the longitudinal witness phase-space in the process, as shown in figure 7.11.

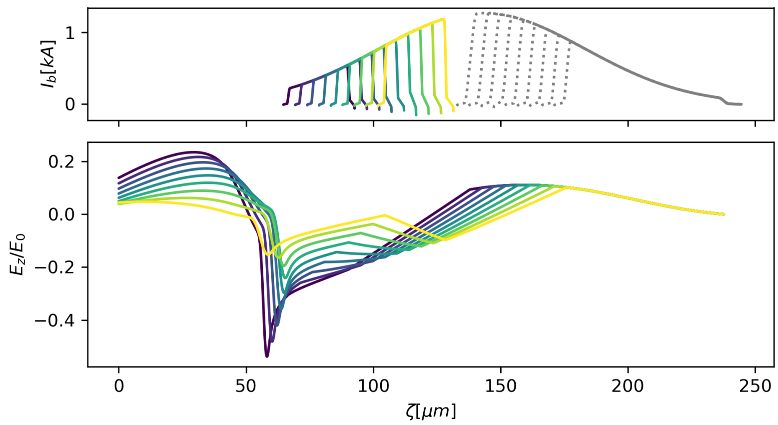


Figure 7.10: The top subplot shows the current profiles of the driver (dashed gray lines) and witness (colored solid lines). Both were obtained by removing a section of a Gaussian distribution along the longitudinal domain, imitating a scraping mechanism. Each driver-witness pair represents a single PIC simulation with a corresponding longitudinal scraper position (its length was kept constant at $\Delta_s \approx 50\,\mu\mathrm{m}$). The resulting longitudinal fields are shown in the bottom subplot (using the same colors as the witness current profiles).

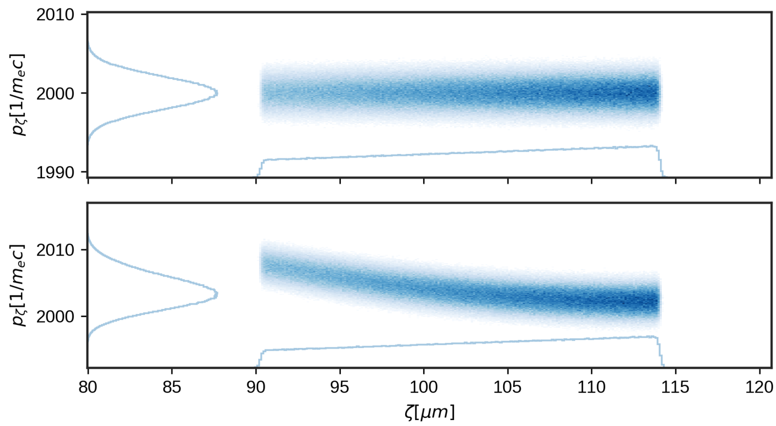


Figure 7.11: Longitudinal phase-space of the witness together with the slice energy spread, before the tapered transition region (top) and after propagation at the onset of the main accelerating region (bottom). There is a non-negligible upwards shift at the back of the beam, leading to an increase in the projected energy spread (from $\Delta\gamma = 0.1\,\%$ to $\Delta\gamma \approx 0.2\,\%$).

Fortunately, the energy increase of the beam particles is a linear process dictated by the local value of the accelerating field. Using that observation and varying the scraper position along the length of the main bunch allows two beams to be produced to facilitate a beam-loaded wakefield capable of reversing the phase-space shift induced by the transition region. The necessary longitudinal field can be defined by considering the longitudinal phase-space properties of the witness beam after the transition. Assuming a simplified model, where the increase in energy along the bunch can be described by

$$\overline{\gamma}(t,\zeta) = -E_z(\zeta) \cdot t + \overline{\gamma_0}(\zeta), \tag{7.8}$$

using the average energy $\overline{\gamma}$ of a slice at longitudinal intra-bunch position $\zeta$ together with its starting value $\overline{\gamma_0}$ as well as the accelerating field at the respective position $E_z$. Introducing a term to describe the deviation from the value of the rightmost starting energy value, $\Delta\overline{\gamma_0} = \overline{\gamma_0}(\zeta_0) - \overline{\gamma_0}(\zeta)$, the requirements concerning the accelerating field distribution over the bunch length can be formulated as

$$E_z(\zeta) = -E_z(\zeta_0) + \frac{\Delta\overline{\gamma_0}}{t_e}, \tag{7.9}$$

using the final time step for the acceleration $t_e$. Given this simple formula and the phase-space of the witness after the transition allows the wakefield required to compensate for the phase-space tilt at the beginning of the acceleration to be calculated, as seen in figure 7.12.

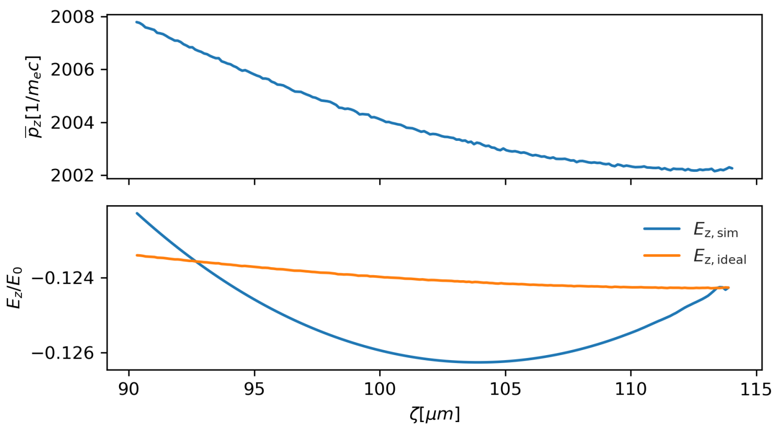


Figure 7.12: Average longitudinal momentum (closely related to the mean slice energy) for a witness beam after a propagation through the vacuum-plasma transition region with scaling parameter $L = 400k_p^{-1}$ (top). Using slice momentum data and the total acceleration length in plasma, $z_e \approx 150\,\mathrm{mm}$, in equation (7.9), the ideal longitudinal field profile can be derived (orange line in bottom plot), shown with the actual longitudinal field profile obtained from the PIC simulation (blue line in bottom plot).

The proper parameters for the scraper width and positions that minimize the deviation of the observed field from the ideal compensating wakefield can be found using an iterative approach. However, because of the non-linear nature of the beam current profile and the small bubble size, a perfect overlap of both curves is not possible, reflected in the development of the projected beam energy spread over the whole acceleration length, as shown in the next and final section.

Limiting the growth of the projected energy spread of the witness beam is a necessary requirement for emittance preservation as well, since a significant increase of the energy spread (up to $\Delta\gamma \approx 1.0\,\%$) leads to a reduction in the decoherence length and thus a quicker approach of the emittance value for full decoherence, dictated by the parameter mismatch. Observing the requirements described so far allows to set up a full simulation run which also includes the two transition sections, as discussed in the next section.

## 7.5 COMPLETE ACCELERATION PROCESS

Using a scraper of optimized width and position to produce a loaded wakefield to achieve the maximum energy gain under the requirement of reduced energy spread growth, a pre-accelerated Gaussian beam described in the previous sections can be divided into a driver and witness, the latter carrying a total charge of $Q_b \approx 60\,\mathrm{pC}$. After propagation through a transition region where it is focused into the plasma cell environment, the beam remains in a non-matched state, oscillating around the matched beta value of $\beta \approx 1.5\,\mathrm{mm}$, defined by the plasma density used ($n_p = 5.0 \times 10^{22}\,\mathrm{m}^{-3}$) and the initial bunch energy ($\overline{\gamma}_0 = 2000$). The optimized loaded wakefield structure helps to keep the energy spread low over the acceleration length ($z \approx 150\,\mathrm{mm}$), which in turn allows the emittance growth to be reduced. The resulting parameter evolution obtained from a PIC simulation is shown in figures 7.13 to 7.15.

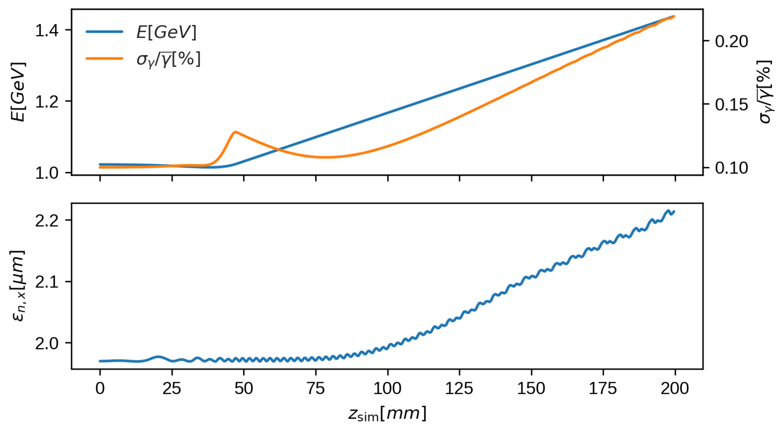


Figure 7.13: (Top plot) energy (blue line), energy spread (orange line, right-hand scale) and emittance evolution (bottom plot) for the witness beam in the acceleration region. A significant increase in energy can be observed, while the energy spread is kept relatively low compared to the non-optimized results in figure 7.7. The emittance increases by about 10 %, driven by the increase in energy spread over the acceleration length.

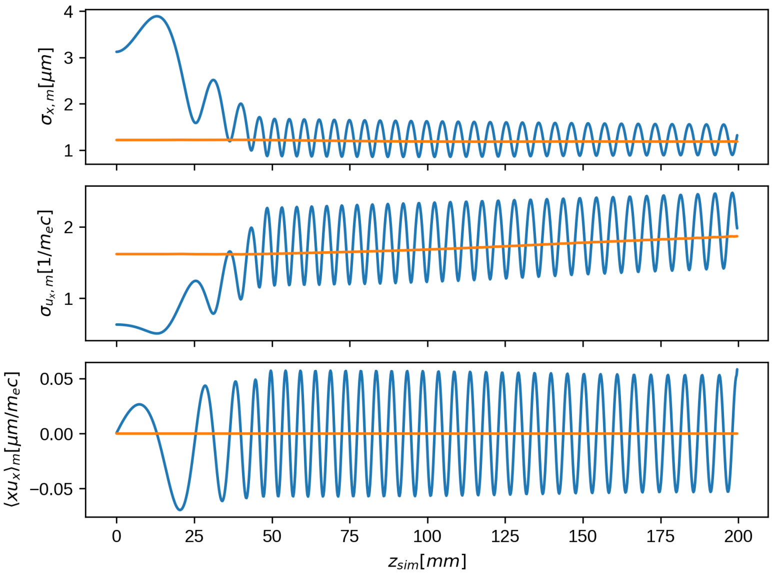


Figure 7.14: Transverse phase-space moment development of the accelerated witness beam (blue lines), together with values for the corresponding parameters (orange lines) as it propagates through the transition and acceleration regions (50 mm and 150 mm, respectively).

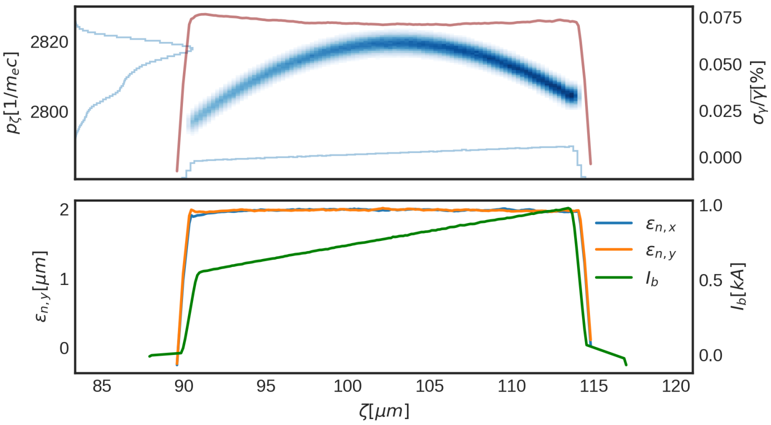


Figure 7.15: Longitudinal phase-space of the accelerated witness beam after its propagation through 150 mm of plasma. The top plot shows a density distribution of the longitudinal momentum, together with its projected histograms (light blue lines) and slice energy spread (red line, right-hand scale). The bottom plot shows slice emittance (blue and orange lines, left-hand scale) and current (green line, right-hand scale).

## 7.6 TRANSITION SECTION INTO VACUUM

After the acceleration, the bunch is extracted from the plasma region using a mirrored version of the initial transition profile (i.e. using an exponential profile defined by a scaling parameter $L$) to produce an adiabatic expansion of the beam into the downstream beamline. The smaller beam size and the corresponding beta function result in a wide range of acceptable scaling parameters $L$, provided the condition $\hat{\beta}/L \ll 1.0$ holds, as seen in figure 7.16. Under the adiabatic condition, the beam expands in the transition region defined by $z = 5 \cdot L$. The wide range of acceptable scaling parameter values and corresponding transition lengths make it possible to transport the witness beam into the post-plasma optics section with the desired beta value, all without significant losses in its quality parameters.

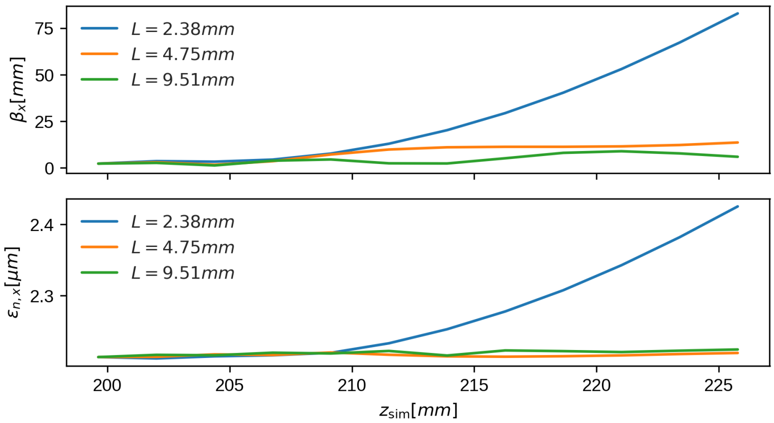


Figure 7.16: Beta function (top) and emittance (bottom) evolution of the witness beam as it propagates through a plasma-to-vacuum transition following its acceleration. A wide range of scaling parameters $L$ can be considered acceptable for emittance preservation, while a significant degradation only occurs once the value of $L$ is too close to the witness beam beta function ($\hat{\beta} \approx 2.0\,\mathrm{mm}$ in this scenario) to guarantee an adiabatic transition.

## 7.7 COMPLETE RUN AT HIGHER DENSITY

The approach presented above relied on the low energy spread and the resulting long decoherence length scale. In keeping the energy-spread low using beam loading, emittance growth can be avoided or at least kept within the percent scale over the whole acceleration distance. This also means that the matching conditions can be relaxed, with a higher possible difference in the beta values allowing for a higher plasma density and thus higher absolute accelerating gradients (the cold non-relativistic wave breaking field for $n_p = 5.0 \times 10^{22}\,\mathrm{m}^{-3}$ is $E_0 \approx 21.5\,\mathrm{GV\,m}^{-1}$ while $n_p = 1.0 \times 10^{23}\,\mathrm{m}^{-3}$ permits $E_0 \approx 30.41\,\mathrm{GV\,m}^{-1}$). Thus, the total accelerating region can be shorter while permitting the same (or potentially higher) gain in energy. Using the same iteration method as described in the last section produces an optimal combination of scraper width and position to minimize energy spread growth given the acceleration environment of the higher plasma density, as shown in figure 7.17.

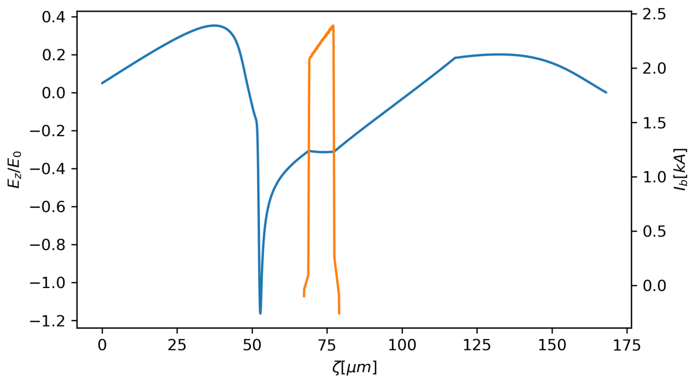


Figure 7.17: Witness-beam current (orange line, right-hand scale) and the accelerating wakefield (blue line, left-hand scale) after transition region propagation, showing an optimized scraper position for minimal longitudinal field variation over the beam length.

It should be noted, however, that the higher density and gradients pose an additional challenge in the form of driver-beam stability. From figure 7.17, a deaccelerating field over the majority of the driver-beam density on the order of $E_z \approx 2.0 \cdot E_0 \approx 6.0\,\mathrm{GV\,m^{-1}}$ can be observed, which would lead to a loss of a significant portion of its charge after the considered total plasma cell length of 250 mm. Based on the initial driver energy of $E_d = 1.0\,\mathrm{GeV}$ the resulting length scale for the energy depletion is approximately 167 mm). The charge loss in the driver has a profound influence on the surrounding wakefields and thus the witness environment, resulting in a loss of the optimized beam-loaded accelerating field and thus a degradation of beam quality. However, the higher gradients also permit a higher energy gain, reducing the acceleration length needed for a given final energy. Figures 7.18 to 7.20 show the evolution of a witness beam propagating through a vacuum-plasma-transition region of $z_t \approx 50\,\mathrm{mm}$, followed by an acceleration section of $z_a \approx 100\,\mathrm{mm}$.

## 7.8 CONCLUSION

The plasma environment offers the potential for significant energy gains, provided with a driver of sufficient current and a witness placed within a well-defined offset behind it. However, this environment, through the forces acting in the blowout regime, also strictly limits viable witness-beam parameters. The focusing force within the bubble, while being helpful in keeping the witness bunch particles confined, also requires careful matching through a tailored transition section. When a proper adiabatic matching section is not possible due to the betatron function of the incoming witness beam, an exponential

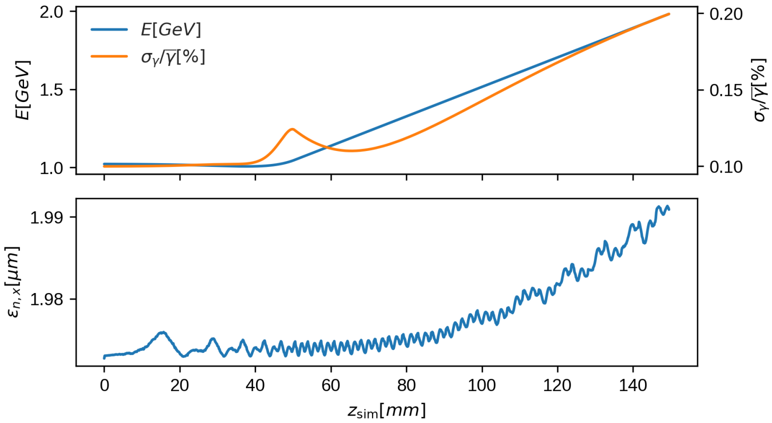


Figure 7.18: Energy (top plot, blue line, left-hand scale), energy spread (top plot, orange line, right-hand scale) and emittance evolution (bottom plot, blue line) for the witness beam in the acceleration region for $n_p = 1.0 \times 10^{23}\,\mathrm{m}^{-3}$. Similar to figure 7.13, a significant increase in energy can be observed, again while the energy spread is kept relatively low.

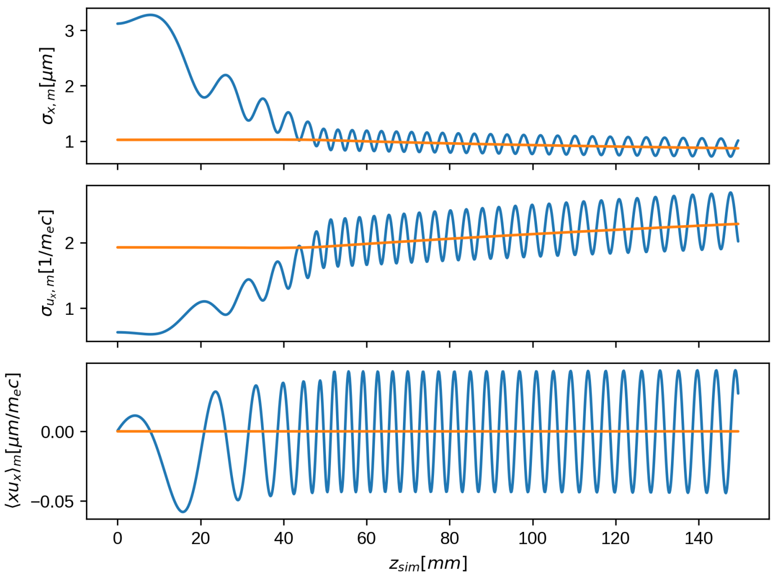


Figure 7.19: Transverse phase-space moment development of the accelerated witness beam (blue lines). The matched parameters are provided for comparison (orange lines).

transition section can nevertheless offer a solution in bringing the beam size closer to the matched value, thus lowering the final emittance value dictated by the mismatch. The emittance growth is further delayed by low energy spread, which results in a decoherence length much longer than the proposed plasma-cell length, provided the energy spread can be kept close to the relatively low initial value.

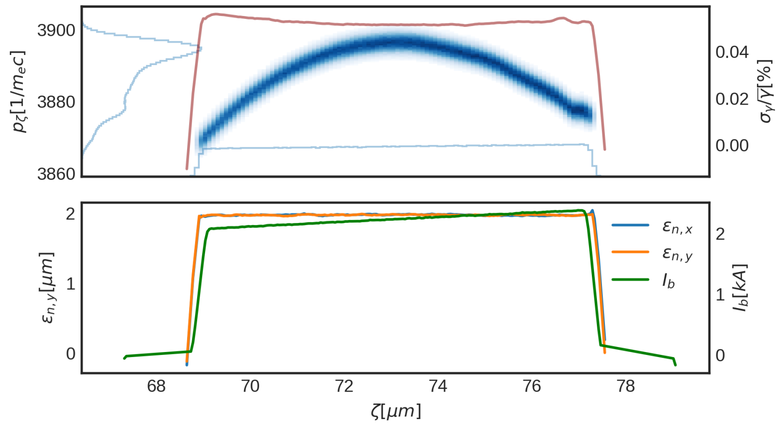


Figure 7.20: Longitudinal phase-space of the accelerated witness beam after its propagation through 150 mm of plasma. The top plot shows a density distribution of the longitudinal momentum, together with its projected histograms (light blue lines) and slice energy spread (red line, right-hand scale). The bottom plot shows slice emittance (blue and orange lines, left-hand scale) and current (green line, right-hand scale).

The accelerating gradient and its magnitude, on the other hand, is one of the advantages of plasma-wakefield acceleration compared to conventional designs – but without a specifically modeled longitudinal witness density profile, it would imprint a significant energy chirp and increase the energy spread. In short, both the transverse and the longitudinal properties need to be carefully adjusted to fit within the plasma wake and avoid severe degradation of beam properties. Working through these limitations and the associated mechanisms, a working point can be established based on realistic assumptions about beams produced by an existing accelerator. This study can form the basis of both more realistic simulations of the beam line preceding the plasma cell and the matching, focusing and diagnostic sections in the post-plasma region.

# 8 PHASE-SPACE MANIPULATION USING DECHIRPING

The wakefield environment in a plasma-based acceleration regime offers distinct advantages such as focusing and high accelerating gradients, allowing for the acceleration and propagation of an injected bunch over much shorter distances than possible in conventional accelerator designs. However, it is also this regime which poses challenges when it comes to the phase-space development of a witness beam within the plasma, greatly affecting its properties and potentially degrading its quality parameters in the process. Some of the aspects, such as emittance growth and energy spread, together with mitigation strategies, were addressed in previous sections of this work. The mitigation strategies revolved around properly designed transition sections to address the parameter mismatch problem, together with optimized wakefield structures to reduce energy spread degradation. Assuming that beam-loading is not achievable on the desired scale (or is unwanted for beams requiring hosing mitigation, see below), however, the witness is presented with a wakefield which shows a strong longitudinal dependency over its length, a situation commonly found in the plasma-acceleration regime.

Consequently, an acceleration process within such an environment will significantly impact the longitudinal phase-space of the beam, imprinting an energy chirp and thus increasing the energy spread in the process, thus degrading one of its essential quality parameters (additionally, an increase of the energy spread can severely increase emittance growth, as discussed in chapter 7). This can help reduce the hosing instability [Mehrling et al., 2017], however, and will be briefly discussed in the concluding remarks of this chapter.

A potential mitigation strategy dealing with a preaccelerated beam exhibiting a significant negative chirp in its energy is based on the observation that a beam driving a plasma wakefield will be subjected to a decelerating longitudinal field with a particular longitudinal dependency. By carefully matching the plasma density to the beam properties, it is possible to reduce and potentially remove the energy chirp of a witness-turned-driver — a process referred to as dechirping [D'Arcy, 2018].

This chapter focuses on the description of the plasma environment relevant for dechirping, the resulting beam properties as well as the dechirping process itself, followed by a presentation of simulation studies done in preparation for an experiment at the Brookhaven National Laboratory Accelerator Test Facility (ATF) [Swinson et al., 2018], exploring a promising parameter range. It then presents a successful dechirping study performed at the FLASHForward facility [D'Arcy, 2018], before discussing the dechirping potential of the accelerated FLASHForward beam produced in the previous chapter and concludes with considerations regarding emittance preservation in the given dechirping scenarios.

## 8.1 BASIC DECHIRPING CONSIDERATIONS

A witness beam within a plasma-based acceleration regime that provides non-existent or sub-optimal beam-loading conditions will undergo a significant longitudinal phase-space shift, commonly leading to an increase in the projected energy spread due to a chirp established over its length. As seen in figure 8.1, a driver propagating through a plasma environment will be followed by an accelerating field with a clear longitudinal chirp.

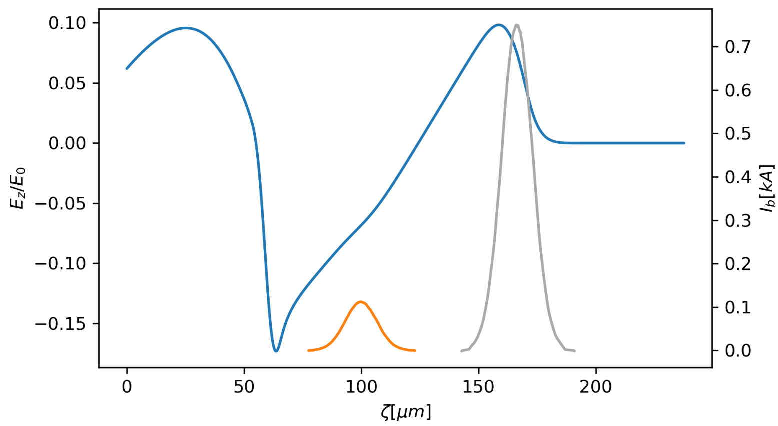


Figure 8.1: Witness current (orange line, right-hand scale), driver current (gray line, right-hand scale) and accelerating wakefield gradient (blue line, left-hand scale) for plasma density $n_p = 1.0 \times 10^{20}\,\mathrm{m}^{-3}$.

A witness beam placed with a specific offset behind the driver will thus be subjected to the accelerating properties of the wakefield, while also shifting its longitudinal momentum distribution accordingly. Figure 8.2 shows the longitudinal phase-space distribution of a possible witness beam after an acceleration process. A clear energy chirp can be observed for the presented case, leading to an increased energy spread and thus a degradation of an important beam-quality parameter.

At the same time, figure 8.2 leads to another interesting observation — the driver beam in turn is subjected to a decelerating field with almost inverse properties when compared to the witness beam. This leads to the conclusion that, given a new plasma environment where it can act as a driver, a preaccelerated witness beam will exhibit a

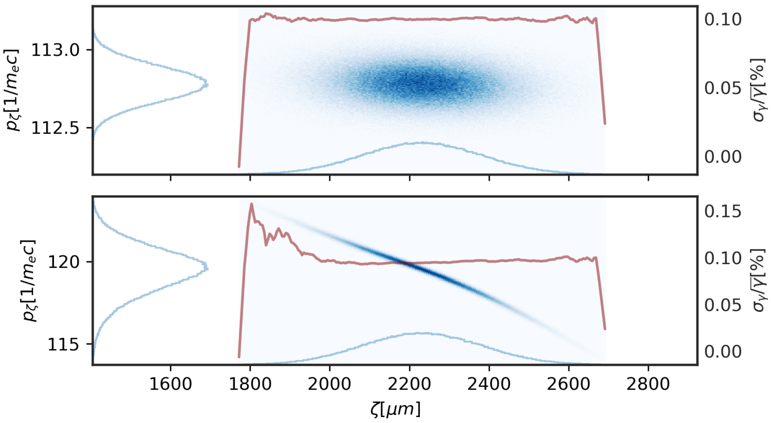


Figure 8.2: Longitudinal phase-space overview of a witness beam before (top) and after the propagation through the introduced environment (bottom), including projected histograms of the distribution (light blue lines). A clear energy chirp is present, while the slice energy spread, presented here and in all comparable plots using a red line, remains low over the main section of the beam. The initial projected energy spread of the witness beam, $\Delta\gamma_)$ = 0.1 %, was increased to $\Delta\gamma \approx 1.0\,\%$ after a propagation length of $z \approx 53\,\text{mm}$ in a plasma environment with $n_p = 1.0 \times 10^{20}\,\text{m}^{-3}$.

phase-space shift that could potentially counter the degrading effect of its chirp, reducing the projected energy spread in the process.

The properties of the plasma environment, such as the possible field strengths, will need to be carefully adjusted to fit the properties of an injected beam. An essential requirement stems from the plasma wakefield geometry itself, which will need to be able to accommodate the beam in a specific decelerating region. Taking the plasma wavelength $\lambda_p$ as a crucial characteristic allows a rough limit for the longitudinal beam size to be estimated as

$$6 \cdot \sigma_\zeta \lesssim \frac{\lambda_p}{4} \tag{8.1}$$

following the requirement that the majority of the beam needs to fit in the initial, decelerating quarter of the plasma wave to optimize chirp removal and energy spread minimization. In commonly used normalized units, this condition can be simplified to $\sigma_{\zeta,n} \lesssim 1/4$. It should be noted that, strictly speaking, it only holds for the linear case $n_b/n_0 \ll 1.0$, when the plasma-density evolution can be described as a sinusoidal perturbation with the characteristic wavelength. However, since a high-density driver in a non-linear case ($n_b/n_0 \gg 1.0$) results in a bigger perturbation length scale by creating a cavity in its wake, the condition can be seen as an upper longitudinal beam-size limit for efficient dechirping.

Apart from its geometry, it is the energy distribution of the beam which provides the main limitation on the plasma density, through

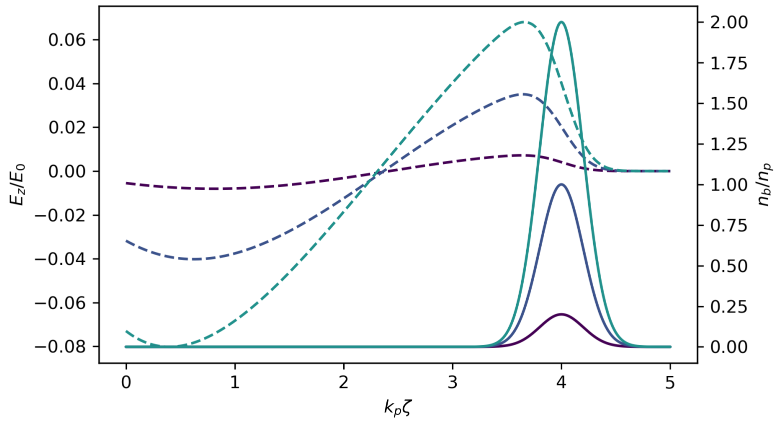


Figure 8.3: Longitudinal wakefields (dashed lines, left-hand scale) for three driver peak densities $n_b/n_0 = 0.2$, $n_b/n_0 = 1.0$ and $n_b/n_0 = 2.0$ (solid lines, right-hand scale, same colors as the resulting wakefields), all with $k_p\sigma_r = 0.25$, $k_p\sigma_\zeta = 0.2$.

the longitudinal fields required for energy chirp compensation over a given length. Figure 8.3 shows the longitudinal wakefields caused by an electron beam driver with varying peak density and constant beam size, obtained from HIPACE simulations. The magnitude of the field, together with its characteristic length scale, is influenced by the driver density, which acts as the cause for the sinusoidal perturbation behind it. Additionally, the dechirping field length scales with the longitudinal beam dimensions, commonly reaching its maximum value at the tail portion of the driver. Despite this advantageous characteristic, it should be noted that the wakefield shape over the beam length is not suitable for complete dechirping of a linear chirp, given its non-linear shape. Instead, a Gaussian beam with a negative linear energy chirp subjected to the wakefield will exhibit a lower projected energy spread after a certain propagation distance in a plasma environment, approaching its own slice energy spread in the process.

Assuming a simplified distribution of the wakefield established over the witness length used as a driver with a linear chirp in its energy, the chirp compensation requirement can be formulated in the normalized unit description as

$$6 \cdot \sigma_\gamma = E_0 \cdot t_e, \tag{8.2}$$

with the energy spread $\sigma_\gamma$ expressed in the Lorentz factor $\gamma$ the wakefield gradient value at the tail of the bunch $E_0$ and the total acceleration time $t_e$.

Apart from the non-linear nature of the wakefield on axis, another limiting characteristic needs to be pointed out. The wakefield generated by the witness beam can have a significant radial dependency, as depicted in figure 8.4. Thus, particles positioned away from the central axis will be subjected to a lower wakefield gradient, which can

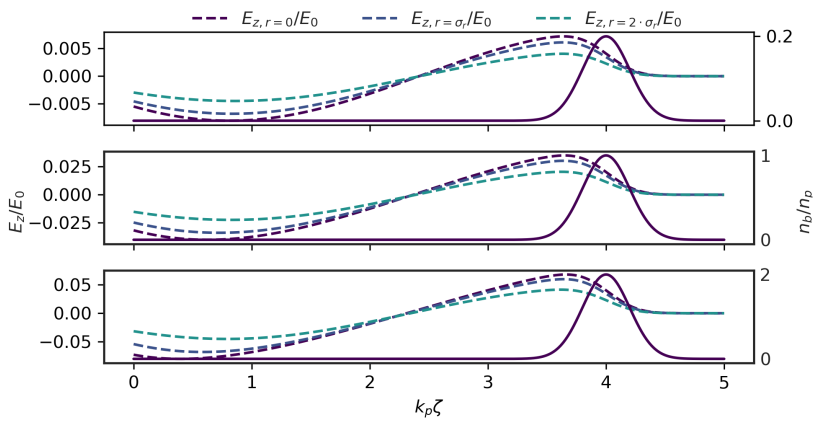


Figure 8.4: Longitudinal wakefields (dashed lines, left-hand scale) for three driver peak densities (solid lines, right-hand scale), $n_b/n_0 = 0.2$, $n_b/n_0 = 1.0$ and $n_b/n_0 = 2.0$, all with $k_p\sigma_r = 0.25$, $k_p\sigma_\zeta = 0.2$. The field values were taken from a HIPACE simulation at different radial offsets in units of the transverse beam size $\sigma_r$.

increase the energy spread in the individual slices and thus reduce the potentially lowest attainable value for dechirping. Two potential strategies can be applied to avoid a degradation in the beam slice energy spread. First, the beam can be limited to a transverse beam size $k_p\sigma_r \ll 0.25$, either by beam optics design or the choice of a specific plasma density. Second, establishing a non-linear regime through a high-current beam can widen the wakefield and thus reduce its radial dependency as well.

Figure 8.5 depicts the longitudinal phase-space of a witness beam both before (upper plot) and after (lower plot) its propagation through a plasma section of $z \approx 20$ mm. A clear energy chirp is present initially, which is rotated during the propagation, reducing the energy spread from $\Delta\gamma = 1.0\,\%$ to $\Delta\gamma \approx 0.3\,\%$. However, this happens at the cost of an increased slice energy spread specifically present in longitudinal beam portions with a significant radial wakefield dependency—mainly the tail regions of the beam.

The limitations of the dechirping approach both for the longitudinal and transverse aspects — the former affecting the projected and the latter affecting the slice-energy spreads, respectively — raises the question of an optimal dechirping regime. That is, a beam-plasma configuration where the resulting wakefield allows the driver to be rotated in phase-space such that the lowest possible value of the projected energy spread — the slice-energy spread — is achieved. Considering the longitudinal distribution, a deviation from a Gaussian profile is beneficial, to avoid sampling the wakefield over its maximum with the elongated tail section. A trapezoidal profile is well-suited, although similar shapes are also possible, as long as they do not carry any charge too far behind the main wakefield-generating front section.

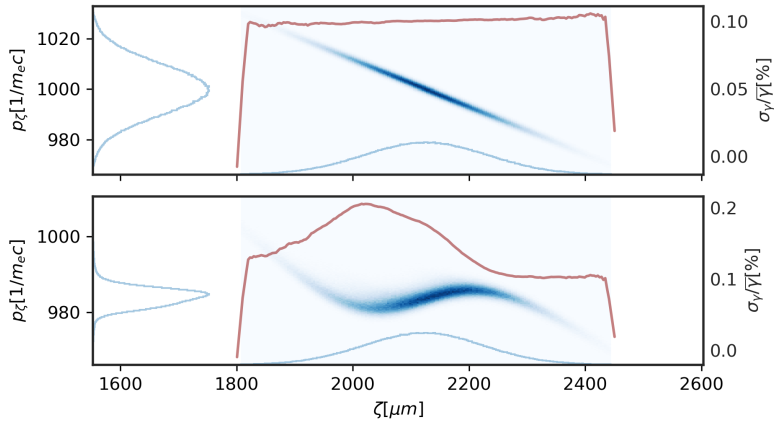


Figure 8.5: Longitudinal phase-space overview of a witness beam with a clear linear chirp with an initial projected energy spread of $\Delta\gamma = 1.0\,\%$, before (top), and after (bottom) a propagation through $z \approx 20\,\mathrm{mm}$ of plasma with density $n_p = 1.0 \times 10^{22}\,\mathrm{m}^{-3}$. Also shown are the slice energy spread (red lines, right-hand scale) and histogram axis projections of the distribution (blue lines) for both times. The beam follows size requirements proposed above — $k_p\sigma_\zeta = 0.1$, $k_p\sigma_r = 0.1$ and shows a reduced energy spread of $\Delta\gamma \approx 0.3\,\%$ after propagation.

The increase in slice-energy spread caused by the radial wakefield dependency can be reduced by using a high-current beam, which creates a bubble with little radial variation. The results of a study observing these considerations are presented in figures 8.6 to 8.7, where the front half of a high-current Gaussian beam with a negative linear chirp was used. A clear longitudinal phase-space rotation is observable for this example, which approaches the slice-energy spread, while avoiding its significant degradation. For specific realistic beam distributions, this case can be seen as an upper dechirping limit, with their longitudinal distributions and current profiles determining the degree of deviation towards a sub-optimal setup.

To facilitate optimal dechirping, certain parameter restrictions need to be observed. The plasma density needs to be adjusted to the beam length, since the corresponding plasma wavelength determines the area of the wakefield that defines the dechirping characteristics. Additionally, the gradients available for dechirping, dictated by both the plasma density and the witness current, need to be able to counter the energy chirp, placing a second restriction on the available parameter space. A beam which is too long for the plasma scale will be subjected to a wakefield with a longitudinal shape not suitable for optimal chirp reduction, potentially degrading its energy-spread profile even further. Consequently, a plasma environment with insufficient density will not be able to reduce the witness tail energy enough for a given propagation length to minimize the energy spread, while a density

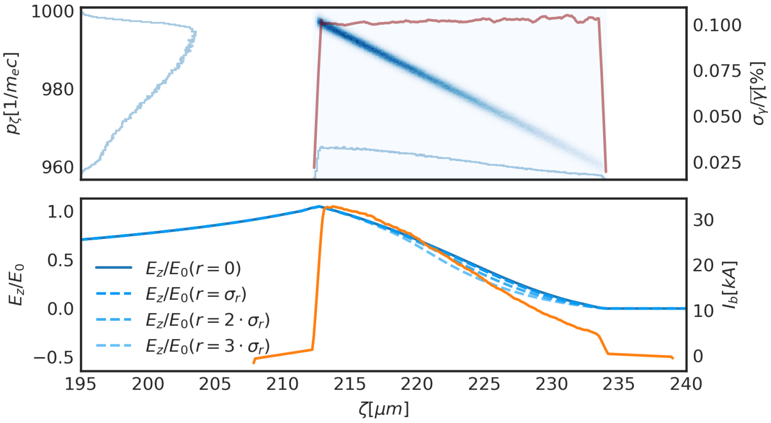


Figure 8.6: (Top plot) longitudinal phase-space distribution (blue, left-hand scale), together with axis histogram projections of the distribution (light blue lines) and slice energy spread (red line, right-hand scale) of a beam optimized for dechirping. (Bottom plot) longitudinal wakefields taken on-axis and at three different radial offsets (dashed lines, left-hand scale), together with the beam current profile (orange line, right-hand scale). The beam is shown before its injection into a plasma stage.

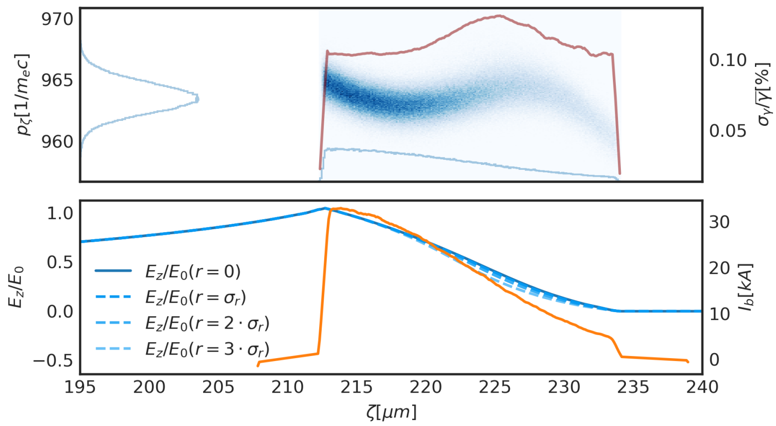


Figure 8.7: (Top plot) longitudinal phase-space distribution (blue, left-hand scale), together with axis histogram projections (light blue lines) and slice energy spread (red line, right-hand scale) of a high-current beam after dechirping. (Bottom plot) longitudinal wakefields taken on-axis and at three different radial offsets (dashed lines, left-hand scale), together with the beam current profile (orange line, right-hand scale), shown after a propagation distance of $z_{\text{sim}} \approx 1.7\,\text{mm}$ in a plasma with density $n_p = 1.0 \times 10^{22}\,\text{m}^{-3}$. The observed reduction in projected energy spread is significantly more pronounced for this optimized profile compared to figure 8.5, going from the initial value $\Delta\gamma \approx 1.0\,\%$ to $\Delta\gamma \approx 0.13\,\%$.

above the required range will overchirp the beam and increase the energy spread after a minimum has been reached prematurely. Additionally, the length of the plasma cell provides another optimization parameter, influencing both the projected and slice energy spreads. These parameters need to be adjusted given a specific beam provided by an initial accelerating structure, while observing the potential of the beam to drive a plasma wake in a linear or non-linear regime. The process begins by considering the beam size, which provides an upper limit on the density and thus the potentially available maximum wakefield. The propagation distance required for dechirping is estimated from the wakefield distribution over the driver-beam length — either derived analytically or obtained from simulations. However, the parameter space is often constructed from the physical dimensions of the experimental area, such as the plasma-cell length, while the beam parameters can be adjusted within a specific machine-dependent range. If that is the case, then an iterative approach aimed at finding a good working point based on initial parameters might be helpful in setting up an experiment and probing its potential limitations. The following section describes such an approach, taken in preparation for a dechirping experiment at the ATF.

## 8.2 PARAMETER ITERATIONS FOR ATF EXPERIMENT

The accelerator at the Brookhaven National Laboratory Accelerator Test Facility provides an electron beam within a promising parameter range suitable for testing the applicability of dechirping under realistic experimental conditions. In preparation for the experimental run, a parameter range of potential plasma densities, beam-focusing settings and energy-chirp values needed to be analyzed to find a good working point based on the physical limitations of the facility. This serves not only as preparation for the experiment itself, but as an insightful study on the dechirping properties presented above.

According to recent parameter studies [Swinson et al., 2018], the beam at the ATF is within the energy range $E = 30\,\mathrm{MeV} - 80\,\mathrm{MeV}$, has a charge $Q_b = 0.1\,\mathrm{nC} - 1\,\mathrm{nC}$, a duration of $t_b \approx 100\,\mathrm{fs}$, a transverse size of $\sigma_t \approx 50\,\mu\mathrm{m}$, while exhibiting an emittance of $\epsilon_n = 1.0\,\mu\mathrm{m}$. These values are assumed under optimal focusing conditions, but can be adjusted within a certain range. The plan for the experiment was to propagate the beam off-crest in the accelerating cavities, thus obtaining a beam with a quasi-linear chirp within a modifiable range of up to several percent. The plasma cell itself had a total length of $L = 40\,\mathrm{mm}$.

Given these limiting conditions, one of the first questions to pursue is the amount of dechirping expected from different plasma densities, starting with a beam exhibiting a negative linear chirp of $\sigma_\gamma/\sigma_\zeta = 1.0\,\%$, for a mean energy $E = 70\,\mathrm{MeV}$. Injecting a beam at a specific density value not only changes the wakefield gradient available, it also introduces size limits on the beam expressed in normalized plasma units.

Given the dimensions of the ATF beam, the assumed plasma densities were in the range $n_p = 1.0 \times 10^{20}\,\mathrm{m}^{-3} - 1.0 \times 10^{21}\,\mathrm{m}^{-3}$.

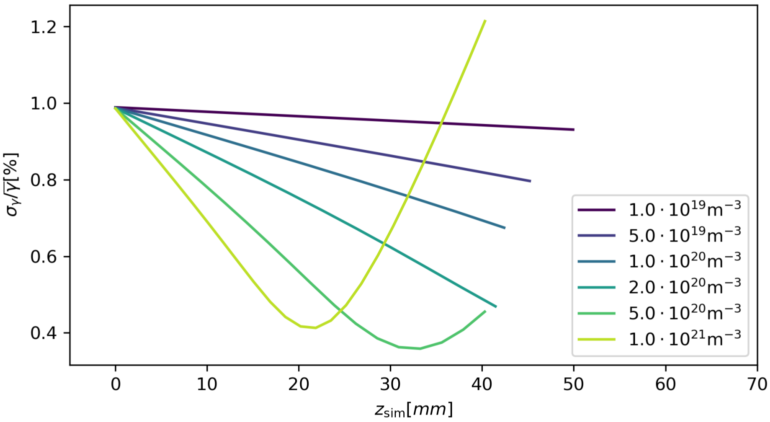


Figure 8.8: Evolution of the projected energy spread for the beam driving a wakefield based on the ATF beam parameters. The charge was set to $Q_b = 120\,\mathrm{pC}$, with the beam length $\sigma_\zeta = 30\,\mu\mathrm{m}$ and a transverse spot size $\sigma_r = 50\,\mu\mathrm{m}$ for a varying density.

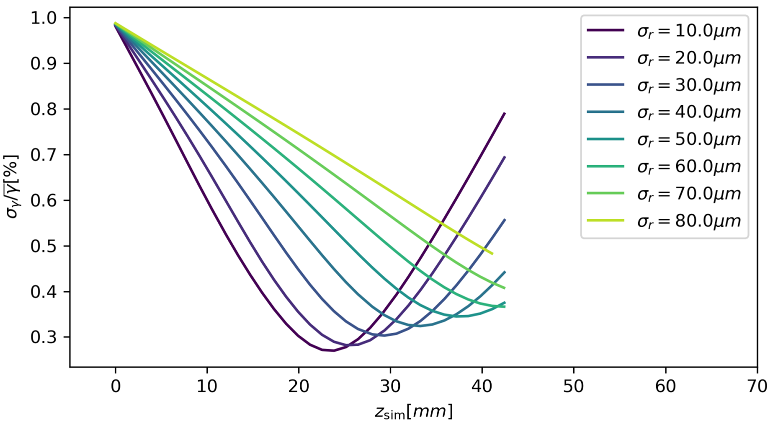


Figure 8.9: Evolution of the projected energy spread for the beam driving a wakefield based on the ATF beam parameters with varying transverse spot size and thus focusing. The charge was set to $Q_b = 120\,\mathrm{pC}$, with the beam length $\sigma_\zeta = 30\,\mu\mathrm{m}$ and a plasma density $n_p = 4.0 \times 10^{20}\,\mathrm{m}^{-3}$.

The results of the initial iterations can be seen in figures 8.8 to 8.9. As expected, a lower plasma density might not allow for a gradient high enough to compensate the chirp, while a higher density can lead to an overchirping effect, rotating the beam too far in the longitudinal phase space by virtue of its high gradient.

The lowest attainable energy-spread value depends on the density not only through the gradient, but also through the transverse wakefield dependency — a beam with a high local peak density and small

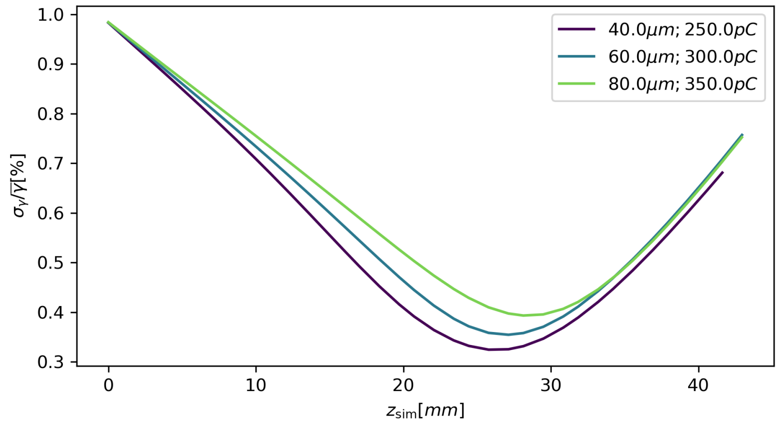


Figure 8.10: Evolution of the projected energy spread for the beam driving a wakefield based on the ATF beam parameters, for three different transverse beam size and charge combinations chosen to obtain comparable wakefield distributions with a constant beam length $\sigma_\zeta = 60\,\mu\text{m}$. As expected, the lowest obtainable value for the energy spread is defined by the beam size and thus the transverse wakefield variation of the beam samples.

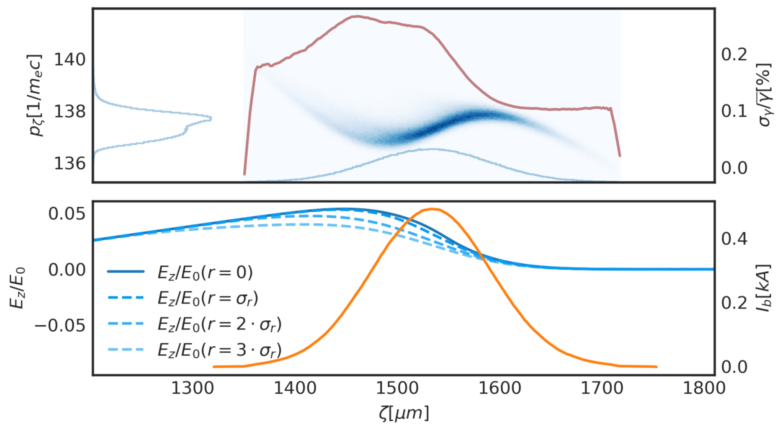


Figure 8.11: (Top plot) longitudinal phase-space distribution (blue, left-hand scale), together with axis histogram projections (light blue lines) and slice energy spread (red line, right-hand scale) of the ATF beam focused to a transverse spot size of $\sigma_r = 40\,\mu\text{m}$. (Bottom plot) longitudinal wakefields taken on-axis and at three different radial offsets (dashed lines, left-hand scale), together with the beam current profile (orange line, right-hand scale). The beam is shown after a propagation distance of $z_{\text{sim}} \approx 25.0\,\text{mm}$ through a plasma with density $n_p = 3.0 \times 10^{20}\,\text{m}^{-3}$. Compared to figure 8.12, the beam samples less variation of the longitudinal wakefield over its width, which results in a lower growth of the slice energy spread (up to $\Delta\gamma \approx 0.26\,\%$ in this case).

radial footprint, as expressed in plasma-based units, will generate a larger wake and be subjected to less transverse variations over its spot size. This is evident in figure 8.9 — not only does the more focused beam see higher dechirping through an increased wakefield, it can also approach a lower energy spread value when compared to bigger beams, all having the same charge. All beams experience growth of their slice-energy spread over the propagation length, however, making it a significant limiting factor of the dechirping process and a potential trade-off to reduce the projected energy spread. Relaxing the condition of constant beam charge, this effect can be studied further by setting this parameter in such a way as to obtain comparable wakefield distributions for varying transverse beam sizes. As presented in figure 8.10, a variation in transverse beam size while the charge is tuned to keep the wakefield produced by the beam nearly constant, will change the lowest attainable energy-spread value, since the beam will sample less wakefield variation over the transverse domain. This observation is supported by the phase-space plots shown in figures 8.11 to 8.12, where the beam with a smaller transverse footprint exhibits a smaller increase in the projected energy spread.

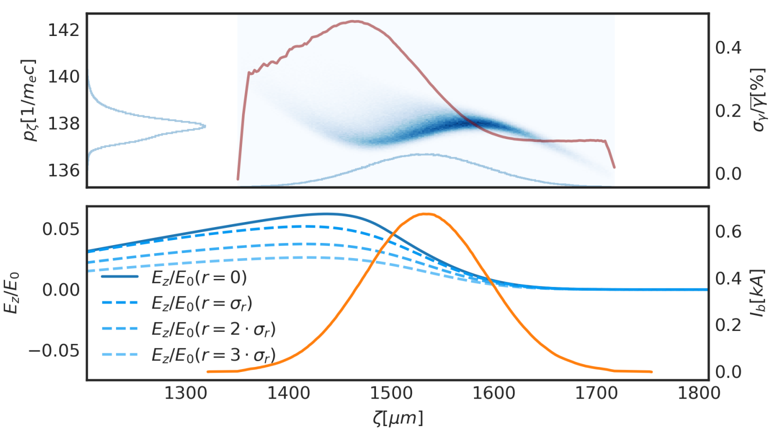


Figure 8.12: (Top plot) longitudinal phase-space distribution (blue, left-hand scale), together with axis histogram projections (light blue lines) and slice energy spread (red line, right-hand scale) of the ATF beam focused to a transverse spot size of $\sigma_r = 80\,\mu\text{m}$. (Bottom plot) longitudinal wakefields taken on-axis and at three different radial offsets (dashed lines, left-hand scale), together with the beam current profile (orange line, right-hand scale). The beam is shown after a propagation distance of $z_{\text{sim}} \approx 25.0\,\text{mm}$ through a plasma with density $n_p = 3.0 \times 10^{20}\,\text{m}^{-3}$. Compared to figure 8.11, the beam samples more variation of the longitudinal wakefield over its width, which results in a higher slice-energy spread (up to $\Delta\gamma \approx 0.48\,\%$ in this case).

Despite the limitations outlined in this section, the simulations show a clear potential for dechirping given the presented parameters, albeit without complete minimization of the energy spread to initial slice values.

## 8.3 FLASHFORWARD DECHIRPING EXPERIMENT

The dechirping principles outlined in the previous sections formed the basis of a dedicated experiment at the FLASHForward facility [D'Arcy, 2018]. The FLASH accelerator was used to obtain a single beam with a measured energy of $E \approx 681\,\mathrm{MeV}$, a charge of $Q = 300 \pm 2\,\mathrm{pC}$, accelerated off-crest to obtain a negative chirp of 1.31 % FWHM before being compressed to a spot size of $\sigma_t \approx 60\,\mu\mathrm{m} \times 20\,\mu\mathrm{m}$ and a length of $t_b \approx 6\,\mathrm{ps}$. According to previous considerations (cf. equations (8.1) to (8.2)), the optimal plasma density due to the beam size and mean energy, given the total length of the plasma capillary of $z_p \approx 33\,\mathrm{mm}$, can be calculated as $n_p = 2 \times 10^{21}\,\mathrm{m}^{-3}$, which puts the beam in a linear regime with a corresponding maximum dechirping gradient of $E_z \approx 210\,\mathrm{MV\,m}^{-1}$ at its tail. PIC simulations for a range of plasma densities were performed in preparation for this work, sending a Gaussian representation of the beam with the same rms parameters and charge into a flattop plasma and calculating the final FWHM energy spread. Figure 8.13 shows the simulation results together with the experimental data, taken at varying temporal offsets following the discharge corresponding to different plasma densities. The simulations show excellent agreement with one of the first observed dechirping experiments in the plasma environment.

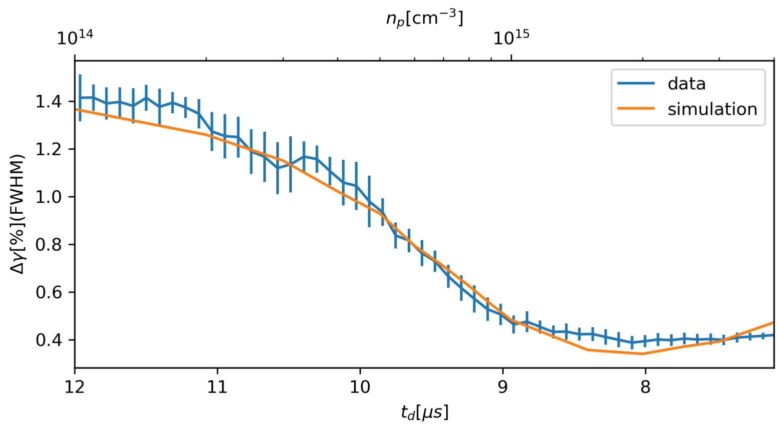


Figure 8.13: The FWHM energy spread of the experimental beam and simulated Gaussian, both after propagation through a plasma stage of $z_p \approx 33\,\mathrm{mm}$, given for different PIC plasma densities (top scale) and discharge times relative to the electron bunch arrival time (bottom scale). The experimental data is provided with symmetric rms error bars, given as the standard deviation of the observed data points at each delay step and representing shot-to-shot fluctuations.

## 8.4 DECHIRPING POTENTIAL OF THE FLASHFORWARD BEAM AFTER ACCELERATION

As depicted in the preceding chapters, the result of the external injection acceleration process in FLASHForward is a beam which exhibits a low slice-energy spread, lending itself to potential post-acceleration phase-space manipulation to retain or optimize its beam-quality parameters through dechirping. However, since the core dechirping mechanism can also lead to a significant increase in slice-energy spread, the potential usefulness of this technique for the beam distribution obtained in the main acceleration study will be further analyzed in this section.

As shown in a previous chapter, the parameter space of the proposed FLASHForward accelerator enables the acceleration of an externally injected witness beam, provided a scraper can be used with sufficient precision to obtain two optimized beam distributions from an initial preaccelerated Gaussian bunch. The resulting witness beam was shown to preserve its emittance ($\epsilon_{n,rms} = 2.0\,\mu\text{m}$) while increasing the projected energy spread from $\Delta\gamma = 0.1\,\%$ to $\Delta\gamma \approx 0.2\,\%$, all while nearly doubling its energy over an acceleration distance of $z_{\text{sim}} \approx 20\,\text{cm}$ in PIC simulations. In absolute terms, the projected energy spread obtained in the simulation is equivalent to $\sigma_\gamma \approx 7.7641/m_e c$, corresponding to $\sigma_E = 3.97\,\text{MeV}$. Consequently, the witness would need to generate a wakefield of sufficient gradient for a given propagation length for successful dechirping. Ideally, it would do so while entering the region with a longitudinal phase-space distribution showing a negative linear or quasi-linear chirp, mimicking the longitudinal wakefield structure for optimized reduction of the energy spread. The beam in question, however, shows a more complex longitudinal distribution (cf. corresponding chapter and phase-space plots post-acceleration), albeit with a suitably low slice energy spread. Nevertheless, a study of the parameter range and its dechirping potential can form the basis of possible mitigation measures in case of beam quality degradation following the acceleration, specifically focusing on a suitable plasma density range.

Based on the considerations above, the witness beam obtained in the previous chapter was reinjected into a plasma section with density $n_p = 5.0 \times 10^{22}\,\text{m}^{-3}$ following its acceleration. The results of the corresponding PIC simulation for a witness beam with the initial longitudinal configuration shown in figure 8.14 are presented in figure 8.15 and exhibit a promising shift in the longitudinal phase-space after a short propagation distance of $z_{\text{sim}} \approx 3.0\,\text{mm}$, with a minor increase in slice energy spread, confirming the beam to be within an acceptable parameter range for dechirping to be effective given its energy profile. Because of the inherent, non-linear shape of the witness phase-space chirp of this particular distribution, however, it is not possible to cause a significant reduction in projected rms energy spread, despite the accompanying rotation in longitudinal phase space (it can be noted that the more linear front-section of the beam, amounting to about 4/5 of the overall charge, shows a reduction of the projected energy spread down to the initial value $\Delta\gamma \approx 0.1\,\%$).

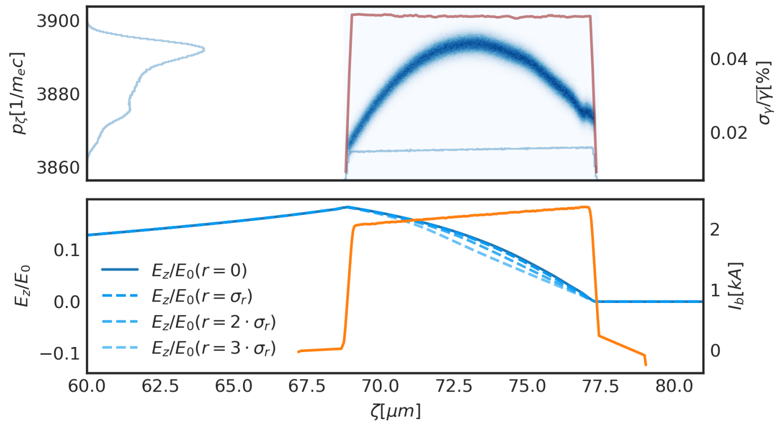


Figure 8.14: (Top plot) longitudinal phase-space distribution (blue, left-hand scale), together with axis histogram projections of the distribution (light blue lines) and slice energy spread (red line, right-hand scale) of the FLASHForward beam after its acceleration in a plasma section with a density $n_p = 1.0 \times 10^{23}\,\mathrm{m}^{-3}$ and before injection into a dechirping stage. (Bottom plot) longitudinal wakefields taken on-axis and at three different radial offsets (dashed lines, left-hand scale), together with the beam current profile (orange line, right-hand scale).

The central question of this section was whether an appropriate plasma density environment can be found to enact a significant shift in the longitudinal phase-space profile of a preaccelerated FLASHForward type beam, such as the one described at the end of chapter 7. It was found that the plasma density range around $n_p = 5.0 \times 10^{22}\,\mathrm{m}^{-3}$ is suitable to fulfill this requirement. However, it was not possible to reduce the projected energy spread for the whole beam given the non-linear nature of its longitudinal phase-space profile. Nevertheless, the dechirping technique can potentially be used in this scenario as well, to counter driver-witness configurations with non-optimal beam loading. It should be noted that this consideration additionally does not take into account the problem of drive-beam removal.

## 8.5 EMITTANCE EVOLUTION DURING DECHIRPING

The main focus of this chapter was the dechirping effect induced on a driver beam to reduce its energy spread. However, this discussion is not complete without a description of the beam-emittance evolution. The starting point for further consideration is the matching mechanism

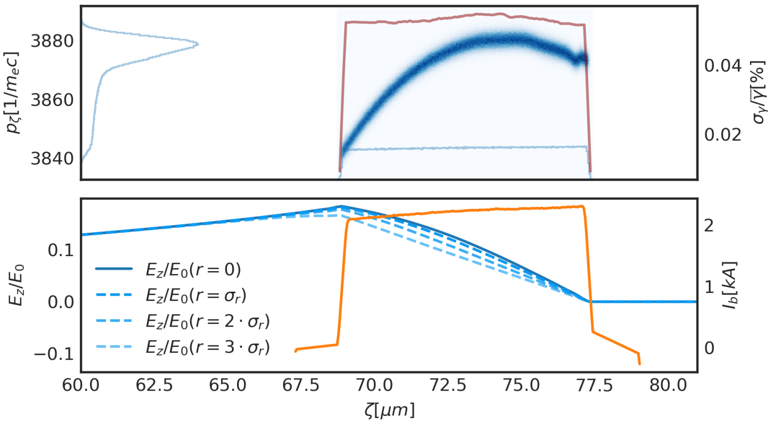


Figure 8.15: (Top plot) longitudinal phase-space distribution (blue, left-hand scale), together with axis histogram projections of the distribution (light blue lines) and slice energy spread (red line, right-hand scale) of the FLASHForward beam after a dechirping stage. (Bottom plot) longitudinal wakefields taken on-axis and at three different radial offsets (dashed lines, left-hand scale), together with the beam current profile (orange line, right-hand scale). The beam is shown after its propagation through $z_{\text{sim}} \approx 3.0\,\text{mm}$ of plasma with a density of $n_p = 5.0 \times 10^{22}\,\text{m}^{-3}$, obtained from a PIC simulation. While a clear shift in its longitudinal phase-space is observable, it does not result in a reduced projected energy spread due to the non-linear nature of the chirp.

mentioned in chapter 7. It dictates that a beam propagating through a focusing plasma channel needs to have properly matched transverse parameters to avoid emittance growth through betatron decoherence. It should be noted that the previous descriptions are a special case in that regard, since the beam generates the focusing environment itself. Therefore, the degrading effects for a mismatched case would be evident mostly in the tail section, and for plasma wavelengths at the limit of the condition described in equation (8.1). Figure 8.16 shows the same simulations as depicted in figure 8.8, together with the emittance evolution. The beam is mismatched for all considered densities, with an initial beta value of $\hat{\beta} \approx 28.2\,\text{cm}$ and the matched counterpart ranging from 25.2 cm to 2.5 cm. The emittance increases more severely for higher density values due to the higher degree of mismatch while the beam additionally samples a bigger section of the focusing environment it generated in its wake. Consequently, it is the tail section of the beam that experiences the highest increase in emittance, as shown in figure 8.17 for $n_p = 1 \times 10^{21}\,\text{m}^{-3}$.

However, the matching mechanism is not the only factor contributing to emittance growth. Since the beam is only partially subjected to a focusing channel, its spot size does not remain constant, growing during propagation and increasing emittance even for matched cases. This effect is shown in figure 8.20, where the beam used in fig-

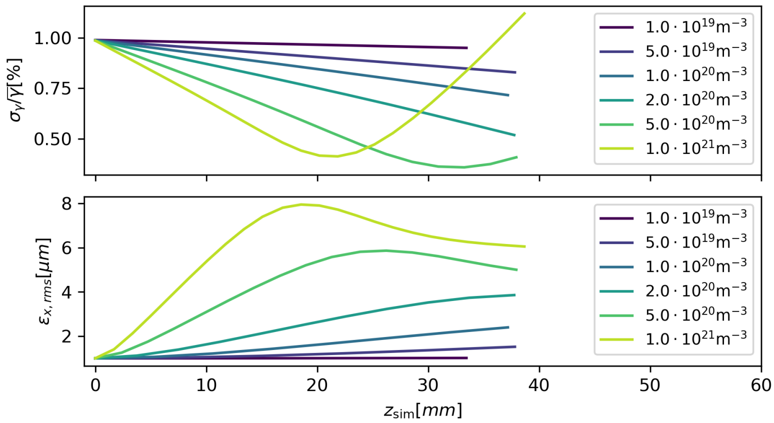


Figure 8.16: Evolution of the projected energy spread for the beam driving a wakefield based on the ATF beam parameters (top plot). The charge was set to $Q_b = 120\,\mathrm{pC}$, with the beam length $\sigma_\zeta = 30\,\mu\mathrm{m}$ and a transverse spot size $\sigma_r = 50\,\mu\mathrm{m}$) for a varying density. The lower plot shows the corresponding emittance evolution. An increase is evident with higher density values (the turn over can be explained by the cutoff mechanism removing heavily degraded tail portions of the beam).

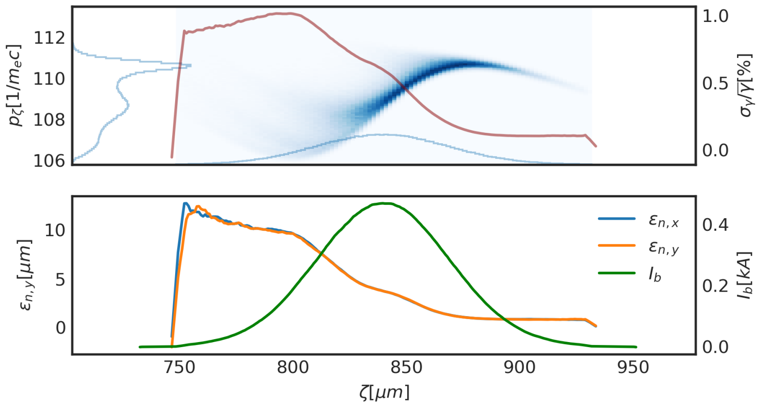


Figure 8.17: (Top plot) longitudinal phase-space distribution (blue, left-hand scale), together with axis histogram projections of the distribution (light blue lines) and slice energy spread (red line, right-hand scale) of the ATF beam after its propagation through $z_{\rm sim} \approx 40\,\mathrm{mm}$ of plasma with the highest considered density, $n_p = 1 \times 10^{21}\,\mathrm{m}^{-3}$. (Bottom plot) slice emittance values (blue and orange lines, left-hand scale) and current profile (green line, right-hand scale) of the same beam. The parameters are not matched, showing clear quality degradation of the slice quantities (energy spread and emittance) for the tail section reaching into the focusing wake.

ure 8.16 was focused to transverse parameters matched to the plasma density $n_p = 2 \times 10^{20}\,\mathrm{m}^{-3}$ in a blowout regime. While this behavior is an unavoidable consequence of the wakefield environment, it is mostly confined to the front section of the beam, where the phase-space rotation through defocussing is most pronounced, as shown in figure 8.18.

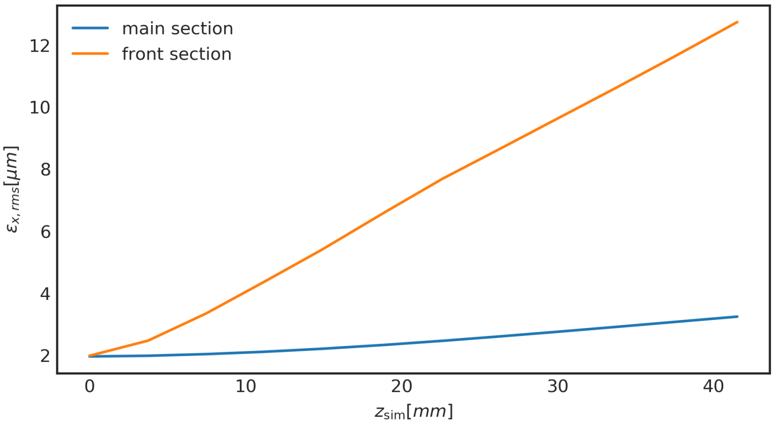


Figure 8.18: Evolution of the projected emittance for the ATF beam driving a wakefield matched to a plasma density of $n_p = 2 \times 10^{20}\,\mathrm{m}^{-3}$, provided for both its front and main sections. The beam was separated at $\zeta = 0.9 \cdot \Delta\zeta$. The two sections exhibit distinct emittance growth rates due to their different plasma and wakefield environments.

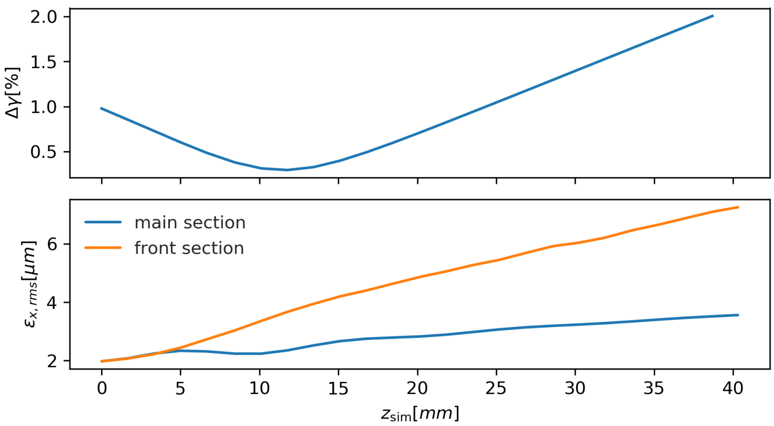


Figure 8.19: Evolution of the projected energy spread (top) and emittance for the ATF beam provided for both its front and main sections (bottom). The beam was matched to a plasma density of $n_p = 1 \times 10^{21}\,\mathrm{m}^{-3}$ and separated at $\zeta = 0.9 \cdot \Delta\zeta$.

Since the main interest of dechirping considerations is in the main section of the beam where the energy profile alteration is most pronounced, it is reasonable to neglect the emittance degradation of the front beam section. However, an emittance increase is unavoidable even for the rest of the beam, as evident in figure 8.18, where it increases from $\epsilon_{n,rms} = 2.0\,\mu m$ to $\epsilon_{n,rms} \approx 3.26\,\mu m$. Thus, the preferable application scenario for the ATF parameter range would aim to limit the propagation distance as much as possible, using higher densities to achieve the longitudinal phase-space rotation. This approach is depicted in figure 8.19, where the highest considered density for ATF studies, $n_p = 1 \times 10^{21}\,m^{-3}$ was used to achieve quick dechirping after $z_{\text{sim}} \approx 11\,mm$ and a comparatively modest emittance growth from $\epsilon_{n,rms} = 2.0\,\mu m$ to $\epsilon_{n,rms} \approx 2.35\,\mu m$.

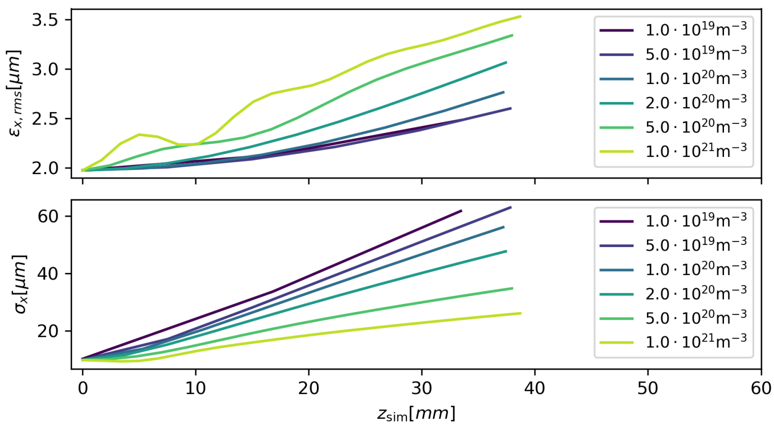


Figure 8.20: Evolution of the projected energy spread for the beam driving a wakefield matched to a plasma density of $n_p = 2 \times 10^{20}\,m^{-3}$. The charge was set to $Q_b = 120\,pC$, with the beam length $\sigma_\zeta = 30\,\mu m$, a transverse spot size $\sigma_r = 10\,\mu m$ and a normalized emittance $\epsilon_{n,rms} = 2.0\,\mu m$, for a varying density. The lower plot shows the corresponding emittance evolution. Despite the matching, the emittance increases, albeit at a significantly lower rate, owing to beam defocussing.

The discussion can be extended to the FLASHForward dechirping experiment described in section 8.3. The used setup, primarily concerned with the demonstration of successful phase-space rotation, shows clear increases in emittance at the end of the plasma stage for all but the lowest densities, as depicted in figure 8.21. However, the beam was not matched to this environment, with an initial beta function of $\hat{\beta} \approx 27.7\,cm$ in the x domain, while the matched beta varies between 88.5 mm for the lowest and 4.4 mm for the highest densities. At $\sigma_\zeta \approx 62.8\,\mu m$, the beam samples most of the wake it generates in the most effective density range ($5 \times 10^{14}\,m^{-3}$ to $4 \times 10^{15}\,m^{-3}$ with the corresponding plasma wavelengths $\lambda_p$ varying from 1.49 mm to 0.53 mm). Consequently, the mismatch mechanism is expected to have the biggest effect on emittance degradation. Indeed, compressing the beam to match the transverse parameters at a density of $n_p = 2 \times 10^{21}\,m^{-3}$ — chosen for the high degree of dechirping evident in figure 8.13 — results in a significant suppression of emittance growth, shown in figure 8.22. Additionally, this figure shows that the remaining emittance growth can be mostly attributed to the degradation of the front section, since its removal results in near-constant emittance. The necessary spot size of $\sigma_{x,y} \approx 3.0\,\mu\text{m}$ is close to the parameters obtained from tracking codes describing the upstream FLASHForward beamline in table 9.2. While not a sufficient argument in itself due to the different energy profile, this observation nevertheless points toward a feasible implementation of the matching approach in this context and plasma environment.

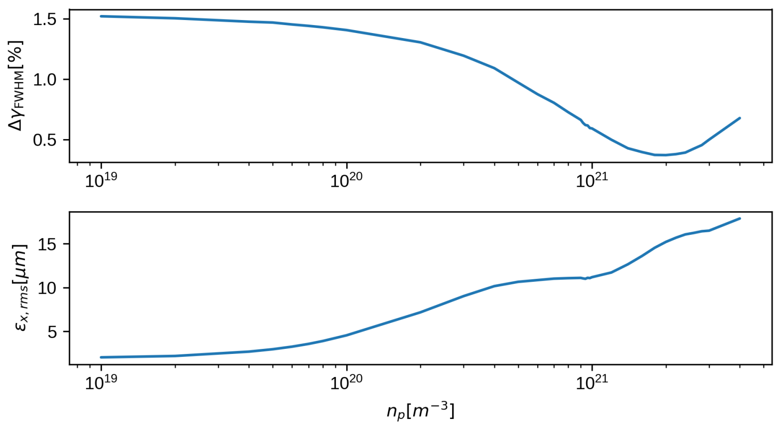


Figure 8.21: Final FWHM energy spread and emittance values of the beam used in the FLASHForward dechirping experiment simulations after propagation through $z_p \approx 33\,\text{mm}$ of plasma at varying densities.

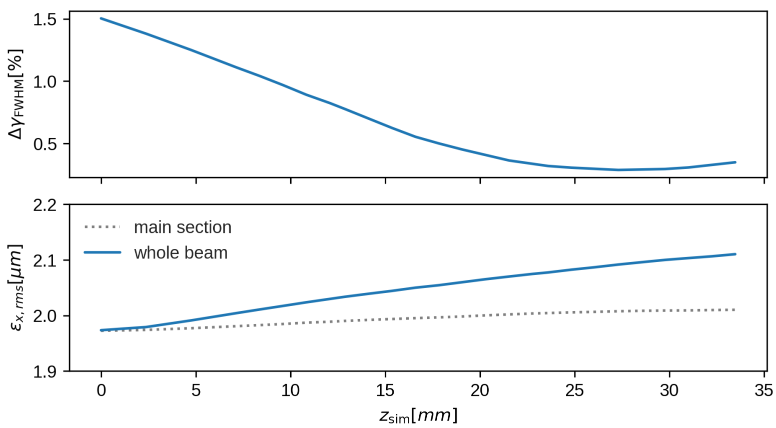


Figure 8.22: Evolution of the projected energy spread (top plot) and emittance (bottom plot) of the beam used in FLASHForward dechirping experiment simulations, modified to match the plasma environment with $n_p = 2 \times 10^{21}\,\text{m}^{-3}$. The resulting spot size in both transverse directions is $\sigma_{x,y} \approx 3.0\,\mu\text{m}$. The gray dotted line in the bottom plot represents the emittance evolution of the main beam section, obtained by considering only particles at longitudinal positions smaller than $\zeta = 0.7 \cdot \Delta\zeta$.

The above discussion is not limited to the parameter space outlined by the ATF beam or the FLASHForward dechirping experiment, but can be applied to any dechirping scenario. For a beam that fits into the plasma domain defined by its energy spread and chirp (e.g. the right length and current), emittance growth can be suppressed provided it can be matched to the density regime.

## 8.6 CONCLUDING REMARKS

Beams accelerated in plasma-wakefield environments can be subjected to accelerating fields with significant variations over the beam length, leading to a corresponding energy chirp imprinted during the acceleration process. The idea behind dechirping is to reinject the accelerated beam into a new plasma density section, thus creating a wakefield that can potentially reduce the energy chirp for a given propagation distance. Because of the inherent wakefield properties, however, the witness-turned-driver needs to satisfy certain requirements with respect to its size and current, dictated by the absolute energy and the corresponding necessary plasma density. A beam which is too long will oversample the wakefield in its tail section, increasing projected energy spread. Additionally, a beam which is too wide given the wakefield profile it can generate will be subjected to the radial variations of the wakefield, which can negatively impact its slice energy spread. The width or spot size is also related to the matching requirements of the plasma density under consideration, causing emittance growth for mismatched parameters. All of these effects are interconnected — a beam that might be narrow and short enough for a low plasma density might not be able to experience a gradient high enough for a short dechirping distance, necessitating a longer propagation and thus increased slice energy spread, which can be seen as a lower limit for the projected energy spread. To accommodate all of these considerations and aspects for a given beam parameter setup, extensive iterations can help narrow down the acceptable plasma density region and expected dechirping potential, as was presented in the case for a proposed experiment at the ATF facility. Comparable iteration runs supported the experiment performed at the newly commissioned FLASHForward facility, showing excellent agreement between theory and experiment and positioning this technology as a suitable measure for beam optimization and phase-space modification. Additionally, the case for dechirping given the FLASHForward beam parameter range, exemplified by the distribution taken from the simulations presented in the last chapter, was analyzed for potential usefulness, confirming a phase-space shift for a plasma density range around $n_p = 5.0 \times 10^{22}\,\mathrm{m}^{-3}$ and distances below 5 mm.

Finally, it should be noted that the observations presented in this chapter can also be used in the context of beams with asymmetric transverse phase-space distributions which have been shown to seed a transverse oscillation leading to eventual beam breakup, a severe destabilization known as hosing [Whittum et al., 1991]. Recent results [Mehrling et al., 2017] indicate that a driver with an initial energy chirp can mitigate this instability, since the resulting betatron decoherence helps to decouple the slice oscillations from resonant plasma background oscillation. In this context, dechirping can form an important part of an elaborate strategy, reversing a deliberately induced initial chirp in beams used for stabilization of the acceleration process in the PWFA regime.

# 9 START-TO-END SIMULATIONS

## 9.1 INTRODUCTION

In the previous chapters, the FLASHForward beam parameter space was analyzed with respect to its suitability for driving a plasma-acceleration regime, provided a scraper can select two optimized beam portions from an initially Gaussian beam charge distribution with otherwise favorable attributes such as emittance and energy spread. It could be shown that even this optimized regime is sensitive to changes in the setup parameters such as plasma density, the vacuum-to-plasma transition region, as well as the longitudinal beam distributions after their separation by an idealized scraper. It is clear, however, that more realistic distributions lead to additional unwanted qualities that need to be analyzed to understand their impact and to allow the introduction of potential mitigation strategies. This chapter thus focuses on investigating the properties of beam distributions obtained from beamline simulations describing electron behavior in the FLASH preaccelerator, assumed to be more realistic depictions of the actual beam expected at the plasma stage. Starting with a comparison of the distribution to the idealized case used above, the chapter then proceeds to identify the most significant deviations and resulting instabilities, before moving on to the presentation of corresponding mitigation strategies and finishing with a complete acceleration description mirroring the final sections of chapter 7.

## 9.2 INITIAL COMPARISON BETWEEN BEAM DISTRIBUTIONS

The simulations presented in the previous chapters — describing the external injection scenario based on the parameter space of a beam obtained from the FLASH accelerator — all assumed a Gaussian shape for the initial phase-space distribution. However, the actual beam provided by the preaccelerator can significantly deviate from this idealized distribution, showing asymmetric behavior in both the longitudinal and transverse dimensions — with a potentially severe impact on its suitability for efficient plasma-based acceleration. To obtain a more realistic beam depiction before the plasma cell, an ELEGANT [Michael Borland, 2000] simulation modeling the design of the FLASH accelerator, together with the proposed setup of the FLASHForward beamline up to the plasma cell [Aschikhin et al., 2016] was used. A start-to-end simulation pipeline was set up, allowing the beam to be obtained from the ELEGANT file format and its 6D coordinates to be transformed into the plasma-normalized format preferred by HiPACE, calculating the quasiparticle weight from the total beam charge, the number of particles and simulation grid dimensions. The first beam distributions were optimized for the expected length scales of a plasma environment with a density of $n_p = 5.0 \times 10^{22}\,\mathrm{m}^{-3}$ to allow for higher tolerances with respect to beam focusing and matching from the beam line compared to the density $n_p = 1.0 \times 10^{23}\,\mathrm{m}^{-3}$ proposed in the final sections of chapter 7.

A comparison between the driver-witness current configuration used for the simulated acceleration process in section 7.5 and the current profile of the beam obtained through ELEGANT is depicted in figure 9.1. While the more realistic beam distribution roughly observes the same length scales at the relevant longitudinal positions, it is the clear deviation of the longitudinal profile from the idealized Gaussian distribution assumed in previous simulations that necessitates changes in the simulation configuration and scraper position, specifically due to the different wakefield caused by the charge profile in the front section.

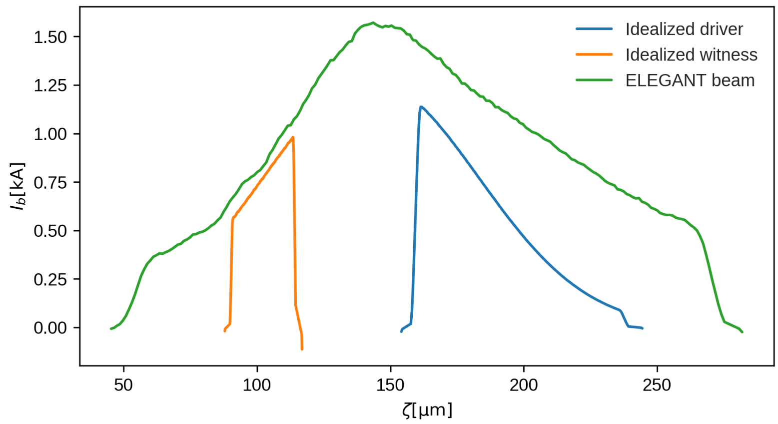


Figure 9.1: Comparison between the ELEGANT-sourced current profile of a beam before application of the scraper and the idealized driver-witness profiles used for the acceleration procedure description in section 7.5.

The theme of the departure from the idealized symmetric picture continues when considering the transverse domain, both through a comparison of the Twiss parameters, seen in table 9.1 and the phase-space depictions in figure 9.2. While crucial attributes of the ELEGANT distribution are similar to those of the idealized case, the deviations need to be scrutinized with respect to their potential repercussions for wakefield and beam stability during acceleration.

While the overall beam picture makes a strong case for asymmetries being present, it does not provide a clear indication whether they are due to possible phase-space correlations over the beam length, and thus suppressible through beam separation into a driver and witness.

| Parameter | Ideal Beam | ELEGANT Beam |
|---|---|---|
| $\beta_x$ | 9.9 mm | 44.5 mm |
| $\beta_y$ | 9.9 mm | 6.6 mm |
| $\alpha_x$ | 0.0 | 0.0 |
| $\alpha_y$ | 0.0 | $-0.1$ |
| $\Delta\gamma$ | 0.1 % | 0.2 % |
| $\epsilon_{n,x}$ | 2.0 µm | 4.7 µm |
| $\epsilon_{n,y}$ | 2.0 µm | 1.4 µm |
| $\sigma_x$ | 3.1 µm | 10.3 µm |
| $\sigma_x$ | 3.1 µm | 2.2 µm |

Table 9.1: A comparison of relevant beam quality parameters between the idealized and ELEGANT beams, showing asymmetries for crucial transverse parameters such as the beta function.

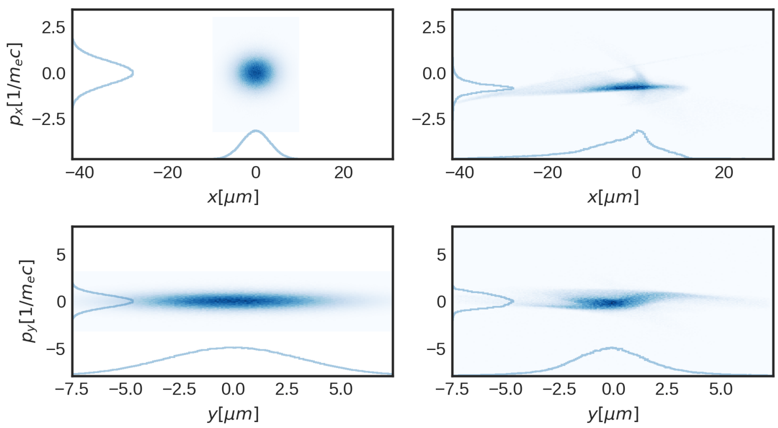


Figure 9.2: Comparison between the proposed idealized beam (left) and ELEGANT beam (right) distribution phase spaces, showing clear deviations from the symmetric picture assumed in previous simulations.

Therefore, the consideration will follow chapter 7 and establish a simulation regime from a single beam by applying an idealized scraper at a position suitable for optimal beam-loading to obtain a driver-witness pair.

## 9.3 LONGITUDINAL OPTIMIZATION

The electron beam distribution obtained from a simulated beam line description before the plasma cell is not fixed — it can be adjusted and modified within a wide parameter range, constrained by the specific setup of the preaccelerator. To form the basis of the ongoing optimization, however, some considerations based on this initial distribution can be helpful in steering the efforts in a sustainable and efficient direction. An essential feature of an externally injected beam is its position and current profile, determining the degree of beam loading in the wake behind the driver. The approach taken for the idealized distribution and depicted in chapter 7 was an iterative process considering the longitudinal domain only, since the nature of the blowout regime permitted the transverse properties with respect to the accelerating gradient to be ignored provided the witness-beam spot size was sufficiently small (this condition can be violated if the beam deviates significantly from the driver propagation axis, as seen below). Based on the available distribution, the approach will be similar — assuming a scraper of a certain thickness and iterating through its longitudinal position to minimize the variation of the resulting longitudinal fields over the witness-beam length. While the scraper definition is only an approximation and does not describe the corresponding physical processes behind the beamline component with sufficient accuracy, it can nevertheless guide further optimizations by limiting the permissible parameter range.

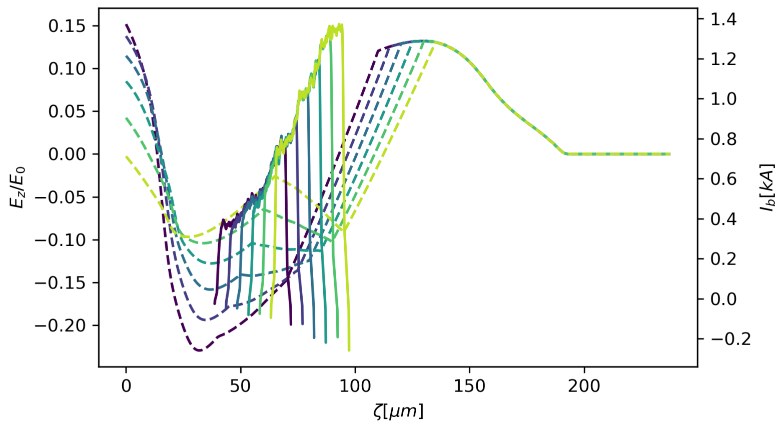


Figure 9.3: Longitudinal field (dashed lines, left-hand scale) and witness current profiles (solid lines, right-hand scale). Each color represents a single HIPACE simulation with a specific longitudinal position of the scraper that was applied to the ELEGANT-sourced distribution shown in figure 9.1.

Figure 9.3 depicts the iteration process of the idealized scraper position and width, mirroring similar considerations in previous chapters. Despite the clear deviations from a theoretical profile, the wakefield shows promising beam-loading results with a stable wakefield over the witness length. The next step following considerations focused on the longitudinal domain is more elaborate, since it involves longer simulation distances concerned with matching mechanisms transporting the beams from the vacuum to the plasma environments. Again, results obtained from earlier optimized simulations form the basis for the parameters chosen in PIC simulations using the more realistic beam distribution. However, its significant deviations from the radially symmetric picture have the potential to disrupt beam transport and acceleration by driving the hosing instability mechanism through off-axis oscillations [Mehrling et al., 2017; Whittum et al., 1991].

Figure 9.4 depicts the propagation of the sliced beam through a transition region (with a scaling parameter $L = 400k_p^{-1}$) and into the following plasma region with has a plateau density $n_p = 5.0 \times 10^{22}\,\mathrm{m}^{-3}$. The two beams show mutual transverse displacement, resulting in a clear degradation of the witness beam spot size. This observation is supported by the statistical data in table 9.2, now given for the two beams after their separation and the witness beam from the idealized simulation. As an example, the Twiss parameter $\hat{\alpha} = -\langle xx' \rangle / \hat{\epsilon}$, which needs to fulfill $\hat{\alpha} \approx 0$ to allow for proper matching (as mentioned in the previous chapters), clearly deviates from its optimal value in in table 9.1 once the beam is separated.

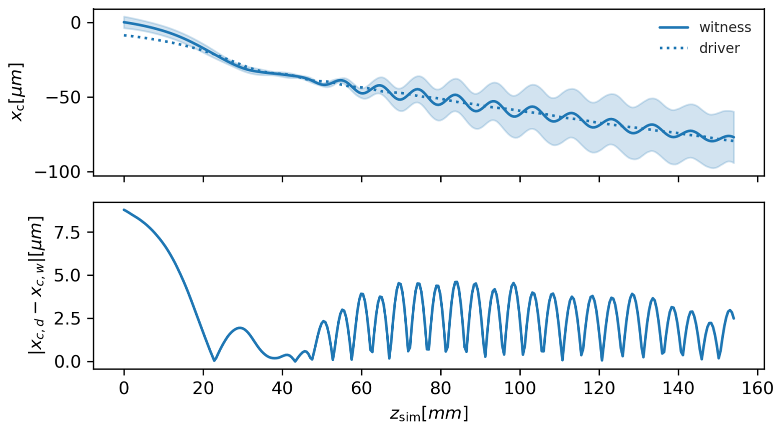


Figure 9.4: Beam centroid evolution of both the driver and witness obtained from the ELEGANT-beam distribution after applying a simplified scraper for separation. The witness beam shows an oscillation around the driver path driving growth in the rms beam-spot size, which is represented here and in the following as the shaded area around the beam.

## 9.4 WITNESS-BEAM STABILIZATION

The generation of beam distributions with favorable properties is anything but straight-forward, since it requires careful tuning of a multitude of parameters with intertwined dependencies (e.g. evident in CSR effects [Borland, 2001]) throughout the simulated beam line. The start-to-end approach is thus meant to foster constructive coordination between two separate areas of the accelerator, with the PIC simulations serving as a benchmark for the quality of the beams tracked through the upstream sections. It does not however prevent

| Parameter | Idealized Parameters | S2E Driver | S2E Witness |
|---|---|---|---|
| $\beta_x$ | 9.9 mm | 73.32 mm | 15.0 mm |
| $\beta_y$ | 9.9 mm | 3.94 mm | 3.6 mm |
| $\alpha_x$ | 0.0 | −1.8 | 0.7 |
| $\alpha_y$ | 0.0 | −0.5 | 0.5 |
| $\Delta\gamma$ | 0.1 % | 0.093 % | 0.155 % |
| $\epsilon_{n,x}$ | 2.0 µm | 2.21 µm | 2.0 µm |
| $\epsilon_{n,y}$ | 2.0 µm | 1.08 µm | 0.636 µm |
| $\sigma_x$ | 3.1 µm | 9.1 µm | 3.9 µm |
| $\sigma_x$ | 3.1 µm | 1.5 µm | 1.1 µm |

Table 9.2: A comparison of some relevant beam quality parameters between the proposed FLASHForward setup and two beams after a simple scraper-based separation of an ELEGANT-sourced beam.

the plasma environment from helping to suppress potentially destabilizing properties such as strong asymmetries initially present in the distributions, which seed the hosing instability [Whittum et al., 1991] observed in figure 9.4.

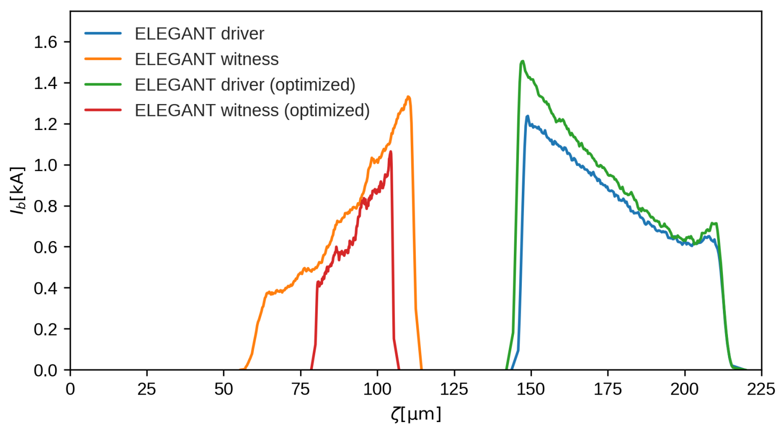


Figure 9.5: Comparison between the ELEGANT-sourced current profiles of a witness and driver used in the previous section and their retuned counterparts which form the basis for subsequent stabilization considerations.

As a first measure, a second scraper was introduced that removed a tail section of the witness beam, limiting its length to $\approx$ 25 µm. It can be observed in figure 9.3 that this witness-beam section is in close proximity to the plasma wave crest, located behind the minimum of the longitudinal field. Since this area is very sensitive to oscillations of the electron bubble sheath caused by the driver, limiting its interaction with the witness is expected to help with the latter's stability. Additionally, the beam distribution was retuned to increase driver current, leading to a larger bubble. A comparison of both the initial and retuned driver and witness current profiles is provided in figure 9.5. Figure 9.6 shows the evolution of the driver and witness beams obtained from the retuned configuration as they propagate through a tapered section (of length $z \approx 50\,\text{mm}$) and into the plasma. The increase in stability is evident both in the betatron oscillation of the witness beam as well as its spot size, compared to the results shown in figure 9.4. However, while the destabilization of the witness beam is significantly suppressed, the oscillations still drive a betatron decoherence and thus an emittance increase, also evident in the plot.

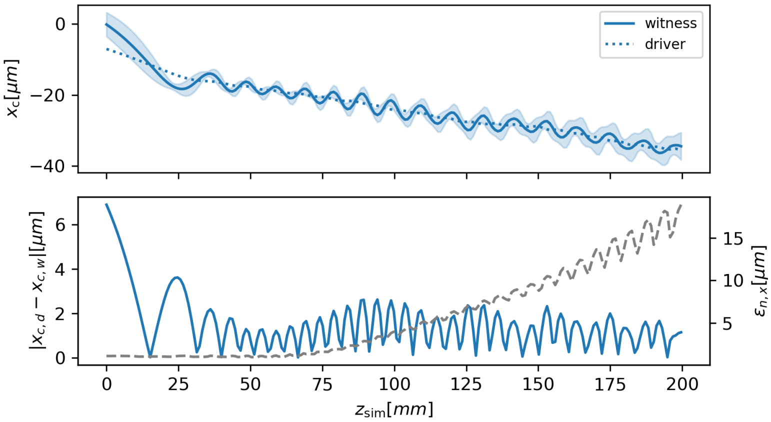


Figure 9.6: Beam centroid evolution of the driver and witness (top), together with the absolute difference in their centroids (bottom) obtained from an ELEGANT-beam distribution with an optimized tail section. The witness oscillation, while smaller than in figure 9.4, nevertheless leads to beam quality degradation, as seen in the emittance evolution (shown by the gray line in the lower plot and corresponding to the right-hand vertical axis).

The focus thus shifts to measures proposed against the hosing instability in order to minimize decoherence effects and limit beam quality degradation (e.g. emittance growth). One of the proposed solutions was already applied to all simulations in this chapter. As discussed in [Mehrling et al., 2017], a tapered vacuum-to-plasma transition section can greatly reduce the initial hosing seed of the beam distributions. An exponential profile of the tapering, with the scaling parameters used throughout this work (see chapter 7), was found to be optimal in reducing the oscillation compared to a step-like transition and will thus be applied to all further simulations. Unfortunately, it can be considered as the only tuning parameter unrelated to the more complex beamline design simulations. All other strategies — from driver defocussing to pre-chirping — demand a

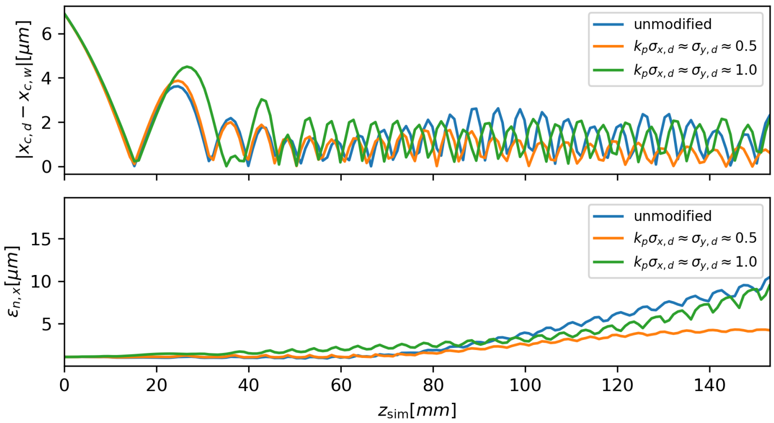


Figure 9.7: Comparison between the unmodified beam distributions and a configuration with an artificially widened beam. A reduction in the overall witness oscillation is evident once it reaches the plasma density plateau (which starts after $z_{\text{sim}} \approx 48$ mm).

more elaborate modification of the beam phase-space, as discussed below.

### 9.4.1 *Drive beam defocussing*

As shown in [Ossa, Mehrling, et al., 2018], the hosing instability in PWFAs is rapidly suppressed for drive beams with an initial transverse size comparable to the blowout radius. To test the effectiveness of this approach in the presented scenario, the driver obtained by the aforementioned separation of an ELEGANT single-beam distribution was widened numerically by multiplying the transverse positions with scaling factors, thus approximating a selective beam-spoiling mechanism before the plasma cell. As shown in figure 9.7, this leads to a more stable propagation with respect to the inter-beam oscillations when compared to a non-modified beam after separation (the same transition region is used for both, with a length of $z_0 \approx 50$ mm). Of the two beam spot sizes obtained, $k_p\sigma_x = k_p\sigma_y = 0.5$ shows the smaller oscillation amplitude, with a better overall stability — interpreted as the variation in the amplitude overall and reduced emittance growth.

### 9.4.2 *Drive beam prechirping*

One of the crucial aspects of the hosing instability is the beam-plasma interaction, which can drive a resonant oscillation in the ion channel and destabilize the bunch. However, as shown in [Mehrling et al., 2017], this effect can be dampened if the beams exhibit strong decoherence due to a non-negligible energy spread. In the case of an energy chirp, the individual longitudinal slices would oscillate at different frequencies, disrupting the resonance and damping the constructive ion-channel feedback loop. As a possible mitigation measure for the present case, the beams could be introduced with an initial chirp, potentially necessitating a dechirping mechanism (as discussed in chapter 8) after the plasma cell. It should be noted, however, that the best-case scenario would involve the modification of the drive beam only, since a significant correlated energy spread of the witness would reduce the decoherence length and thus spoil the emittance during acceleration for unmatched cases such as the one under consideration (see chapter 7). Figure 9.8 depicts a setup with a numerically prechirped drive beam for three values of the correlated energy spread. As with the case of the widened beam, the methods suggested by previous studies help to suppress the oscillations to a small degree, more evident as an impact on emittance growth.

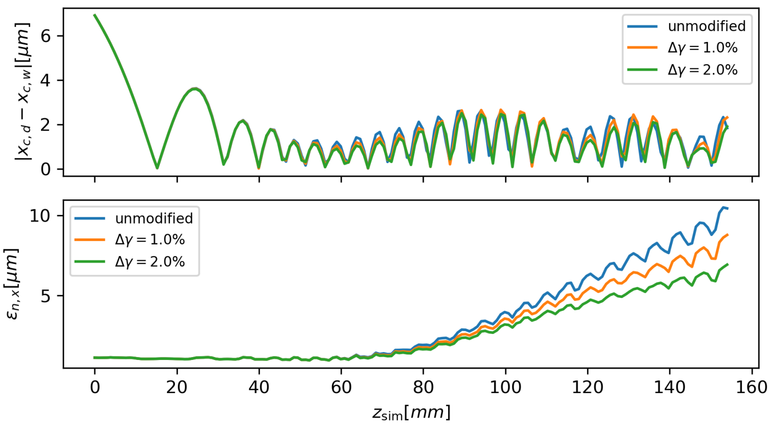


Figure 9.8: Comparison between PIC simulations featuring a non-modified double-beam setup juxtaposed with a witness following a prechirped driver. The oscillations are slightly damped for cases with higher energy spreads, suggesting a disruption of the resonant coupling via the onset of a decoherence. This effect is more pronounced for the emittance evolution shown in the bottom figure.

To complete the analysis considering the applicability of three of the currently prevalent mitigation methods — a tapered transition, the defocussing of the driver and its prechirping — a simulation including all three was performed. The results are depicted in figure 9.9. The configuration used the values which lead to the lowest oscillation amplitudes over the propagation length — a spot size of $k_p\sigma_{x,d} = 0.5$ and a prechirped energy spread $\Delta\gamma = 2\,\%$.

### 9.4.3 *Initial centroid offset*

Having explored two measures offered for the hosing instability, the most evident deviation from the symmetric picture — the clear offset

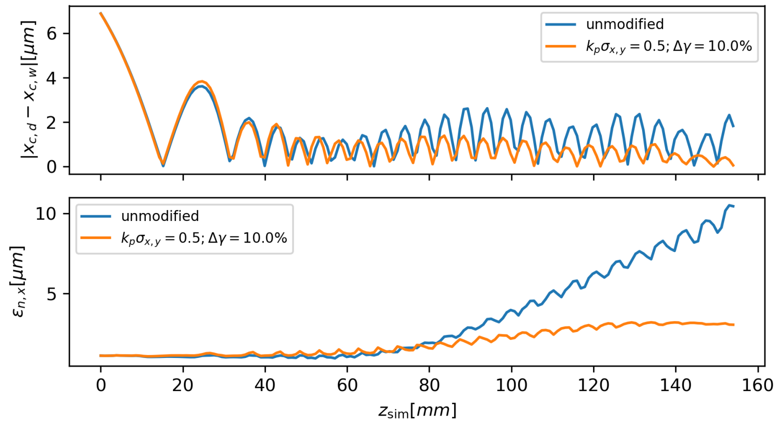


Figure 9.9: Comparison between two PIC simulations featuring a non-modified double-beam setup juxtaposed with a witness following a prechirped and widened driver. The witness oscillations are damped, suggesting a reduction of the betatron decoherence and showing suppressed emittance growth.

between the two beams evident from the start of the simulations — can be considered as well. While it is reduced due to the focusing channel established by the driver, it nevertheless contributes to the initial hosing seed. Additionally, the initial analysis of the Twiss parameters showed a clear divergence, especially pronounced after the single beam was divided into a driver-witness pair. In simple terms, this is related to a corresponding offset in the transverse momentum phase space. To test the influence of these asymmetries, the transverse phase-space positions of the quasiparticles were centered by subtracting the respective mean values as a simple approximation of a symmetric picture neglecting potential correlations. The resulting simulation, together with an unmodified case, is shown in figure 9.10. The difference between the unmodified and recentered setups is most evident in the emittance evolution, with the centered setup showing reduced emittance growth. However, the amplitude of the centroid differences remains largely comparable to the non-centered case. Thus, removing the phase-space offset in this scenario does not suppress the development of witness beam oscillations, which develop during its propagation in the plasma bubble.

It should be noted that such a modification of the quasiparticle phase-space constitutes the least experimentally viable option, since it cannot be related to a beamline component facilitating the necessary beam adjustments, leaving only iterations performed in ELEGANT as a means of approximation. As such, this approach nevertheless follows the argument presented at the beginning of this chapter, which aimed to discuss the instabilities and their causes to derive a direction for potential further optimizations, weighing the importance of beam parameters and asymmetries. Having established a possible optimization

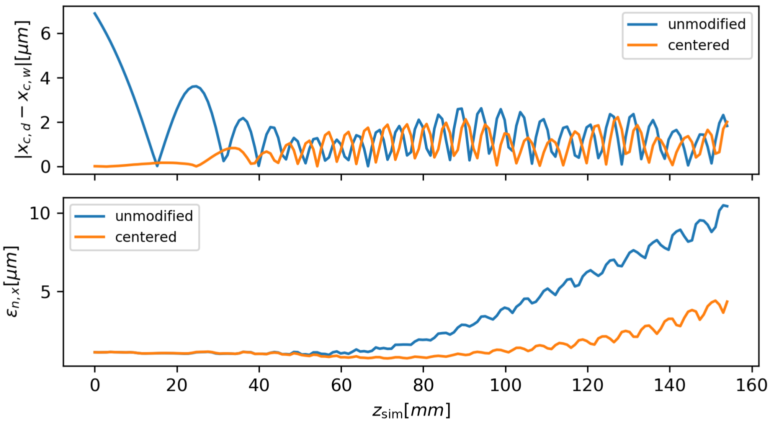


Figure 9.10: Comparison between two PIC simulations featuring a non-modified double-beam setup together with a system where the offsets of the beams were removed following their separation.

path together with mitigation strategies, the study follows chapter 7 in considering a complete acceleration procedure.

## 9.5 COMPLETE ACCELERATION RUN

The hosing mitigation strategies presented above resulted in a witness beam propagation exhibiting a smaller oscillation amplitude when compared to the non-modified case of two beams obtained using the simplified scraping mechanism. However, the considerations so far have been limited to the beam stability problem evident in the hosing regime and leading to growth in the beam-spot size and oscillation. To obtain a full picture of the acceleration process, together with the evolution of crucial quality parameters such as emittance and energy spread, the beam setup which uses a driver modified to be more conductive to hosing mitigation as discussed above, was introduced into the plasma stage with the aforementioned transition section and a plateau density of $n_p = 5.0 \times 10^{22}\,\mathrm{m}^{-3}$, as used in chapter 7.

Figure 9.11 shows the evolution of the energy, energy spread and normalized emittance for the PIC simulated acceleration process, both for the separated beams without any phase-space modifications and the configuration featuring a widened driver (with $k_p\sigma_r = 0.5$) showing an energy chirp of $\Delta\gamma = 2\,\%$. The witness beam reaches a final energy of $E \approx 1.5\,\mathrm{GeV}$, comparable to the results obtained in chapter 7. However, both the energy spread and emittance are not preserved, owing both to a non-optimal witness position with respect to the beam loading effect and its oscillation around the driver propagation axis. However, the slice quantities, presented in figures 9.12 to 9.13 are preserved over the acceleration distance, which might enable the application of the dechirping technique after the plasma.

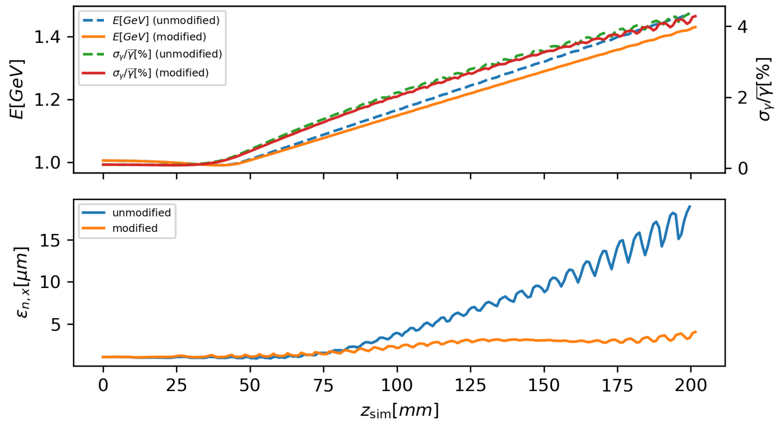


Figure 9.11: Evolution of the energy and energy spread (top) as well as the normalized rms emittance (bottom) of the beam configuration modified for hosing mitigation, together with the non-modified case. The energy gain is accompanied by a significant increase in the energy spread, which in turn contributes to the witness betatron decoherence, and consequent saturation of the emittance growth, as discussed in section 7.4. However, the growth is significantly damped in the modified case, mirroring the increased beam stability.

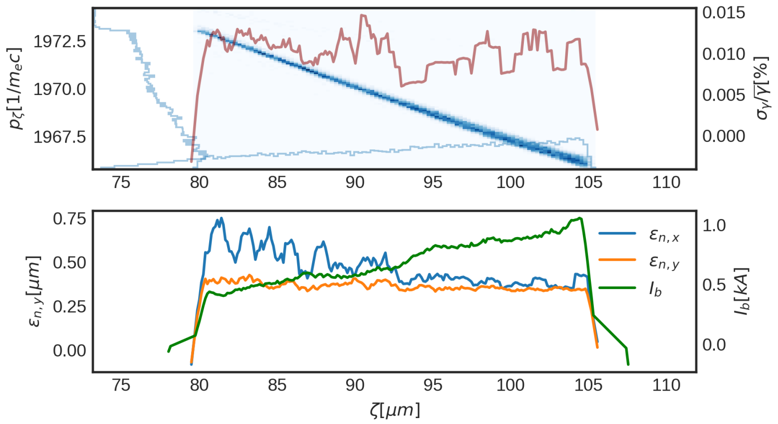


Figure 9.12: (Top plot) longitudinal phase-space distribution (blue, left-hand scale), together with axis histogram projections of the distribution (light blue lines) and slice energy spread (red line, right-hand scale) of the witness bunch. (Bottom plot) slice emittance in both transverse directions (left-hand scale) and witness bunch current profile (green line, right-hand scale). The beam is shown at the start of the simulation.

The plots shown in figures 9.11 to 9.13 can be seen the verification that the stabilization strategies applied can lead to successful acceleration of a preselected electron bunch trailing a modified driver. Further optimizations of the scraper position are clearly necessary to retain the advantageous energy spread and emittance values in line with

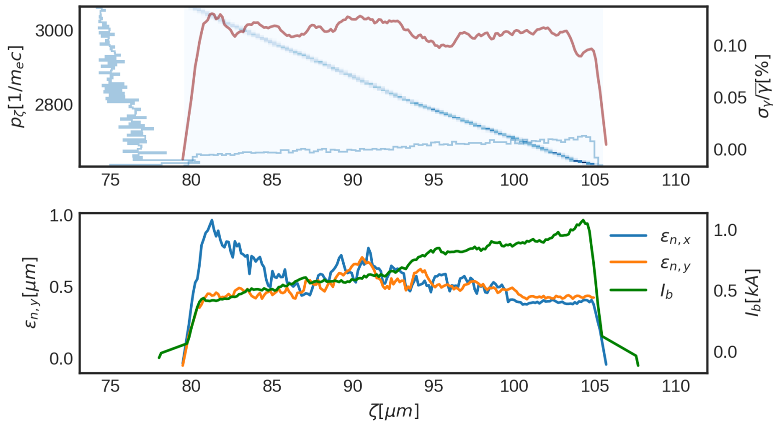


Figure 9.13: (Top plot) longitudinal phase-space distribution (blue, left-hand scale), together with axis histogram projections of the distribution (light blue lines) and slice energy spread (red line, right-hand scale) of the witness bunch. (Bottom plot) slice emittance in both transverse directions (left-hand scale) and witness bunch current profile (green line, right-hand scale). The beam is shown after a propagation distance of $z = 150\,\mathrm{mm}$ in plasma with $n_p = 5.0 \times 10^{22}\,\mathrm{m}^{-3}$ following the transition section introduced in previous sections.

observations presented in chapter 7. However, need to be considered not only in the perspective of a PIC simulation, but within the start-to-end framework as a whole. Instead of implementing the necessary phase-space modifications as numerical tools, the descriptions should incorporate the beam-line designs featuring the components necessary for the adequate preparation and tuning of the beam upstream, since the changes proposed are bound to introduce further deviations from the ideal symmetric picture.

## 9.6 CONCLUSION

The beam descriptions used in the previous chapters all followed common assumptions made when using numerical tools to probe the processes under investigation — a beam with a radial symmetry in the transverse domain, allowing for a straightforward description of its phase-space shape and the corresponding quality parameters. Even then, mechanisms such as mismatched parameters and longitudinal wakefield dependencies could lead to significant losses in beam quality and stability. However, the introduction of quasiparticle distributions obtained from tracking codes immediately uncovered a more problematic nature of the beam distributions expected at the plasma cell—clear phase-space asymmetries with potential higher-order correlations. While the beam moments and resulting beam parameters such as the beta function and emittance were well within the favorable conditions outlined in chapter 7, the particular shape of the beam-density distributions resulted in an unstable propagation once the beams entered the plasma, resulting in witness beam destabilization caused by the plasma wake coupling into the coherent driver oscillations. The observed behavior can be related to the hosing instability, which is seeded by the deviations from the ideal picture observed for more realistic beam distributions. Recent works such as [Lehe et al., 2017; Mehrling et al., 2017; Ossa, Mehrling, et al., 2018; Vieira et al., 2014] have provided potential mitigation strategies, some of which were explored in section 9.4, leading to promising results and showing improvements in beam stability over the initial, non-modified case. The corresponding implementations, however, would involve a more complex setup to allow for stable acceleration, potentially necessitating additional structures in the upstream beam-line sections (e.g. to defocus the driver). As such, the focus remains on the careful modification of the beam phase-space through iterative parameter adjustments in the beam-line description, since it had the biggest impact on beam stability, as evident in the comparison between the initial (e.g. figure 9.4) and retuned (e.g. figure 9.6) distributions. This approach points towards a promising optimization regime, which couples tracking code results with PIC simulations using the established framework.

# FINAL REMARKS

## SUMMARY

For all its extraordinary potential, the plasma-based acceleration technology still faces some challenges on the path toward first mainstream applications. Collision experiments and FEL undulators for synchrotron radiation generation have stringent requirements with respect to beam quality and stability, while the conventional beamline components upstream and downstream of the plasma interaction region place certain limits on the beam parameter range. These conditions need to be carefully navigated during the acceleration process of an externally injected witness bunch. Thankfully, the modern numerical methods and tools available help in probing potential parameter ranges and beam configurations, forming a solid basis for follow-up experiments. However, their theoretical picture can be expanded by both analytical descriptions of the beam moments evolution and consistent particle tracking simulations. Between these two aspects, the current work focused on the considerations revolving around the phase-space development of the witness beam in an external injection scenario and the necessary configurations enabling its effective acceleration, together with strategies aimed at subsequent corrections of its energy spread. Starting with the introduction of an analytic beam moment description in chapter 6, which helped motivate certain assumptions regarding the connection between the beam energy spread and emittance evolution, the work progressed toward a complete numerical description of the acceleration process assuming a preaccelerated beam with a certain parameter range, as discussed in chapter 7. The chapter focused on building a case for an efficient acceleration process with preserved beam-quality parameters, identifying crucial beam-plasma interaction mechanisms such as parameter matching and beam loading and employing numerical iterations based on theoretical considerations to identify optimal configurations. The specifics of the plasma wakefield can imprint a significant energy chirp on the witness. However, a beam driving the wakefield is subjected to a longitudinal gradient which can potentially reduce the resulting energy spread, given favorable plasma environments, a mitigation strategy known as dechirping. Chapter 8 introduced this technique and its potential limitations, before considering the parameter range of a proposed experiment at the ATF and presenting data taken from a successful demonstration at the FLASHForward facility, concluding with a test run involving the accelerated beam distribution obtained from the previous chapter. The capacity of the main numerical tool used in this work, HiPACE, to accept distributions obtained from either previous simulations or other numerical methods, was instrumental in chapter 9. This final chapter described a start-to-end simulation pipeline allowing for a more realistic treatment of the acceleration process taking into account the upstream beamline configuration and its impact on the beam distributions. Clear deviations from the idealized picture used for preceding analyses were identified, necessitating the introduction of potential mitigation strategies centered around the resulting hosing instability mechanism. The chapter concluded with a complete simulation of an external injection acceleration involving beam distributions obtained from a particle tracking code and modified for increased stabilization, showing promising results supporting the argument for further optimizations.

## CONCLUSION

The significant differences in the environments encountered by the proposed beam configurations, from the vacuum of a conventional beamline design to the ion channel in plasma into the focusing optics channel downstream, need to be carefully navigated to allow for successful acceleration and phase-space manipulation in external injection scenarios. Their theoretical description can be provided by multiple numerical and theoretical methods, each based on certain assumptions and accuracy requirements.

The analytic approach presented in chapter 6 could successfully reproduce the simulated behavior of a witness slice given certain plasma environment conditions, supporting conclusions derived in following chapters with respect to emittance development, its final value and the length scales required to reach it, especially given non-optimal matching conditions. Their role was one of the major aspects of the numerical analysis presented in chapter 7. Based on the advantageous properties of the low initial energy spread and the corresponding large decoherence length, the proposed solution to the significant difference between the initial and matched beta functions consisted of a tapered profile allowing for semi-adiabatic vacuum-to-plasma transition. However, the method relies on the preservation of the low energy spread to avoid shortening the decoherence length, leading to the next section introducing the beam loading mechanism. Starting with a single Gaussian beam distribution in six-dimensional phase-space, an idealized scraper could be shown to allow for near-optimal selection of a witness-driver configuration as subsets of the original bunch, allowing the energy spread growth to be suppressed sufficiently for emittance preservation. The chapter concluded with the demonstration of a complete simulation process, including a plasma-to-vacuum transition section exhibiting a wide range of acceptable scaling parameters tunable to the requirements of the downstream optics and diagnostics section.

Due to the large gradients, the wakefield structure can imprint the longitudinal phase-space of the witness with a significant energy chirp, a common result in all but the optimal current distributions allowing for perfect beam loading. Chapter 8 discussed a potential strategy meant to reverse such beam-quality degradation by using the chirped beam as a driver. Provided both the plasma density and the beam distribution can be combined into a favorable setup, which was the subject of the first section of the chapter, the simulations showed reductions in the projected energy spread, albeit at the cost of increased slice energy spread for all but the high-current beam configurations. The observations formed the basis for iterative preparations of a dechirping experiment planned at the ATF as well as a successful demonstration at the newly commissioned FLASHForward facility, with a section dedicated to a comparison of the data gathered at the latter and supporting PIC results. The chapter finally explored the dechirping potential of the beam produced in chapter 7, concluding that a plasma density similar to the acceleration region plateau value can lead to shifts in phase-space and a lower energy spread in the head sections of the distribution under consideration.

The last chapter of this work focused on more deviations from the idealized profiles used before, keeping with the theme of increasing accuracy and subsequent analysis of resulting instabilities, by introducing the results of particles tracked through the FLASH and FLASHForward beamlines using the ELEGANT code into the plasma environment. Despite promising initial beam parameters for the whole distribution, significant deviations from the symmetric picture after witness-driver separation using a simple scraping method could be observed. The initially presented configuration was then shown to eventually destabilize within the plasma stage, despite a near-optimal initial current configuration and resulting beam loading. A second beam distribution was subsequently introduced, optimized for better matching conditions in the tail section corresponding to the witness beam origin, yet still exhibiting instabilities within plasma. The chapter thus focused on potential hosing mitigation strategies, based on approaches and discussions presented in recent publications. Using a combination of driver defocusing to a transverse size of $k_p\sigma_{x,y} \approx 0.5$ and its prechirping to an energy spread of $\Delta\gamma = 2\%$ resulted in clear increases in stability in PIC simulations and lower emittance growth when compared to the non-modified case.

The present work considered the phase-space development of beams within the plasma acceleration environment for external injection scenarios. It discussed the constituent mechanisms and their impact while assembling complete descriptions of the procedure using analytic and numerical methods. While the process itself demands careful observation of many interacting components and attributes, from the beam line design to the plasma density and transitions, from the beam profiles to their transverse parameters, the results provide a sound foundation for the numerical and experimental domains on the path to the successful application of the ideas presented in this thesis.

## OUTLOOK

The results presented in this work were often demonstrated in the context of currently planned experiments and commissioned facilities, aiming to provide the theoretical context for their configurations. Their nature serves as an insightful representation of the current situation of plasma-based acceleration facing increasingly complex setups on its way to mainstream adoption. The promising initial experimental results confirming the extraordinary properties of this method provided the impetus behind new collaborations and experiments, fuelled by theoretical advances and improvements in numerical description methods. In the case of external injection, critical aspects of beam transport, injection and parameter preservation needed to be tackled not only in theory, but also in experiments. The latest results, such as the successful dechirping demonstration at FLASHForward [D'Arcy, 2018], are thus crucial milestones of a maturing technology, while new facilities presently going online ([Adli et al., 2018] and [Aschikhin et al., 2016]) or undergoing construction [Joshi et al., 2018] promise to offer the dedicated platforms for its full-scale realization. The optimizations performed in this work are thus mirrored by the progress within the field, focusing on narrowing down parameter ranges and configurations to enable the next generation of acceleration facilities, which could potentially provide the building blocks of scientific advances in such diverse fields as high-energy physics and drug research.

# Part IV

# APPENDIX

# A BEAM MOMENTS FOR BEAM SLICE WITH ENERGY GAIN

Starting from the solution to equation (6.13),

$$x(t) \simeq x_0 A(t)\cos[\varphi(t)] + \frac{p_{x,0}}{m_e\gamma_0\omega_{\beta,0}} A(t)\sin[\varphi(t)], \tag{A.1}$$

the single particle depiction is transferred into the distribution picture using the phase-advance approximation,

$$\varphi_d(t) = \int \omega_\beta \mathrm{d}t = \overline{\varphi}\left(1 - \frac{\delta\gamma}{2\overline{\gamma_0}}\frac{\overline{\omega_\beta}}{\overline{\omega_{\beta,0}}}\right), \tag{A.2}$$

with the quantities as provided in section 6.2.1. The momentum expression is found using $p_x(t) = m_e\gamma(t)x'(t)$ using the approximation

$$\omega_\beta(t) \simeq \overline{\omega_\beta}\left(1 - \frac{\delta_\gamma}{2\gamma(t)}\right), \tag{A.3}$$

giving

$$\begin{aligned} p_{x,d}(t) = p_{x,0}&\left(\frac{\gamma(t)A'(t)\sin(\varphi(t))}{\overline{\gamma_0\omega_{\beta,0}}} + \frac{A(t)\overline{\omega_\beta}\left(2\gamma(t)-\delta_\gamma\right)\cos(\varphi(t))}{2\overline{\gamma_0\omega_{\beta,0}}}\right) \\ &+ x_0\left(A(t)m_e\overline{\omega_\beta}\left(\delta_\gamma - 2\gamma(t)\right)\sin(\varphi(t)) + m_e\gamma(t)A'(t)\cos(\varphi(t))\right). \end{aligned} \tag{A.4}$$

Using the chosen energy distribution function $f_\gamma(\delta_\gamma) = \frac{1}{\sqrt{2\pi}\sigma_\gamma}e^{-\frac{\delta_\gamma^2}{2\sigma_\gamma^2}}$ with the rms energy spread $\sigma_\gamma$, allows to find the beam momenta as convolutions,

$$\langle x^2\rangle(t) = \int_{-\infty}^{\infty}(x^2(t))f_\gamma dx_0 dp_{x,0}d\delta_\gamma, \tag{A.5a}$$

$$\langle p_x^2\rangle(t) = \int_{-\infty}^{\infty}(p_x^2(t))f_\gamma dx_0 dp_{x,0}d\delta_\gamma, \tag{A.5b}$$

$$\langle xp_x\rangle(t) = \int_{-\infty}^{\infty}\left(x(t)p_x(t)\right)f_\gamma dx_0 dp_{x,0}d\delta_\gamma. \tag{A.5c}$$

Assuming the separability of the underlying phase-space distributions, a necessary condition outlined in chapter 6, yields the following depictions for the moments (unless indicated by an index, all quantities are time-dependent),

$$\begin{aligned}\langle x^2\rangle(t) = A(t)^2&\left(\frac{\langle p_x^2\rangle_0}{2\overline{\gamma_0}^2 m_e^2\overline{\omega_{\beta,0}}^2} + \frac{\langle x^2\rangle_0}{2}\right) + A(t)^2 e^{-\frac{\overline{\varphi}^2\sigma_\gamma^2\overline{\omega_\beta}^2}{2\overline{\gamma_0}^2\overline{\omega_{\beta,0}}^2}} \\ &\times\left(-\frac{\cos(2\overline{\varphi})\langle p_x^2\rangle_0}{2\overline{\gamma_0}^2 m_e^2\overline{\omega_{\beta,0}}^2} + \frac{\sin(2\overline{\varphi})\langle xp_x\rangle_0}{\overline{\gamma_0}m_e\overline{\omega_{\beta,0}}} + \frac{1}{2}\cos(2\overline{\varphi})\left\langle x^2\right\rangle_0\right)\end{aligned}$$

$$
\begin{aligned}
&\langle p_x^2\rangle(t)\\
&= \frac{\left(A^2\overline{\omega_\beta}^2\left(\sigma_\gamma^2+4\gamma^2\right)+4\gamma^2A'^2\right)\left(\overline{\gamma_0}^2m_e^2\left\langle x^2\right\rangle_0\overline{\omega_{\beta,0}}^2+\left\langle p_x^2\right\rangle_0\right)}{8\overline{\gamma_0}^2\overline{\omega_{\beta,0}}^2}+\frac{e^{-\frac{\overline{\varphi}^2\sigma_\gamma^2\overline{\omega_\beta}^2}{2\overline{\gamma_0}^2\overline{\omega_{\beta,0}}^2}}}{8\overline{\gamma_0}^4\overline{\omega_{\beta,0}}^4}\\
&\quad\times\Big(4\overline{\gamma_0}A\gamma\overline{\omega_\beta}A'\overline{\omega_{\beta,0}}\Big(\cos(2\overline{\varphi})\Big(\overline{\varphi}\sigma_\gamma^2\overline{\omega_\beta}\Big(\left\langle p_x^2\right\rangle_0-\overline{\gamma_0}^2m_e^2\left\langle x^2\right\rangle_0\overline{\omega_{\beta,0}}^2\Big)\\
&\quad+4\overline{\gamma_0}^2m_e\gamma\overline{\omega_{\beta,0}}^2\left\langle xp_x\right\rangle_0\Big)\\
&\quad-2\overline{\gamma_0}\sin(2\overline{\varphi})\overline{\omega_{\beta,0}}\Big(\gamma\Big(\overline{\gamma_0}^2m_e^2\left\langle x^2\right\rangle_0\overline{\omega_{\beta,0}}^2-\left\langle p_x^2\right\rangle_0\Big)+\overline{\varphi}\sigma_\gamma^2m_e\overline{\omega_\beta}\left\langle xp_x\right\rangle_0\Big)\Big)\\
&\quad+4\overline{\gamma_0}^2\gamma^2A'^2\overline{\omega_{\beta,0}}^2\Big(\cos(2\overline{\varphi})\Big(\overline{\gamma_0}^2m_e^2\left\langle x^2\right\rangle_0\overline{\omega_{\beta,0}}2-\left\langle p_x^2\right\rangle_0\Big)\\
&\quad+2\overline{\gamma_0}m_e\sin(2\overline{\varphi})\overline{\omega_{\beta,0}}\left\langle xp_x\right\rangle_0\Big)\\
&\quad+A^2\overline{\omega_\beta}^2\Big(4\overline{\gamma_0}\overline{\varphi}\sigma_\gamma^2\gamma\overline{\omega_\beta}\overline{\omega_{\beta,0}}\Big(\sin(2\overline{\varphi})\Big(\overline{\gamma_0}^2m_e^2\left\langle x^2\right\rangle_0\overline{\omega_{\beta,0}}^2-\left\langle p_x^2\right\rangle_0\Big)\\
&\quad-2\overline{\gamma_0}m_e\cos(2\overline{\varphi})\overline{\omega_{\beta,0}}\left\langle xp_x\right\rangle_0\Big)\\
&\quad-4\overline{\gamma_0}^2\gamma^2\overline{\omega_{\beta,0}}^2\Big(\cos(2\overline{\varphi})\Big(\overline{\gamma_0}^2m_e^2\left\langle x^2\right\rangle_0\overline{\omega_{\beta,0}}^2-\left\langle p_x^2\right\rangle_0\Big)\\
&\quad+2\overline{\gamma_0}m_e\sin(2\overline{\varphi})\overline{\omega_{\beta,0}}\left\langle xp_x\right\rangle_0\Big)\\
&\quad+\sigma_\gamma^2\Big(\overline{\varphi}^2\sigma_\gamma^2\overline{\omega_\beta}^2-\overline{\gamma_0}^2\overline{\omega_{\beta,0}}^2\Big)\Big(\cos(2\overline{\varphi})\Big(\overline{\gamma_0}^2m_e^2\left\langle x^2\right\rangle_0\overline{\omega_{\beta,0}}^2-\left\langle p_x^2\right\rangle_0\Big)\\
&\quad+2\overline{\gamma_0}m_e\sin(2\overline{\varphi})\overline{\omega_{\beta,0}}\left\langle xp_x\right\rangle_0\Big)\Big)\Big)
\end{aligned}
$$

$$
\begin{aligned}
\left\langle xp_x\right\rangle(t) &= \frac{A\gamma A'\left(\frac{\left\langle p_x^2\right\rangle_0}{\overline{\gamma_0}^2\overline{\omega_{\beta,0}}^2}+m_e^2\left\langle x^2\right\rangle_0\right)}{2m_e}+A\frac{e^{-\frac{\overline{\varphi}^2\sigma_\gamma^2\overline{\omega_\beta}^2}{2\overline{\gamma_0}^2\overline{\omega_{\beta,0}}^2}}}{4\overline{\gamma_0}^3m_e\overline{\omega_{\beta,0}}^3}\\
&\quad\times\Big(2\overline{\gamma_0}\gamma A'\overline{\omega_{\beta,0}}\Big(\cos(2\overline{\varphi})\Big(\overline{\gamma_0}^2m_e^2\left\langle x^2\right\rangle_0\overline{\omega_{\beta,0}}^2-\left\langle p_x^2\right\rangle_0\Big)\\
&\quad+2\overline{\gamma_0}m_e\sin(2\overline{\varphi})\overline{\omega_{\beta,0}}\left\langle xp_x\right\rangle_0\Big)\\
&\quad+A\overline{\omega_\beta}\times\Big(2\overline{\gamma_0}\gamma(t)\overline{\omega_{\beta,0}}\Big(\sin(2\overline{\varphi})\Big(\left\langle p_x^2\right\rangle_0-\overline{\gamma_0}^2m_e^2\left\langle x^2\right\rangle_0\overline{\omega_{\beta,0}}^2\Big)\\
&\quad+2\overline{\gamma_0}m_e\cos(2\overline{\varphi})\overline{\omega_{\beta,0}}\left\langle xp_x\right\rangle_0\Big)\\
&\quad+\overline{\varphi}\sigma_\gamma^2\overline{\omega_\beta}\Big(\cos(2\overline{\varphi})\Big(\left\langle p_x^2\right\rangle_0-\overline{\gamma_0}^2m_e^2\left\langle x^2\right\rangle_0\overline{\omega_{\beta,0}}^2\Big)\\
&\quad-2\overline{\gamma_0}m_e\sin(2\overline{\varphi})\overline{\omega_{\beta,0}}\left\langle xp_x\right\rangle_0\Big)\Big)\Big).
\end{aligned}
$$

Finally, the normalized emittance squared, based on

$$\epsilon_n=\frac{1}{m_ec}\sqrt{\langle x^2\rangle\langle p_x^2\rangle-\langle xp_x\rangle^2},$$

can be given using the new expressions as

$$
\begin{aligned}
\epsilon^2_{\mathrm{n,rms}}(t) = {} & \frac{A^4\overline{\omega_\beta}^2}{32c^2\overline{\gamma_0}^6\overline{\omega_{\beta,0}}^6 m_e^4} \\
& e^{-\frac{\overline{\varphi}^2\overline{\omega_\beta}^2\sigma_\gamma^2}{\overline{\gamma_0}^2\overline{\omega_{\beta,0}}^2}} \Bigg( -\cos\left(4\overline{\varphi}\right)\overline{\gamma_0}^6 m_e^4\sigma_\gamma^2 \left\langle x^2\right\rangle_0^2 \overline{\omega_{\beta,0}}^6 \\
& - \overline{\gamma_0}^6 m_e^4\sigma_\gamma^2 \left\langle x^2\right\rangle_0^2 \overline{\omega_{\beta,0}}^6 - 8\overline{\gamma_0}^6 m_e^4 \left\langle x^2\right\rangle_0^2 \gamma(t)^2\overline{\omega_{\beta,0}}^6 \\
& - 4\overline{\gamma_0}^5 \sin\left(4\overline{\varphi}\right) m_e^3\sigma_\gamma^2 \left\langle x^2\right\rangle_0 \left\langle xp_x\right\rangle_0 \overline{\omega_{\beta,0}}^5 \\
& - 8\overline{\gamma_0}^4 \sin^2\left(2\overline{\varphi}\right) m_e^2\sigma_\gamma^2 \left\langle xp_x\right\rangle_0^2 \overline{\omega_{\beta,0}}^4 \\
& - 32\overline{\gamma_0}^4 m_e^2 \left\langle xp_x\right\rangle_0^2 \gamma(t)^2\overline{\omega_{\beta,0}}^4 + 16\overline{\gamma_0}^4 m_e^2 \left\langle x^2\right\rangle_0 \left\langle p_x^2\right\rangle_0 \gamma(t)^2\overline{\omega_{\beta,0}}^4 \\
& + 2\cos\left(4\overline{\varphi}\right)\overline{\gamma_0}^4 m_e^2\sigma_\gamma^2 \left\langle x^2\right\rangle_0 \left\langle p_x^2\right\rangle_0 \overline{\omega_{\beta,0}}^4 \\
& + 2\overline{\gamma_0}^4 m_e^2\sigma_\gamma^2 \left\langle x^2\right\rangle_0 \left\langle p_x^2\right\rangle_0 \overline{\omega_{\beta,0}}^4 \\
& + 4\overline{\gamma_0}^3 \sin\left(4\overline{\varphi}\right) m_e\sigma_\gamma^2 \left\langle p_x^2\right\rangle_0 \left\langle xp_x\right\rangle_0 \overline{\omega_{\beta,0}}^3 \\
& - \cos\left(4\overline{\varphi}\right)\overline{\gamma_0}^2\sigma_\gamma^2 \left\langle p_x^2\right\rangle_0^2 \overline{\omega_{\beta,0}}^2 - \overline{\gamma_0}^2\sigma_\gamma^2 \left\langle p_x^2\right\rangle_0^2 \overline{\omega_{\beta,0}}^2 \\
& - 8\overline{\gamma_0}^2 \left\langle p_x^2\right\rangle_0^2 \gamma(t)^2\overline{\omega_{\beta,0}}^2 \\
& + 2e^{\frac{\overline{\varphi}^2\overline{\omega_\beta}^2\sigma_\gamma^2}{\overline{\gamma_0}^2\overline{\omega_{\beta,0}}^2}} \overline{\gamma_0}^2 \left(\overline{\gamma_0}^2\overline{\omega_{\beta,0}}^2 \left\langle x^2\right\rangle_0 m_e^2 + \left\langle p_x^2\right\rangle_0\right)^2 \left(\sigma_\gamma^2 + 4\gamma(t)^2\right)\overline{\omega_{\beta,0}}^2 \\
& + 2e^{\frac{\overline{\varphi}^2\overline{\omega_\beta}^2\sigma_\gamma^2}{2\overline{\gamma_0}^2\overline{\omega_{\beta,0}}^2}} \overline{\varphi\omega_\beta}\sigma_\gamma^2 \left(\overline{\gamma_0}^2\overline{\omega_{\beta,0}}^2 \left\langle x^2\right\rangle_0 m_e^2\right. \\
& \left. + \left\langle p_x^2\right\rangle_0\right) \left(\overline{\varphi\omega_\beta}\left(\cos\left(2\overline{\varphi}\right)\left(\overline{\gamma_0}^2\overline{\omega_{\beta,0}}^2 m_e^2 \left\langle x^2\right\rangle_0 - \left\langle p_x^2\right\rangle_0\right)\right.\right. \\
& \left. + 2\overline{\gamma_0\omega_{\beta,0}} \sin\left(2\overline{\varphi}\right) m_e \left\langle xp_x\right\rangle_0\right)\sigma_\gamma^2 \\
& + 4\overline{\gamma_0\omega_{\beta,0}}\left(\sin\left(2\overline{\varphi}\right)\left(\overline{\gamma_0}^2\overline{\omega_{\beta,0}}^2 m_e^2 \left\langle x^2\right\rangle_0 - \left\langle p_x^2\right\rangle_0\right)\right. \\
& \left.\left. - 2\cos\left(2\overline{\varphi}\right)\overline{\gamma_0\omega_{\beta,0}} m_e \left\langle xp_x\right\rangle_0\right)\gamma(t)\right)\Bigg)
\end{aligned}
$$

It should be noted that the amplitude term only describes the slice energy average evolution, allowing it to be carried through the integration, which can then be done in a relatively straightforward way using the analytical code *Mathematica*. A path incorporating the full amplitude energy dependency in the convolution and leading to the beam moment description could not be identified in the context of this work. This approximation might help explain the slight deviations in the emittance evolution when compared with semi-numerical methods and PIC simulations as seen in chapter 6.

# B

# SIMULATION PARAMETERS

| Simulation Parameters | | Driver Parameters | |
|---|---|---|---|
| $k_p\Delta\zeta$ | 0.0073 | $n_b/n_p$ | 4.000 |
| $k_p\Delta x$ | 0.0098 | $k_p\bar{\zeta}$ | 0.000 |
| $k_p\Delta y$ | 0.0098 | $k_p\bar{x}$ | 0.000 |
| $k_pL_\zeta$ | 15.0000 | $k_p\bar{y}$ | 0.000 |
| $k_pL_x$ | 10.0000 | $k_p\sigma_\zeta$ | 0.500 |
| $k_pL_y$ | 10.0000 | $k_p\sigma_x$ | 0.800 |
| **Plasma Parameters** | | $k_p\sigma_y$ | 0.800 |
| | | $k_p\epsilon_x$ | 0.100 |
| $n_p[\mathrm{cm}^{-3}]$ | $1.0 \times 10^{17}$ | $k_p\epsilon_y$ | 0.100 |
| $k_p^{-1}[\mu\mathrm{m}]$ | 16.805 | $\gamma$ | 2000.000 |
| $E_0[\mathrm{GeV}]$ | 30.408 | $\Delta\gamma[\%]$ | 0.100 |
| $n/n_p(z)$ | 1.0 | | |

Table B.1: PIC Simulation Parameters used for Figure 2.3

| Simulation Parameters | | Driver Parameters | | Witness Parameters | |
|---|---|---|---|---|---|
| $k_p\Delta\zeta$ | 0.0098 | $n_b/n_p$ | 28.500 | $n_b/n_p$ | 0.001 |
| $k_p\Delta x$ | 0.0156 | $k_p\bar{\zeta}$ | 7.600 | $k_p\bar{\zeta}$ | 5.500 |
| $k_p\Delta y$ | 0.0156 | $k_p\bar{x}$ | 0.000 | $k_p\bar{x}$ | 0.000 |
| $k_pL_\zeta$ | 10.0000 | $k_p\bar{y}$ | 0.000 | $k_p\bar{y}$ | 0.000 |
| $k_pL_x$ | 8.0000 | $k_p\sigma_\zeta$ | 0.594 | $k_p\sigma_\zeta$ | 0.000 |
| $k_pL_y$ | 8.0000 | $k_p\sigma_x$ | 0.110 | $k_p\sigma_x$ | 0.300 |
| **Plasma Parameters** | | $k_p\sigma_y$ | 0.110 | $k_p\sigma_y$ | 0.300 |
| | | $k_p\epsilon_x$ | 0.100 | $k_p\epsilon_x$ | 0.120 |
| $n_p[\mathrm{cm}^{-3}]$ | $1.0 \times 10^{17}$ | $k_p\epsilon_y$ | 0.100 | $k_p\epsilon_y$ | 0.120 |
| $k_p^{-1}[\mu\mathrm{m}]$ | 16.805 | $\gamma$ | 2000.000 | $\gamma$ | 2000.000 |
| $E_0[\mathrm{GeV}]$ | 30.408 | $\Delta\gamma[\%]$ | 0.100 | $\Delta\gamma[\%]$ | 10.000 |
| $n/n_p(z)$ | 1.0 | | | | |

Table B.2: PIC Simulation Parameters used for Figures 6.1 to 6.4

| Simulation Parameters | | Driver Parameters | | Witness Parameters | |
|---|---|---|---|---|---|
| $k_p\Delta\zeta$ | 0.0098 | $n_b/n_p$ | 28.500 | $n_b/n_p$ | 0.001 |
| $k_p\Delta x$ | 0.0156 | $k_p\bar{\zeta}$ | 7.600 | $k_p\bar{\zeta}$ | 4.200 |
| $k_p\Delta y$ | 0.0156 | $k_p\bar{x}$ | 0.000 | $k_p\bar{x}$ | 0.000 |
| $k_pL_\zeta$ | 10.0000 | $k_p\bar{y}$ | 0.000 | $k_p\bar{y}$ | 0.000 |
| $k_pL_x$ | 8.0000 | $k_p\sigma_\zeta$ | 0.594 | $k_p\sigma_\zeta$ | 0.000 |
| $k_pL_y$ | 8.0000 | $k_p\sigma_x$ | 0.110 | $k_p\sigma_x$ | 0.300 |
| Plasma Parameters | | $k_p\sigma_y$ | 0.110 | $k_p\sigma_y$ | 0.300 |
| | | $k_p\epsilon_x$ | 0.100 | $k_p\epsilon_x$ | 0.120 |
| $n_p[\mathrm{cm}^{-3}]$ | $1.0 \times 10^{17}$ | $k_p\epsilon_y$ | 0.100 | $k_p\epsilon_y$ | 0.120 |
| $k_p^{-1}[\mu\mathrm{m}]$ | 16.805 | $\gamma$ | 2000.000 | $\gamma$ | 2000.000 |
| $E_0[\mathrm{GeV}]$ | 30.408 | $\Delta\gamma[\%]$ | 0.100 | $\Delta\gamma[\%]$ | 10.000 |
| $n/n_p(z)$ | 1.0 | | | | |

Table B.3: PIC Simulation Parameters used for Figures 6.5 to 6.8

| Simulation Parameters | | Driver Parameters | | Witness Parameters | |
|---|---|---|---|---|---|
| $k_p\Delta\zeta$ | 0.0049 | $n_b/n_p$ | 4.000 | $n_b/n_p$ | 4.000 |
| $k_p\Delta x$ | 0.0156 | $k_p\bar{\zeta}$ | 8.000 | $k_p\bar{\zeta}$ | 5.000 |
| $k_p\Delta y$ | 0.0156 | $k_p\bar{x}$ | 0.000 | $k_p\bar{x}$ | 0.000 |
| $k_pL_\zeta$ | 10.0000 | $k_p\bar{y}$ | 0.000 | $k_p\bar{y}$ | 0.000 |
| $k_pL_x$ | 8.0000 | $k_p\sigma_\zeta$ | 1.000 | $k_p\sigma_\zeta$ | 0.300 |
| $k_pL_y$ | 8.0000 | $k_p\sigma_x$ | 0.133 | $k_p\sigma_x$ | 0.133 |
| Plasma Parameters | | $k_p\sigma_y$ | 0.133 | $k_p\sigma_y$ | 0.133 |
| | | $k_p\epsilon_x$ | 0.084 | $k_p\epsilon_x$ | 0.084 |
| $n_p[\mathrm{cm}^{-3}]$ | $5.0 \times 10^{16}$ | $k_p\epsilon_y$ | 0.084 | $k_p\epsilon_y$ | 0.084 |
| $k_p^{-1}[\mu\mathrm{m}]$ | 23.765 | $\gamma$ | 2000.000 | $\gamma$ | 2000.000 |
| $E_0[\mathrm{GeV}]$ | 21.502 | $\Delta\gamma[\%]$ | 0.100 | $\Delta\gamma[\%]$ | 0.100 |
| $n/n_p(z)$ | 1.0 | | | | |

Table B.4: PIC Simulation Parameters used for Figures 7.1 to 7.7

| Simulation Parameters | | Driver Parameters | | Witness Parameters | |
|---|---|---|---|---|---|
| $k_p\Delta\zeta$ | 0.0049 | $n_b/n_p$ | 4.000 | $n_b/n_p$ | 4.000 |
| $k_p\Delta x$ | 0.0195 | $k_p\bar{\zeta}$ | 7.000 | $k_p\bar{\zeta}$ | 4.000 |
| $k_p\Delta y$ | 0.0195 | $k_p\bar{x}$ | 0.000 | $k_p\bar{x}$ | 0.000 |
| $k_pL_\zeta$ | 10.0000 | $k_p\bar{y}$ | 0.000 | $k_p\bar{y}$ | 0.000 |
| $k_pL_x$ | 10.0000 | $k_p\sigma_\zeta$ | 1.000 | $k_p\sigma_\zeta$ | 0.300 |
| $k_pL_y$ | 10.0000 | $k_p\sigma_x$ | 0.133 | $k_p\sigma_x$ | 0.133 |
| Plasma Parameters | | $k_p\sigma_y$ | 0.133 | $k_p\sigma_y$ | 0.133 |
| | | $k_p\epsilon_x$ | 0.084 | $k_p\epsilon_x$ | 0.084 |
| $n_p[\mathrm{cm}^{-3}]$ | $5.0 \times 10^{16}$ | $k_p\epsilon_y$ | 0.084 | $k_p\epsilon_y$ | 0.084 |
| $k_p^{-1}[\mu\mathrm{m}]$ | 23.765 | $\gamma$ | 2000.000 | $\gamma$ | 2000.000 |
| $E_0[\mathrm{GeV}]$ | 21.502 | $\Delta\gamma[\%]$ | 0.100 | $\Delta\gamma[\%]$ | 0.100 |
| $n/n_p(z)$ | f (z) | | | | |

Table B.5: PIC Simulation Parameters used for Figure 7.3

| Simulation Parameters | | Driver Parameters | | Witness Parameters | |
|---|---|---|---|---|---|
| $k_p\Delta\zeta$ | 0.0049 | $n_b/n_p$ | 4.000 | $n_b/n_p$ | 4.000 |
| $k_p\Delta x$ | 0.0195 | $k_p\bar{\zeta}$ | 7.000 | $k_p\bar{\zeta}$ | 4.000 |
| $k_p\Delta y$ | 0.0195 | $k_p\bar{x}$ | 0.000 | $k_p\bar{x}$ | 0.000 |
| $k_pL_\zeta$ | 10.0000 | $k_p\bar{y}$ | 0.000 | $k_p\bar{y}$ | 0.000 |
| $k_pL_x$ | 10.0000 | $k_p\sigma_\zeta$ | 1.000 | $k_p\sigma_\zeta$ | 0.300 |
| $k_pL_y$ | 10.0000 | $k_p\sigma_x$ | 0.133 | $k_p\sigma_x$ | 0.133 |
| Plasma Parameters | | $k_p\sigma_y$ | 0.133 | $k_p\sigma_y$ | 0.133 |
| | | $k_p\epsilon_x$ | 0.084 | $k_p\epsilon_x$ | 0.084 |
| $n_p[\mathrm{cm}^{-3}]$ | $5.0 \times 10^{16}$ | $k_p\epsilon_y$ | 0.084 | $k_p\epsilon_y$ | 0.084 |
| $k_p^{-1}[\mu\mathrm{m}]$ | 23.765 | $\gamma$ | 2000.000 | $\gamma$ | 2000.000 |
| $E_0[\mathrm{GeV}]$ | 21.502 | $\Delta\gamma[\%]$ | 0.100 | $\Delta\gamma[\%]$ | 0.100 |
| $n/n_p(z)$ | f (z) | | | | |

Table B.6: PIC Simulation Parameters used for Figure 7.4

| Simulation Parameters | | Driver Parameters | | Witness Parameters | |
|---|---|---|---|---|---|
| $k_p\Delta\zeta$ | 0.0049 | $n_b/n_p$ | 4.000 | $n_b/n_p$ | 4.000 |
| $k_p\Delta x$ | 0.0195 | $k_p\bar{\zeta}$ | 7.000 | $k_p\bar{\zeta}$ | 4.000 |
| $k_p\Delta y$ | 0.0195 | $k_p\bar{x}$ | 0.000 | $k_p\bar{x}$ | 0.000 |
| $k_pL_\zeta$ | 10.0000 | $k_p\bar{y}$ | 0.000 | $k_p\bar{y}$ | 0.000 |
| $k_pL_x$ | 10.0000 | $k_p\sigma_\zeta$ | 1.000 | $k_p\sigma_\zeta$ | 0.300 |
| $k_pL_y$ | 10.0000 | $k_p\sigma_x$ | 0.133 | $k_p\sigma_x$ | 0.133 |
| Plasma Parameters | | $k_p\sigma_y$ | 0.133 | $k_p\sigma_y$ | 0.133 |
| | | $k_p\epsilon_x$ | 0.084 | $k_p\epsilon_x$ | 0.084 |
| $n_p[\mathrm{cm}^{-3}]$ | $5.0 \times 10^{16}$ | $k_p\epsilon_y$ | 0.084 | $k_p\epsilon_y$ | 0.084 |
| $k_p^{-1}[\mu\mathrm{m}]$ | 23.765 | $\gamma$ | 2000.000 | $\gamma$ | 2000.000 |
| $E_0[\mathrm{GeV}]$ | 21.502 | $\Delta\gamma[\%]$ | 0.100 | $\Delta\gamma[\%]$ | $[0.100 - 10.000]$ |
| $n/n_p(z)$ | f (z) | | | | |

Table B.7: PIC Simulation Parameters used for Figure 7.5

| Simulation Parameters | | Driver Parameters | | Witness Parameters | |
|---|---|---|---|---|---|
| $k_p\Delta\zeta$ | 0.0049 | $n_b/n_p$ | 4.000 | $n_b/n_p$ | 4.000 |
| $k_p\Delta x$ | 0.0195 | $k_p\bar{\zeta}$ | 7.000 | $k_p\bar{\zeta}$ | 4.000 |
| $k_p\Delta y$ | 0.0195 | $k_p\bar{x}$ | 0.000 | $k_p\bar{x}$ | 0.000 |
| $k_pL_\zeta$ | 10.0000 | $k_p\bar{y}$ | 0.000 | $k_p\bar{y}$ | 0.000 |
| $k_pL_x$ | 10.0000 | $k_p\sigma_\zeta$ | 1.000 | $k_p\sigma_\zeta$ | 0.300 |
| $k_pL_y$ | 10.0000 | $k_p\sigma_x$ | 0.133 | $k_p\sigma_x$ | 0.133 |
| Plasma Parameters | | $k_p\sigma_y$ | 0.133 | $k_p\sigma_y$ | 0.133 |
| | | $k_p\epsilon_x$ | 0.084 | $k_p\epsilon_x$ | 0.084 |
| $n_p[\mathrm{cm}^{-3}]$ | $5.0 \times 10^{16}$ | $k_p\epsilon_y$ | 0.084 | $k_p\epsilon_y$ | 0.084 |
| $k_p^{-1}[\mu\mathrm{m}]$ | 23.765 | $\gamma$ | 2000.000 | $\gamma$ | 2000.000 |
| $E_0[\mathrm{GeV}]$ | 21.502 | $\Delta\gamma[\%]$ | 0.100 | $\Delta\gamma[\%]$ | 0.100 |
| $n/n_p(z)$ | f (z) | | | | |

Table B.8: PIC Simulation Parameters used for Figure 7.6

| Simulation Parameters | | Driver Parameters | | Witness Parameters | |
|---|---|---|---|---|---|
| $k_p\Delta\zeta$ | 0.0049 | $n_b/n_p$ | 5.000 | $n_b/n_p$ | 5.000 |
| $k_p\Delta x$ | 0.0195 | $k_p\bar{\zeta}$ | 7.000 | $k_p\bar{\zeta}$ | 3.500 |
| $k_p\Delta y$ | 0.0195 | $k_p\bar{x}$ | 0.000 | $k_p\bar{x}$ | 0.000 |
| $k_pL_\zeta$ | 10.0000 | $k_p\bar{y}$ | 0.000 | $k_p\bar{y}$ | 0.000 |
| $k_pL_x$ | 10.0000 | $k_p\sigma_\zeta$ | 1.000 | $k_p\sigma_\zeta$ | 0.300 |
| $k_pL_y$ | 10.0000 | $k_p\sigma_x$ | 0.200 | $k_p\sigma_x$ | 0.200 |
| **Plasma Parameters** | | $k_p\sigma_y$ | 0.200 | $k_p\sigma_y$ | 0.200 |
| $n_p[\mathrm{cm}^{-3}]$ | $5.0 \times 10^{16}$ | $k_p\epsilon_x$ | 0.100 | $k_p\epsilon_x$ | 0.100 |
| $k_p^{-1}[\mu\mathrm{m}]$ | 23.765 | $k_p\epsilon_y$ | 0.100 | $k_p\epsilon_y$ | 0.100 |
| $E_0[\mathrm{GeV}]$ | 21.502 | $\gamma$ | 2000.000 | $\gamma$ | 2000.000 |
| $n/n_p(z)$ | 1.0 | $\Delta\gamma[\%]$ | 0.100 | $\Delta\gamma[\%]$ | 0.100 |

Table B.9: PIC Simulation Parameters used for Figure 7.8

| Simulation Parameters | | Driver Parameters | | Witness Parameters | |
|---|---|---|---|---|---|
| $k_p\Delta\zeta$ | 0.0049 | $n_b/n_0(\zeta)$ | $f(\zeta)$ | $n_b/n_0(\zeta)$ | $f(\zeta)$ |
| $k_p\Delta x$ | 0.0195 | $k_p\zeta_0$ | 6.000 | $k_p\zeta_0$ | [3.100 – 3.500] |
| $k_p\Delta y$ | 0.0195 | $k_p\zeta_1$ | 10.000 | $k_p\zeta_1$ | [3.500 – 4.000] |
| $k_pL_\zeta$ | 10.0000 | $k_p\bar{x}$ | 0.000 | $k_p\bar{x}$ | 0.000 |
| $k_pL_x$ | 10.0000 | $k_p\bar{y}$ | 0.000 | $k_p\bar{y}$ | 0.000 |
| $k_pL_y$ | 10.0000 | $k_p\sigma_x$ | 0.133 | $k_p\sigma_x$ | 0.133 |
| **Plasma Parameters** | | $k_p\sigma_y$ | 0.133 | $k_p\sigma_y$ | 0.133 |
| $n_p[\mathrm{cm}^{-3}]$ | $5.0 \times 10^{16}$ | $k_p\epsilon_x$ | 0.084 | $k_p\epsilon_x$ | 0.084 |
| $k_p^{-1}[\mu\mathrm{m}]$ | 23.765 | $k_p\epsilon_y$ | 0.084 | $k_p\epsilon_y$ | 0.084 |
| $E_0[\mathrm{GeV}]$ | 21.502 | $\gamma$ | 2000.000 | $\gamma$ | 2000.000 |
| $n/n_p(z)$ | 1.0 | $\Delta\gamma[\%]$ | 0.100 | $\Delta\gamma[\%]$ | 0.100 |

Table B.10: PIC Simulation Parameters used for Figure 7.9

| Simulation Parameters | | Driver Parameters | | Witness Parameters | |
|---|---|---|---|---|---|
| $k_p\Delta\zeta$ | 0.0049 | $n_b/n_0(\zeta)$ | $f(\zeta)$ | $n_b/n_0(\zeta)$ | $f(\zeta)$ |
| $k_p\Delta x$ | 0.0195 | $k_p\zeta_0$ | [5.800 – 10.000] | $k_p\zeta_0$ | [2.800 – 3.800] |
| $k_p\Delta y$ | 0.0195 | $k_p\zeta_1$ | [6.000 – 10.000] | $k_p\zeta_1$ | [3.000 – 4.000] |
| $k_pL_\zeta$ | 10.0000 | $k_p\bar{x}$ | 0.000 | $k_p\bar{x}$ | 0.000 |
| $k_pL_x$ | 10.0000 | $k_p\bar{y}$ | 0.000 | $k_p\bar{y}$ | 0.000 |
| $k_pL_y$ | 10.0000 | $k_p\sigma_x$ | 0.133 | $k_p\sigma_x$ | 0.133 |
| **Plasma Parameters** | | $k_p\sigma_y$ | 0.133 | $k_p\sigma_y$ | 0.133 |
| $n_p[\mathrm{cm}^{-3}]$ | $5.0 \times 10^{16}$ | $k_p\epsilon_x$ | 0.084 | $k_p\epsilon_x$ | 0.084 |
| $k_p^{-1}[\mu\mathrm{m}]$ | 23.765 | $k_p\epsilon_y$ | 0.084 | $k_p\epsilon_y$ | 0.084 |
| $E_0[\mathrm{GeV}]$ | 21.502 | $\gamma$ | 2000.000 | $\gamma$ | 2000.000 |
| $n/n_p(z)$ | 1.0 | $\Delta\gamma[\%]$ | 0.100 | $\Delta\gamma[\%]$ | 0.100 |

Table B.11: PIC Simulation Parameters used for Figure 7.10

| Simulation Parameters | |
|---|---|
| $k_p\Delta\zeta$ | 0.0049 |
| $k_p\Delta x$ | 0.0156 |
| $k_p\Delta y$ | 0.0156 |
| $k_pL_\zeta$ | 10.0000 |
| $k_pL_x$ | 8.0000 |
| $k_pL_y$ | 8.0000 |
| **Plasma Parameters** | |
| $n_p[\mathrm{cm}^{-3}]$ | $5.0 \times 10^{16}$ |
| $k_p^{-1}[\mu\mathrm{m}]$ | 23.765 |
| $E_0[\mathrm{GeV}]$ | 21.502 |
| $n/n_p(z)$ | f (z) |

| Driver Parameters | |
|---|---|
| $n_b/n_0(\zeta)$ | $f(\zeta)$ |
| $k_p\zeta_0$ | 6.700 |
| $k_p\zeta_1$ | 10.000 |
| $k_p\bar{x}$ | 0.000 |
| $k_p\bar{y}$ | 0.000 |
| $k_p\sigma_x$ | 0.133 |
| $k_p\sigma_y$ | 0.133 |
| $k_p\epsilon_x$ | 0.084 |
| $k_p\epsilon_y$ | 0.084 |
| $\gamma$ | 2000.000 |
| $\Delta\gamma[\%]$ | 0.100 |

| Witness Parameters | |
|---|---|
| $n_b/n_0(\zeta)$ | $f(\zeta)$ |
| $k_p\zeta_0$ | 3.800 |
| $k_p\zeta_1$ | 4.800 |
| $k_p\bar{x}$ | 0.000 |
| $k_p\bar{y}$ | 0.000 |
| $k_p\sigma_x$ | 0.133 |
| $k_p\sigma_y$ | 0.133 |
| $k_p\epsilon_x$ | 0.084 |
| $k_p\epsilon_y$ | 0.084 |
| $\gamma$ | 2000.000 |
| $\Delta\gamma[\%]$ | 0.100 |

Table B.12: PIC Simulation Parameters used for Figures 7.11 to 7.12

| Simulation Parameters | |
|---|---|
| $k_p\Delta\zeta$ | 0.0049 |
| $k_p\Delta x$ | 0.0156 |
| $k_p\Delta y$ | 0.0156 |
| $k_pL_\zeta$ | 10.0000 |
| $k_pL_x$ | 8.0000 |
| $k_pL_y$ | 8.0000 |
| **Plasma Parameters** | |
| $n_p[\mathrm{cm}^{-3}]$ | $1.0 \times 10^{17}$ |
| $k_p^{-1}[\mu\mathrm{m}]$ | 16.805 |
| $E_0[\mathrm{GeV}]$ | 30.408 |
| $n/n_p(z)$ | 1.0 |

| Driver Parameters | |
|---|---|
| $n_b/n_0(\zeta)$ | $f(\zeta)$ |
| $k_p\zeta_0$ | 7.000 |
| $k_p\zeta_1$ | 10.000 |
| $k_p\bar{x}$ | 0.000 |
| $k_p\bar{y}$ | 0.000 |
| $k_p\sigma_x$ | 0.188 |
| $k_p\sigma_y$ | 0.188 |
| $k_p\epsilon_x$ | 0.119 |
| $k_p\epsilon_y$ | 0.119 |
| $\gamma$ | 2000.000 |
| $\Delta\gamma[\%]$ | 0.100 |

| Witness Parameters | |
|---|---|
| $n_b/n_0(\zeta)$ | $f(\zeta)$ |
| $k_p\zeta_0$ | 4.100 |
| $k_p\zeta_1$ | 4.600 |
| $k_p\bar{x}$ | 0.000 |
| $k_p\bar{y}$ | 0.000 |
| $k_p\sigma_x$ | 0.188 |
| $k_p\sigma_y$ | 0.188 |
| $k_p\epsilon_x$ | 0.119 |
| $k_p\epsilon_y$ | 0.119 |
| $\gamma$ | 2000.000 |
| $\Delta\gamma[\%]$ | 0.100 |

Table B.13: PIC Simulation Parameters used for Figure 7.17

| Simulation Parameters | |
|---|---|
| $k_p\Delta\zeta$ | 0.0049 |
| $k_p\Delta x$ | 0.0156 |
| $k_p\Delta y$ | 0.0156 |
| $k_pL_\zeta$ | 10.0000 |
| $k_pL_x$ | 8.0000 |
| $k_pL_y$ | 8.0000 |
| **Plasma Parameters** | |
| $n_p[\mathrm{cm}^{-3}]$ | $5.0 \times 10^{16}$ |
| $k_p^{-1}[\mu\mathrm{m}]$ | 23.765 |
| $E_0[\mathrm{GeV}]$ | 21.502 |
| $n/n_p(z)$ | f (z) |

| Driver Parameters | |
|---|---|
| $n_b/n_0(\zeta)$ | $f(\zeta)$ |
| $k_p\zeta_0$ | 6.700 |
| $k_p\zeta_1$ | 10.000 |
| $k_p\bar{x}$ | 0.000 |
| $k_p\bar{y}$ | 0.000 |
| $k_p\sigma_x$ | 0.133 |
| $k_p\sigma_y$ | 0.133 |
| $k_p\epsilon_x$ | 0.084 |
| $k_p\epsilon_y$ | 0.084 |
| $\gamma$ | 2000.000 |
| $\Delta\gamma[\%]$ | 0.100 |

| Witness Parameters | |
|---|---|
| $n_b/n_0(\zeta)$ | $f(\zeta)$ |
| $k_p\zeta_0$ | 3.800 |
| $k_p\zeta_1$ | 4.800 |
| $k_p\bar{x}$ | 0.000 |
| $k_p\bar{y}$ | 0.000 |
| $k_p\sigma_x$ | 0.133 |
| $k_p\sigma_y$ | 0.133 |
| $k_p\epsilon_x$ | 0.084 |
| $k_p\epsilon_y$ | 0.084 |
| $\gamma$ | 2000.000 |
| $\Delta\gamma[\%]$ | 0.100 |

Table B.14: PIC Simulation Parameters used for Figures 7.13 to 7.15

| Simulation Parameters | | Driver Parameters | | Witness Parameters | |
|---|---|---|---|---|---|
| $k_p\Delta\zeta$ | 0.0049 | Source | HiPACE | Source | HiPACE |
| $k_p\Delta x$ | 0.0156 | $k_p\bar{\zeta}$ | 7.744 | $k_p\bar{\zeta}$ | 4.348 |
| $k_p\Delta y$ | 0.0156 | $k_p\bar{x}$ | $-0.008$ | $k_p\bar{x}$ | $-0.020$ |
| $k_pL_\zeta$ | 10.0000 | $k_p\bar{y}$ | $-0.007$ | $k_p\bar{y}$ | $-0.002$ |
| $k_pL_x$ | 8.0000 | $k_p\sigma_\zeta$ | 0.775 | $k_p\sigma_\zeta$ | 0.285 |
| $k_pL_y$ | 8.0000 | $k_p\sigma_x$ | 0.287 | $k_p\sigma_x$ | 0.056 |
| Plasma Parameters | | $k_p\sigma_y$ | 0.286 | $k_p\sigma_y$ | 0.055 |
| | | $k_p\epsilon_x$ | 0.397 | $k_p\epsilon_x$ | 0.094 |
| $n_p[\mathrm{cm}^{-3}]$ | $5.0 \times 10^{16}$ | $k_p\epsilon_y$ | 0.395 | $k_p\epsilon_y$ | 0.086 |
| $k_p^{-1}[\mu\mathrm{m}]$ | 23.765 | $\bar{\gamma}$ | 1387.860 | $\bar{\gamma}$ | 2813.008 |
| $E_0[\mathrm{GeV}]$ | 21.502 | $\Delta\gamma[\%]$ | 25263.137 | $\Delta\gamma[\%]$ | 617.483 |
| $n/n_p(z)$ | f (z) | | | | |

Table B.15: PIC Simulation Parameters used for Figure 7.16

| Simulation Parameters | | Driver Parameters | | Witness Parameters | |
|---|---|---|---|---|---|
| $k_p\Delta\zeta$ | 0.0049 | $n_b/n_0(\zeta)$ | $f(\zeta)$ | $n_b/n_0(\zeta)$ | $f(\zeta)$ |
| $k_p\Delta x$ | 0.0156 | $k_p\zeta_0$ | 7.000 | $k_p\zeta_0$ | 4.100 |
| $k_p\Delta y$ | 0.0156 | $k_p\zeta_1$ | 10.000 | $k_p\zeta_1$ | 4.600 |
| $k_pL_\zeta$ | 10.0000 | $k_p\bar{x}$ | 0.000 | $k_p\bar{x}$ | 0.000 |
| $k_pL_x$ | 8.0000 | $k_p\bar{y}$ | 0.000 | $k_p\bar{y}$ | 0.000 |
| $k_pL_y$ | 8.0000 | $k_p\sigma_x$ | 0.188 | $k_p\sigma_x$ | 0.188 |
| Plasma Parameters | | $k_p\sigma_y$ | 0.188 | $k_p\sigma_y$ | 0.188 |
| | | $k_p\epsilon_x$ | 0.119 | $k_p\epsilon_x$ | 0.119 |
| $n_p[\mathrm{cm}^{-3}]$ | $5.0 \times 10^{16}$ | $k_p\epsilon_y$ | 0.119 | $k_p\epsilon_y$ | 0.119 |
| $k_p^{-1}[\mu\mathrm{m}]$ | 23.765 | $\gamma$ | 2000.000 | $\gamma$ | 2000.000 |
| $E_0[\mathrm{GeV}]$ | 21.502 | $\Delta\gamma[\%]$ | 0.100 | $\Delta\gamma[\%]$ | 0.100 |
| $n/n_p(z)$ | f (z) | | | | |

Table B.16: PIC Simulation Parameters used for Figures 7.18 to 7.20

| Simulation Parameters | | Driver Parameters | | Witness Parameters | |
|---|---|---|---|---|---|
| $k_p\Delta\zeta$ | 0.0049 | $n_b/n_p$ | 10.000 | $n_b/n_p$ | 1.500 |
| $k_p\Delta x$ | 0.0312 | $k_p\bar{\zeta}$ | 7.000 | $k_p\bar{\zeta}$ | 4.200 |
| $k_p\Delta y$ | 0.0312 | $k_p\bar{x}$ | 0.000 | $k_p\bar{x}$ | 0.000 |
| $k_pL_\zeta$ | 10.0000 | $k_p\bar{y}$ | 0.000 | $k_p\bar{y}$ | 0.000 |
| $k_pL_x$ | 16.0000 | $k_p\sigma_\zeta$ | 0.282 | $k_p\sigma_\zeta$ | 0.282 |
| $k_pL_y$ | 16.0000 | $k_p\sigma_x$ | 0.094 | $k_p\sigma_x$ | 0.094 |
| Plasma Parameters | | $k_p\sigma_y$ | 0.094 | $k_p\sigma_y$ | 0.094 |
| | | $k_p\epsilon_x$ | 0.002 | $k_p\epsilon_x$ | 0.002 |
| $n_p[\mathrm{cm}^{-3}]$ | $1.0 \times 10^{14}$ | $k_p\epsilon_y$ | 0.002 | $k_p\epsilon_y$ | 0.002 |
| $k_p^{-1}[\mu\mathrm{m}]$ | 531.409 | $\gamma$ | 112.720 | $\gamma$ | 112.720 |
| $E_0[\mathrm{GeV}]$ | 0.962 | $\Delta\gamma[\%]$ | 0.100 | $\Delta\gamma[\%]$ | 0.100 |
| $n/n_p(z)$ | 1.0 | | | | |

Table B.17: PIC Simulation Parameters used for Figures 8.1 to 8.2

| Simulation Parameters | | Driver Parameters | |
|---|---|---|---|
| $k_p\Delta\zeta$ | 0.0049 | $n_b/n_p$ | [0.200 – 2.000] |
| $k_p\Delta x$ | 0.0078 | $k_p\bar{\zeta}$ | 4.000 |
| $k_p\Delta y$ | 0.0078 | $k_p\bar{x}$ | 0.000 |
| $k_pL_\zeta$ | 5.0000 | $k_p\bar{y}$ | 0.000 |
| $k_pL_x$ | 4.0000 | $k_p\sigma_\zeta$ | 0.200 |
| $k_pL_y$ | 4.0000 | $k_p\sigma_x$ | 0.250 |
| **Plasma Parameters** | | $k_p\sigma_y$ | 0.250 |
| | | $k_p\epsilon_x$ | 0.002 |
| $n_p[\mathrm{cm}^{-3}]$ | $1.0\times10^{14}$ | $k_p\epsilon_y$ | 0.002 |
| $k_p^{-1}[\mu\mathrm{m}]$ | 531.409 | $\gamma$ | 112.720 |
| $E_0[\mathrm{GeV}]$ | 0.962 | $\Delta\gamma[\%]$ | 0.100 |
| $n/n_p(z)$ | 1.0 | | |

Table B.18: PIC Simulation Parameters used for Figures 8.3 to 8.4

| Simulation Parameters | | Driver Parameters | |
|---|---|---|---|
| $k_p\Delta\zeta$ | 0.0049 | $n_b/n_p$ | 10.000 |
| $k_p\Delta x$ | 0.0156 | $k_p\bar{\zeta}$ | 4.000 |
| $k_p\Delta y$ | 0.0156 | $k_p\bar{x}$ | 0.000 |
| $k_pL_\zeta$ | 5.0000 | $k_p\bar{y}$ | 0.000 |
| $k_pL_x$ | 8.0000 | $k_p\sigma_\zeta$ | 0.200 |
| $k_pL_y$ | 8.0000 | $k_p\sigma_x$ | 0.100 |
| **Plasma Parameters** | | $k_p\sigma_y$ | 0.100 |
| | | $k_p\epsilon_x$ | 0.100 |
| $n_p[\mathrm{cm}^{-3}]$ | $1.0\times10^{16}$ | $k_p\epsilon_y$ | 0.100 |
| $k_p^{-1}[\mu\mathrm{m}]$ | 53.141 | $\gamma$ | 1000.000 |
| $E_0[\mathrm{GeV}]$ | 9.616 | $\Delta\gamma[\%]$ | 0.100 |
| $n/n_p(z)$ | 1.0 | | |

Table B.19: PIC Simulation Parameters used for Figure 8.5

| Simulation Parameters | | Driver Parameters | |
|---|---|---|---|
| $k_p\Delta\zeta$ | 0.0049 | Source | HiPACE |
| $k_p\Delta x$ | 0.0195 | $k_p\bar{\zeta}$ | 4.145 |
| $k_p\Delta y$ | 0.0195 | $k_p\bar{x}$ | −0.000 |
| $k_pL_\zeta$ | 5.0000 | $k_p\bar{y}$ | −0.000 |
| $k_pL_x$ | 10.0000 | $k_p\sigma_\zeta$ | 0.100 |
| $k_pL_y$ | 10.0000 | $k_p\sigma_x$ | 0.100 |
| **Plasma Parameters** | | $k_p\sigma_y$ | 0.100 |
| | | $k_p\epsilon_x$ | 0.100 |
| $n_p[\mathrm{cm}^{-3}]$ | $1.0\times10^{16}$ | $k_p\epsilon_y$ | 0.100 |
| $k_p^{-1}[\mu\mathrm{m}]$ | 53.141 | $\bar{\gamma}$ | 984.575 |
| $E_0[\mathrm{GeV}]$ | 9.616 | $\Delta\gamma[\%]$ | 967.041 |
| $n/n_p(z)$ | 1.0 | | |

Table B.20: PIC Simulation Parameters used for Figures 8.6 to 8.7

| Simulation Parameters | | Driver Parameters | |
|---|---|---|---|
| $k_p\Delta\zeta$ | 0.0059 | $n_b/n_p$ | [63.407 – 0.634] |
| $k_p\Delta x$ | 0.0156 | $k_p\overline{\zeta}$ | 5.000 |
| $k_p\Delta y$ | 0.0156 | $k_p\overline{x}$ | 0.000 |
| $k_pL_\zeta$ | 6.0000 | $k_p\overline{y}$ | 0.000 |
| $k_pL_x$ | 4.0000 | $k_p\sigma_\zeta$ | [0.018 – 0.179] |
| $k_pL_y$ | 4.0000 | $k_p\sigma_x$ | [0.030 – 0.298] |
| **Plasma Parameters** | | $k_p\sigma_y$ | [0.030 – 0.298] |
| $n_p[\mathrm{cm}^{-3}]$ | $1.0\times10^{13} - 5.0\times10^{15}$ | $k_p\epsilon_x$ | [0.001 – 0.006] |
| $k_p^{-1}[\mu\mathrm{m}]$ | 1680.464 – 75.153 | $k_p\epsilon_y$ | [0.001 – 0.006] |
| $E_0$[GeV] | 0.304 – 6.799 | $\gamma$ | 112.720 |
| $n/n_p(z)$ | 1.0 | $\Delta\gamma[\%]$ | 0.100 |

Table B.21: PIC Simulation Parameters used for Figures 8.8 to 8.19

| Simulation Parameters | | Driver Parameters | |
|---|---|---|---|
| $k_p\Delta\zeta$ | 0.0059 | $n_b/n_p$ | [39.630 – 0.619] |
| $k_p\Delta x$ | 0.0156 | $k_p\overline{\zeta}$ | 5.000 |
| $k_p\Delta y$ | 0.0156 | $k_p\overline{x}$ | 0.000 |
| $k_pL_\zeta$ | 6.0000 | $k_p\overline{y}$ | 0.000 |
| $k_pL_x$ | 4.0000 | $k_p\sigma_\zeta$ | [0.113 – 0.113] |
| $k_pL_y$ | 4.0000 | $k_p\sigma_x$ | [0.038 – 0.301] |
| **Plasma Parameters** | | $k_p\sigma_y$ | [0.038 – 0.301] |
| $n_p[\mathrm{cm}^{-3}]$ | $4.0\times10^{14}$ | $k_p\epsilon_x$ | [0.004 – 0.004] |
| $k_p^{-1}[\mu\mathrm{m}]$ | 265.705 | $k_p\epsilon_y$ | [0.004 – 0.004] |
| $E_0$[GeV] | 1.923 | $\gamma$ | [112.720 – 112.720] |
| $n/n_p(z)$ | 1.0 | $\Delta\gamma[\%]$ | 0.100 |

Table B.22: PIC Simulation Parameters used for Figure 8.9

| Simulation Parameters | | Driver Parameters | |
|---|---|---|---|
| $k_p\Delta\zeta$ | 0.0059 | $n_b/n_p$ | [3.440 – 1.204] |
| $k_p\Delta x$ | 0.0156 | $k_p\overline{\zeta}$ | 5.000 |
| $k_p\Delta y$ | 0.0156 | $k_p\overline{x}$ | 0.000 |
| $k_pL_\zeta$ | 6.0000 | $k_p\overline{y}$ | 0.000 |
| $k_pL_x$ | 4.0000 | $k_p\sigma_\zeta$ | [0.196 – 0.196] |
| $k_pL_y$ | 4.0000 | $k_p\sigma_x$ | [0.130 – 0.261] |
| **Plasma Parameters** | | $k_p\sigma_y$ | [0.130 – 0.261] |
| $n_p[\mathrm{cm}^{-3}]$ | $3.0\times10^{14} - 3.0\times10^{14}$ | $k_p\epsilon_x$ | [0.003 – 0.003] |
| $k_p^{-1}[\mu\mathrm{m}]$ | 306.809 – 306.809 | $k_p\epsilon_y$ | [0.003 – 0.003] |
| $E_0$[GeV] | 1.666 – 1.666 | $\gamma$ | [140.000 – 140.000] |
| $n/n_p(z)$ | 1.0 | $\Delta\gamma[\%]$ | 0.100 |

Table B.23: PIC Simulation Parameters used for Figures 8.10 to 8.12

| Simulation Parameters | | Witness Parameters | |
|---|---|---|---|
| $k_p\Delta\zeta$ | 0.0035 | Source | HiPACE |
| $k_p\Delta x$ | 0.0110 | $k_p\overline{\zeta}$ | 3.080 |
| $k_p\Delta y$ | 0.0110 | $k_p\overline{x}$ | $-0.011$ |
| $k_pL_\zeta$ | 7.0711 | $k_p\overline{y}$ | $-0.008$ |
| $k_pL_x$ | 5.6569 | $k_p\sigma_\zeta$ | 0.102 |
| $k_pL_y$ | 5.6569 | $k_p\sigma_x$ | 0.044 |
| **Plasma Parameters** | | $k_p\sigma_y$ | 0.044 |
| $n_p[\mathrm{cm}^{-3}]$ | $5.0 \times 10^{16}$ | $k_p\epsilon_x$ | 0.085 |
| $k_p^{-1}[\mu\mathrm{m}]$ | 23.765 | $k_p\epsilon_y$ | 0.084 |
| $E_0[\mathrm{GeV}]$ | 21.502 | $\overline{\gamma}$ | 3885.496 |
| $n/n_p(z)$ | 1.0 | $\Delta\gamma[\%]$ | 776.762 |

Table B.24: PIC Simulation Parameters used for Figures 8.14 to 8.15

| Simulation Parameters | | Driver Parameters | |
|---|---|---|---|
| $k_p\Delta\zeta$ | [0.0098 – 0.0098] | $n_b/n_p$ | [157.360 – 0.393] |
| $k_p\Delta x$ | [0.0007 – 0.0139] | $k_p\overline{\zeta}$ | 6.000 |
| $k_p\Delta y$ | [0.0007 – 0.0139] | $k_p\overline{x}$ | 0.000 |
| $k_pL_\zeta$ | [10.0000 – 10.0000] | $k_p\overline{y}$ | 0.000 |
| $k_pL_x$ | [0.3570 – 7.1408] | $k_p\sigma_\zeta$ | [0.037 – 0.749] |
| $k_pL_y$ | [0.3570 – 7.1408] | $k_p\sigma_x$ | [0.012 – 0.238] |
| **Plasma Parameters** | | $k_p\sigma_y$ | [0.036 – 0.714] |
| $n_p[\mathrm{cm}^{-3}]$ | $1.0 \times 10^{13} - 4.0 \times 10^{15}$ | $k_p\epsilon_x$ | [0.001 – 0.024] |
| $k_p^{-1}[\mu\mathrm{m}]$ | 1680.464 – 84.023 | $k_p\epsilon_y$ | [0.001 – 0.024] |
| $E_0[\mathrm{GeV}]$ | 0.304 – 6.082 | $\gamma$ | [1386.000 – 1386.000] |
| $n/n_p(z)$ | 1.0 | $\Delta\gamma[\%]$ | 0.100 |

Table B.25: PIC Simulation Parameters used for Figures 8.13 to 8.21

| Simulation Parameters | | Driver Parameters | |
|---|---|---|---|
| $k_p\Delta\zeta$ | 0.0117 | $n_b/n_p$ | [1585.200 – 15.852] |
| $k_p\Delta x$ | 0.0156 | $k_p\overline{\zeta}$ | 5.000 |
| $k_p\Delta y$ | 0.0156 | $k_p\overline{x}$ | 0.000 |
| $k_pL_\zeta$ | 6.0000 | $k_p\overline{y}$ | 0.000 |
| $k_pL_x$ | 4.0000 | $k_p\sigma_\zeta$ | [0.018 – 0.179] |
| $k_pL_y$ | 4.0000 | $k_p\sigma_x$ | [0.006 – 0.060] |
| **Plasma Parameters** | | $k_p\sigma_y$ | [0.006 – 0.060] |
| $n_p[\mathrm{cm}^{-3}]$ | $1.0 \times 10^{13} - 1.0 \times 10^{15}$ | $k_p\epsilon_x$ | [0.001 – 0.012] |
| $k_p^{-1}[\mu\mathrm{m}]$ | 1680.464 – 168.046 | $k_p\epsilon_y$ | [0.001 – 0.012] |
| $E_0[\mathrm{GeV}]$ | 0.304 – 3.041 | $\gamma$ | [112.720 – 112.720] |
| $n/n_p(z)$ | 1.0 | $\Delta\gamma[\%]$ | 0.100 |

Table B.26: PIC Simulation Parameters used for Figure 8.20

| Simulation Parameters | | Driver Parameters | |
|---|---|---|---|
| $k_p\Delta\zeta$ | 0.0195 | $n_b/n_p$ | [209.810 – 69.938] |
| $k_p\Delta x$ | 0.0156 | $k_p\overline{\zeta}$ | 6.000 |
| $k_p\Delta y$ | 0.0156 | $k_p\overline{x}$ | 0.000 |
| $k_pL_\zeta$ | 10.0000 | $k_p\overline{y}$ | 0.000 |
| $k_pL_x$ | 4.0000 | $k_p\sigma_\zeta$ | [0.375 – 0.649] |
| $k_pL_y$ | 4.0000 | $k_p\sigma_x$ | [0.018 – 0.031] |
| **Plasma Parameters** | | $k_p\sigma_y$ | [0.018 – 0.031] |
| $n_p[\mathrm{cm}^{-3}]$ | $1.0 \times 10^{15} - 3.0 \times 10^{15}$ | $k_p\epsilon_x$ | [0.012 – 0.021] |
| $k_p^{-1}[\mu\mathrm{m}]$ | 168.046 – 97.022 | $k_p\epsilon_y$ | [0.012 – 0.021] |
| $E_0$[GeV] | 3.041 – 5.267 | $\gamma$ | [1386.000 – 1386.000] |
| $n/n_p(z)$ | 1.0 | $\Delta\gamma[\%]$ | 0.100 |

Table B.27: PIC Simulation Parameters used for Figure 8.22

| Simulation Parameters | | Electron Parameters | |
|---|---|---|---|
| $k_p\Delta\zeta$ | 0.0098 | Source | ELEGANT |
| $k_p\Delta x$ | 0.0156 | $k_p\overline{\zeta}$ | [4.862 – 6.876] |
| $k_p\Delta y$ | 0.0156 | $k_p\overline{x}$ | [−0.159 – −0.225] |
| $k_pL_\zeta$ | 20.0000 | $k_p\overline{y}$ | [−0.001 – −0.001] |
| $k_pL_x$ | 8.0000 | $k_p\sigma_\zeta$ | [1.543 – 2.182] |
| $k_pL_y$ | 8.0000 | $k_p\sigma_x$ | [0.414 – 0.586] |
| **Plasma Parameters** | | $k_p\sigma_y$ | [0.072 – 0.102] |
| | | $k_p\epsilon_x$ | [0.217 – 0.307] |
| $n_p[\mathrm{cm}^{-3}]$ | $5.0 \times 10^{16}$ | $k_p\epsilon_y$ | [0.053 – 0.075] |
| $k_p^{-1}[\mu\mathrm{m}]$ | 23.765 | $\overline{\gamma}$ | [1962.592 – 1962.592] |
| $E_0$[GeV] | 21.502 | $\Delta\gamma[\%]$ | [442.411 – 442.411] |
| $n/n_p(z)$ | 1.0 | | |

Table B.28: PIC Simulation Parameters used for Figures 9.1 to 9.2

| Simulation Parameters | | Driver Parameters | | Witness Parameters | |
|---|---|---|---|---|---|
| $k_p\Delta\zeta$ | 0.0098 | Source | ELEGANT | Source | ELEGANT |
| $k_p\Delta x$ | 0.0312 | $k_p\overline{\zeta}$ | [6.036 – 6.721] | $k_p\overline{\zeta}$ | [2.405 – 3.448] |
| $k_p\Delta y$ | 0.0312 | $k_p\overline{x}$ | [−0.280 – −0.437] | $k_p\overline{x}$ | [0.091 – −0.056] |
| $k_pL_\zeta$ | 10.0000 | $k_p\overline{y}$ | [0.019 – 0.026] | $k_p\overline{y}$ | [−0.025 – −0.034] |
| $k_pL_x$ | 16.0000 | $k_p\sigma_\zeta$ | [0.962 – 0.679] | $k_p\sigma_\zeta$ | [0.363 – 0.356] |
| $k_pL_y$ | 16.0000 | $k_p\sigma_x$ | [0.496 – 0.564] | $k_p\sigma_x$ | [0.223 – 0.092] |
| **Plasma Parameters** | | $k_p\sigma_y$ | [0.076 – 0.063] | $k_p\sigma_y$ | [0.060 – 0.042] |
| | | $k_p\epsilon_x$ | [0.119 – 0.119] | $k_p\epsilon_x$ | [0.120 – 0.028] |
| $n_p[\mathrm{cm}^{-3}]$ | $5.0 \times 10^{16}$ | $k_p\epsilon_y$ | [0.059 – 0.058] | $k_p\epsilon_y$ | [0.029 – 0.027] |
| $k_p^{-1}[\mu\mathrm{m}]$ | 23.765 | $\overline{\gamma}$ | [1959.471 – 1958.051] | $\overline{\gamma}$ | [1971.305 – 1966.089] |
| $E_0$[GeV] | 21.502 | $\Delta\gamma[\%]$ | [210.848 – 168.588] | $\Delta\gamma[\%]$ | [203.688 – 161.588] |
| $n/n_p(z)$ | 1.0 | | | | |

Table B.29: PIC Simulation Parameters used for Figure 9.3

| Simulation Parameters | | Driver Parameters | | Witness Parameters | |
|---|---|---|---|---|---|
| $k_p\Delta\zeta$ | 0.0098 | Source | ELEGANT | Source | ELEGANT |
| $k_p\Delta x$ | 0.0312 | $k_p\overline{\zeta}$ | 7.310 | $k_p\overline{\zeta}$ | 3.970 |
| $k_p\Delta y$ | 0.0312 | $k_p\overline{x}$ | $-0.296$ | $k_p\overline{x}$ | $-0.004$ |
| $k_pL_\zeta$ | 10.0000 | $k_p\overline{y}$ | $-0.004$ | $k_p\overline{y}$ | $-0.024$ |
| $k_pL_x$ | 16.0000 | $k_p\sigma_\zeta$ | 0.817 | $k_p\sigma_\zeta$ | 0.296 |
| $k_pL_y$ | 16.0000 | $k_p\sigma_x$ | 0.382 | $k_p\sigma_x$ | 0.148 |
| **Plasma Parameters** | | $k_p\sigma_y$ | 0.135 | $k_p\sigma_y$ | 0.048 |
| | | $k_p\epsilon_x$ | 0.105 | $k_p\epsilon_x$ | 0.054 |
| $n_p[\text{cm}^{-3}]$ | $5.0\times10^{16}$ | $k_p\epsilon_y$ | 0.068 | $k_p\epsilon_y$ | 0.028 |
| $k_p^{-1}[\mu\text{m}]$ | 23.765 | $\overline{\gamma}$ | 1958.728 | $\overline{\gamma}$ | 1968.960 |
| $E_0$[GeV] | 21.502 | $\Delta\gamma[\%]$ | 180.074 | $\Delta\gamma[\%]$ | 200.407 |
| $n/n_p(z)$ | f (z) | | | | |

Table B.30: PIC Simulation Parameters used for Figures 9.5 to 9.6

| Simulation Parameters | | Driver Parameters | | Witness Parameters | |
|---|---|---|---|---|---|
| $k_p\Delta\zeta$ | 0.0098 | Source | ELEGANT | Source | ELEGANT |
| $k_p\Delta x$ | 0.0312 | $k_p\overline{\zeta}$ | [7.310 – 7.310] | $k_p\overline{\zeta}$ | [3.970 – 3.970] |
| $k_p\Delta y$ | 0.0312 | $k_p\overline{x}$ | [$-0.296$ – $-0.296$] | $k_p\overline{x}$ | [$-0.004$ – $-0.004$] |
| $k_pL_\zeta$ | 10.0000 | $k_p\overline{y}$ | [$-0.004$ – $-0.004$] | $k_p\overline{y}$ | [$-0.024$ – $-0.024$] |
| $k_pL_x$ | 16.0000 | $k_p\sigma_\zeta$ | [0.817 – 0.817] | $k_p\sigma_\zeta$ | [0.296 – 0.296] |
| $k_pL_y$ | 16.0000 | $k_p\sigma_x$ | [0.501 – 0.993] | $k_p\sigma_x$ | [0.148 – 0.148] |
| **Plasma Parameters** | | $k_p\sigma_y$ | [0.501 – 1.002] | $k_p\sigma_y$ | [0.048 – 0.048] |
| | | $k_p\epsilon_x$ | [0.138 – 0.274] | $k_p\epsilon_x$ | [0.054 – 0.054] |
| $n_p[\text{cm}^{-3}]$ | $5.0\times10^{16}$ | $k_p\epsilon_y$ | [0.252 – 0.503] | $k_p\epsilon_y$ | [0.028 – 0.028] |
| $k_p^{-1}[\mu\text{m}]$ | 23.765 | $\overline{\gamma}$ | [1958.728 – 1958.728] | $\overline{\gamma}$ | [1968.960 – 1968.960] |
| $E_0$[GeV] | 21.502 | $\Delta\gamma[\%]$ | [180.074 – 180.074] | $\Delta\gamma[\%]$ | [200.407 – 200.407] |
| $n/n_p(z)$ | f (z) | | | | |

Table B.31: PIC Simulation Parameters used for Figure 9.7

| Simulation Parameters | | Driver Parameters | | Witness Parameters | |
|---|---|---|---|---|---|
| $k_p\Delta\zeta$ | 0.0098 | Source | ELEGANT | Source | ELEGANT |
| $k_p\Delta x$ | 0.0312 | $k_p\overline{\zeta}$ | [7.310 – 7.310] | $k_p\overline{\zeta}$ | [3.970 – 3.970] |
| $k_p\Delta y$ | 0.0312 | $k_p\overline{x}$ | [$-0.296$ – $-0.296$] | $k_p\overline{x}$ | [$-0.004$ – $-0.004$] |
| $k_pL_\zeta$ | 10.0000 | $k_p\overline{y}$ | [$-0.004$ – $-0.004$] | $k_p\overline{y}$ | [$-0.024$ – $-0.024$] |
| $k_pL_x$ | 16.0000 | $k_p\sigma_\zeta$ | [0.817 – 0.817] | $k_p\sigma_\zeta$ | [0.296 – 0.296] |
| $k_pL_y$ | 16.0000 | $k_p\sigma_x$ | [0.382 – 0.382] | $k_p\sigma_x$ | [0.148 – 0.148] |
| **Plasma Parameters** | | $k_p\sigma_y$ | [0.135 – 0.135] | $k_p\sigma_y$ | [0.048 – 0.048] |
| | | $k_p\epsilon_x$ | [0.105 – 0.105] | $k_p\epsilon_x$ | [0.054 – 0.054] |
| $n_p[\text{cm}^{-3}]$ | $5.0\times10^{16}$ | $k_p\epsilon_y$ | [0.068 – 0.068] | $k_p\epsilon_y$ | [0.028 – 0.028] |
| $k_p^{-1}[\mu\text{m}]$ | 23.765 | $\overline{\gamma}$ | [1958.728 – 1958.728] | $\overline{\gamma}$ | [1968.960 – 1968.960] |
| $E_0$[GeV] | 21.502 | $\Delta\gamma[\%]$ | [1148.954 – 19755.109] | $\Delta\gamma[\%]$ | [200.407 – 200.407] |
| $n/n_p(z)$ | f (z) | | | | |

Table B.32: PIC Simulation Parameters used for Figure 9.8

| Simulation Parameters | |
|---|---|
| $k_p\Delta\zeta$ | 0.0098 |
| $k_p\Delta x$ | 0.0312 |
| $k_p\Delta y$ | 0.0312 |
| $k_pL_\zeta$ | 10.0000 |
| $k_pL_x$ | 16.0000 |
| $k_pL_y$ | 16.0000 |

| Plasma Parameters | |
|---|---|
| $n_p[\mathrm{cm}^{-3}]$ | $5.0 \times 10^{16}$ |
| $k_p^{-1}[\mu\mathrm{m}]$ | 23.765 |
| $E_0$[GeV] | 21.502 |
| $n/n_p(z)$ | f (z) |

| Driver Parameters | |
|---|---|
| Source | ELEGANT |
| $k_p\overline{\zeta}$ | [7.310 – 7.310] |
| $k_p\overline{x}$ | [−0.296 – −0.296] |
| $k_p\overline{y}$ | [−0.004 – −0.004] |
| $k_p\sigma_\zeta$ | [0.817 – 0.817] |
| $k_p\sigma_x$ | [0.501 – 0.501] |
| $k_p\sigma_y$ | [0.501 – 0.501] |
| $k_p\epsilon_x$ | [0.138 – 0.138] |
| $k_p\epsilon_y$ | [0.252 – 0.252] |
| $\overline{\gamma}$ | [1958.728 – 1958.728] |
| $\Delta\gamma[\%]$ | [4085.700 – 19755.109] |

| Witness Parameters | |
|---|---|
| Source | ELEGANT |
| $k_p\overline{\zeta}$ | [3.970 – 3.970] |
| $k_p\overline{x}$ | [−0.004 – −0.004] |
| $k_p\overline{y}$ | [−0.024 – −0.024] |
| $k_p\sigma_\zeta$ | [0.296 – 0.296] |
| $k_p\sigma_x$ | [0.148 – 0.148] |
| $k_p\sigma_y$ | [0.048 – 0.048] |
| $k_p\epsilon_x$ | [0.054 – 0.054] |
| $k_p\epsilon_y$ | [0.028 – 0.028] |
| $\overline{\gamma}$ | [1968.960 – 1968.960] |
| $\Delta\gamma[\%]$ | [200.407 – 200.407] |

Table B.33: PIC Simulation Parameters used for Figure 9.9

| Simulation Parameters | |
|---|---|
| $k_p\Delta\zeta$ | 0.0098 |
| $k_p\Delta x$ | 0.0312 |
| $k_p\Delta y$ | 0.0312 |
| $k_pL_\zeta$ | 10.0000 |
| $k_pL_x$ | 16.0000 |
| $k_pL_y$ | 16.0000 |

| Plasma Parameters | |
|---|---|
| $n_p[\mathrm{cm}^{-3}]$ | $5.0 \times 10^{16}$ |
| $k_p^{-1}[\mu\mathrm{m}]$ | 23.765 |
| $E_0$[GeV] | 21.502 |
| $n/n_p(z)$ | f (z) |

| Driver Parameters | |
|---|---|
| Source | ELEGANT |
| $k_p\overline{\zeta}$ | 7.310 |
| $k_p\overline{x}$ | −0.000 |
| $k_p\overline{y}$ | 0.000 |
| $k_p\sigma_\zeta$ | 0.817 |
| $k_p\sigma_x$ | 0.382 |
| $k_p\sigma_y$ | 0.135 |
| $k_p\epsilon_x$ | 0.105 |
| $k_p\epsilon_y$ | 0.068 |
| $\overline{\gamma}$ | 1958.728 |
| $\Delta\gamma[\%]$ | 180.074 |

| Witness Parameters | |
|---|---|
| Source | ELEGANT |
| $k_p\overline{\zeta}$ | 3.970 |
| $k_p\overline{x}$ | 0.000 |
| $k_p\overline{y}$ | −0.000 |
| $k_p\sigma_\zeta$ | 0.296 |
| $k_p\sigma_x$ | 0.148 |
| $k_p\sigma_y$ | 0.048 |
| $k_p\epsilon_x$ | 0.054 |
| $k_p\epsilon_y$ | 0.028 |
| $\overline{\gamma}$ | 1968.960 |
| $\Delta\gamma[\%]$ | 200.407 |

Table B.34: PIC Simulation Parameters used for Figure 9.10

| Simulation Parameters | |
|---|---|
| $k_p\Delta\zeta$ | 0.0098 |
| $k_p\Delta x$ | 0.0391 |
| $k_p\Delta y$ | 0.0391 |
| $k_pL_\zeta$ | 10.0000 |
| $k_pL_x$ | 20.0000 |
| $k_pL_y$ | 20.0000 |

| Plasma Parameters | |
|---|---|
| $n_p[\mathrm{cm}^{-3}]$ | $5.0 \times 10^{16}$ |
| $k_p^{-1}[\mu\mathrm{m}]$ | 23.765 |
| $E_0$[GeV] | 21.502 |
| $n/n_p(z)$ | f (z) |

| Driver Parameters | |
|---|---|
| Source | ELEGANT |
| $k_p\overline{\zeta}$ | 6.452 |
| $k_p\overline{x}$ | −0.364 |
| $k_p\overline{y}$ | 0.024 |
| $k_p\sigma_\zeta$ | 0.794 |
| $k_p\sigma_x$ | 0.539 |
| $k_p\sigma_y$ | 0.069 |
| $k_p\epsilon_x$ | 0.120 |
| $k_p\epsilon_y$ | 0.059 |
| $\overline{\gamma}$ | 1958.631 |
| $\Delta\gamma[\%]$ | 187.126 |

| Witness Parameters | |
|---|---|
| Source | ELEGANT |
| $k_p\overline{\zeta}$ | 2.940 |
| $k_p\overline{x}$ | 0.025 |
| $k_p\overline{y}$ | −0.030 |
| $k_p\sigma_\zeta$ | 0.621 |
| $k_p\sigma_x$ | 0.259 |
| $k_p\sigma_y$ | 0.047 |
| $k_p\epsilon_x$ | 0.133 |
| $k_p\epsilon_y$ | 0.029 |
| $\overline{\gamma}$ | 1968.587 |
| $\Delta\gamma[\%]$ | 316.158 |

Table B.35: PIC Simulation Parameters used for Figure 9.4

| Simulation Parameters | | Driver Parameters | | Witness Parameters | |
|---|---|---|---|---|---|
| $k_p \Delta\zeta$ | 0.0098 | Source | HiPACE | Source | HiPACE |
| $k_p \Delta x$ | 0.0312 | $k_p \bar{\zeta}$ | 7.247 | $k_p \bar{\zeta}$ | 3.970 |
| $k_p \Delta y$ | 0.0312 | $k_p \bar{x}$ | $-1.628$ | $k_p \bar{x}$ | $-1.654$ |
| $k_p L_\zeta$ | 10.0000 | $k_p \bar{y}$ | $-2.204$ | $k_p \bar{y}$ | $-2.340$ |
| $k_p L_x$ | 16.0000 | $k_p \sigma_\zeta$ | 0.782 | $k_p \sigma_\zeta$ | 0.296 |
| $k_p L_y$ | 16.0000 | $k_p \sigma_x$ | 0.648 | $k_p \sigma_x$ | 0.065 |
| **Plasma Parameters** | | $k_p \sigma_y$ | 1.285 | $k_p \sigma_y$ | 0.052 |
| | | $k_p \epsilon_x$ | 1.505 | $k_p \epsilon_x$ | 0.137 |
| $n_p[\mathrm{cm}^{-3}]$ | $5.0 \times 10^{16}$ | $k_p \epsilon_y$ | 2.515 | $k_p \epsilon_y$ | 0.118 |
| $k_p^{-1}[\mu\mathrm{m}]$ | 23.765 | $\bar{\gamma}$ | 1433.184 | $\bar{\gamma}$ | 2544.750 |
| $E_0[\mathrm{GeV}]$ | 21.502 | $\Delta\gamma[\%]$ | 13144.297 | $\Delta\gamma[\%]$ | 8544.349 |
| $n/n_p(z)$ | 1.0 | | | | |

Table B.36: PIC Simulation Parameters used for Figures 9.11 to 9.13

# LIST OF FIGURES

# BIBLIOGRAPHY

Adli, E, A Ahuja, O Apsimon, R Apsimon, A-M Bachmann, D Barrientos, F Batsch, J Bauche, VK Olsen, M Bernardini, et al. (2018). "Acceleration of electrons in the plasma wakefield of a proton bunch." In: *arXiv preprint arXiv:1808.09759*.

Altarelli, M (2011). "The European X-ray free-electron laser facility in Hamburg." In: *Nuclear Instruments and Methods in Physics Research Section B: Beam Interactions with Materials and Atoms* 269.24, pp. 2845–2849.

An, Weiming, Viktor K Decyk, Warren B Mori, and Thomas M Antonsen Jr (2013). "An improved iteration loop for the three dimensional quasi-static particle-in-cell algorithm: QuickPIC." In: *Journal of Computational Physics* 250, pp. 165–177.

Aschikhin, A., C. Behrens, S. Bohlen, J. Dale, N. Delbos, L. di Lucchio, E. Elsen, J.-H. Erbe, M. Felber, B. Foster, et al. (2016). "The FLASHForward facility at DESY." In: *Nuclear Instruments and Methods in Physics Research Section A: Accelerators, Spectrometers, Detectors and Associated Equipment* 806, pp. 175–183.

Ben-Kiki, Oren, Clark Evans, and Brian Ingerson (2005). "Yaml ain't markup language (yaml$^{\text{TM}}$) version 1.1." In: *yaml. org, Tech. Rep*, p. 23.

Benedetti, C, CB Schroeder, E Esarey, CGR Geddes, and WP Leemans (2010). "Efficient Modeling of Laser-Plasma Accelerators with INF&RNO." In: *Aip conference proceedings*. Vol. 1299. 1. AIP, pp. 250–255.

Blumenfeld, I., C. E. Clayton, F.-J. Decker, M. J. Hogan, C. Huang, R. Ischebeck, R. Iverson, C. Joshi, T. Katsouleas, N. Kirby, et al. (2007). "Energy doubling of 42 GeV electrons in a metre-scale plasma wakefield accelerator." In: *Nature* 445.7129, pp. 741–744.

Borland, M (2001). "Simple method for particle tracking with coherent synchrotron radiation." In: *Physical Review Special Topics-Accelerators and Beams* 4.7, p. 070701.

Borland, Michael (2000). *Elegant: A flexible SDDS-compliant code for accelerator simulation*. Tech. rep. Argonne National Lab., IL (US).

Bulanov, Sergei, Nataria Naumova, Francesco Pegoraro, and Junichi Sakai (1998). "Particle injection into the wave acceleration phase due to nonlinear wake wave breaking." In: *Physical Review E* 58.5, R5257.

Callen, JD (2006). *Fundamentals of Plasma Physics, University of Wisconsin, Madison WI (2006)*.

Charles, K Birdsall and A Bruce Langdon (1985). *Plasma physics via computer simulation*. New York: McGraw-Hill Book Company.

Chen, Francis F (2012). *Introduction to plasma physics*. Springer Science & Business Media.

Chen, Pisin, JM Dawson, Robert W Huff, and T Katsouleas (1985). "Acceleration of electrons by the interaction of a bunched electron beam with a plasma." In: *Physical review letters* 54.7, p. 693.

Courant, E. D. and H. S. Snyder (1958). "Theory of the alternating gradient synchrotron." In: *Annals Phys.* 3. [Annals Phys.281,360(2000)], pp. 1–48. DOI: 10.1016/0003-4916(58)90012-5.

Courant, Richard, Kurt Friedrichs, and Hans Lewy (1928). "Über die partiellen Differenzengleichungen der mathematischen Physik." In: *Mathematische annalen* 100.1, pp. 32–74.

D'Arcy, Richard (2018). "A tunable plasma-based energy dechirper." In: arXiv: 1810.06307 [physics.plasm-ph].

Dawson, J. M (1959). "Nonlinear electron oscillations in a cold plasma." In: *Physical Review* 113.2, p. 383.

Dawson, John M (1983). "Particle simulation of plasmas." In: *Reviews of modern physics* 55.2, p. 403.

Dornmair, I., K. Floettmann, and A. R. Maier (2015). "Emittance conservation by tailored focusing profiles in a plasma accelerator." In: *Physical Review Special Topics-Accelerators and Beams* 18.4, p. 041302.

Edwards, DA and HT Edwards (2008). "Particle colliders for high energy physics." In: *Reviews of Accelerator Science and Technology* 1.01, pp. 99–120.

Esarey, E, CB Schroeder, and WP Leemans (2009). "Physics of laser-driven plasma-based electron accelerators." In: *Reviews of Modern Physics* 81.3, p. 1229.

Esarey, Eric, Phillip Sprangle, Jonathan Krall, and Antonio Ting (1996). "Overview of plasma-based accelerator concepts." In: *IEEE Transactions on Plasma Science* 24.2, pp. 252–288.

Esarey, Eric, Phillip Sprangle, Jonathan Krall, Antonio Ting, and Glenn Joyce (1993). "Optically guided laser wake-field acceleration." In: *Physics of Fluids B: Plasma Physics* 5.7, pp. 2690–2697.

Esirkepov, T Zh (2001). "Exact charge conservation scheme for particle-in-cell simulation with an arbitrary form-factor." In: *Computer Physics Communications* 135.2, pp. 144–153.

Floettmann, K. (2003). "Some basic features of the beam emittance." In: *Physical Review Special Topics-Accelerators and Beams* 6.3, p. 034202.

– (2014). "Adiabatic matching section for plasma accelerated beams." In: *Physical Review Special Topics-Accelerators and Beams* 17.5, p. 054402.

Folk, Mike, Albert Cheng, and Kim Yates (1999). "HDF5: A file format and I/O library for high performance computing applications." In: *Proceedings of supercomputing*. Vol. 99, pp. 5–33.

Fonseca, Ricardo A, Luis O Silva, Frank S Tsung, Viktor K Decyk, Wei Lu, Chuang Ren, Warren B Mori, S Deng, S Lee, T Katsouleas, et al. (2002). "OSIRIS: A three-dimensional, fully relativistic particle in cell code for modeling plasma based accelerators." In: *International Conference on Computational Science*. Springer, pp. 342–351.

Forsyth, EB, LM Lederman, and J Sunderland (1965). "The Brookhaven-Columbia plasma lens." In: *IEEE Transactions on Nuclear Science* 12.3, pp. 872–876.

Fuchs, Matthias, Raphael Weingartner, Antonia Popp, Zsuzsanna Major, Stefan Becker, Jens Osterhoff, Isabella Cortrie, Benno Zeitler, Rainer Hörlein, George D Tsakiris, et al. (2009). "Laser-driven soft-X-ray undulator source." In: *Nature physics* 5.11, p. 826.

Geddes, CGR, Cs Toth, J Van Tilborg, E Esarey, CB Schroeder, D Bruhwiler, C Nieter, J Cary, and WP Leemans (2004). "High-quality electron beams from a laser wakefield accelerator using plasma-channel guiding." In: *Nature* 431.7008, p. 538.

Gorbunov, LM and VI Kirsanov (1987). "Excitation of plasma waves by an electromagnetic wave packet." In: *Sov. Phys. JETP* 66.290-294, p. 40.

Grebenyuk, J, A Martinez de la Ossa, T Mehrling, and J Osterhoff (2014). "Beam-driven plasma-based acceleration of electrons with density down-ramp injection at FLASHForward." In: *Nuclear Instruments and Methods in Physics Research Section A: Accelerators, Spectrometers, Detectors and Associated Equipment* 740, pp. 246–249.

Grolimund, D, M Senn, M Trottmann, M Janousch, I Bonhoure, AM Scheidegger, and M Marcus (2004). "Shedding new light on historical metal samples using micro-focused synchrotron X-ray fluorescence and spectroscopy." In: *Spectrochimica Acta Part B: Atomic Spectroscopy* 59.10-11, pp. 1627–1635.

Harlow, Francis H and MW Evans (1955). "A machine calculation method for hydrodynamic problems." In: *LAMS-1956*.

Hidding, B, G Pretzler, JB Rosenzweig, T Königstein, D Schiller, and DL Bruhwiler (2012). "Ultracold electron bunch generation via plasma photocathode emission and acceleration in a beam-driven plasma blowout." In: *Physical review letters* 108.3, p. 035001.

Huang, Chengkun, Viktor K Decyk, Chuang Ren, M Zhou, Wei Lu, Warren B Mori, James H Cooley, Thomas M Antonsen Jr, and T Katsouleas (2006). "QUICKPIC: A highly efficient particle-in-cell code for modeling wakefield acceleration in plasmas." In: *Journal of Computational Physics* 217.2, pp. 658–679.

Joshi, C, E Adli, W An, CE Clayton, S Corde, S Gessner, MJ Hogan, M Litos, W Lu, KA Marsh, et al. (2018). "Plasma wakefield acceleration experiments at FACET II." In: *Plasma Physics and Controlled Fusion* 60.3, p. 034001.

Keinigs, Rhon and Michael E Jones (1987). "Two-dimensional dynamics of the plasma wakefield accelerator." In: *The Physics of fluids* 30.1, pp. 252–263.

Kneip, S., C. McGuffey, J. L. Martins, S. F. Martins, C. Bellei, V. Chvykov, F. Dollar, R. Fonseca, C. Huntington, G. Kalintchenko, et al. (2010). “Bright spatially coherent synchrotron X-rays from a table-top source.” In: *Nature Physics* 6.12, pp. 980–983.

Lehe, Remi, Carl B Schroeder, J-L Vay, Eric Esarey, and Wim P Leemans (2017). “Saturation of the Hosing Instability in Quasilinear Plasma Accelerators.” In: *Physical review letters* 119.24, p. 244801.

Levin, WP, H Kooy, JS Loeffler, and TF DeLaney (2005). “Proton beam therapy.” In: *British journal of Cancer* 93.8, p. 849.

Lotov, KV (2003). “Fine wakefield structure in the blowout regime of plasma wakefield accelerators.” In: *Physical Review Special Topics-Accelerators and Beams* 6.6, p. 061301.

– (2004). “Blowout regimes of plasma wakefield acceleration.” In: *Physical Review E* 69.4, p. 046405.

– (2005). “Efficient operating mode of the plasma wakefield accelerator.” In: *Physics of Plasmas* 12.5, p. 053105.

Marsh, K. A., C. E. Clayton, D. K. Johnson, C. Huang, C. Joshi, W. Lu, W. B. Mori, M. Zhou, C. D. Barnes, F.-J. Decker, et al. (2005). “Beam matching to a plasma wake field accelerator using a ramped density profile at the plasma boundary.” In: *Particle Accelerator Conference, 2005. PAC 2005. Proceedings of the*. IEEE, pp. 2702–2704.

Maxwell, James Clerk (1873). *A Treatise on Electricity and Magnetism*. Vol. 1. Clarendon Press.

Mehrling, T. J., R. E. Robson, J.-H. Erbe, and J. Osterhoff (Sept. 2016). “Efficient numerical modelling of the emittance evolution of beams with finite energy spread in plasma wakefield accelerators.” In: *Nuclear Instruments and Methods in Physics Research A* 829, pp. 367–371. DOI: 10.1016/j.nima.2016.01.091.

Mehrling, T., C. Benedetti, C. B. Schroeder, and J. Osterhoff (2014). “HiPACE: a quasi-static particle-in-cell code.” In: *Plasma physics and controlled fusion* 56.8, p. 084012.

Mehrling, T., R. A. Fonseca, A. Martinez de la Ossa, and J. Vieira (2017). “Mitigation of the hose instability in plasma-wakefield accelerators.” In: *Physical Review Letters* 118.17, p. 174801.

Mehrling, T., J. Grebenyuk, F. S. Tsung, K. Floettmann, and J. Osterhoff (2012). “Transverse emittance growth in staged laser-wakefield acceleration.” In: *Physical Review Special Topics-Accelerators and Beams* 15.11, p. 111303.

Mehrling, Timon Johannes (2014). “Theoretical and numerical studies on the transport of transverse beam quality in plasma-based accelerators.” PhD thesis. Universität Hamburg.

Mehrling, TJ, RA Fonseca, A Martinez de la Ossa, and J Vieira (2017). “Mitigation of the hose instability in plasma-wakefield accelerators.” In: *Physical review letters* 118.17, p. 174801.

Meyer-ter-Vehn, J, A Pukhov, and Zh-M Sheng (2001). “Relativistic laser plasma interaction.” In: *Atoms, Solids, and Plasmas in Super-Intense Laser Fields*. Springer, pp. 167–192.

Michel, P., C. B. Schroeder, B. A. Shadwick, E. Esarey, and W. P. Leemans (2006). "Radiative damping and electron beam dynamics in plasma-based accelerators." In: *Physical Review E* 74.2, p. 026501.

Modena, A, Z Najmudin, AE Dangor, CE Clayton, KA Marsh, C Joshi, Victor Malka, CB Darrow, C Danson, D Neely, et al. (1995). "Electron acceleration from the breaking of relativistic plasma waves." In: *nature* 377.6550, p. 606.

Mora, Patrick and Thomas M Antonsen Jr (1996). "Electron cavitation and acceleration in the wake of an ultraintense, self-focused laser pulse." In: *Physical Review E* 53.3, R2068.

Mora, Patrick and Thomas M Antonsen Jr (1997). "Kinetic modeling of intense, short laser pulses propagating in tenuous plasmas." In: *Physics of Plasmas* 4.1, pp. 217–229.

Nicholson, Dwight Roy (1983). *Introduction to plasma theory*. Wiley New York.

Ossa, A Martinez de la, J Grebenyuk, T Mehrling, L Schaper, and J Osterhoff (2013). "High-quality electron beams from beam-driven plasma accelerators by wakefield-induced ionization injection." In: *Physical review letters* 111.24, p. 245003.

Ossa, A Martinez de la, Z Hu, MJV Streeter, TJ Mehrling, O Kononenko, B Sheeran, and J Osterhoff (2017). "Optimizing density down-ramp injection for beam-driven plasma wakefield accelerators." In: *Physical Review Accelerators and Beams* 20.9, p. 091301.

Ossa, A Martinez de la, TJ Mehrling, and J Osterhoff (2018). "Intrinsic Stabilization of the Drive Beam in Plasma-Wakefield Accelerators." In: *Physical Review Letters* 121.6, p. 064803.

Oz, E, S Deng, T Katsouleas, P Muggli, CD Barnes, I Blumenfeld, FJ Decker, P Emma, MJ Hogan, R Ischebeck, et al. (2007). "Ionization-induced electron trapping in ultrarelativistic plasma wakes." In: *Physical review letters* 98.8, p. 084801.

Petrov, GM and J Davis (2011). "A generalized implicit algorithm for multi-dimensional particle-in-cell simulations in Cartesian geometry." In: *Physics of Plasmas* 18.7, p. 073102.

Pritchett, Philip L (2003). "Particle-in-Cell Simulation of Plasmas—A Tutorial." In: *Space Plasma Simulation*. Springer, pp. 1–24.

Reiser, Martin (2008). *Theory and design of charged particle beams*. John Wiley & Sons.

Robson, RE, T Mehrling, and J Osterhoff (2015). "Phase-space moment-equation model of highly relativistic electron-beams in plasma-wakefield accelerators." In: *Annals of physics* 356, pp. 306–319.

Rosenzweig, JB, B Breizman, T Katsouleas, and JJ Su (1991). "Acceleration and focusing of electrons in two-dimensional nonlinear plasma wake fields." In: *Physical Review A* 44.10, R6189.

Schaper, Lucas, Lars Goldberg, Tobias Kleinwächter, Jan-Patrick Schwinkendorf, and Jens Osterhoff (2014). "Longitudinal gas-density profilometry for plasma-wakefield acceleration targets." In: *Nuclear*

*Instruments and Methods in Physics Research Section A: Accelerators, Spectrometers, Detectors and Associated Equipment* 740, pp. 208–211.

Seryi, A., M. Hogan, S. Pei, T. Raubenheimer, P. Tenenbaum, T. Katsouleas, U. Duke, C. Huang, C. Joshi, W. Mori, et al. (2009). *A concept of plasma wake field acceleration linear collider (PWFA-LC)*. Tech. rep. Stanford Linear Accelerator Center (SLAC).

Spatschek, KH, EW Laedke, Chr Marquardt, S Musher, and H Wenk (1990). "Dipole and monopole vortices in nonlinear drift waves." In: *Physical review letters* 64.25, p. 3027.

Suk, Hyyong, Nick Barov, James Benjamine Rosenzweig, and E Esarey (2000). "Plasma electron trapping and acceleration in a plasma wake field using a density transition." In: *The Physics Of High Brightness Beams*. World Scientific, pp. 404–417.

Suortti, Pekka and W Thomlinson (2003). "Medical applications of synchrotron radiation." In: *Physics in Medicine & Biology* 48.13, R1.

Swinson, Christina, M Fedurin, MA Palmer, and I Pogorelsky (2018). "ATF Facilities Upgrades and Deflector Cavity Commissioning." In: *Energy (MeV)* 57, p. 80.

Tajima, T and JM Dawson (1979). "Laser electron accelerator." In: *Physical Review Letters* 43.4, p. 267.

Tzoufras, M., W. Lu, F. S. Tsung, C. Huang, W. B. Mori, T. Katsouleas, J. Vieira, R. A. Fonseca, and L. O. Silva (2009). "Beam loading by electrons in nonlinear plasma wakes." In: *Physics of Plasmas* 16.5, p. 056705.

Tzoufras, Michail, W Lu, FS Tsung, C Huang, WB Mori, T Katsouleas, J Vieira, RA Fonseca, and LO Silva (2008). "Beam loading in the nonlinear regime of plasma-based acceleration." In: *Physical review letters* 101.14, p. 145002.

Vay, J-L (2007). "Noninvariance of space-and time-scale ranges under a Lorentz transformation and the implications for the study of relativistic interactions." In: *Physical review letters* 98.13, p. 130405.

– (2008). "Simulation of beams or plasmas crossing at relativistic velocity." In: *Physics of Plasmas* 15.5, p. 056701.

Veksler, VA (1956). "Principles of acceleration of charged particles." In: *The Soviet Journal of Atomic Energy* 1.1, pp. 77–83.

Vieira, J, WB Mori, and P Muggli (2014). "Hosing instability suppression in self-modulated plasma wakefields." In: *Physical Review Letters* 112.20, p. 205001.

Whittum, David H (1997). "Transverse two-stream instability of a beam with a Bennett profile." In: *Physics of Plasmas* 4.4, pp. 1154–1159.

Whittum, David H, William M Sharp, S Yu Simon, Martin Lampe, and Glenn Joyce (1991). "Electron-hose instability in the ion-focused regime." In: *Physical review letters* 67.8, p. 991.

Yee, Kane (1966). "Numerical solution of initial boundary value problems involving Maxwell's equations in isotropic media." In: *IEEE Transactions on antennas and propagation* 14.3, pp. 302–307.

# EIDESSTATTLICHE VERSICHERUNG / DECLARATION ON OATH

Hiermit versichere ich an Eides statt, die vorliegende Dissertationsschrift selbst verfasst und keine anderen als die angegebenen Hilfsmittel und Quellen benutzt zu haben. Die eingereichte schriftliche Fassung entspricht der auf dem elektronischen Speichermedium. Die Dissertation wurde in der vorgelegten oder einer ähnlichen Form nicht schon einmal in einem früheren Promotionsverfahren angenommen oder als ungenügend beurteilt.

Hamburg, January 2019

Alexander Aschikhin